METALLOGRAPHIC INVESTIGATION

OF

THE IRON, IRON-CARBIDE, IRON-BORIDE SYSTEM

Thesis by

Donald S. Clark

In Partial Fulfillment of the Requirements for the Degree of

Doctor of Philosophy

California Institute of Technology,

Pasadena, California,

1934.

TABLE OF CONTENTS

ACKNOWLEDGMENTS

The writer desires to express his appreciation to The Industrial Research Laboratories of Los Angeles, California, for furnishing all materials and much of the equipment used in carrying out this research and for bearing the entire financial burden of the work. Appreciation is expecially extended to Mr. Walter F. Hirsch, Chief Metallurgist of the Industrial Research Laboratories, for his untiring efforts in assisting in the preparation and analysis of alloys for this research. Appreciation is also extended to the other members of the staff of the Industrial Research Laboratories who have made this investigation possible.

Deep appreciation is extended to Professor William Howard Clapp of the California Institute of Technology for his helpful criticism in this work and to all others who have contributed in any way to this investigation.

The writer also wishes to extend his appreciation to Professor G. Tammann of Gottingen, Germany, for suggestions in connection with the literature and to Professor Franz Wever of Dusseldorf, Germany, for his assistance in the review of the literature.

METALLOGRAPHIC INVESTIGATION

OF

THE IRON, IRON-CARBIDE, IRON-BORIDE SYSTEM

INTRODUCTION

This thesis presents the results of certain investigations which the author has carried out during the last three years on alloys of the ternary system iron, iron-carbide, iron-boride. The report deals largely with metallographic features but there is also given a discussion of certain physical properties of a group of these alloys which is commercially important.

The system, iron-carbon, has been investigated and discussed more fully than any other binary alloy. The system, iron-boron, has also been reported upon by a number of investigators. With one exception, no work has been done upon the ternary system. This is probably due to a feeling that these alloys are of no commercial importance. Within the last three years, however, it has been shown that a certain group of these alloys is extremely hard and wear-resistant and that they also possess other valuable properties. Some of these properties are a low melting temperature, an ability to form a strong metallic bond with steel and other alloys, and low thermal conductivity. This combination of properties has made it possible to flow the metal onto a backing surface

of steel to form a thin wear-resistant welded overlay, suitable for liners and other applications requiring wear resistance. Because of its relatively low cost, it competes with other processes such as nitriding, carburizing and chrome plating.

An investigation of the ternary system, iron, carbon, boron was made in 1922 at Göttingen by R. Vögel and G. Tammann. Cooling curves of numerous alloys were determined and used to establish equilibrium relations of the phases. The authors did not discuss the mechanical properties, except for those alloys having a very low boron and carbon content. The work on the equilibrium relations was carefully performed and the present author has been guided by it in his investigation of micro-structure and phase relations.

Some work appears in the literature on the iron-boron system, the most important of which is that by Vögel and Tammann[1], and Wever and Müller[2]. The work of Vögel and Tammann was in connection with their investigation of the ternary system, which has been discussed briefly above. Other work was done on this system by G. Hannesen[3], and N. Tscheschewsky and A. Herdt[4]. In general, Vögel and Tammann, Hannesen, and Tscheschewsky and Herdt agree on the phase relations, with some minor exceptions with regard to transformation temperatures. Wever and Müller at Düsseldorf, however, show some disagreement with the other investigators in the increasing

solubility of boron in gamma iron. They attribute this difference to the impurity of the melts used by the first mentioned investigators in that carbon, silicon, and particularly aluminum being present effected this difference, yielding false results. However, Wever and Müller, in their investigation to determine the effect of these elements on the equilibrium relations of iron and boron, considered only small amounts of carbon. Hence, little information can be obtained from their research with regard to the ternary system as concerns the phase relations and none with regard to the properties of such ternary alloys. The effect of impurities such as silicon and aluminum will be considered in the theoretical considerations in the next section, based on the investigation of Wever and Müller.

In general it can be said, from the existing information, that the effect of boron on iron-carbon alloys low in carbon is to increase hardness and brittleness, resulting in a relatively useless product. No mention has been made of the effect with higher carbon contents, other than the assumption that the same effect is carried to higher carbon alloys. The writer has found by experience that iron-carbon alloys with high carbon contents containing boron have commercial applications because of their resistance to wear. Henceforth in this thesis emphasis will be placed on the alloys with relatively high carbon content.

References:-

1. Vögel and Tammann - Zeit. f. An. und Alge. Chemie 121-123, 225-275.

2. Wever and Müller - Mitl. K. W. Inst. f. Eisenforschung zu. Düsseldorf Band XI L. 12 (1929).

3. Hannesen - Z. anorg. Chem. 89 (1915) S. 257.

4. Tscheschewsky and Herdt - J. Russ. Met. Ges. 1915 Ref. Iron Age 98 (1918) S. 396.

PART I.

THEORETICAL CONSIDERATIONS

In order to give a clear understanding of the experimental results of this research it is necessary to present the phase relations existing in the iron-iron-carbide-iron-boride system.

The equilibrium relations of this ternary system are represented in the usual way by a three-dimensional figure with a triangular base representing the composition and the vertical direction representing temperature. One side of the triangular prism represents the binary system iron-iron carbide, the second side represents the binary system iron-iron boride, and the third side represents the binary system iron carbide-iron boride. The various transformations are represented by surfaces in the space figure.

The phase relations of the binary system iron-iron carbide are represented as shown in Figure 1 with composition plotted as the abscissae and temperature as ordinates. Pure iron is represented at the extreme left of the diagram and pure iron carbide containing 6.67% carbon at the extreme right. This system exhibits a eutectic composed of 4.2% carbon with a melting point of 1150°C., a eutectoid at 0.9% carbon having a transformation temperature of 730°C. The phase fields of this binary system are indicated in the figure. The delta and beta transformations are intentionally omitted because of complications involved in an already complicated system and because of their minor importance in the ternary system which is to be considered.

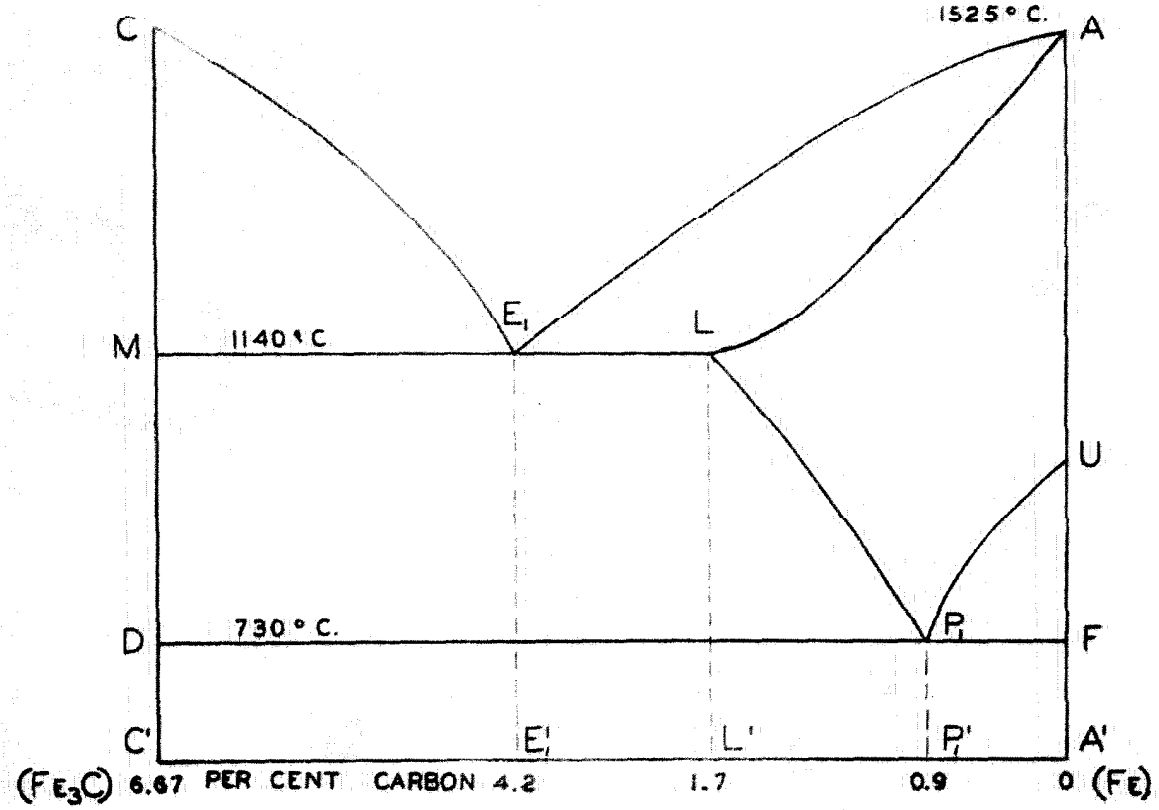

FIG. 1

IRON – IRON CARBIDE SYSTEM

The phase relations of the binary system iron-iron boride are represented as shown in Figure 2 with compositions plotted as abscissae and temperature as ordinates. Considerable argument exists as to the true form of the equilibrium diagram of this binary system. Figure 2 is the diagram proposed by Vogel and Tammann which shows a eutectic with 3.8% boron with a melting point of 1165°C. This diagram also shows that the solubility of boron in gamma iron increases with decreasing temperature to about 780°C. with a maximum of 3.2% boron. It also shows a solubility of boron in alpha iron up to 0.08% boron. The phase fields of this system are indicated in the figure.

Figure 3 shows the diagram proposed by Hannesen which is similar to that of Vogel and Tammann with the exception of the compositions and transformation temperatures.

The results of Tschewsky and Herdt are shown in Figure 4, which is more nearly like that of Vogel and Tammann differing somewhat in compositions and transformation temperatures.

Wever and Müller propose the diagram given in Figure 5 in which they show no increasing solubility of boron in gamma iron. Their contention is that the method of melting the alloys employed in the previous work introduced carbon and silicon which falsified the results of the previous workers. Further, the ferro-boron used in preparing the melts contained about 4.5% aluminum thus leaving the final melts containing about 1% aluminum, which they feel alters considerably the equilibrium conditions of the binary system. Henceforth in their

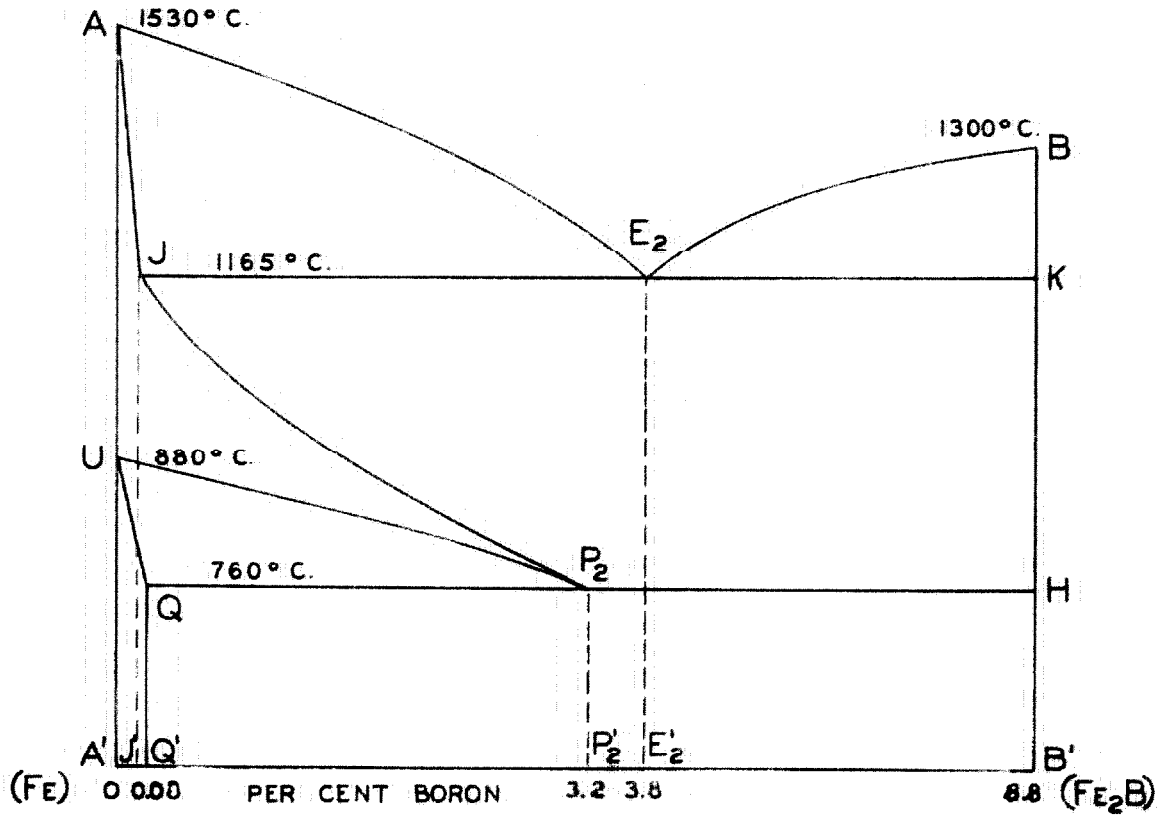

FIG. 2

IRON-IRON BORIDE SYSTEM

TAMMANN

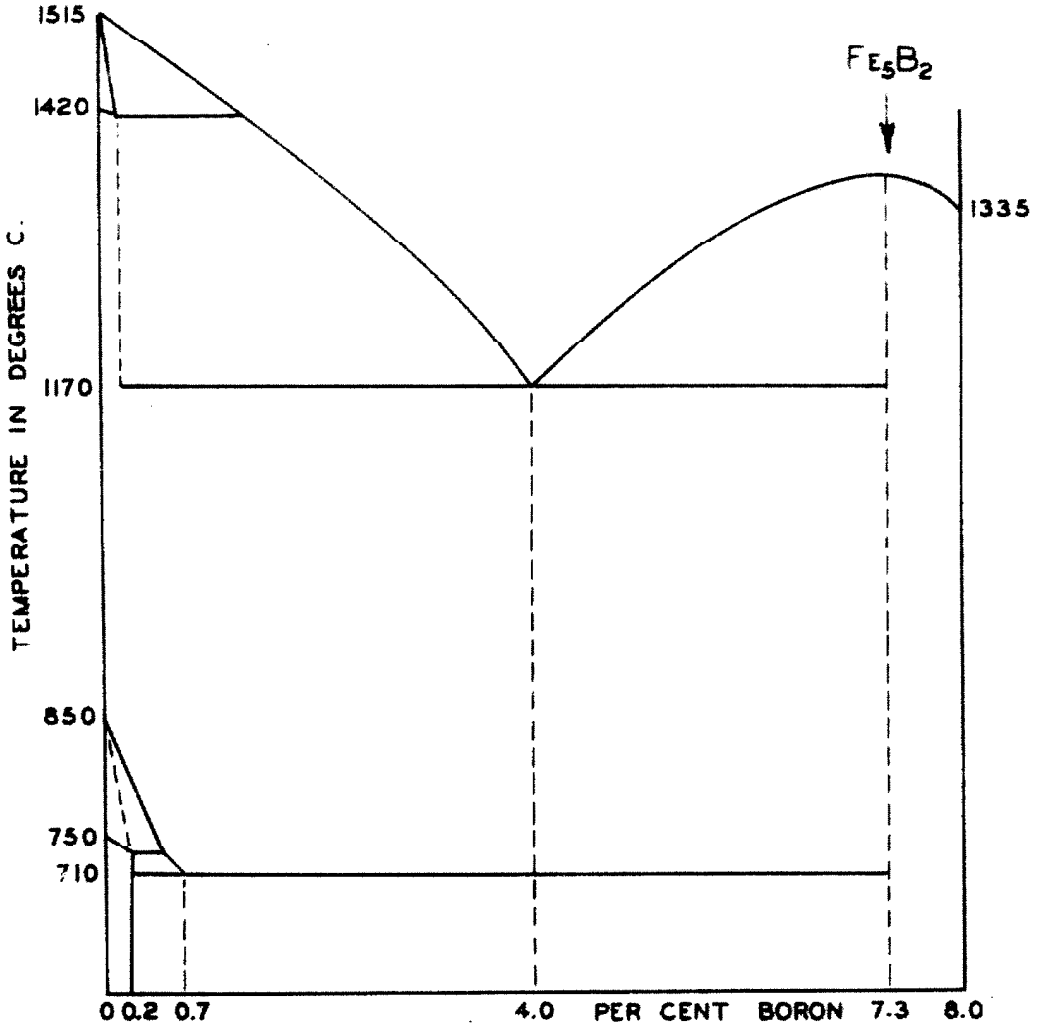

FIG. 3

IRON-IRON BORIDE SYSTEM

HANNESEN

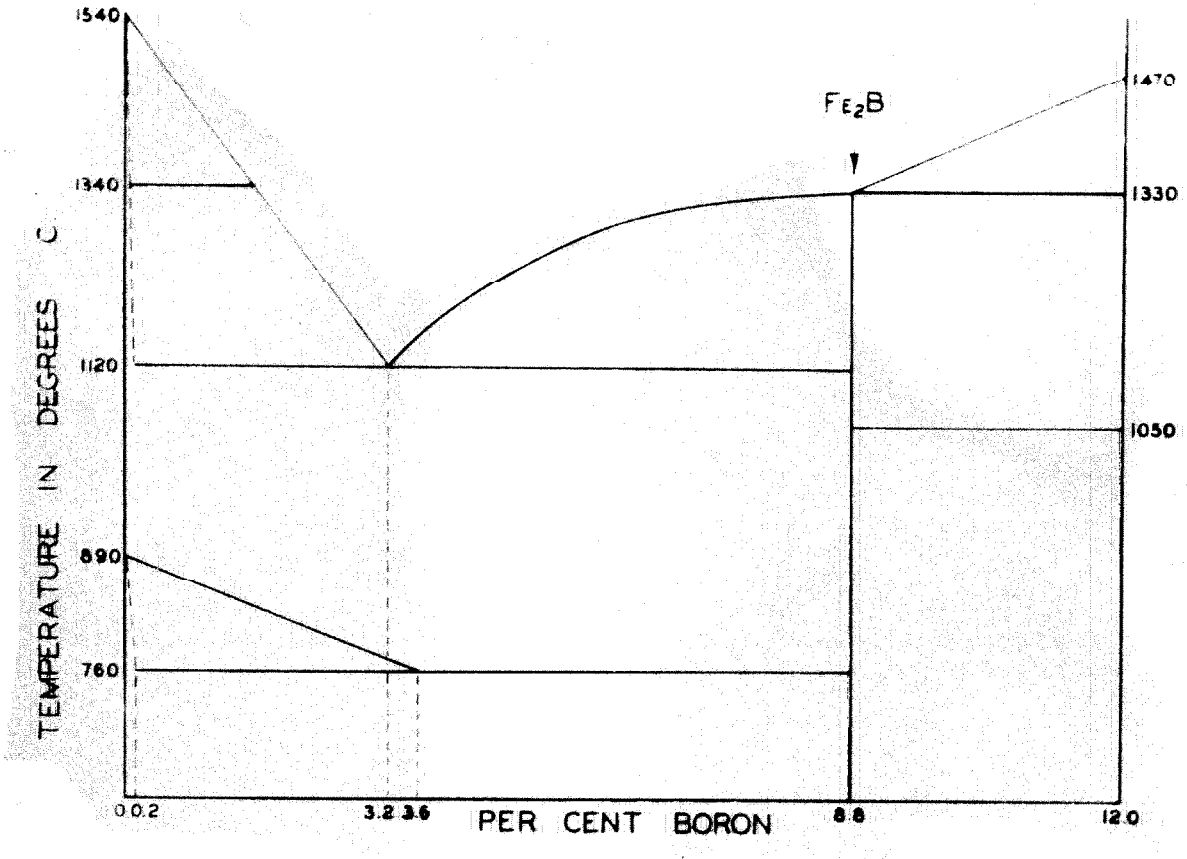

FIG. 4

IRON-BORON SYSTEM

TSCHISCHEWSKY AND HERDT

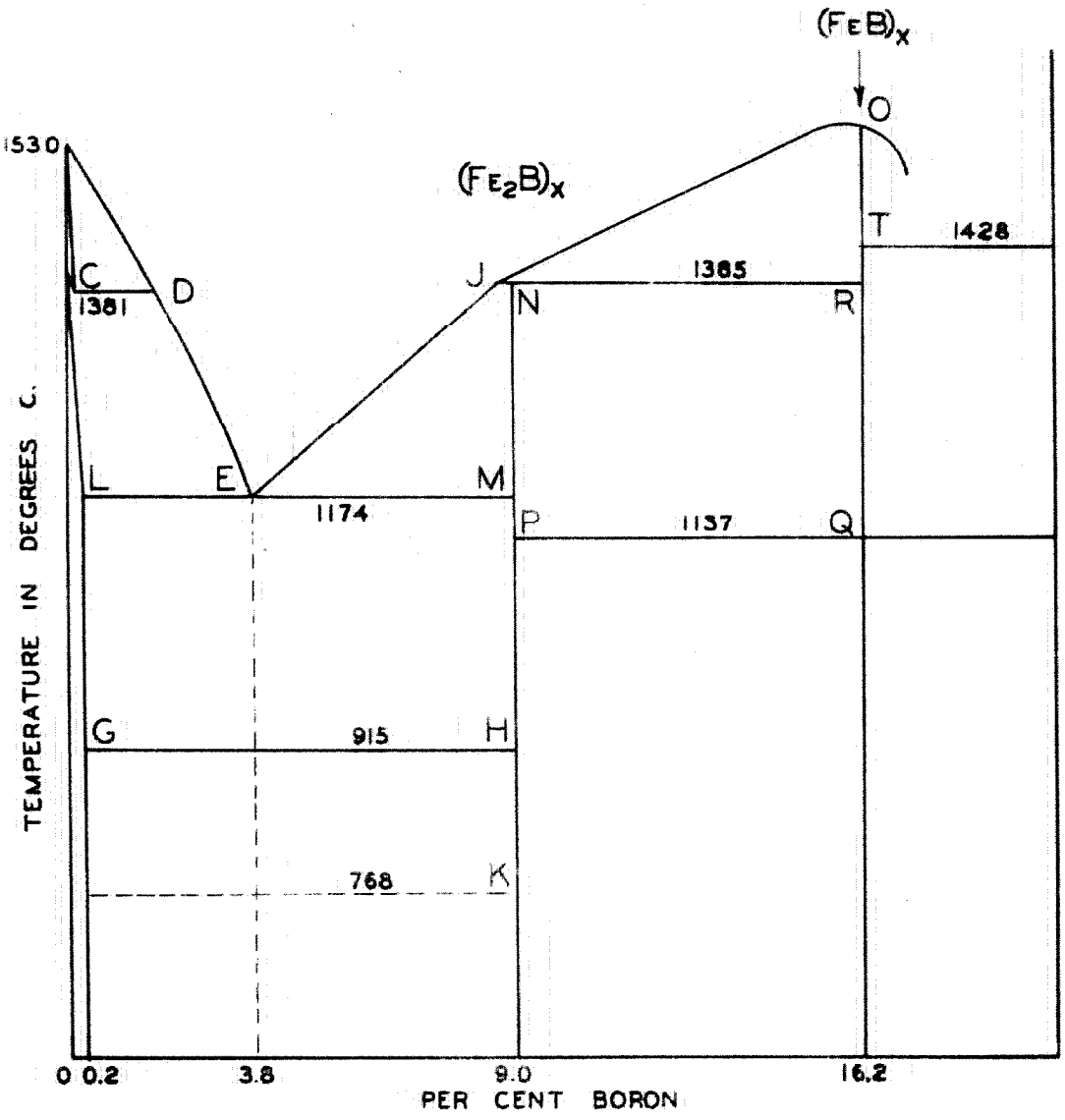

FIG. 5

IRON - BORON SYSTEM

WEVER AND MULLER

research they have attempted to determine the effect of these three elements, carbon, silicon, and aluminum, on the equilibrium diagram of the binary system iron-boron. To do this they studied the effect of each element on the transformation points of iron and assumed an extrapolation of the results in order to obtain their diagram of the binary system.

The work of Wever and Müller can hardly be questioned with regard to accuracy and technique and undoubtedly their diagram is the most correct of the several proposed. According to Wever and Müller the increased solubility of boron in gamma iron is due primarily to very small amounts of carbon. If this is the case, it would be apparent that this condition of increased solubility would occur if not in the pure iron boron alloys, then at a very short distance from the plane of the binary iron boron system. Hence I feel that in the research work for this thesis it is sufficiently accurate to consider that the diagram according to Vogel and Tammann approaches the conditions more closely than that of Wever and Müller. In other words, the surface of the upper limit of solubility of boron in gamma iron, line JP_2 of Figure 2, would turn sharply from the binary plane of iron boron system following the surface as indicated by Tammann and Vogel in their ternary diagram, which will be discussed later.

The phase relations of the binary system iron carbide and iron boride are shown in Figure 6 as proposed by Tammann and Vogel. In this system a eutectic is formed with about 3.2% boron and 4.3% carbon

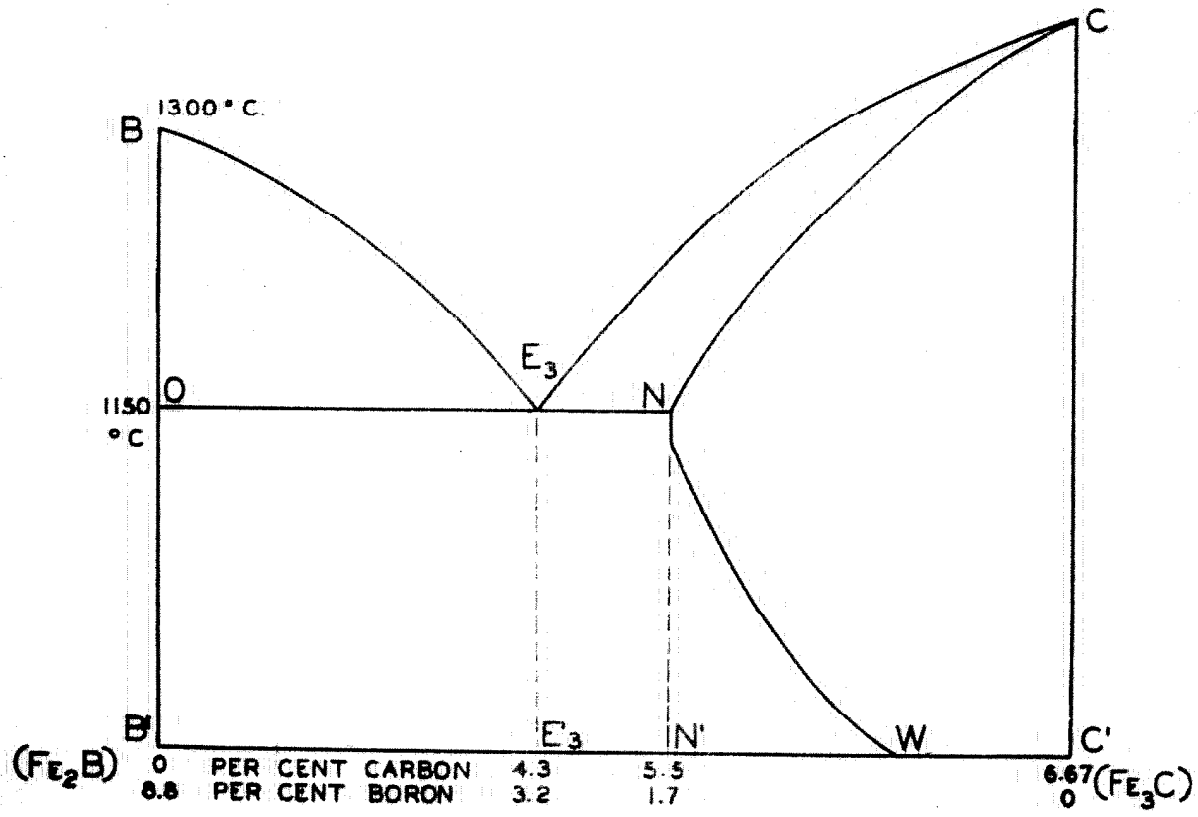

FIG. 6

IRON BORIDE – IRON CARBIDE SYSTEM

TAMMANN

having a melting point at 1150°C. The system shows a solubility of iron boride in iron carbide with a maximum of about 1.7% boron and 5.3% carbon with decreasing solubility with decreasing temperature.

In view of the above discussion the results of Tammann and Vogel will be used to form the three component equilibrium diagram. Hence, Figures 1, 2, and 6 will form the sides of the triangular prism, Figure 7.

In Figure 7 is shown the concentration triangle of the ternary system (iron-iron carbide-iron boride) in which the binary equilibrium diagrams are unflapped. In this figure the projection of the liquid surface is shown bounded by the three eutectic curves $E_1'R'$, $E_2'R'$, and $E_3'R'$ and by the binary liquid curves. The point R' is the projection of the ternary eutectic point onto the concentration triangle. In the discussion to follow, points on the surfaces will be indicated by letters without primes while projected points will be indicated by the corresponding letters with primes. The melting point of this ternary eutectic is 1100°C. In addition to the liquid surfaces, also is shown the boundary of the surfaces of limiting solubility of boron and carbon in gamma iron which terminate in V' along the dotted lines to the level of the ternary eutectic.

According to the diagram there are three types of crystals formed at the liquid surfaces depending upon the region in which the alloy exists. We may call this surface the crystallization surface, i.e., the surface at which crystallization commences. In the field $A'E_1'R'E_2'$ the first crystals to form will be a ternary solid solution composed of gamma iron, carbon and boron, which we may designate with the letter "T".

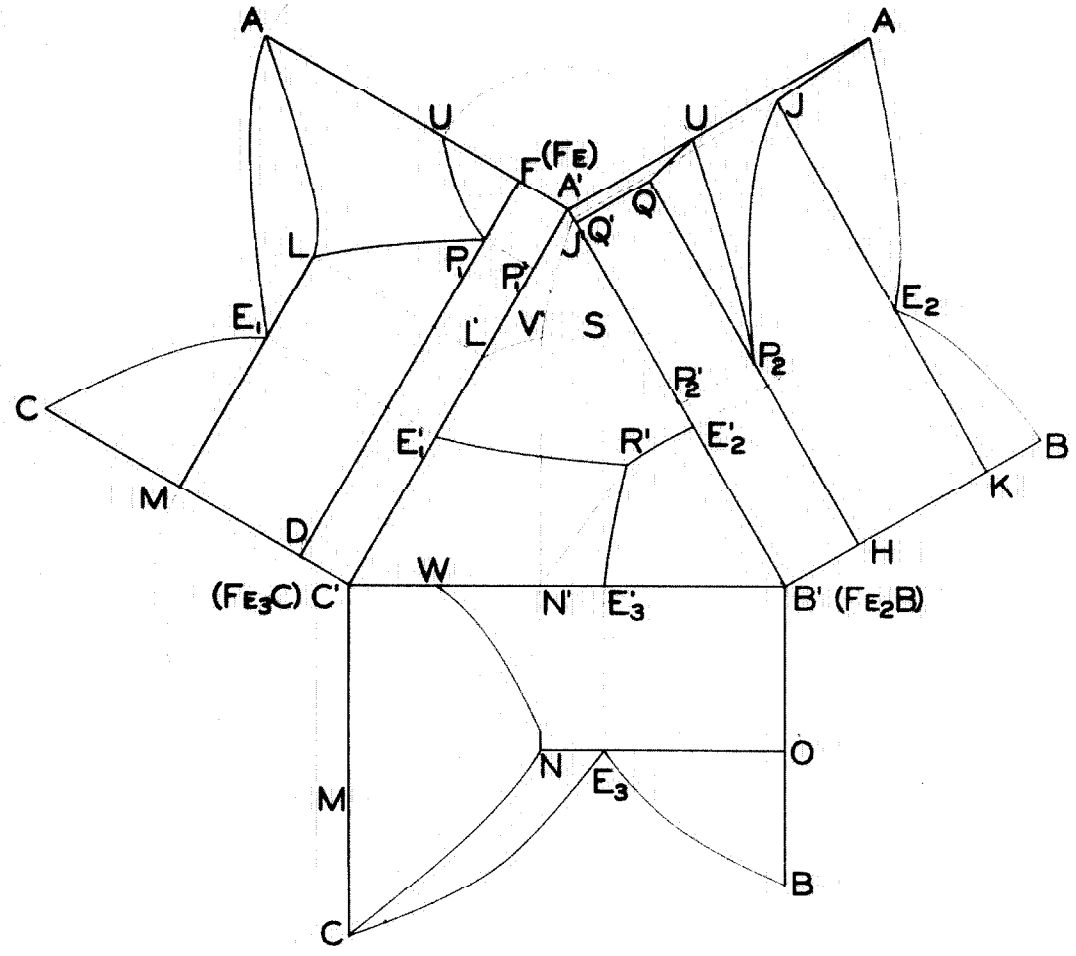

FIG. 7

IRON–IRON CARBIDE–IRON BORIDE SYSTEM

In the field B'E_2'R'E_3' the compound iron boride (Fe_2B) will crystallize upon solidification at the crystallization surface over the field referred to. In the field C'E_1'R'E_3' a solid solution composed of iron carbide and iron boride will form upon crystallization of the melt.

The ternary solid solution T which forms in the field A'E1'R'E_2' changes in composition with decreasing temperature according to the surface A'L'V'J' which we may call a melt surface, since with rising temperature melting will begin when the temperature of the alloy reaches this surface. This surface is bounded by the curve AL on the iron-iron carbide diagram, the curve AJ on the iron-iron boride diagram, the space curve LV, and the space curve JV. Along the curve LV the crystals will be saturated in carbon and along the curve JV they will be saturated in boron, while at V the crystals will be saturated in both carbon and boron.

Upon solidification of alloys in the region L'V'R'E_1' the composition of the melt will move along the surface E_1RE_2A toward the eutectic curve E_1R in some curve until the eutectic curve is reached, whereupon secondary crystallization commences. Alloys in the field J'V'R'E_2' upon solidifying will move along the same surface as mentioned above toward the eutectic curve E_2R in some curve until the eutectic curve is reached, whereupon secondary crystallization will begin. In the region E_2'B'R' the melts will move toward the eutectic curve E_2R on the surface BE_2RE_3 in the same way as in the above case. In the field B'R'E_3' the melt will move along the surface BE_2RE_3 toward the eutectic curve E_3R in a manner

similar to those mentioned above. In the region N'R'E_3' the melt will move along the surface CE_1RE_3 toward the eutectic curve E_3R along some curve until the eutectic curve is reached, whereupon secondary crystallization takes place. In the field C'E_1'R'N' the melt moves toward the eutectic curve E_1R along some curve until it reaches the eutectic curve, whereupon secondary crystallization takes place.

By secondary crystallization is meant crystallization from the melt in which the separation of two types of crystals takes place at the same time and are in equilibrium with the melt. At the end of primary crystallization the composition of the melts will lie along the eutectic curves, as indicated above. Melts lying along the eutectic curve E_1R will be in equilibrium with solid solutions corresponding to the curve LV and with solid solutions corresponding to the curve MN. Melts on the curve E_2R will be in equilibrium with solid solutions corresponding to the curve JV and with the compound iron boride. Melts on E_3R will be in equilibrium with the solid solution N and the iron boride.

A tertiary crystallization will occur for all alloys lying in the composition range V'N'B', since the melts of alloys in this field end in the ternary eutectic point R. The melts ending with this composition precipitate the ternary solid solution saturated in iron, carbon, and boron; iron boride; and the solid solution N of iron carbide and iron boride. Since there are four phases in equilibrium at this point, the transformation or precipitation will take place at constant temperature forming a eutectic structure.

To summarize the foregoing material it might be well to explain what occurs during the crystallization of alloys in the various fields and thereby clarify the conception of the various surfaces existing in the ternary system.

Consider an alloy β in the region L'V'R'E_1' of Figure 8. When the temperature of the liquid alloy has reached the crystallization surface at t_1 it will be in equilibrium with a solid of the composition β' which is on the surface ALVJ at the temperature t_1. This solid will be a solid solution of gamma iron, iron carbide and iron boride. As the temperature decreases the composition of the solid will change according to some curve such as drawn between β' and γ'. The composition of the liquid will change from that of β to that of γ in some curve. The line joining the solid and liquid at any temperature must be straight and must also pass through the vertical through β. The points γ and γ' can easily be located if the isotherms are known because only one straight horizontal line can be drawn through β between the curves LV and E_1R at one given temperature. At temperature t_2 the melt γ will be in equilibrium with the ternary solid solution γ' and the binary solid solution γ''. As the temperature decreases secondary crystallization takes place. The composition of the melt changes according to the curve E_1R and the solid solutions according to their respective curves, C_1N and LV. When the temperature has reached t_3 the line

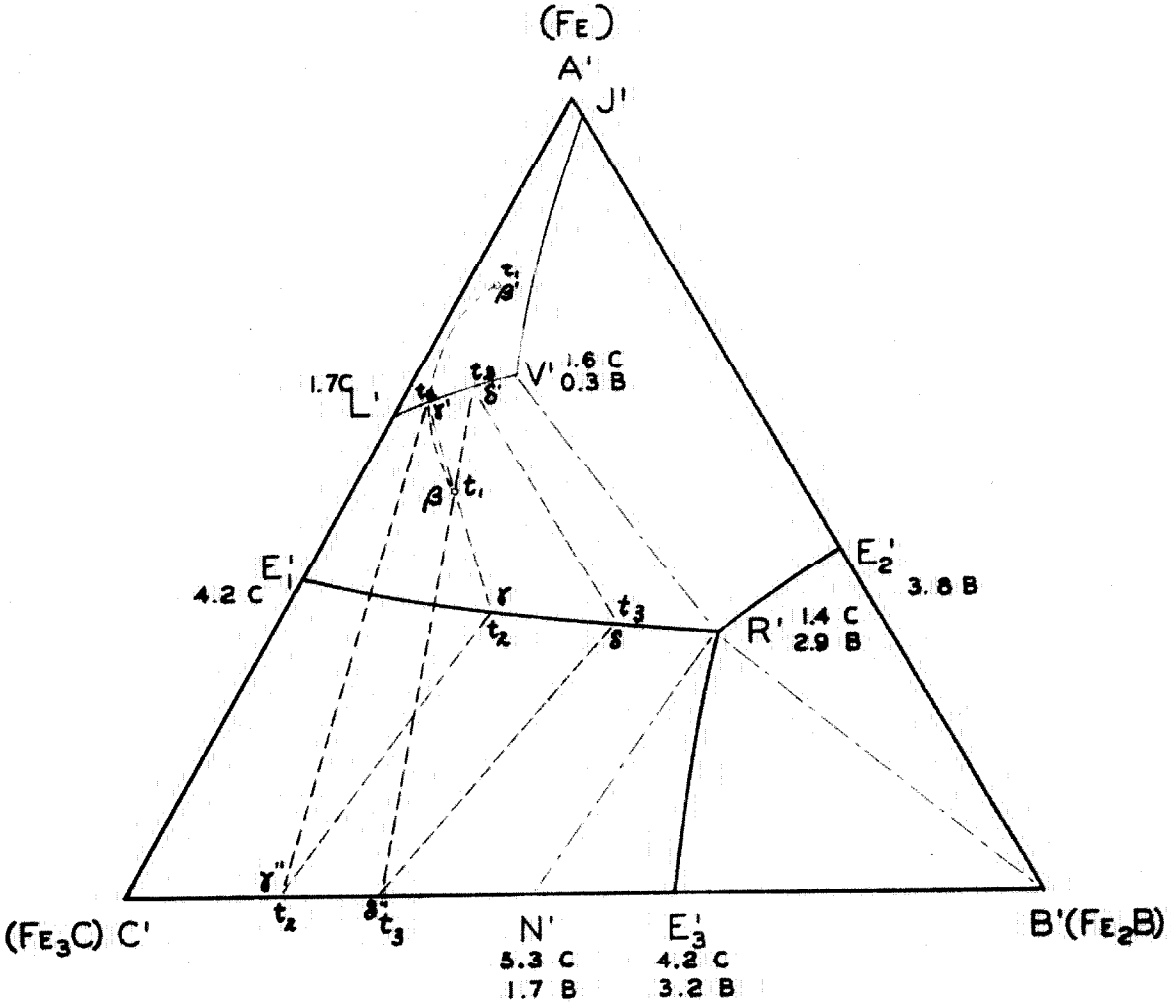

FIG. 8

LIQUID-SOLID SURFACES

connecting delta prime and delta double prime will intersect the vertical through β which indicates that solidification has been completed. The last melt to exist in equilibrium with the solid will be at delta. The triangles formed by the three phases are designated as three phase triangles.

Another way of considering the solidification from the point γ' is to consider the composition of the solid as whole rather than to break it up into its two phases. In this case we would consider the line $\gamma'\gamma$ to rotate around the vertical through β, approaching delta, and γ' approaching β in a curved path which can be easily determined from knowing the position of the isotherms. In this way the lever arm principle can be applied very easily to determine the amounts of phases in equilibrium at any instant.

Now consider an alloy β in the region B'E$_3$'R' of Figure 9. When the termperature of the liquid alloy has reached the crystallization surface at t_1 the melt will be in equilibrium with crystals of iron boride represented at B'. As the temperature continues to decrease more crystals of iron boride will form and the composition of the liquid will follow over the horizontal line γB' until the point γ is reached at temperature t_2 where the primary crystallization will be completed. At this point the melt γ must be in equilibrium with iron boride and the solid solution N'. With further cooling the composition of the melt will change

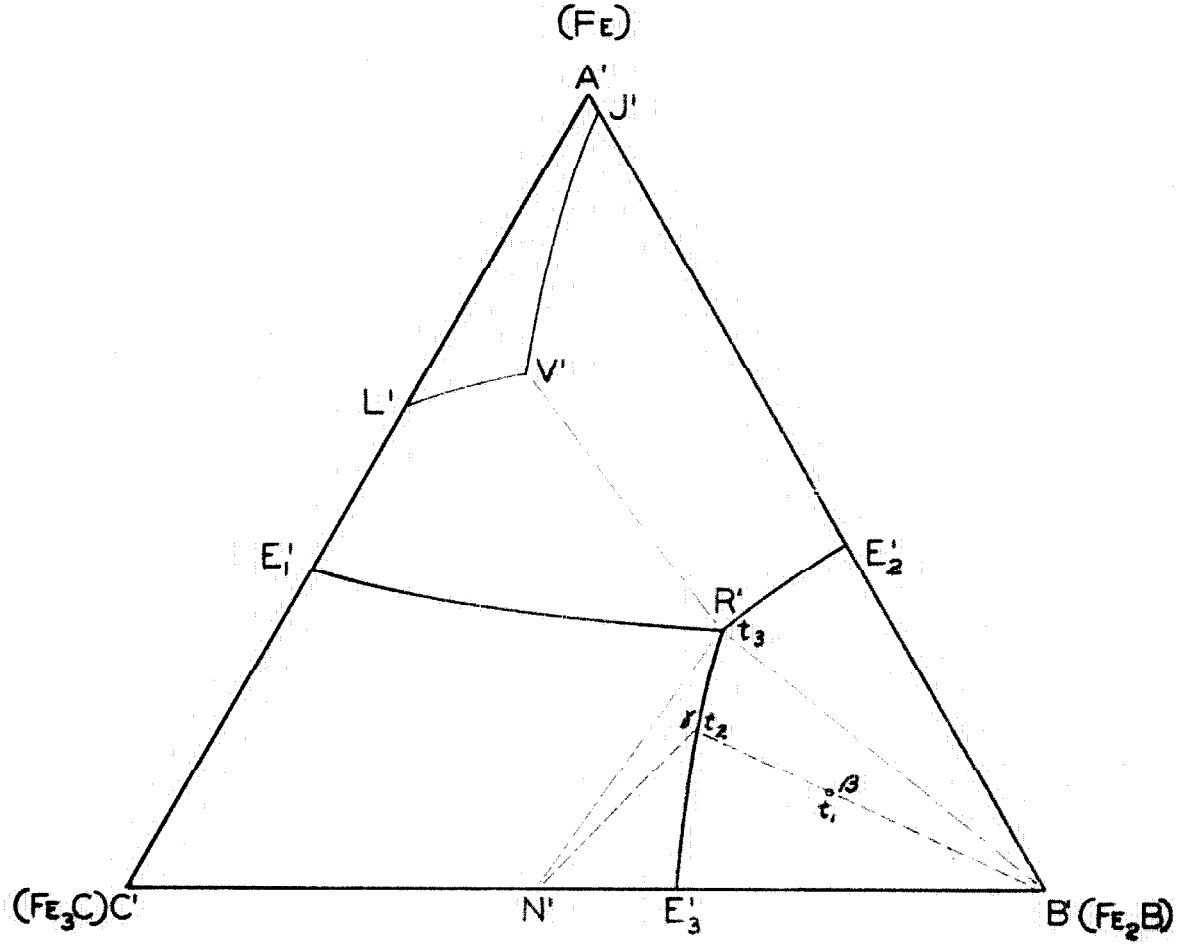

FIG. 9

LIQUID-SOLID SURFACES

according to the curve E_3R and more iron boride will be precipitated and, in addition, solid solution N' will be precipitated. When the temperature t_3 is reached the melt will be of the composition of the ternary eutectic and hence will solidify at constant temperature and will be composed of iron boride, ternary solid solution, and binary solid solution N.

According to the second method of considering the solidification as used in the previous case, when the composition of the melt reaches γ and proceeds along the eutectic curve, the line connecting γ and B' can be considered to turn about the vertical through β thus intersecting the $E_3'B'$ and $E_3'R'$. By this method the relative amounts of each phase can be found by the usual lever arm law.

In the region $E_2'R'V'J'$ the crystallization will be very similar to the process that took place in the region $L'V'R'E_1'$ of Figure 8 except that instead of two solid solutions being in equilibrium with the liquid during the secondary crystallization, there will be an equilibrium between the ternary solid solution represented by the composition along the curve JV and iron boride as represented in Figure 10. In this figure the three phase triangles are given as in the previous cases. The method of analysis is the same as in the previous cases and, hence, will not be taken up again.

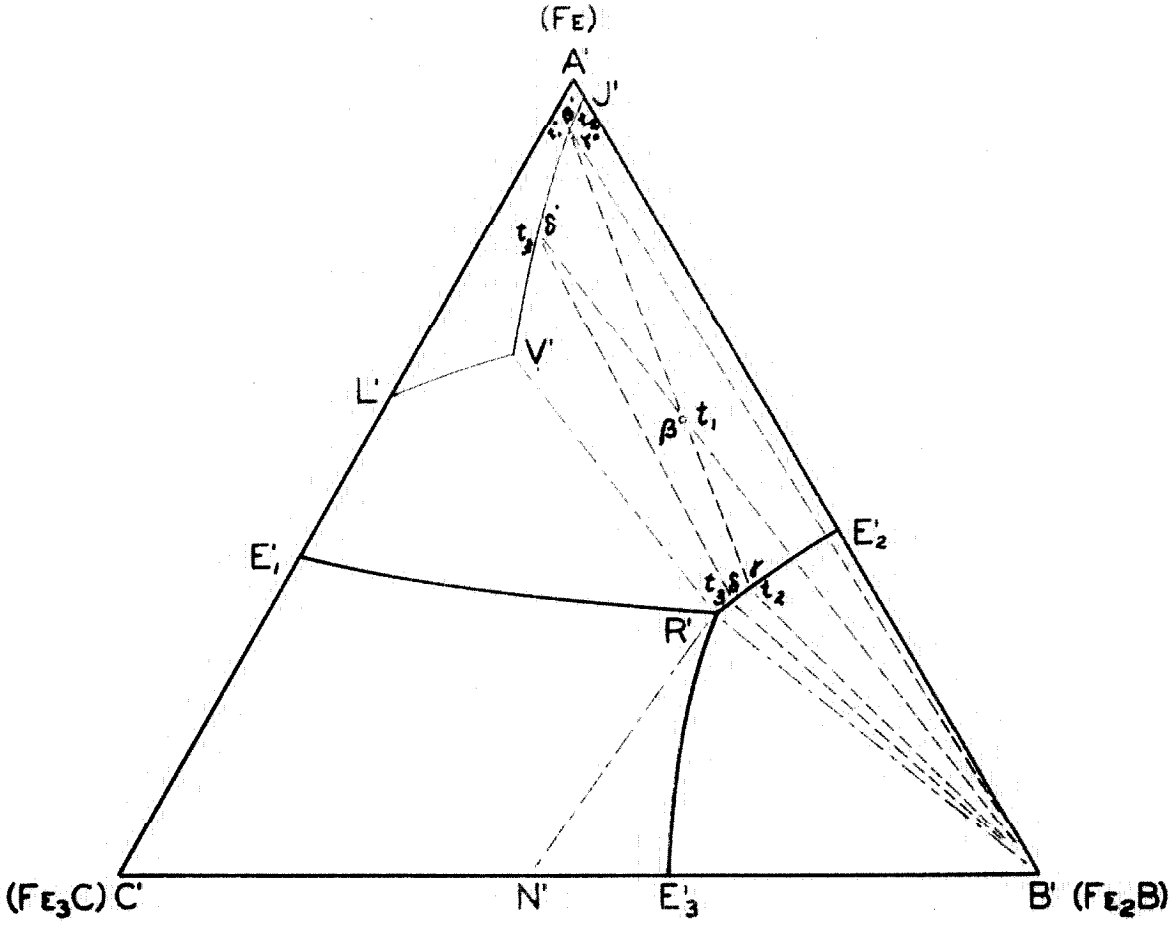

FIG. 10

LIQUID-SOLID SURFACES

Any alloys falling in the region L'V'J'A' will be completely solid at the end of the primary crystallization and will be composed entirely of a ternary solid solution of gamma iron, carbon and boron as represented by its position in the field. An alloy of composition V will end its solidification in a solid solution of gamma iron saturated in both carbon and boron.

The above completes the discussion of the process of crystallization from the melts and it now remains to discuss the transformations in the solid state.

In Figure 11 is shown the concentration triangle on which surfaces of transformation in the solid state are projected. One of the limiting surfaces of the ternary solid solution is given by the projection $J'P_2'SV'J'$ intersecting the iron-iron boride binary system in the curve JP_2. In this case the solubility of boron in gamma iron increases with decreasing temperature. Another of the limiting surfaces of the ternary solid solution is given by the projection $L'V'SP_1'L'$ intersecting the iron-iron carbide binary system in the curve LP_1. This surface shows a decrease in solubility of carbon in gamma iron with decreasing temperature.

Another limiting surface of the ternary solid solution exists in the projection $U'P_2'SP_1'U'$ (U'coincides with A' in the concentration triangle) intersecting the iron-iron boride binary diagram in the curve UP_2 and the iron-iron carbide diagram in the curve UP_1. This surface is the limit of the existence of gamma iron and the

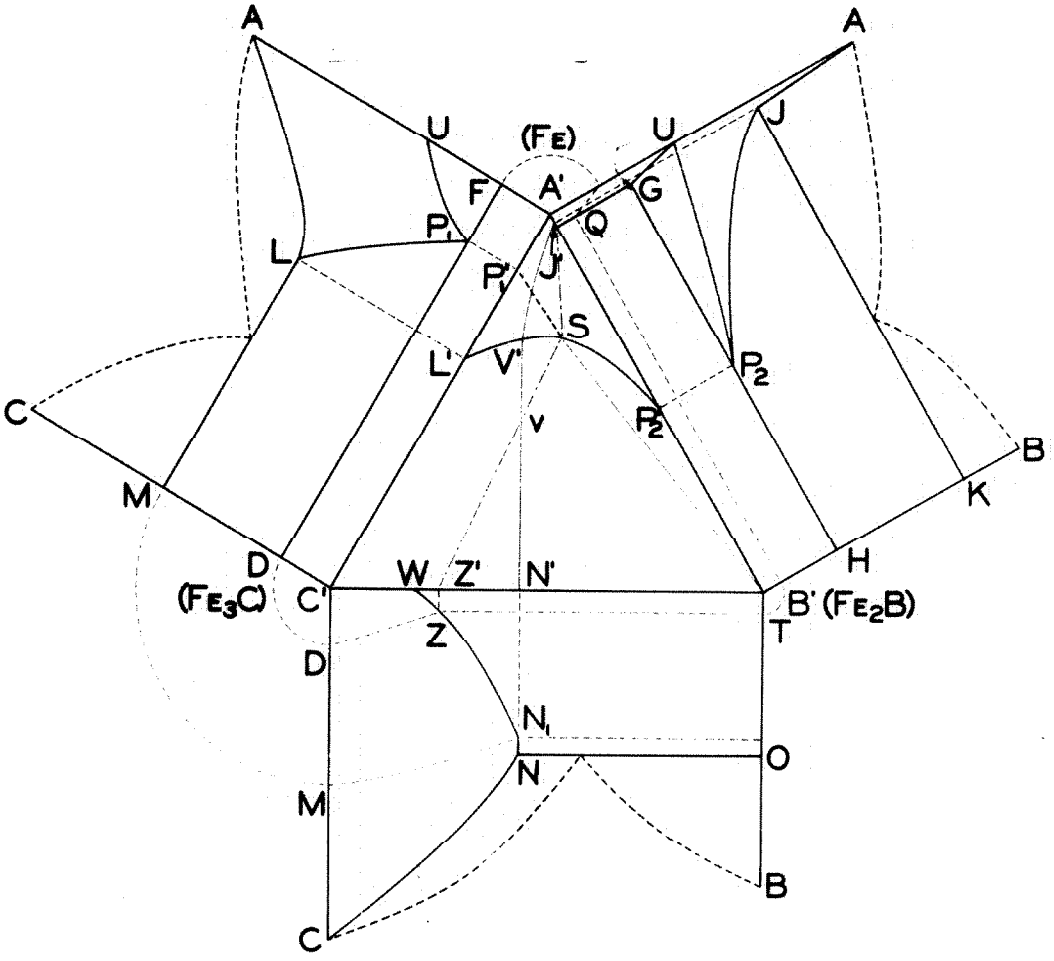

FIG. 11

SOLID TRANSFORMATIONS

beginning of the formation of alpha iron.

In order to make these surfaces clear, let us consider them separately with respect to an alloy within the region of each. In Figure 12 is shown the projection of the surfaces $J'P_2'SV'J'$ and $A'J'V'L'A'$. The cooling of alloys within the region $A'J'V'L'A'$ was considered in crystallization from the liquid state and hence will not be repeated here. Consider an alloy β in the region $J'V'SP_2'J'$, upon completion of crystallization the alloy consisted of ternary solid solution of the composition corresponding to β' and crystals of iron boride. With further cooling the point β' will move toward β over the straight line $\beta'\beta B'$ on the surface under consideration. When the point β is reached the alloy will consist entirely of ternary solid solution of the composition β. Any alloy within the region $P_2'SB'$ would transform in much the same way except that in this case β' would meet the curve P_2S and further transformation would take place along this curve which will be explained later.

Now considering the two surfaces which intersect in P_1S, Figure 13. Take an alloy β in the region $P_2'SQ'$. Above this surface the alloy will be composed entirely of ternary solid solution as noted from the previous example in Figure 12. When the temperature has decreased sufficiently such that the point β touches the plane P_2SP_1U a solid solution of alpha iron and boron will begin to pre-

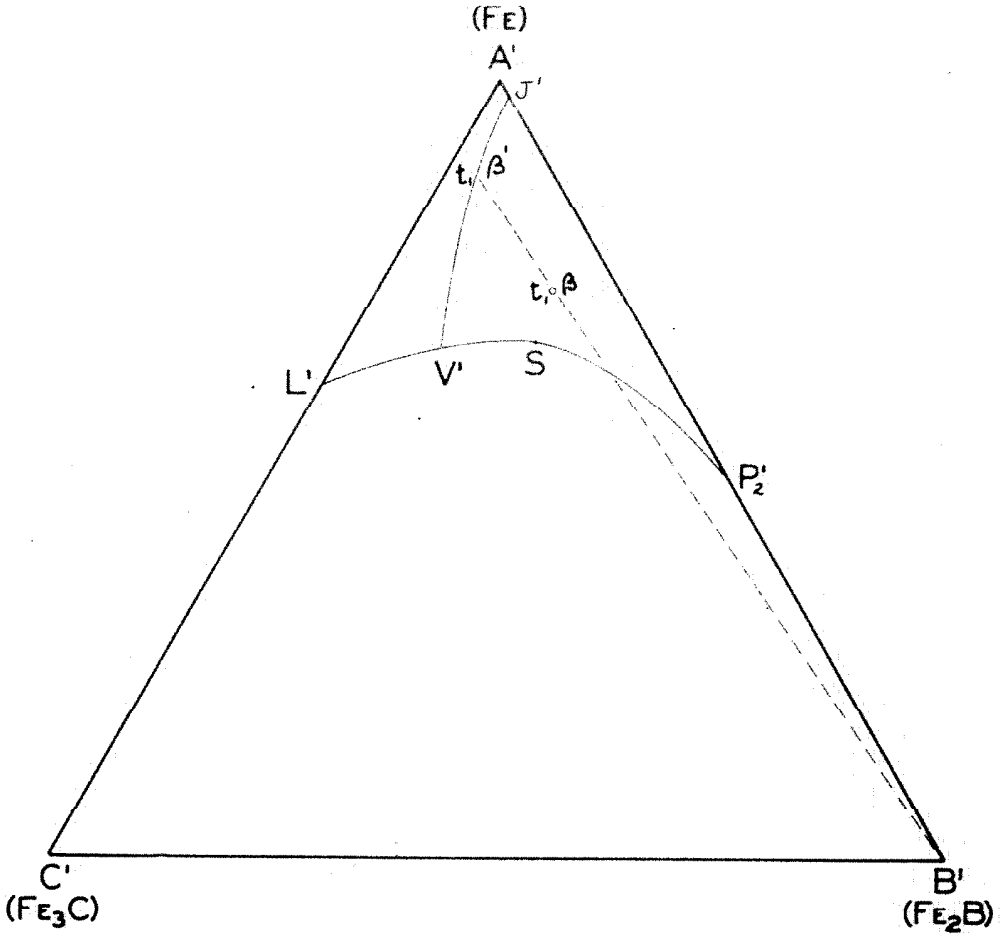

FIG. 12

SOLID TRANSFORMATIONS

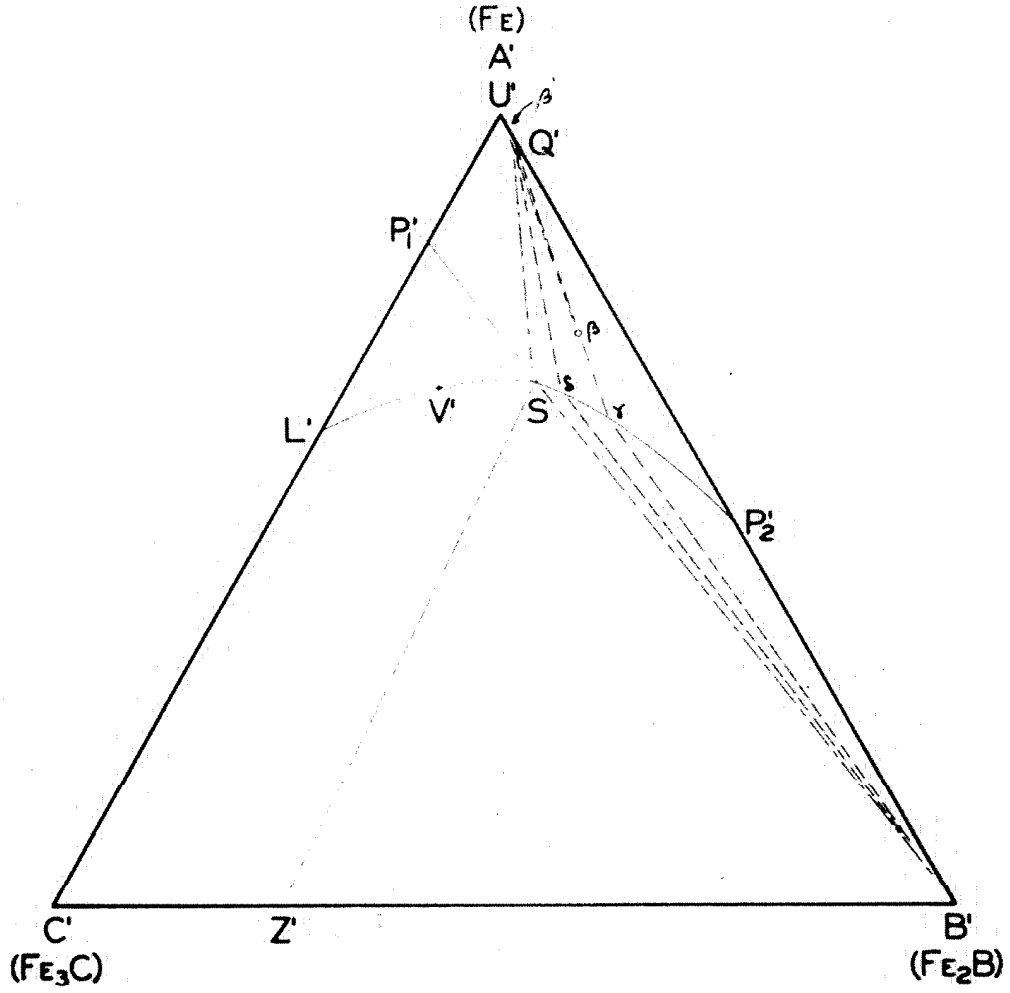

FIG. 13

SOLID TRANSFORMATIONS

cipitate out at β' during further cooling the composition of the alpha solid solution will move on the curve UQ toward Q. At the same time the composition of the ternary solid solution will move on the surface under consideration in some curve from β to γ. When this condition has been reached the ternary solid solution will be in equilibrium with Q' and B'. With further cooling the ternary solid solution moves along the curve P_2S to S passing through the point delta. At S the ternary solid solution of composition corresponding to S is in equilibrium with iron boride (B') and the binary solid solution Q' of iron boride and alpha iron. With further cooling the remaining ternary solid solution transforms into a ternary pearlite composed of iron boride (B'), solid solution of iron boride in alpha iron (Q'), and solid solution of iron boride in iron carbide (Z'). Hence, the resulting alloy will consist of an excess of solid solution Q' and the ternary pearlite. Alloys in the region $P_2'B'S$ will cool in much the same way except that iron boride will continue to precipitate until the curve P_2S is reached. This will produce an alloy with an excess of iron boride with the ternary pearlite.

Consider now an alloy β in the region $P_1'SQ'$ of Figure 14 which will be composed entirely of ternary solid solution above the surface in question. When the temperature has decreased such that β touches the surface under consideration, solid solution of

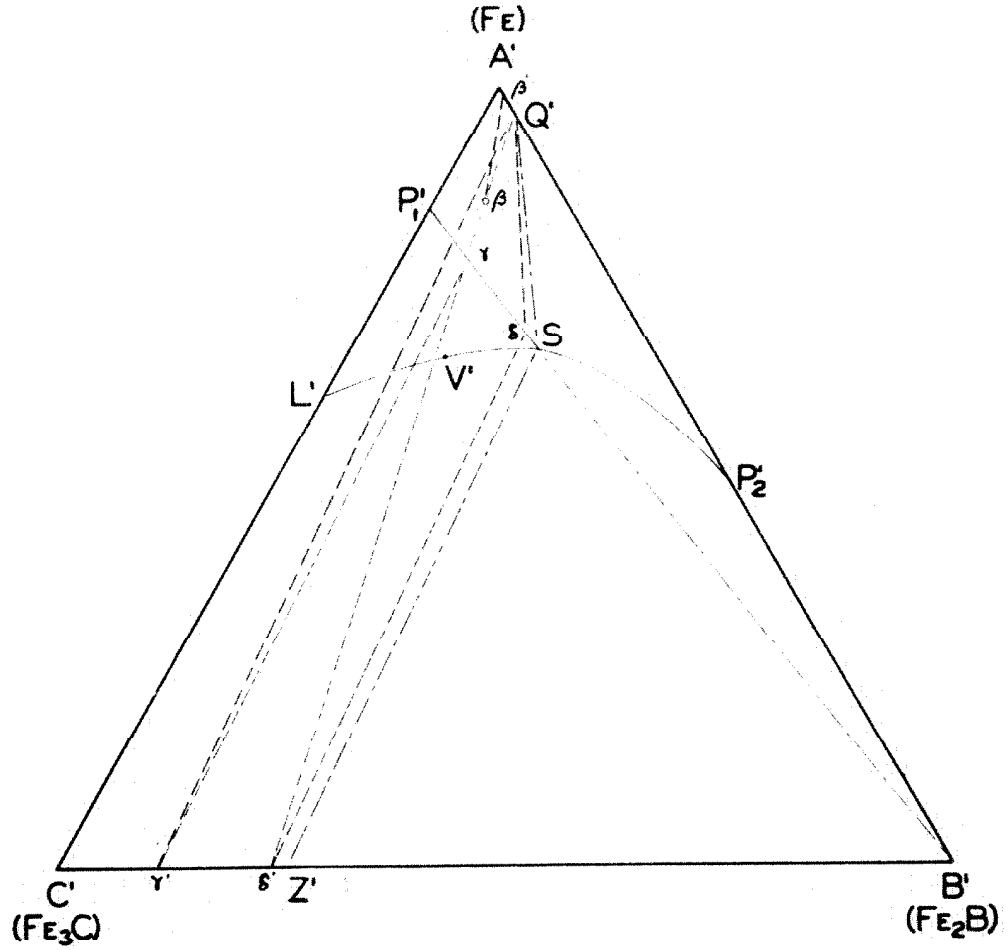

FIG. 14

SOLID TRANSFORMATIONS

alpha iron and boron will be precipitated at β'. With further cooling the composition of the alpha solid solution will change according to the curve UQ and the composition of the ternary solid solution will change along the surface in question moving toward and ending in the point γ on the curve P_1S. At the point γ the ternary solid solution will be in equilibrium with alpha iron boron solid solution and the solid solution of iron boride in iron carbide of composition γ'. With further cooling the composition of the ternary solid solution changes along the curve P_1S. At the temperature at which the line joining Q' and γ' intersects the vertical through β, the ternary solid solution will be completely decomposed, the resulting product being an excess of alpha solid solution with a eutectoid composed of delta prime and Q'. The last composition of the ternary solid solution was that of point delta. If the point β had been within the region Q'Z'B' some ternary pearlite would have been formed.

Alloys lying in the region $P_1'SL'$ will transform in much the same way as in the previous case except when the point β corresponding to the composition in this range touches the surface in question solid solution of iron boride in iron carbide will be precipitated from the ternary solid solution. When β reaches the curve P_1S the transformation will take place as outlined above.

An alloy lying in the region B'SV', in Figure 15, on the surface BVJ will consist of iron boride and ternary solid solution β'. As the temperature is decreased the composition of the ternary solid solution will move on the surface P_2VJ over the straight line $\beta'/\beta B'$ to γ'. At this point the ternary solid solution γ' will be in equilibrium with iron boride and the solid solution γ''. With decreasing temperature the composition of the ternary solid solution will change according to the curve VS moving toward S. The composition of the binary solid solution γ'' will change according to the curve NZ moving toward Z'. When the temperature of S is reached the remaining ternary solid solution will transform to ternary pearlite consisting of Q', B', and Z'. Therefore the resulting alloy should be composed of ternary pearlite, solid solution Z', and iron boride.

Alloys lying in the region N'x'y'B' of Figure 15 will consist of ternary solid solution V', binary solid solution N', and iron boride in the plane of N'V'B'. With decreasing temperature the composition of the ternary solid solution moves down the curve V'S as in the previous case. The composition of the binary solid solution will move down NZ as previously. The end product will consist then of the same phases as in the previous case; namely, ternary pearlite S, iron boride, and binary solid solution Z'.

Alloys in the other portions of this three phase triangle will

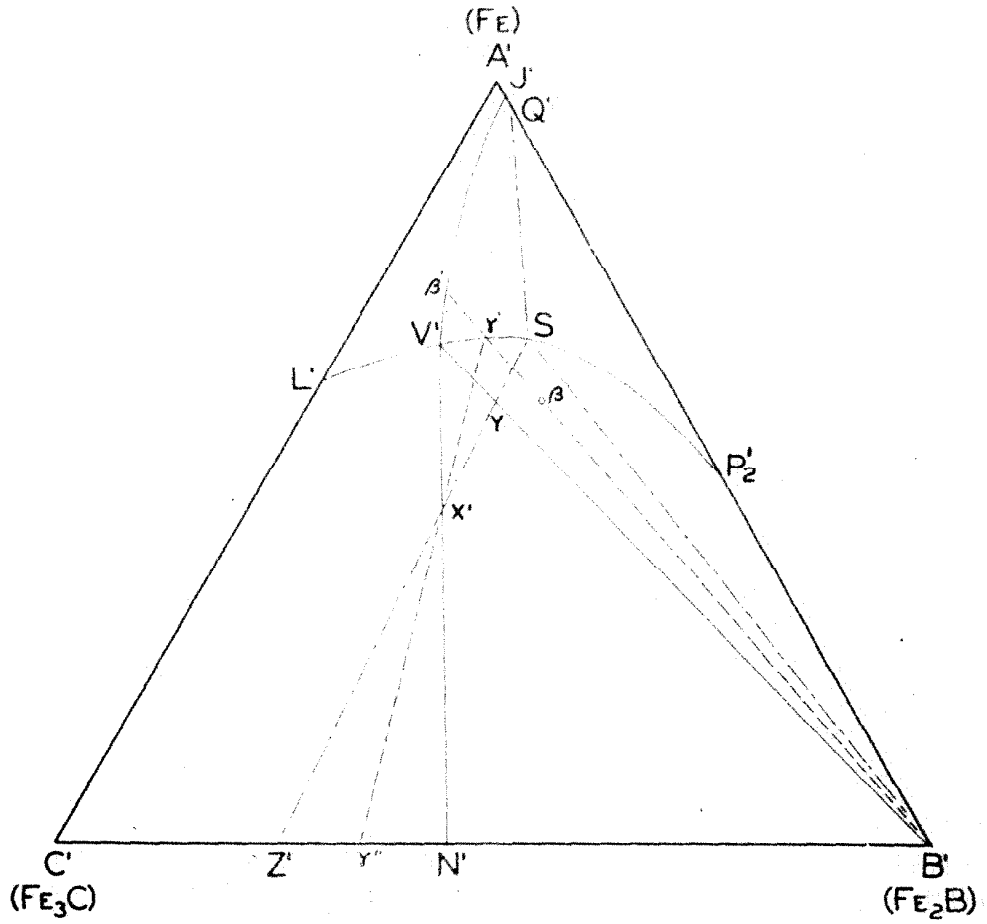

FIG. 15

SOLID TRANSFORMATIONS

decompose in similar manner to the previous case. In these cases just cited it should be noted that the surface N'x'V'SX'Z' has a screw shape.

The phases or constituents in equilibrium in the various areas are shown on the concentration triangle, Figure 16, at room temperature.

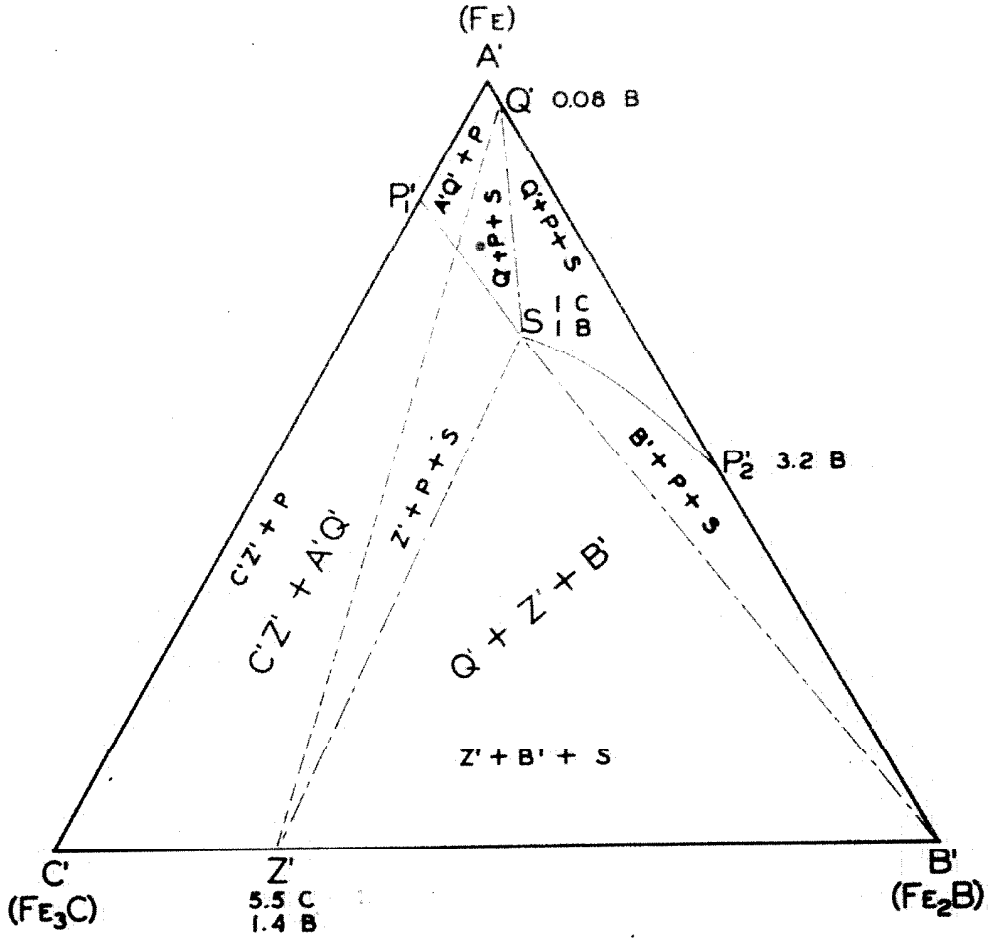

FIG. 16

CONCENTRATION TRIANGLE

PART II.

EXPERIMENTAL CONSIDERATIONS

The experimental part of this research problem may be divided into three parts. First, the investigation of relatively pure alloys of iron, boron, and carbon in order to determine the more nearly perfect structures of the system for comparison with the commercial melts. Second, the investigation of the structure of commercial alloys to study the comparison between the relatively pure melts and their relation to physical properties. Third, the investigation of the physical properties of some of the most important and useful alloys existing in this system.

Experimental Melts

For the first part, seventeen alloys were made up in the induction furnace in which Armco iron, carbon, and Ferro-boron were used as the components. The Ferro-boron was obtained from the Electro Metallurgical Company of New York. It was composed of 19.48% Boron, 1.55% Silicon, 1.34% Aluminum, 0.14% Carbon, and the balance mostly iron. These alloys were melted in Mullite crucibles in small amounts, sufficient for metallographic examinations. The chemical analysis of the alloys produced is given in Table I. The positions of these alloys are plotted in the concentration triangle of Figure 103.

TABLE I.

EXPERIMENTAL ALLOYS

Spec. Number	% C.	% B.	% Si.	% Al.	% P.	Figure Number As Cast	Annealed
1	0.45	3.64				23, 24, 25, 26	27, 28
2	0.23	8.52	0.63	0.37	0.01	17, 18, 19, 20	21, 22
3	1.19	5.86	0.41	0.31	0.01	29, 30, 31	32, 33
4	1.21	4.34				34, 35, 36	37, 38
5	2.83	3.88	0.30	0.08	0.01	43, 44	45, 46
6	2.71	4.20				39, 40	41, 42
8	1.84	3.35				47, 48, 49	50, 51
9	2.18	2.55				62, 63, 64	65, 66
10	3.23	1.16				73, 74, 75	76, 77
11	2.83	2.91				52, 53, 54	55, 56
12	1.21	2.60	0.17	0.09	0.01	83, 84, 85	86, 87
13	2.21	2.31				67, 68, 69, 70	71, 72
14	2.97	2.81				57, 58, 59	60, 61
15	1.22	1.28		0.07		78, 79, 80	81, 82
16	2.14	1.21				88, 89, 90	91, 92
17	2.41	1.18				93, 94, 95	96, 97
18	3.80	0.96	0.04	0.07	0.01	98, 99, 100	101, 102

These alloys were produced by first making an iron carbon alloy from Armco iron and pure carbon in the induction furnace. The proper amount of this iron carbon alloy, Armco iron, and Ferro-boron to make the desired composition was placed in the crucible and covered with borax. The crucible was then placed in the furnace. When the alloy was completely melted it was stirred and then poured into a metal mold. After being cast the alloys were analysed as shown by the table.

After the alloys were cast a portion of each was packed in carbon and annealed at 1800° F. for one hour and allowed to cool slowly from this temperature. In the metallographic description which follows each alloy is given a number. These numbers are shown underlined in Figure 103 from which their composition and position in the ternary system may be seen.

Structures of Experimental Alloys

Let us now consider the structures of these alloys in conjunction with the equilibrium diagram. All specimens were first ground in the automatic polishing machine designed by Professor W. H. Clapp and the author which insured flat surfaces and not too fast but efficient polishing. The specimens were then finished with 600 alundum powder and six hour settlement alumina suspended in water. Most of the specimens were etched five minutes in boiling Murakami's reagent, consisting of 10% sodium hydroxide, 10% potassium Ferricyanide, and

80% distilled water.

A fracture surface of specimen number 2 containing 8.52% boron and 0.23% carbon is shown in Figure 17. The metal itself is very dense, but the ingot showed considerable amount of shrinkage holes. Figure 18 shows the microstructure at a magnification of 100 diameters, Figure 19 at 500 diameters, and Figure 20 at 2000 diameters shows the detail structure. Figures 21 and 22 show the structure after annealing at 1800° F. In this alloy one should expect to find a very large amount of iron carbide and a very small amount of ternary pearlite. The cast structure does not show just this arrangement. Figure 19 shows a ground mass consisting of primary iron boride which separated out during the primary crystallization; the darker stringy structure is composed of the iron boride precipitated from the ternary solution, and the light spots the binary iron carbide-iron boride solid solution precipitated in the ternary pearlite transformation. The structure does not take on the expected appearance because of rapid cooling in the mold. After annealing the two constituents thrown out of solution have agglomerated somewhat although not as completely as shown in Figures 21 and 22.

Figure 23 shows the fracture of specimen number 1 containing 3.64% boron and 0.45% carbon. The fracture shows definite fine needles in a very dense metal. The porosity was not very great, one or two good sized shrinkage holes were observed. Figures 24 to 26,

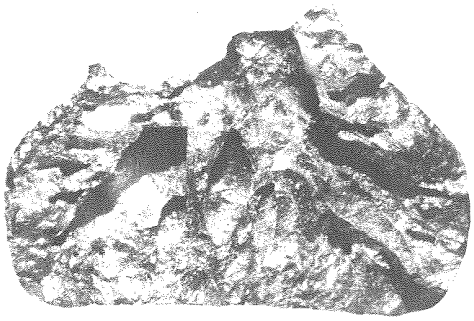

Fig. 17

(2)
As cast
Magnification 2.5X

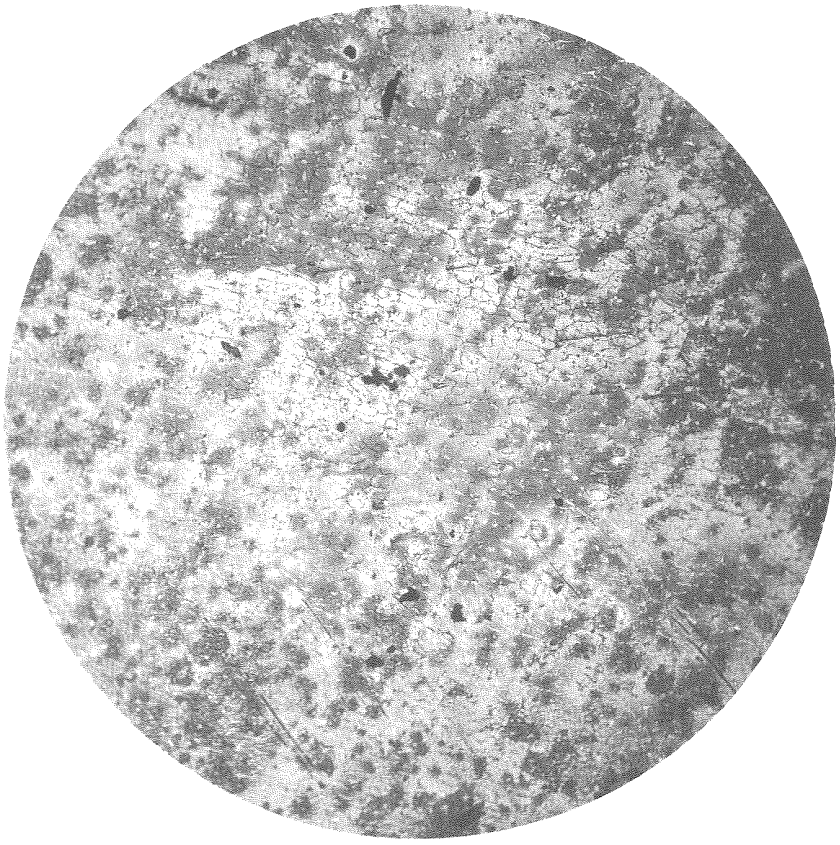

Fig. 18

(2-1)
As cast
Magnification 100X
Etch Murakami

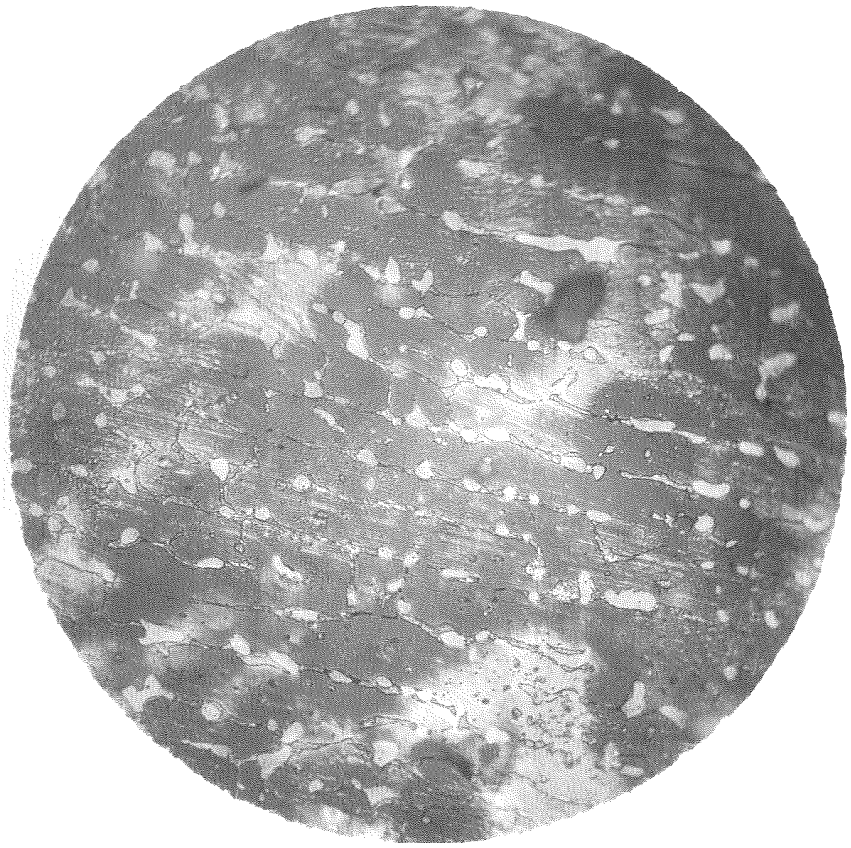

Fig. 19

(2-2)
As cast
Magnification 500X
Etch Murakami

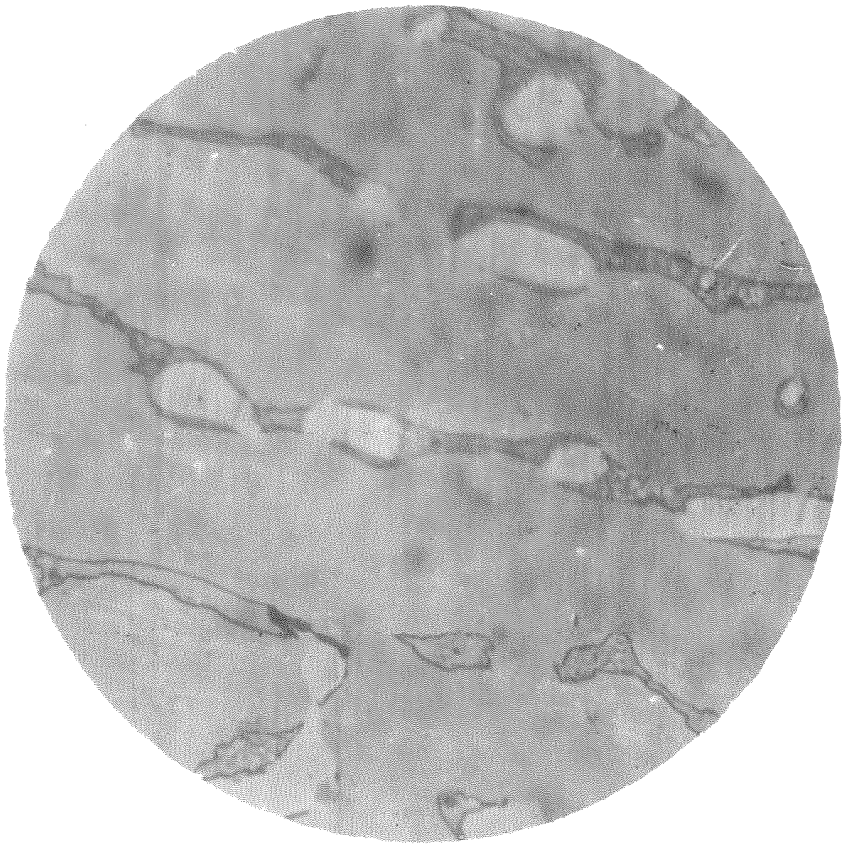

Fig. 20

(2-3)
As cast
Magnification 2000X
Etch Murakami

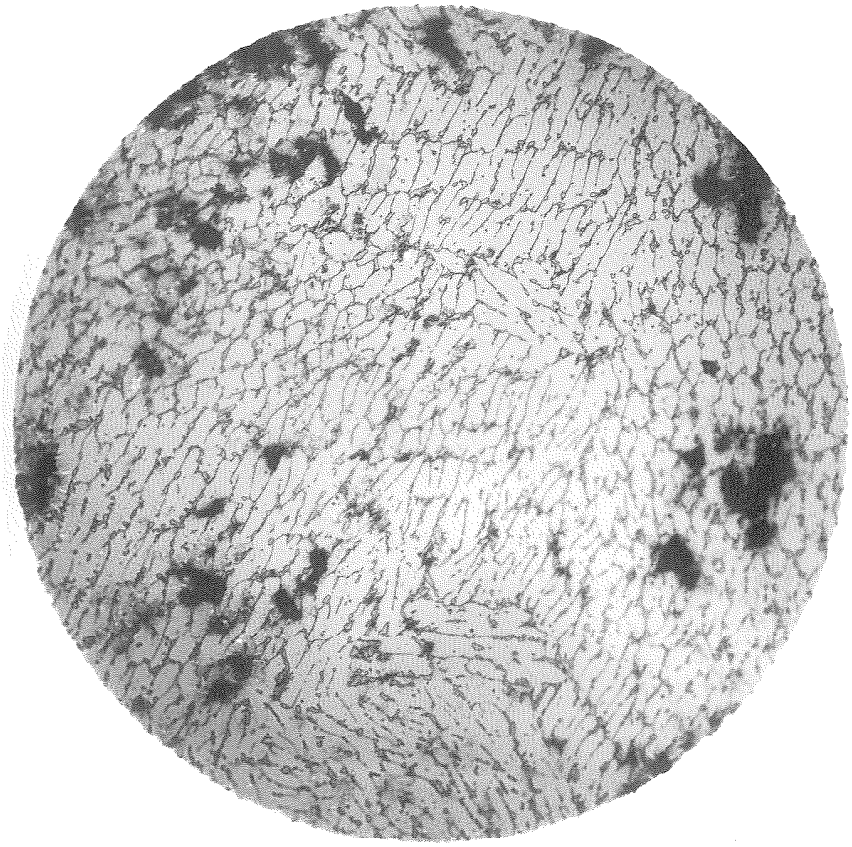

Fig. 21

(2A-1)
Annealed 1800° F.
Magnification 100X
Etch Murakami

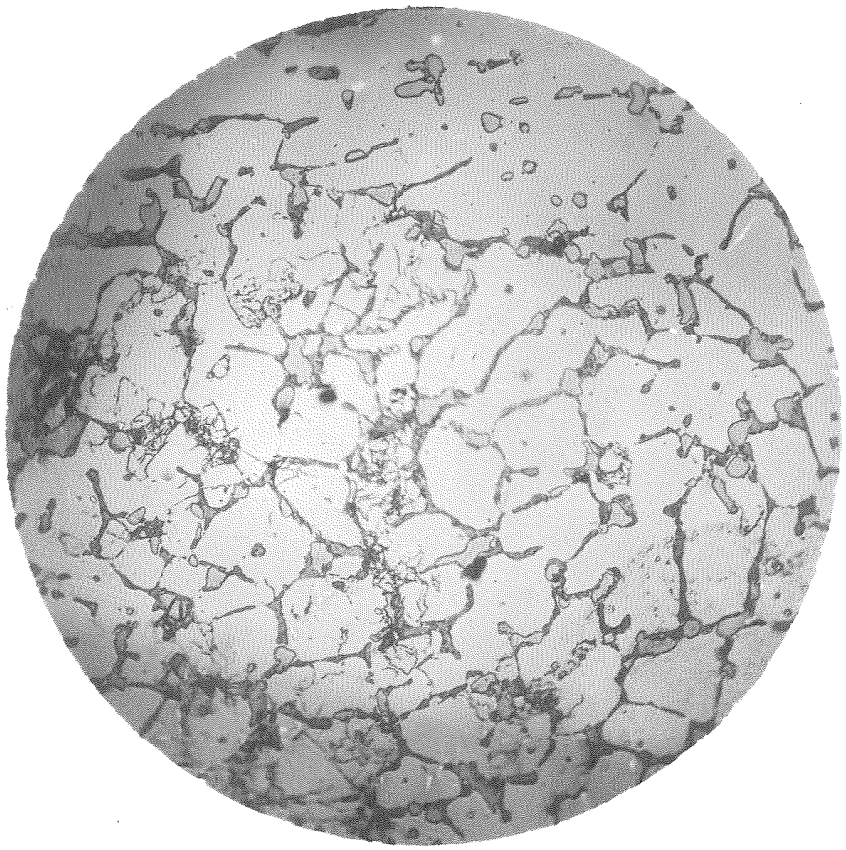

Fig. 22

(2A-2)
Annealed 1800° F.
Magnification 500X
Etch Murakami

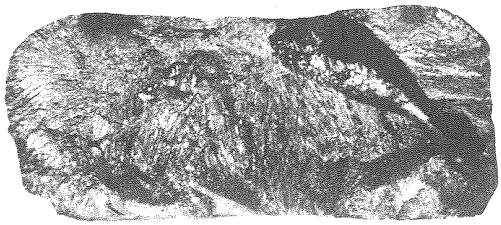

Fig. 23

(1)
As cast
Magnification 2.5X

Fig. 24

(1-1)
As cast
Magnification 100X
Etch Murakami

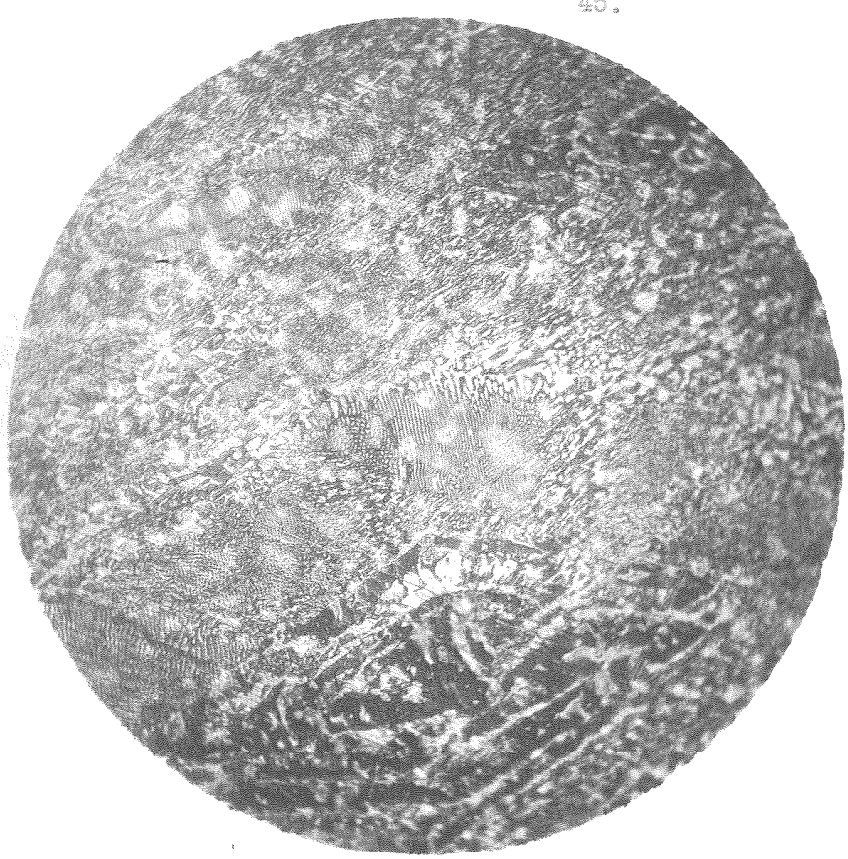

Fig. 25

(1-3)
As cast
Magnification 500X
Etch Murakami

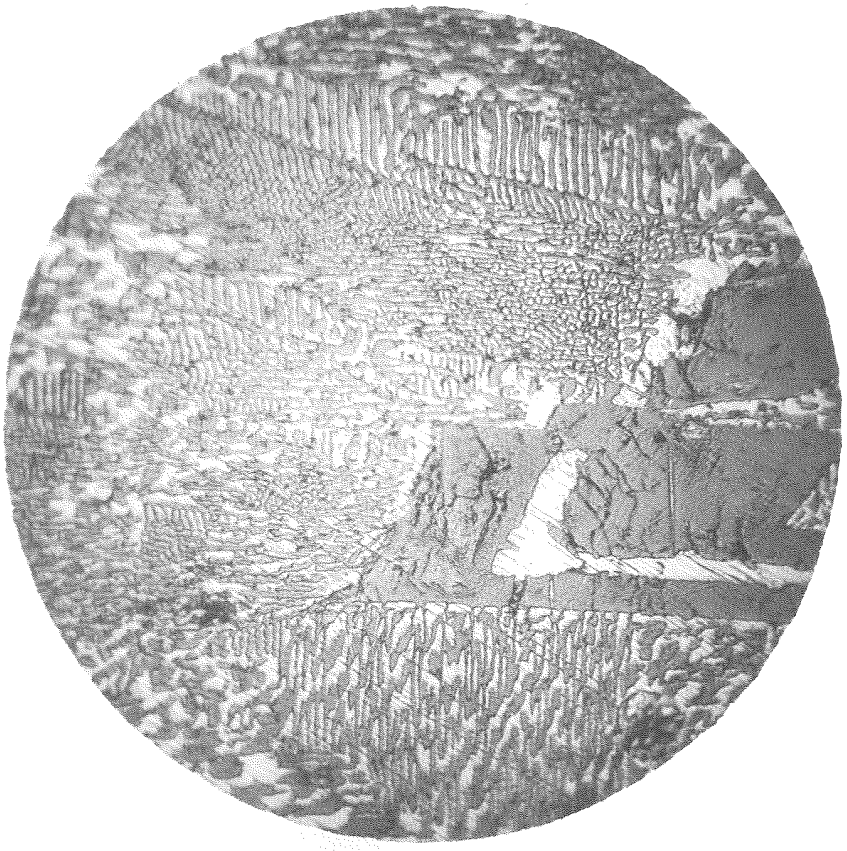

Fig. 26

(1-2)
As cast
Magnification 1000X
Etch Murakami

inclusive, show the microstructure of this alloy as cast and Figures 27 and 28, the structure after annealing at 1800° F. These photomicrographs would indicate that supercooling had again taken place in the cooling of this alloy which effect was not removed by annealing. We would normally expect a structure similar to that predicted for the previous alloy; i.e., primary iron boride with ternary pearlite. These figures show some primary iron boride, the dark fairly regular prisms in Figures 24 to 26, inclusive, and white in Figures 27 and 28. Also, secondarily separated iron boride is shown as the inner gray structure and last the pearlite structure surrounded by the mixture of binary solid solution iron boride in iron carbide and the solid solution of iron boride in iron, shown by the white matrix material. This ternary pearlite is shown in Figures 24 and 27 as dark clusters because of the fineness of the structure.

Figure 29 shows the fracture of specimen number 3 containing 3.86% boron and 1.19% carbon. The fracture shows a very dense material which sparkles, probably due to the iron boride crystals embedded in its matrix. No porosity was evident in this material. The structure expected here shown consist of primary grains of iron boride in rather large amounts together with a relatively large amount of binary solid solution of iron boride in iron carbide with a very small amount of ternary pearlite.

Figures 30 and 31 show the structure obtained on casting and Figures 32 and 33 the structure after annealing at 1800° F. The

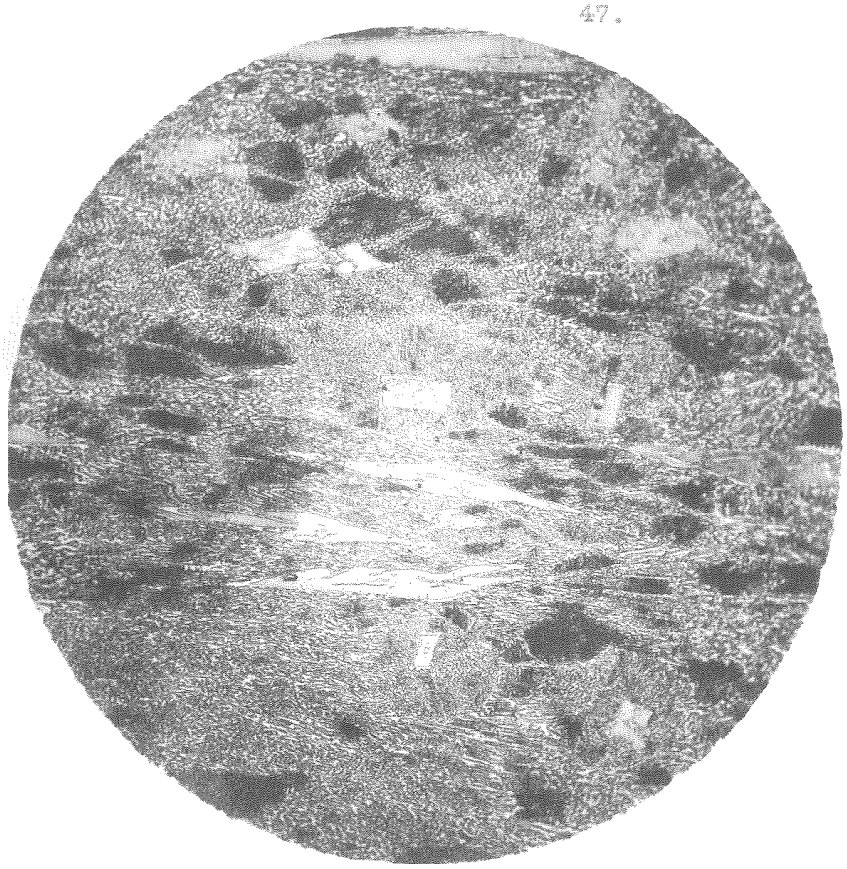

Fig. 27

(1A-1)
Annealed 1800° F.
Magnification 100X
Etch Murakami

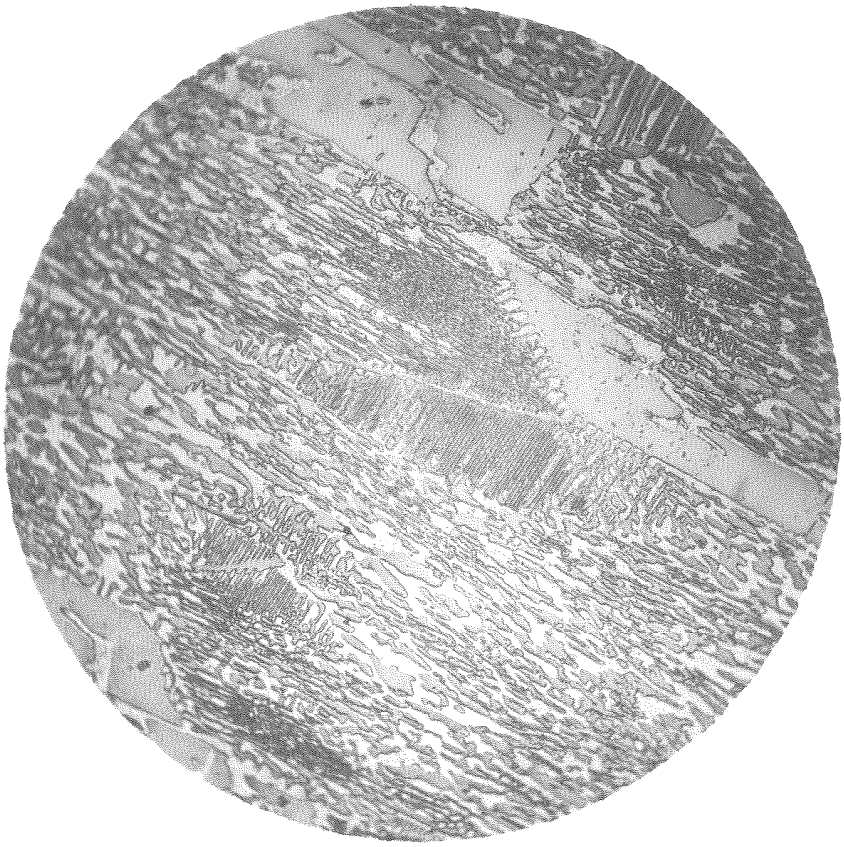

Fig. 28

(1A-2)
Annealed 1800° F.
Magnification 500X
Etch Murakami

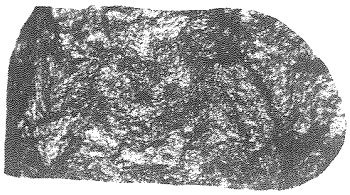

Fig. 29

(3)
As cast
Magnification 2.5X

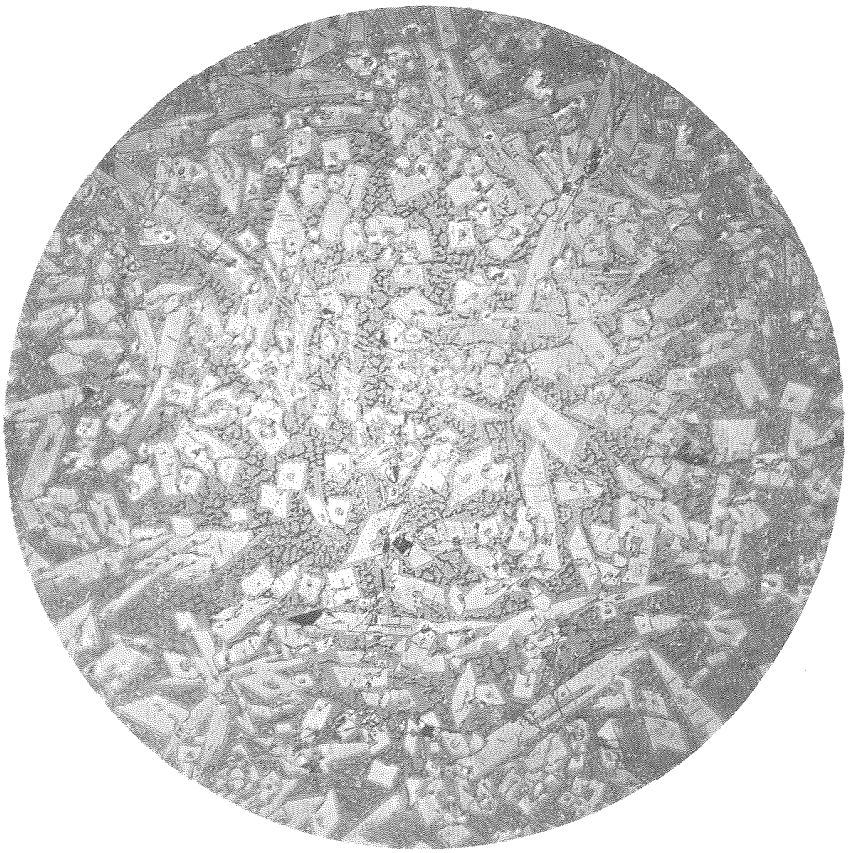

Fig. 30

(3-1)
As cast
Magnification 100X
Etch Murakami

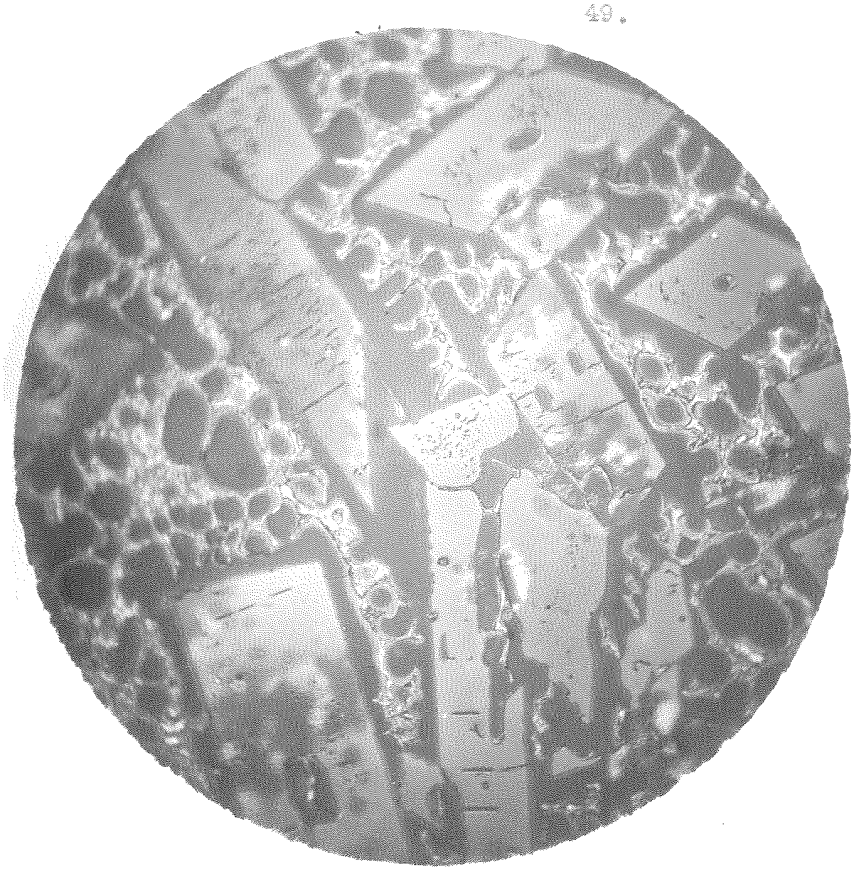

Fig. 31

(3-2)
As cast
Magnification 500X
Etch Murakami

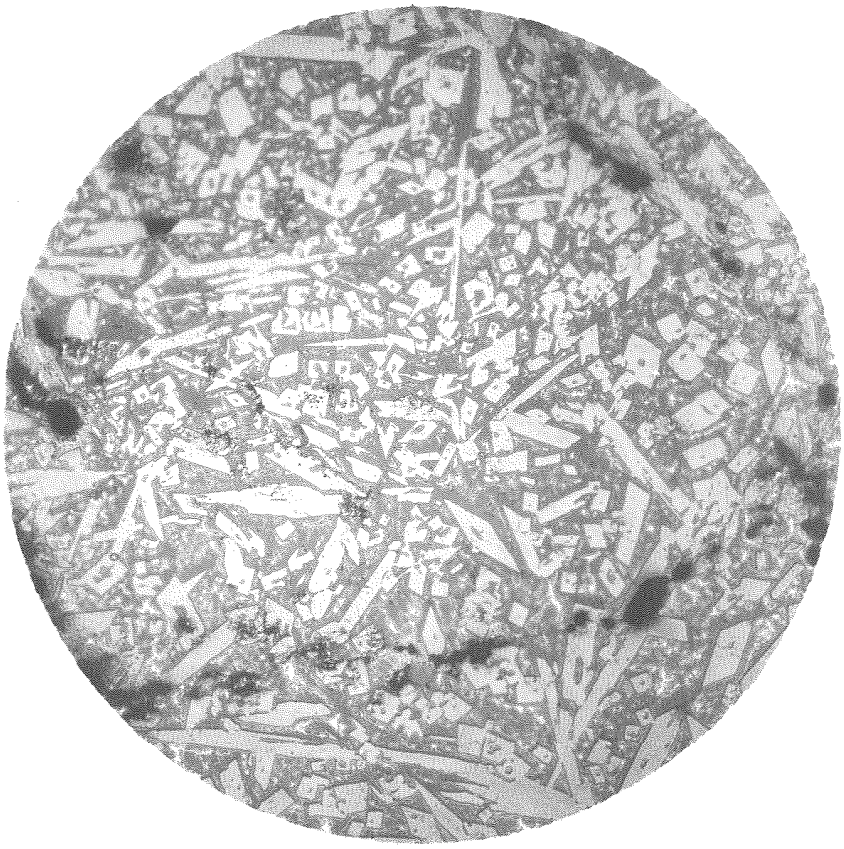

Fig. 32

(3A-1)
Annealed 1800° F.
Magnification 100X
Etch Murakami

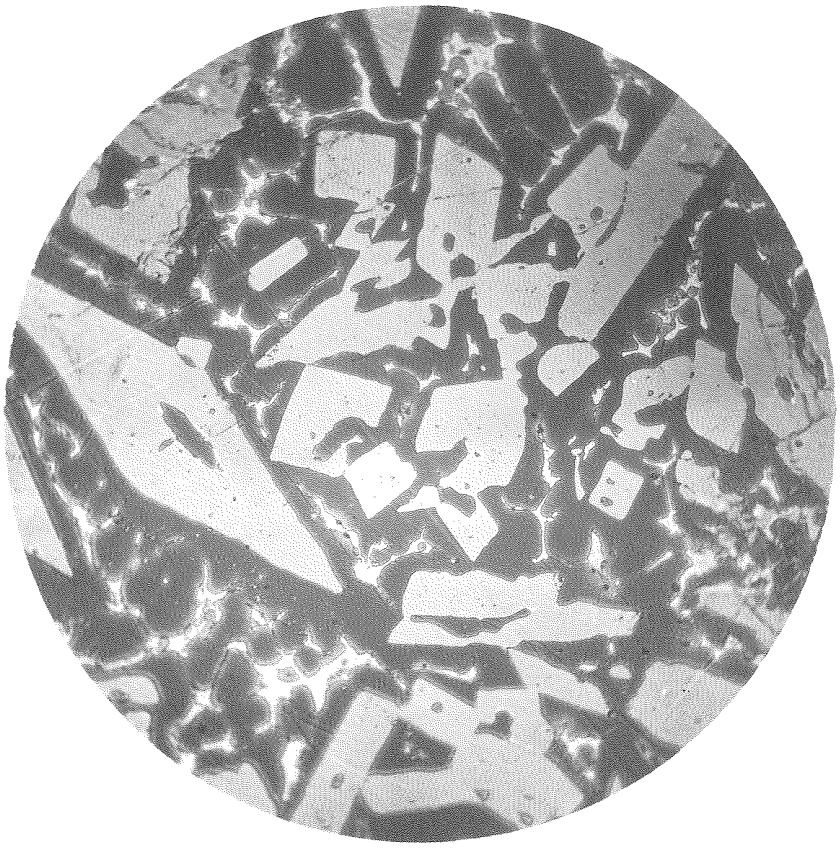

Fig. 33

(3A-2)
Annealed 1800° F.
Magnification 500X
Etch Murakami

primary iron boride is very evident as regular white prisms surrounded by a rather large amount of the iron carbide solid solution in which is embedded the ternary pearlite. In Figure 31 considerable coring is noticeable in the ternary pearlite due to lack of equilibrium conditions. In the case of the annealed structure the binary alpha iron iron boride solid solution has probably mixed with the iron carbide solid solution and hence is not distinguishable. The white finer structure in Figure 33 is probably the iron boride of the ternary pearlite.

Figure 34 shows the fracture of specimen number 4 containing 4.32% boron and 1.21% carbon. This fracture shows quite a dense material with sparkling needles undoubtedly due to the primary iron boride. Some slight porosity is observable.

In this case a structure similar to the previous alloy should be expected except with a smaller proportion of iron boride (primary) and iron carbide solid solution with a greater proportion of ternary pearlite. Figures 35 and 36 show the structure after casting and Figures 37 and 38 after annealing at 1800° F. Very considerable coring is observed in this structure around the primary iron boride. This is probably due to the separation of the ternary eutectic in which the iron boride that separates collects around the crystals existing at that temperature. The remaining material will be composed of the iron-iron boride solid solution and iron carbide solid

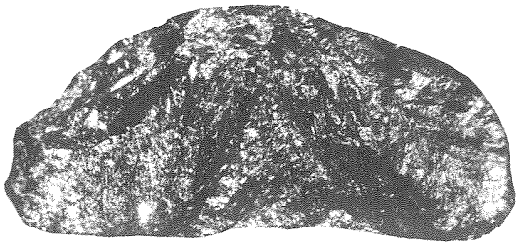

Fig. 34

(4)
As cast
Magnification 2.5X

Fig. 35

(4-1)
As cast
Magnification 100X
Etch Murakami

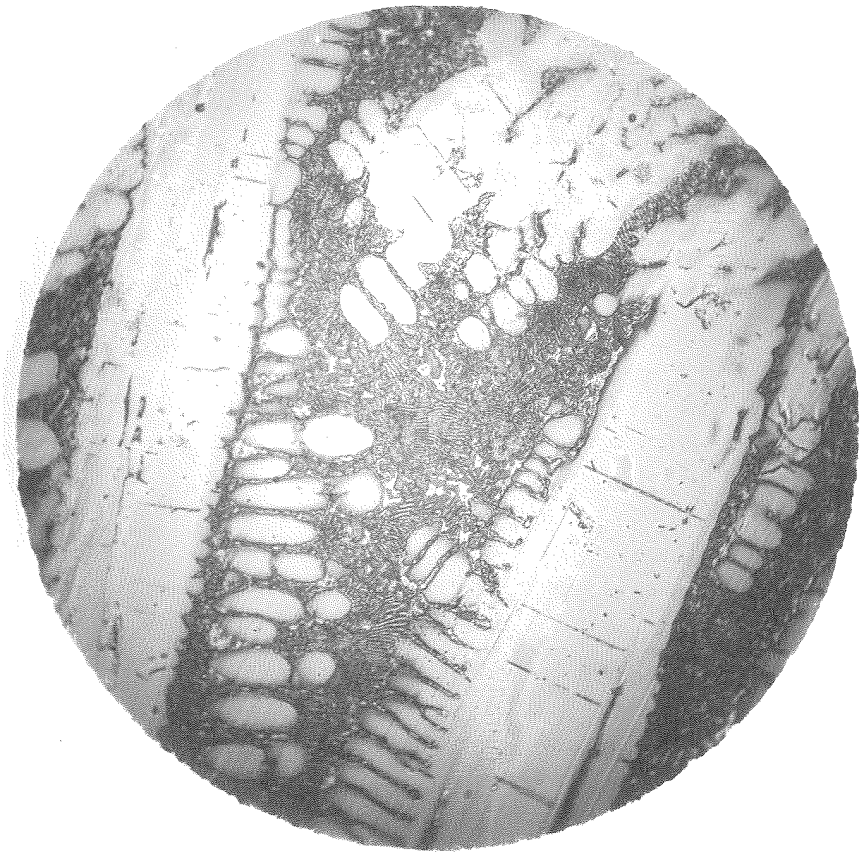

Fig. 36

(4-2)
As cast
Magnification 500X
Etch Murakami

Fig. 37

(4A-1)
Annealed 1800° F.
Magnification 100X
Etch Murakami

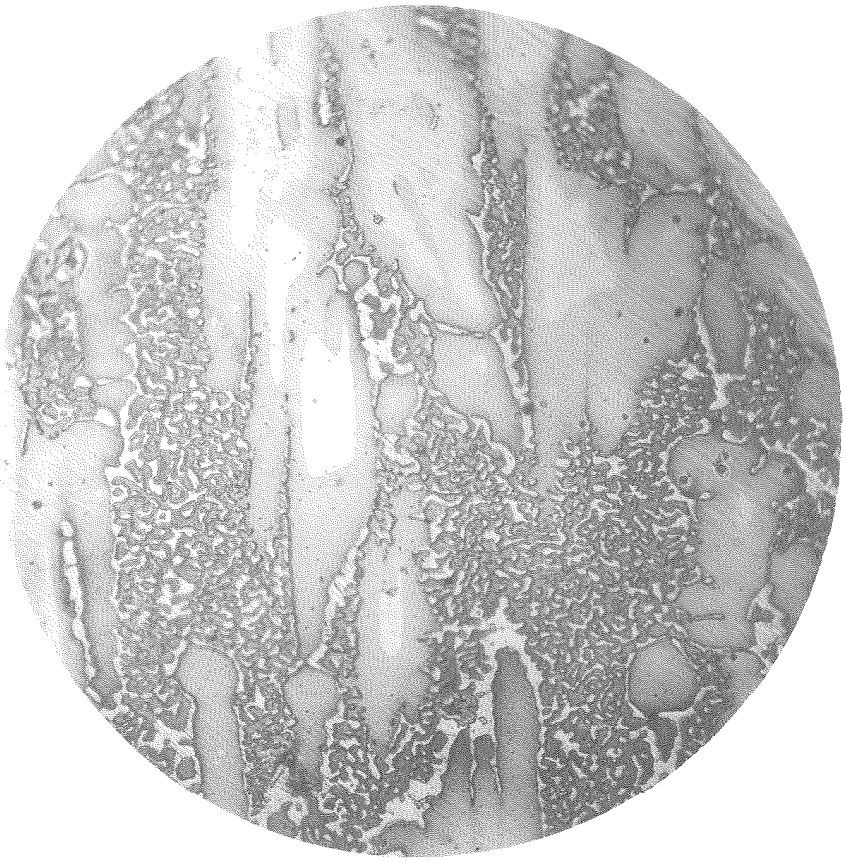

Fig. 38

(4A-2)
Annealed 1800° F.
Magnification 500X
Etch Murakami

solution. This last approaches more nearly a binary pearlite.

Figure 39 shows the fracture of specimen number 6 containing 4.2% boron and 2.71% carbon. The fracture shows a dense structure tending to be granular with some cleavage. No porosity was observed in this specimen.

Figure 40 shows the structure of this alloy as cast and Figures 41 and 42 show the structure after annealing at 1800° F. In this case we should expect considerably more iron carbide solid solution with less primary iron boride than was found in specimen number 3 which lies in the same concentration region. We should also expect a small amount of ternary pearlite. The structure actually shows these constituents to be present. In Figure 40 the primary iron boride is evident as the white regular prisms, the iron carbide solid solution as the gray ground mass in which is embedded the small amount of ternary pearlite. After annealing the primary iron boride appears to be the same as before, but the ternary pearlite has been broken up so that the iron iron-boride solid solution has blended with the iron carbide solid solution leaving only the secondarily separated iron boride in small segregations as shown in Figures 41 and 42.

Figure 43 shows the fracture of specimen number 5 containing 3.88% boron and 2.83% carbon. The fracture shows a dense structure with some cleavage about as shown in Figure 6 and no porosity is observed.

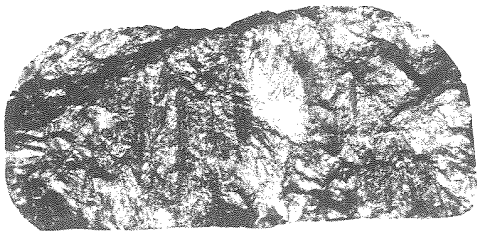

Fig. 39

(6)
As cast
Magnification 2.5X

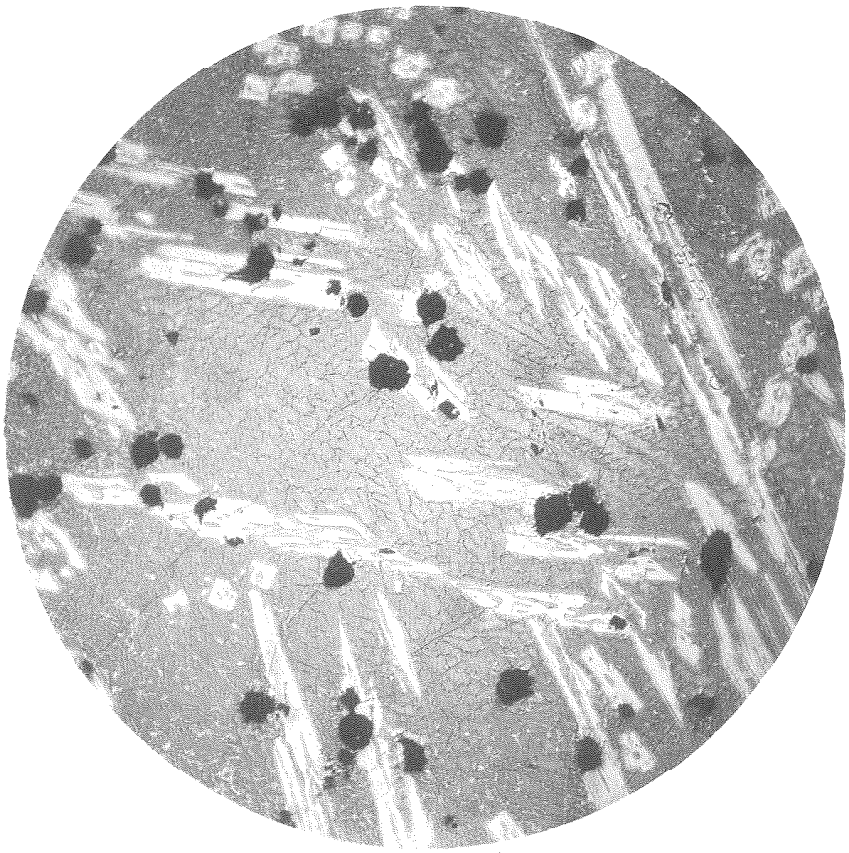

Fig. 40

(6-1)
As cast
Magnification 100X
Etch Murakami

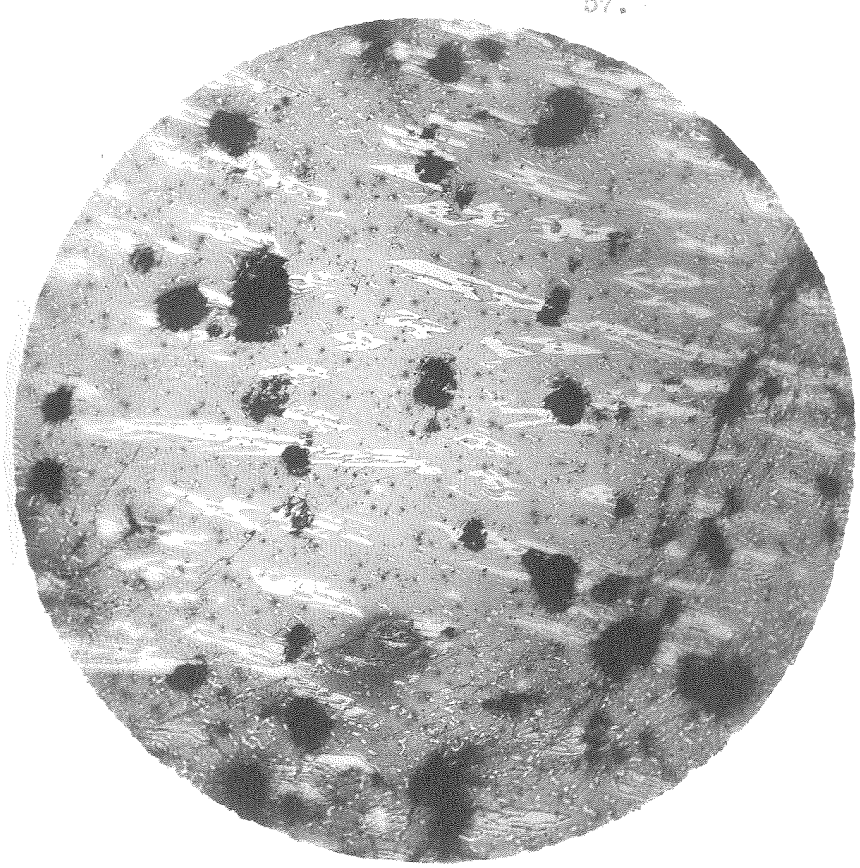

Fig. 41

(6A-1)
Annealed 1800° F.
Magnification 100X
Etch Murakami

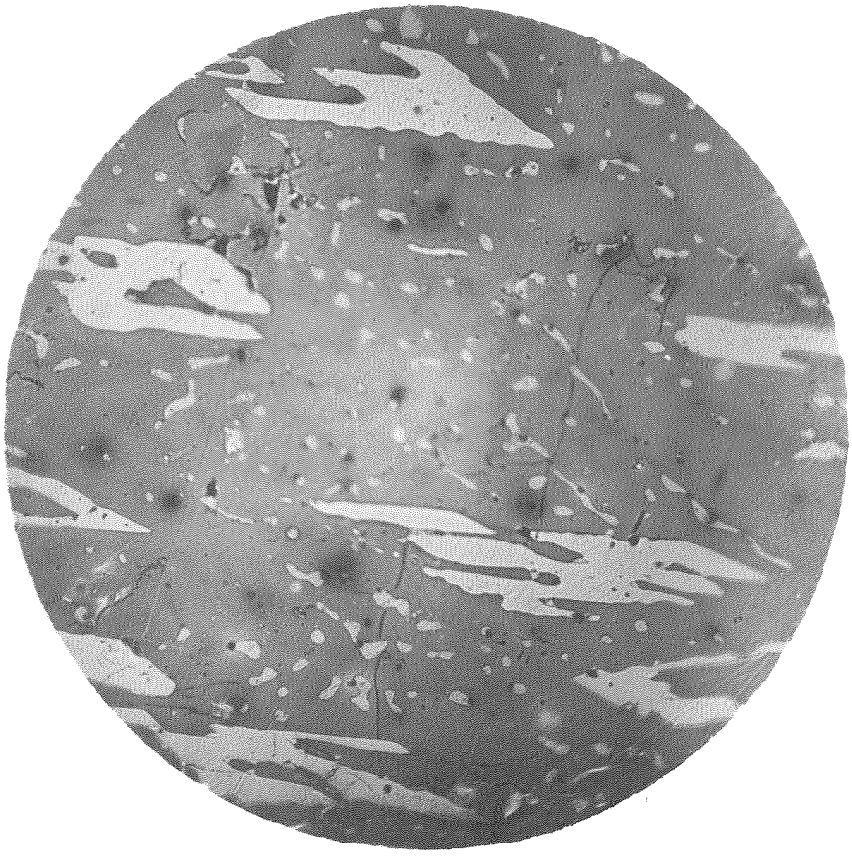

Fig. 42

(6A-2)
Annealed 1800° F.
Magnification 500X
Etch Murakami

Fig. 43

(5)
As cast
Magnification 2.5X

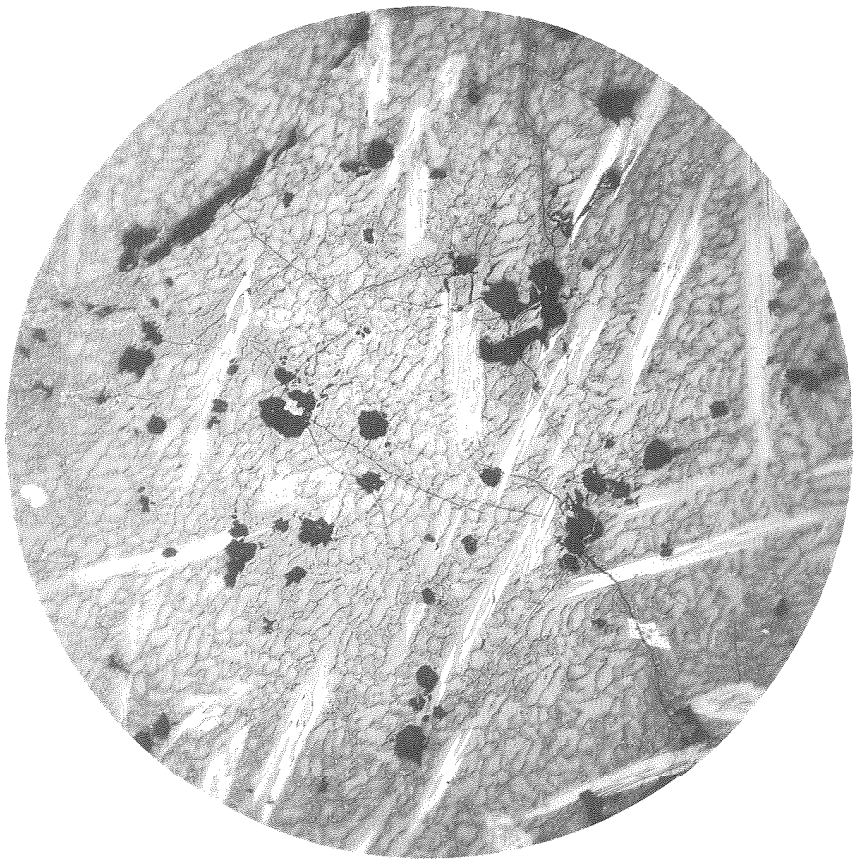

Fig. 44

(5-1)
As cast
Magnification 100X
Etch Murakami

Figure 44 shows the structure after casting and Figures 45 and 46 show the structure after annealing at 1800° F. In comparing this alloy with the structure found in number 6, we find less primary iron boride as predicted by the diagram with somewhat more ternary pearlite.

Figure 47 shows the fracture of specimen number 8 containing 3.35% boron and 1.84% carbon. The fracture shows a very dense structure which is very granular. No porosity was observed in this alloy.

Figures 48 and 49 show the structure after casting and Figures 50 and 51 show the structure after annealing at 1800° F. Some primary iron boride should be expected in this structure in view of its position in the concentration triangle. Some ternary eutectic would be expected which dissociates into the three types of crystals. The photomicrographs do not show any primary iron boride, but show what might be considered to be either primary or secondary iron carbide solid solution precipitated during primary crystallization or during secondary crystallization. Probably the actual case in this alloy was that super-cooling took place preventing the primary separation of iron boride and brought about the separation of the iron carbide solid solution during secondary crystallization. The ternary eutectic dissociates into the iron boride, iron carbide solid solution, and the iron iron-boride solid solution which may be represented by the fine eutectic appearing structure.

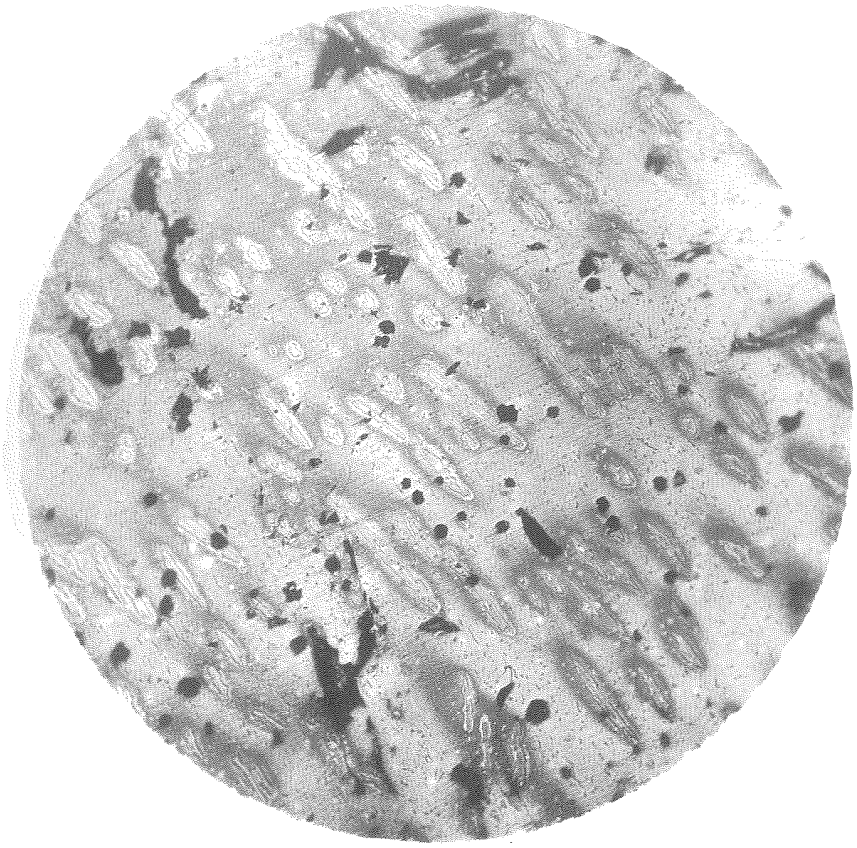

Fig. 45

(5A-1)
Annealed 1800° F.
Magnification 100X
Etch Murakami

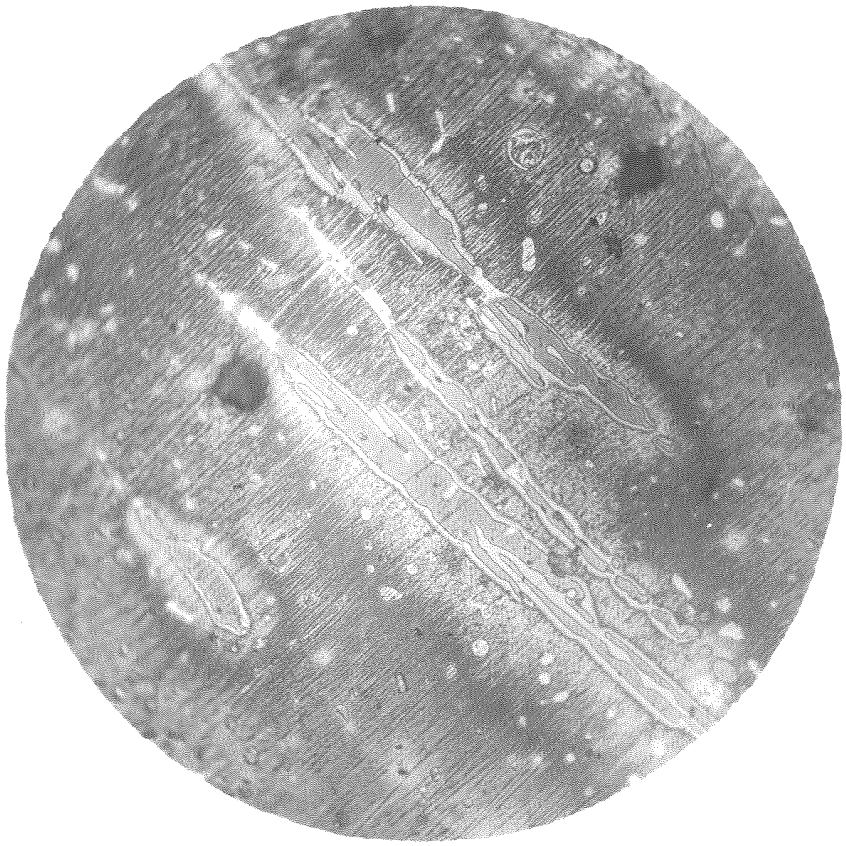

Fig. 46

(5A-2)
Annealed 1800° F.
Magnification 500X
Etch Murakami

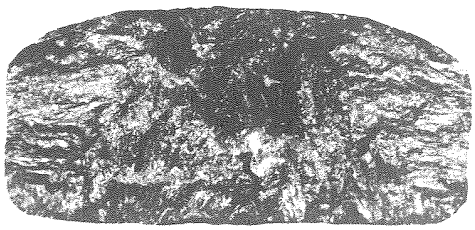

Fig. 47

(8)
As cast
Magnification 2.5X

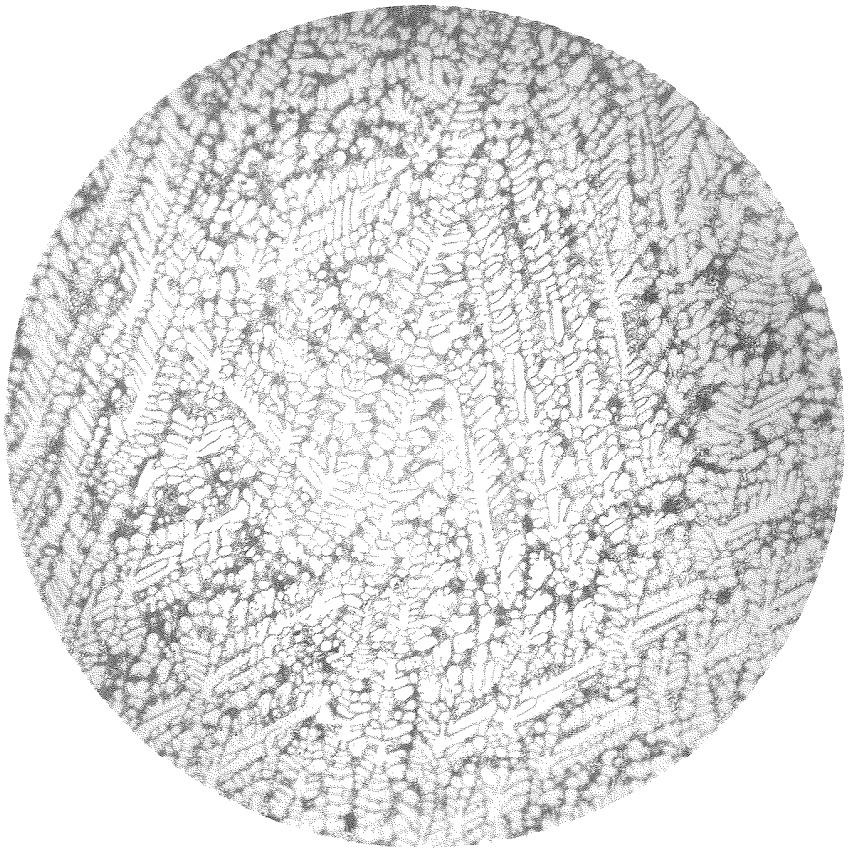

Fig. 48

(8-1)
As cast
Magnification 100X
Etch Murakami

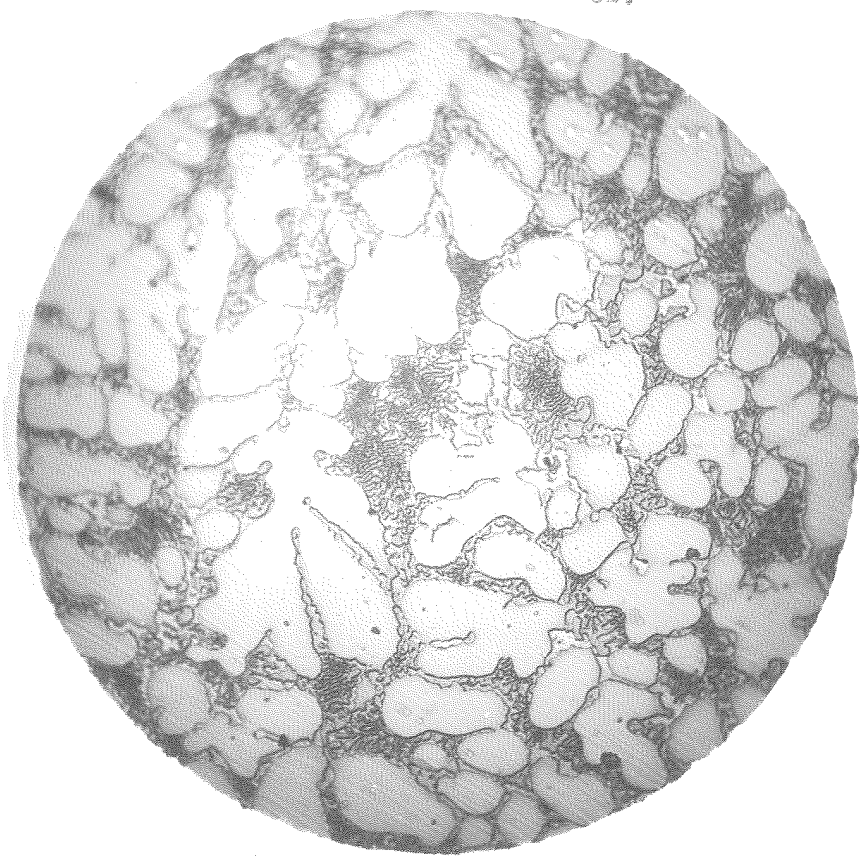

Fig. 49

(8-2)
As cast
Magnification 500X
Etch Murakami

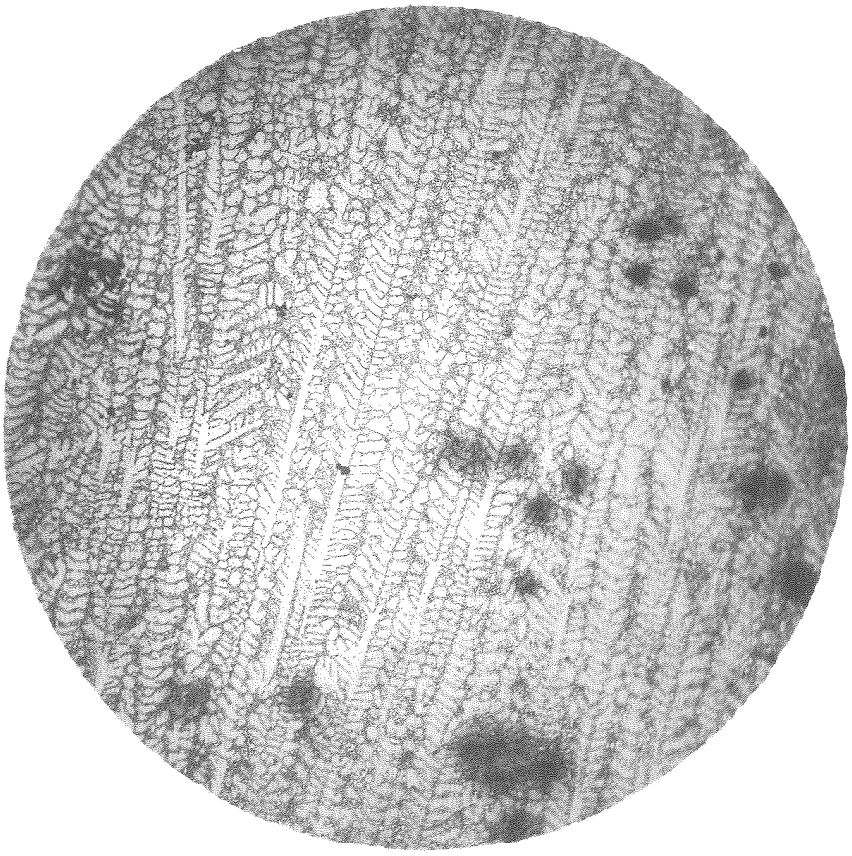

Fig. 50

(8A-1)
Annealed 1800° F.
Magnification 100X
Etch Murakami

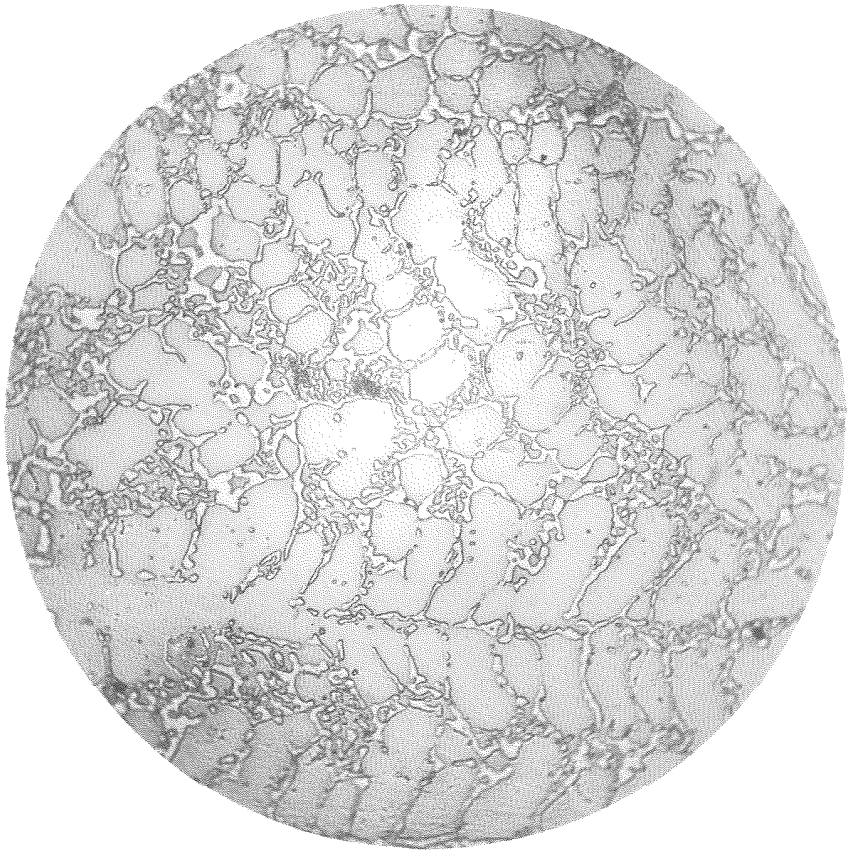

Fig. 51

(8A-2)
Annealed 1800° F.
Magnification 500X
Etch Murakami

This completes the study of those alloys in the region containing primary iron boride. According to the concentration triangle specimen number 11 should lie on the eutectic curve E3R, Figure 103, or possibly a little on the side which would produce primary iron carbide solid solution. Let us see what the structure shows.

Figure 52 shows the fracture of specimen number 11 containing 2.91% boron and 2.83% carbon. The fracture shows a very dense material, which cleaves readily along plates.

Figures 53 and 54 show the structure after casting and Figures 55 and 56, after annealing at 1800° F. The structure appears to lie about on the eutectic curve referred to, in that the photomicrographs show a large mass probably of iron boride and iron carbide solid solution. This is substantiated by the appearance of Figure 54 showing a very fine net work structure within the large rounded gray areas. The remaining material should be ternary pearlite, which, as has been seen before, breaks up into its constituents, as particularly shown in the annealed specimen, Figure 56, in which only iron boride is shown in the ground mass.

Figure 57 shows the fracture of specimen number 14 containing 2.21% boron and 2.97% carbon. The fracture shows a very dense structure having a granular form.

Figures 58 and 59 show the structure after casting and Figures

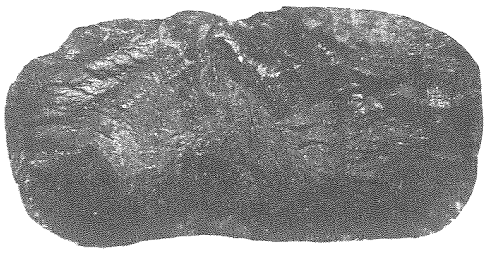

Fig. 52

(11)
As cast
Magnification 2.5X

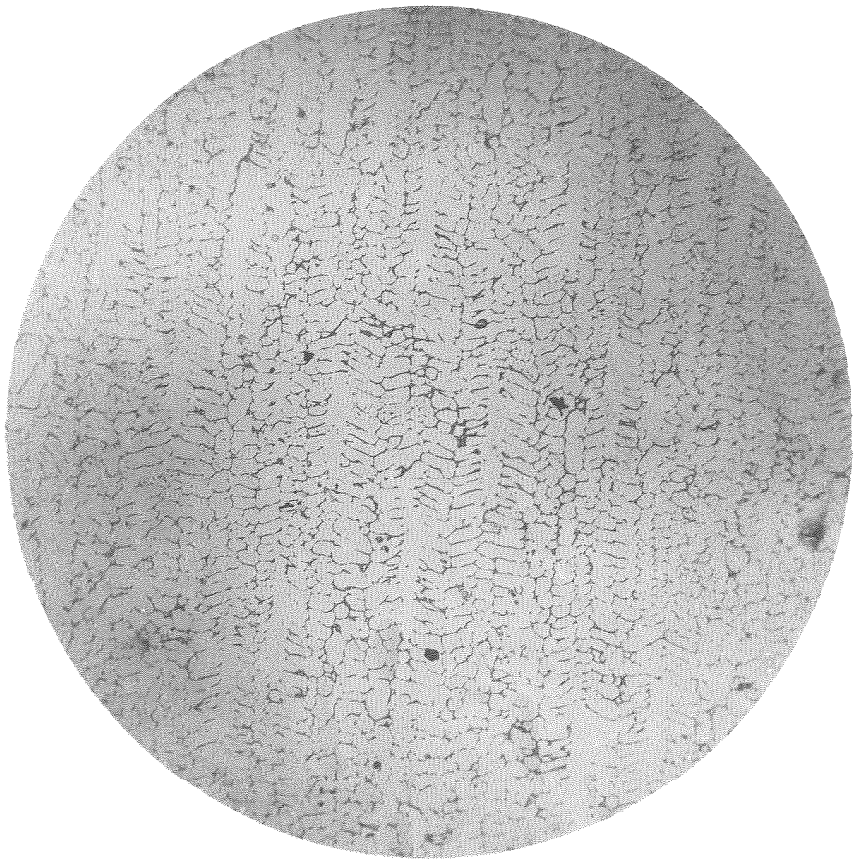

Fig. 53

(11-1)
As cast
Magnification 100X
Etch Murakami

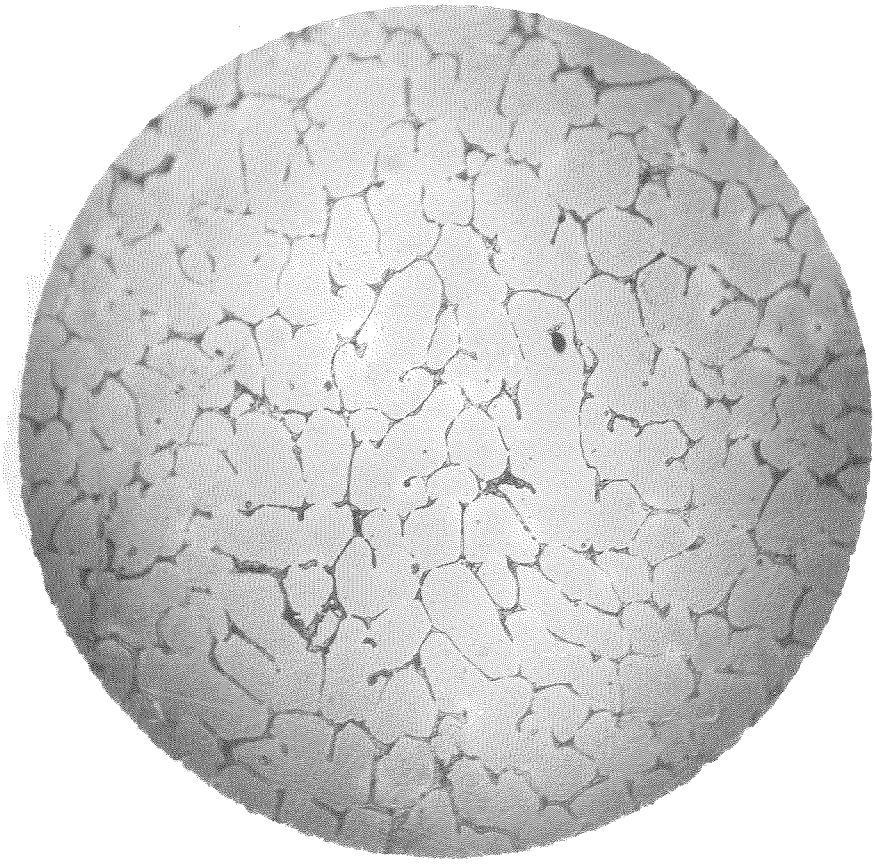

Fig. 54

(11-2)
As cast
Magnification 500X
Etch Murakami

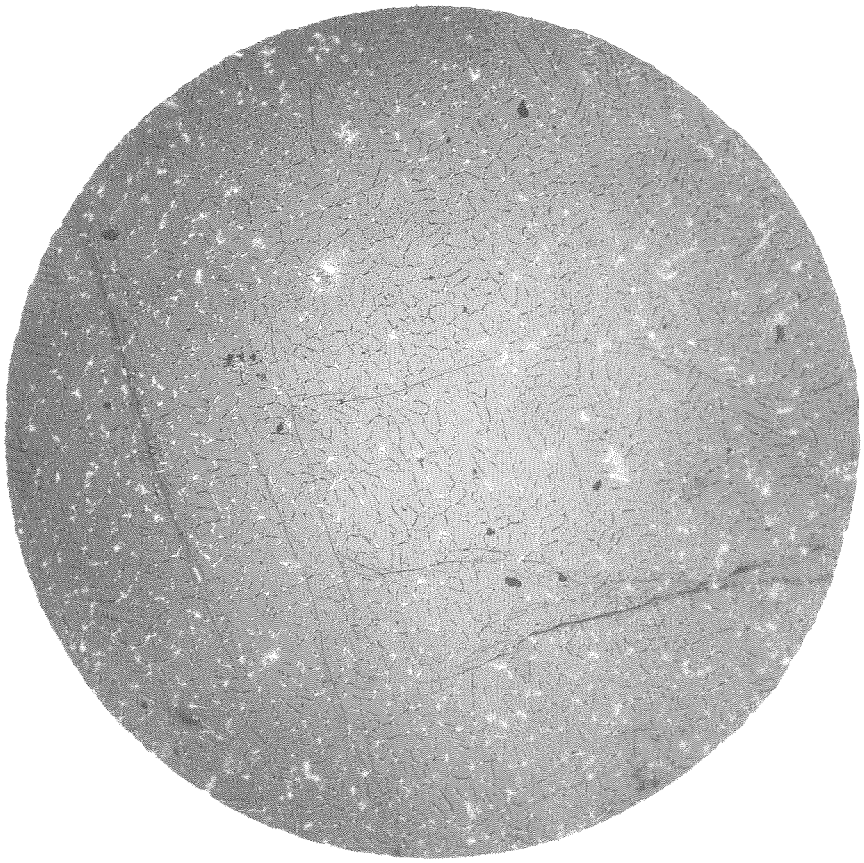

Fig. 55

(11A-1)
Annealed 1800° F.
Magnification 100X
Etch Murakami

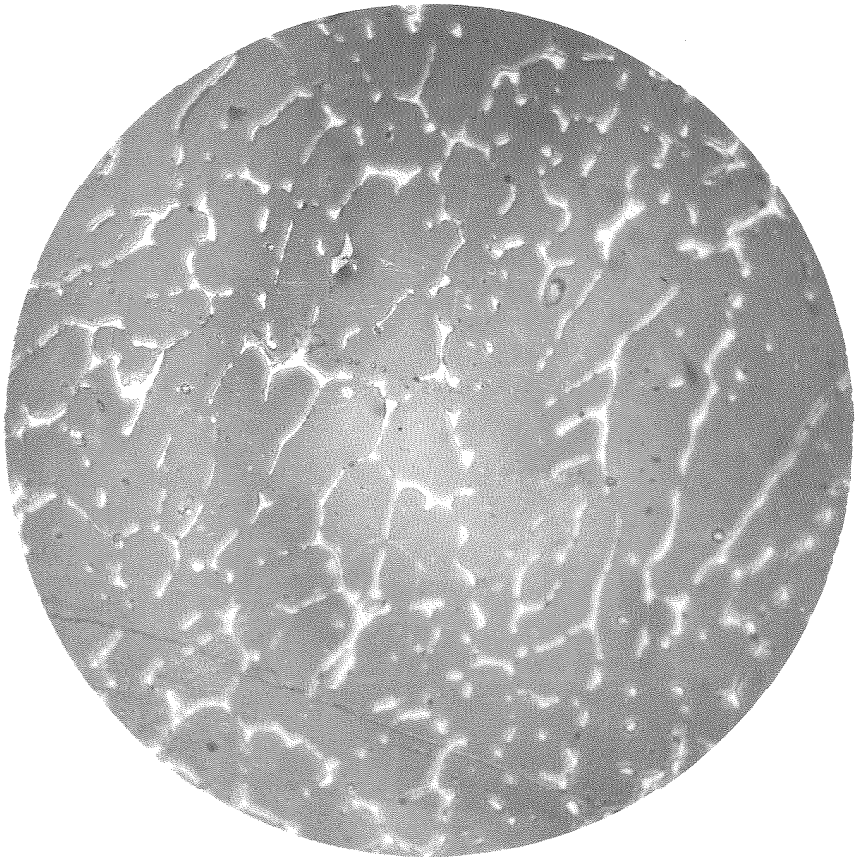

Fig. 56

(11A-2)
Annealed 1800° F.
Magnification 500X
Etch Murakami

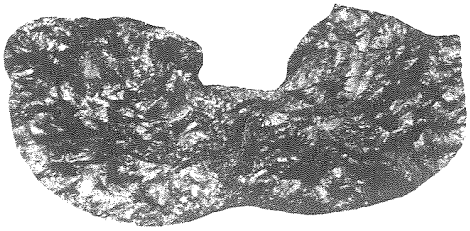

Fig. 57

(14)
As cast
Magnification 2.5X

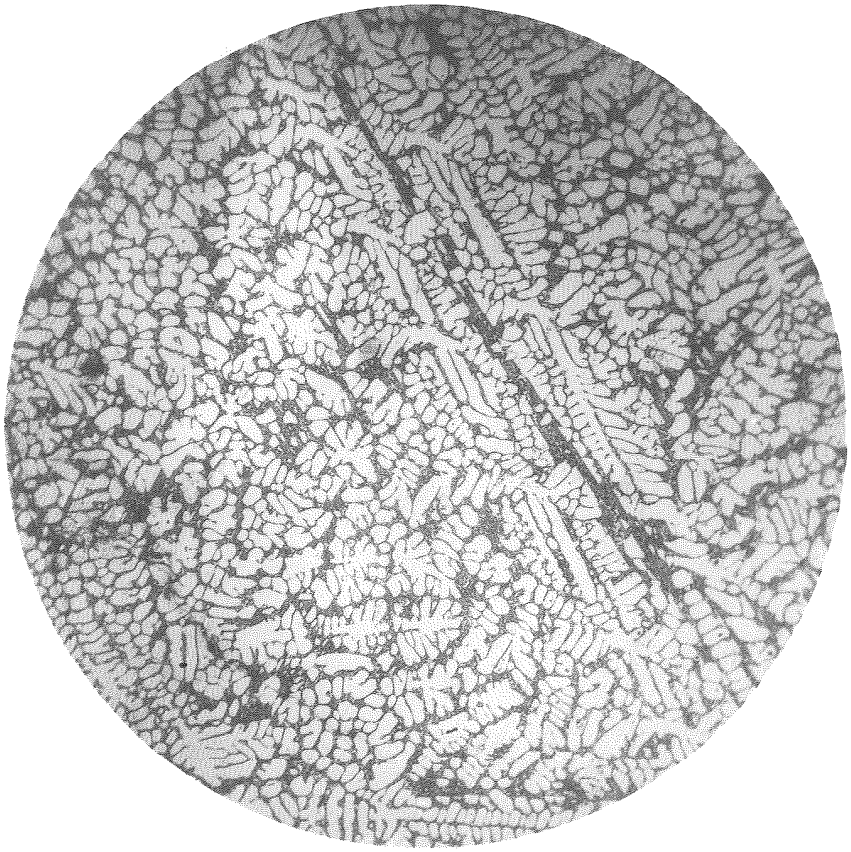

Fig. 58

(14-1)
As cast
Magnification 100X
Etch Murakami

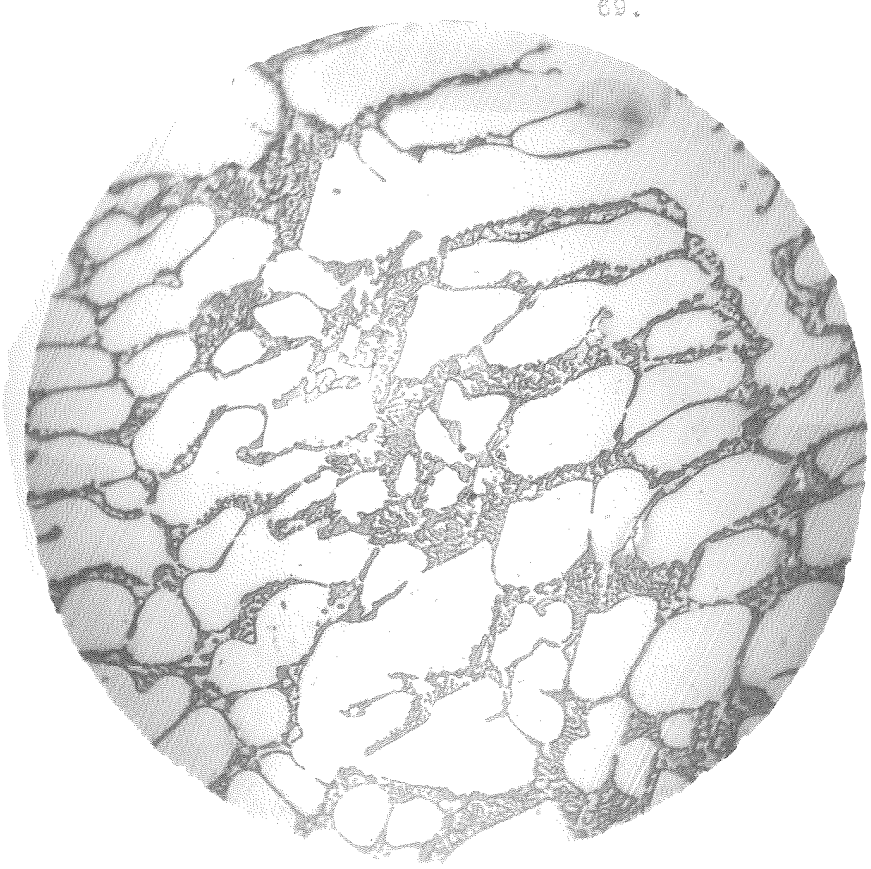

Fig. 59

(14-2)
As cast
Magnification 500X
Etch Murakami

Fig. 60

(14A-1)
Annealed 1800° F.
Magnification 100X
Etch Murakami

60 and 61 show the structure after annealing at 1800° F. The structure expected here should be primary iron carbide solid solution with the ternary pearlite. This is shown to be the case in the photomicrographs. In Figure 58 the white constituent is the iron carbide solid solution while the finer interlacing structure is then ternary pearlite. Figure 59 shows this structure to be relatively homogeneous and hence might be the ternary solid solution which has been too rapidly cooled to allow dissociation into its three components. In Figure 60 is shown about the same structure, except that the colors are reversed and the matrix material has become enlarged. This is undoubtedly due to very slow cooling during the pearlitic transformation which allowed complete separation of the two types of solid solutions leaving the iron boride as the white constituent, as we have seen in some of the previous alloys.

Figure 62 shows the fracture of specimen 9 containing 2.55% boron and 2.18% carbon. The structure shows a very dense granular structure with no porosity.

From the position of this alloy in the system we should expect about the same structure as we found in the previous alloy, except that less iron carbide solid solution should be present with more ternary pearlite. Also, in view of its position in the system, we might expect to find more of the ternary eutectic structure which may explain the eutectic-appearing portion of the structure, as

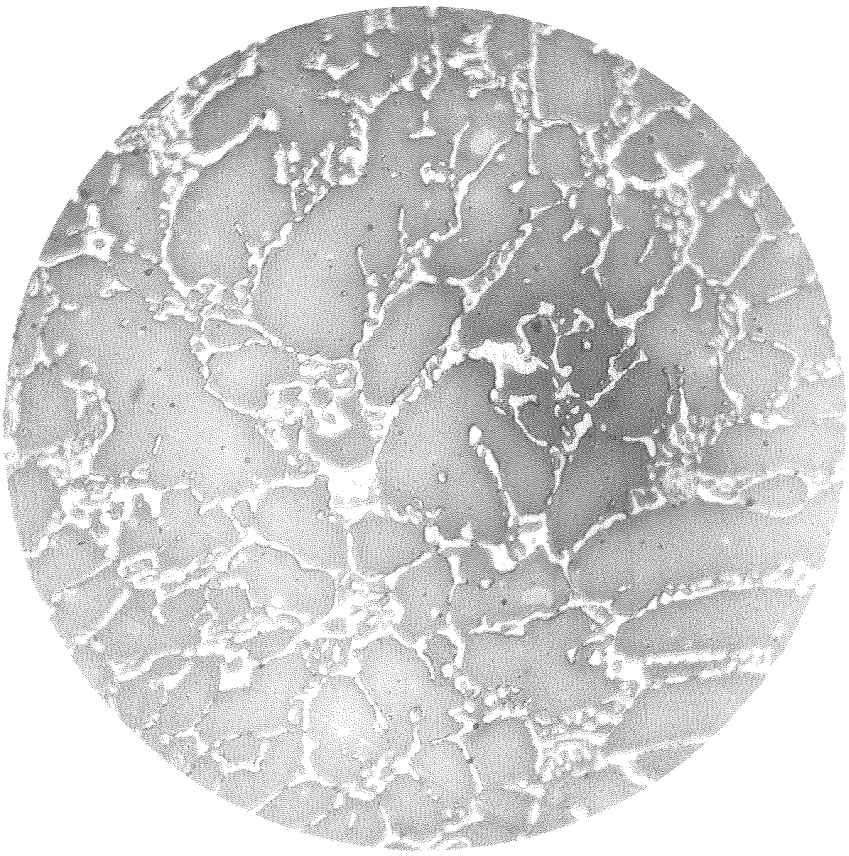

Fig. 61

(14A-2)
Annealed 1800° F.
Etch Murakami

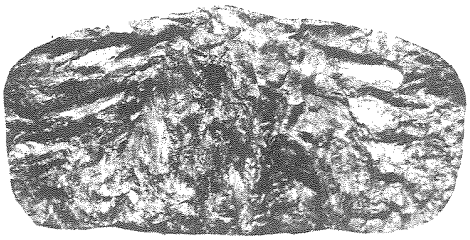

Fig. 62

(9)
As cast
Magnification 2.5X

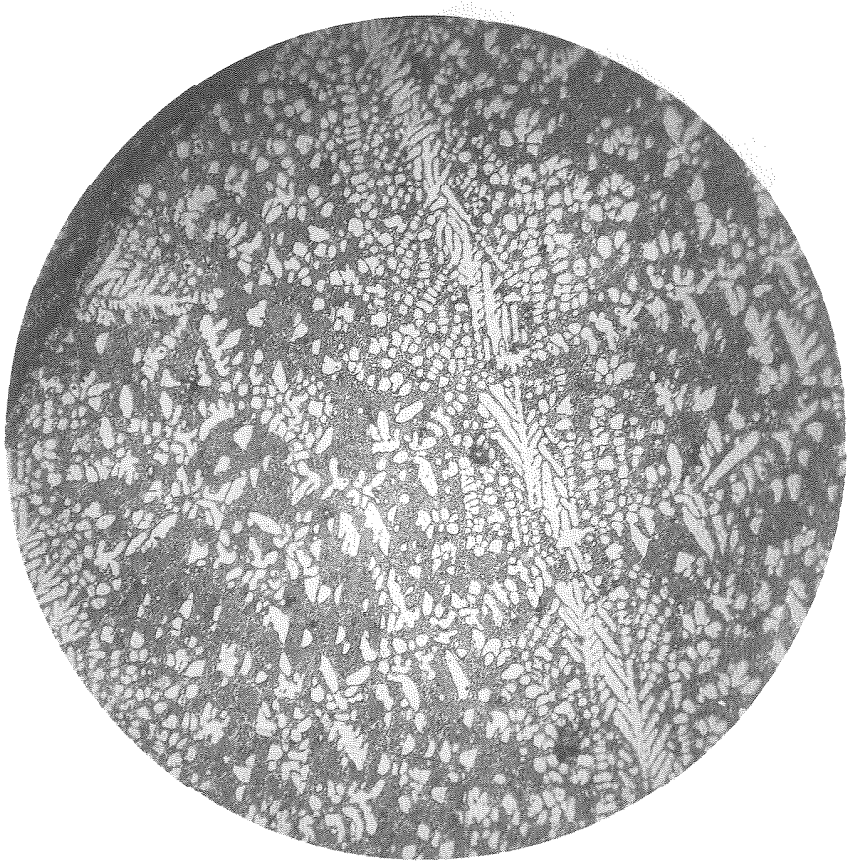

Fig. 63

(9-1)
As cast
Magnification 100X
Etch Murakami

shown in Figures 63 and 64. The white constituent is the primary and secondary iron carbide solid solution. In this case, also, it is apparent that insufficient time has been given to allow the dissociation of the ternary pearlite of which the ternary eutectic will consist. In Figures 65 and 66 is shown the structure after annealing at 1800° F. This shows the same condition as existed in the previous alloy, that after annealing the ternary pearlite was dissociated into its components leaving the iron boride white and the mixture of iron carbide solid solution and iron, iron-boride solid solution dark.

Figure 67 shows the fracture of specimen number 13 containing 2.31% boron and 2.21% carbon. The fracture shows a very porous casting which is mostly due to shrinkage, as is apparent from the white bright surfaces of the holes. The metal itself is dense and granular.

Since the composition of this alloy lies very close to that of the previous alloy, one would expect to obtain a similar structure with somewhat less primary iron carbide solid solution, if any. The composition lies so near to the eutectic curve, E_1R, that it should consist of possibly more ternary solid solution and iron carbide solid solution. In Figures 68, 69, and 70 is shown the structure of this alloy in which there is apparently some primary iron carbide solid solution surrounded by a very large amount of

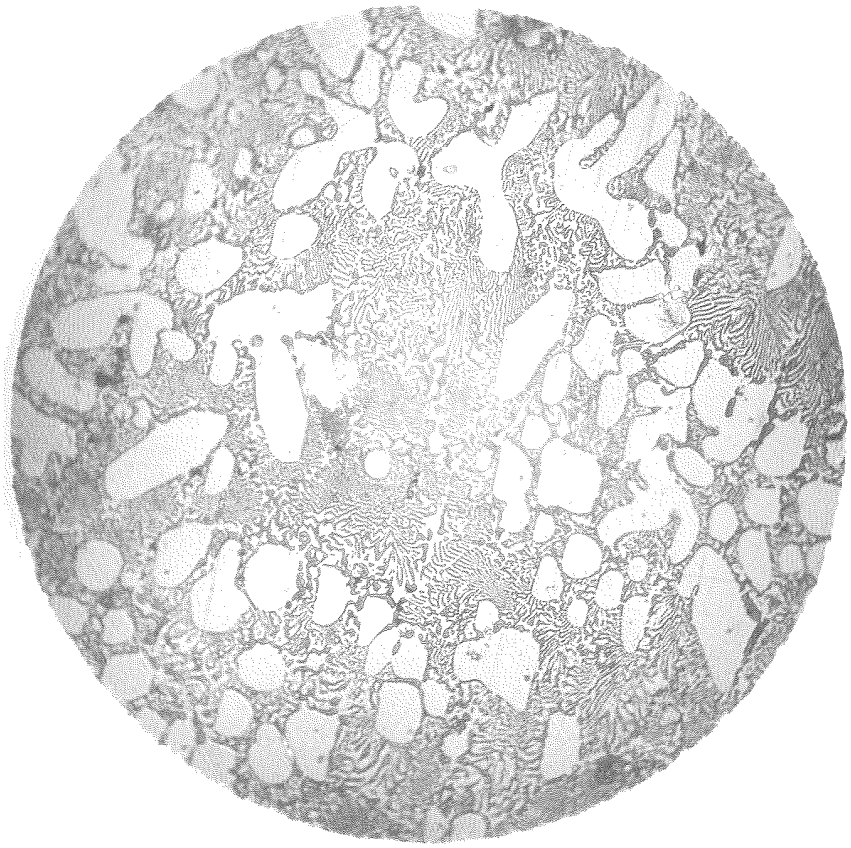

Fig. 64

(9-2)
As cast
Magnification 500X
Etch Murakami

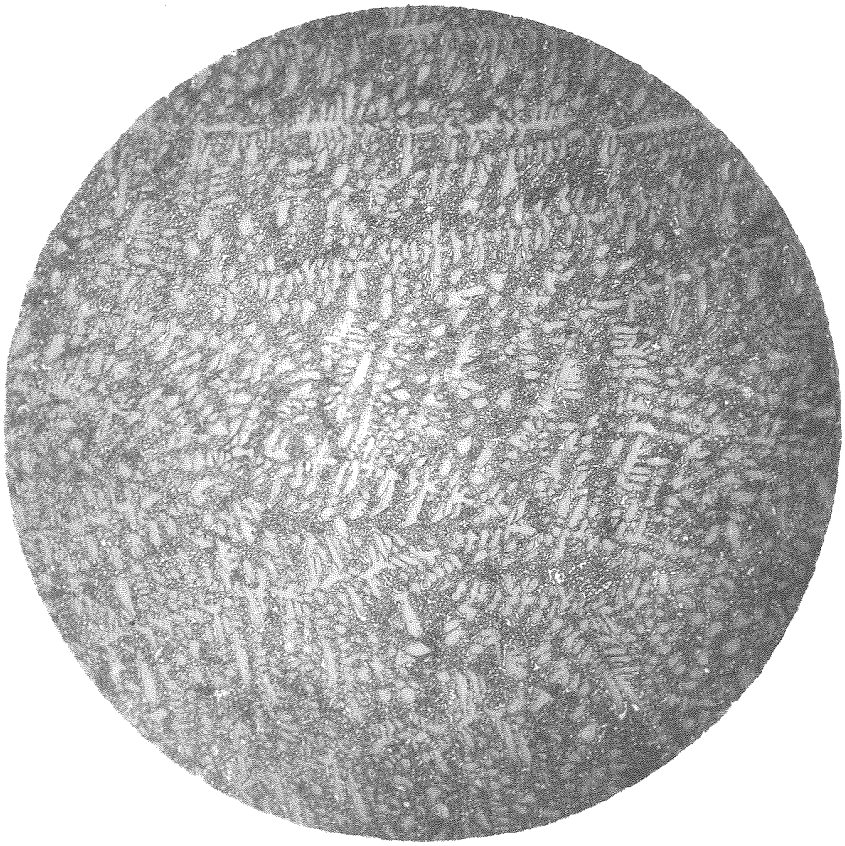

Fig. 65

(9A-1)
Annealed 1800° F.
Magnification 100X
Etch Murakami

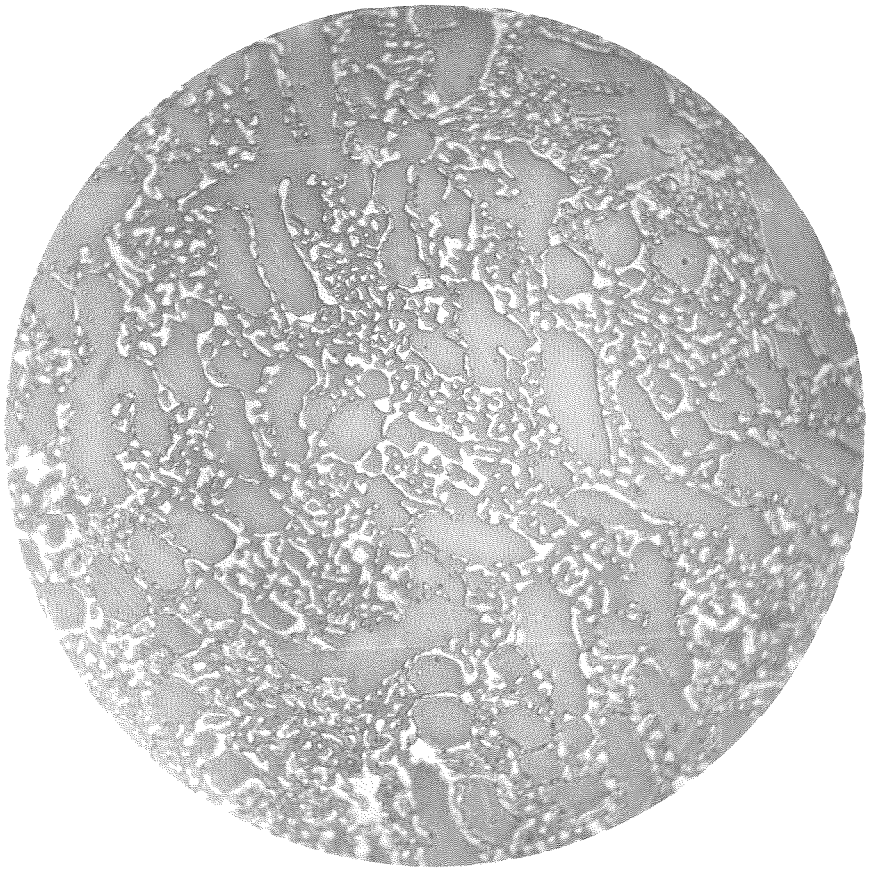

Fig. 66

(9A-2)
Annealed 1800° F.
Magnification 500X
Etch Murakami

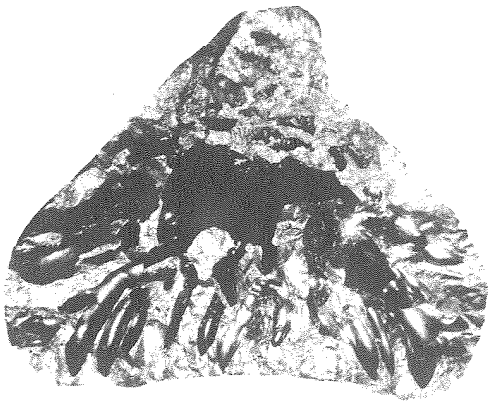

Fig. 67

(13)
As cast
Magnification 2.5X

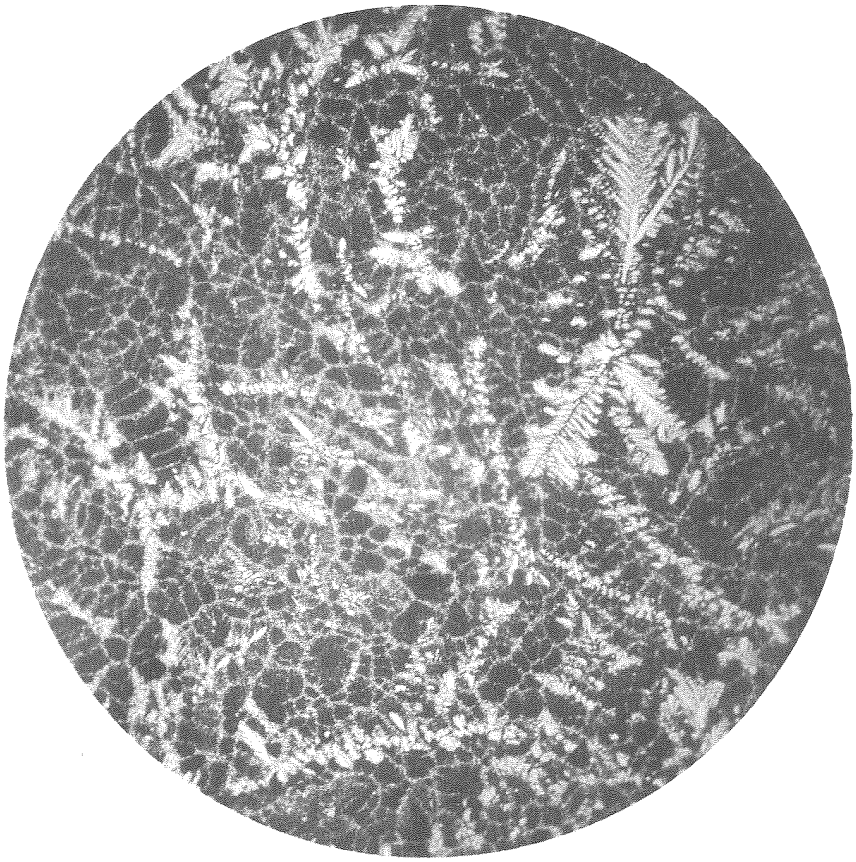

Fig. 68

(13-1)
As cast
Magnification 100X
Etch Murakami

Fig. 69

(13-2)
As cast
Magnification 500X
Etch Murakami

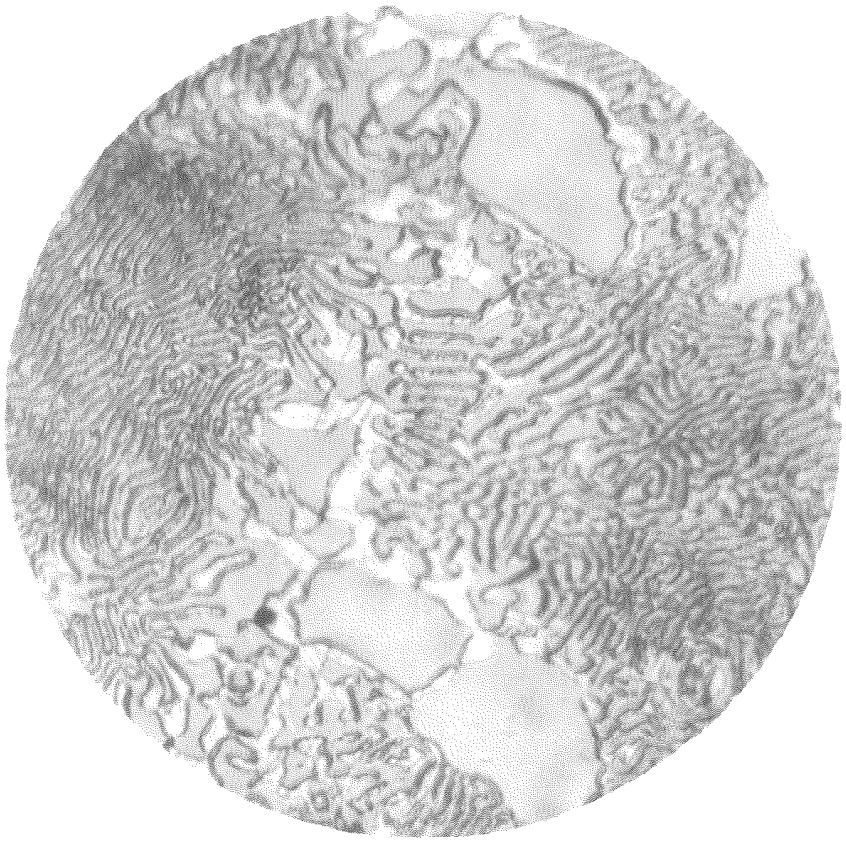

Fig. 70

(13-3)
As cast
Magnification 2000X
Etch Murakami

material of ternary eutectic origin, as might be expected. Figures 71 and 72 show the structure after annealing at 1800° F. in which no extremely large primary solid solution is observed, indicating that the condition shown in the cast state is false. The structure of the ternary eutectic has been obliterated and the usual dissociation has occurred, as indicated above.

Figure 73 shows the fracture of specimen number 10 containing 1.16% boron and 3.23% carbon. The fracture shows a very dense structure with plates which show cleavage and no porosity.

According to the concentration triangle, this alloy should contain ternary pearlite with considerable iron carbide solid solution and a very small amount of iron boride. The structure, as shown in Figures 74 and 75 for the cast condition, present plates of a primarily separated crystal which can only be interpreted to be the iron carbide solid solution which could separate along the CZ curve. The fine eutectic-appearing structure has the appearance of a binary eutectic. Such a structure would indicate that the curve NV was shifted to the right of where it has been placed by Tamman and Vogel, in that such a structure would be expected in the region between C and E_1 and N, in which we have the binary eutectic of iron, iron-boride solid solution and iron carbide solid solution. This conception is further borne out by the structure exhibited by alloy number 18, Figure 98. In Figures 76 and 77 is shown the same

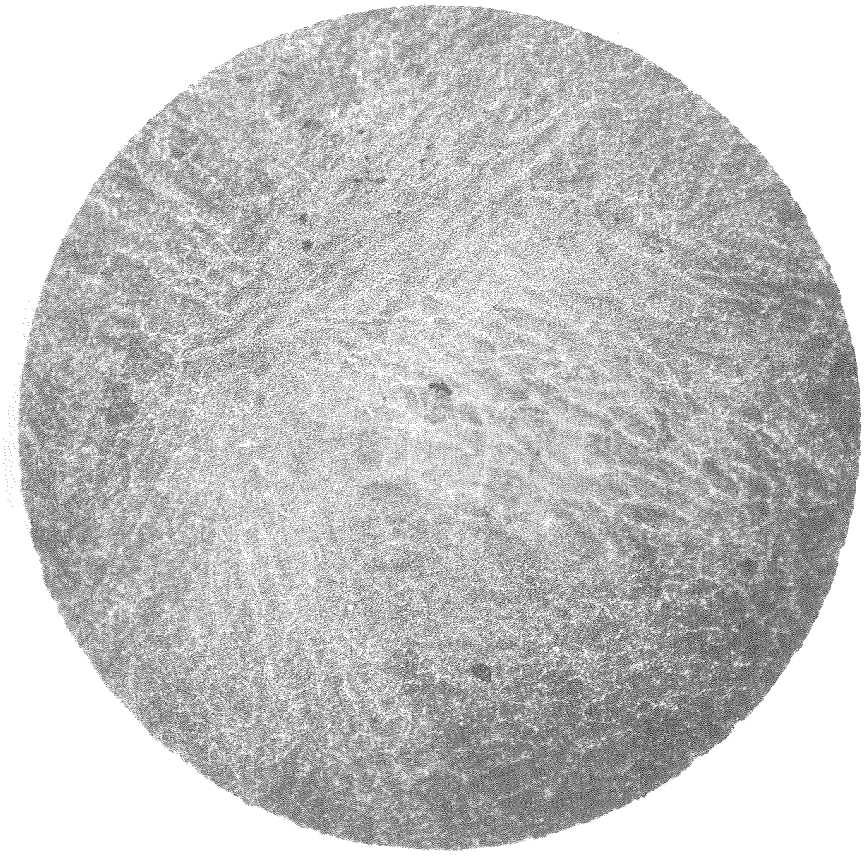

Fig. 71

(13A-1)
Annealed 1800° F.
Magnification 100X
Etch Murakami

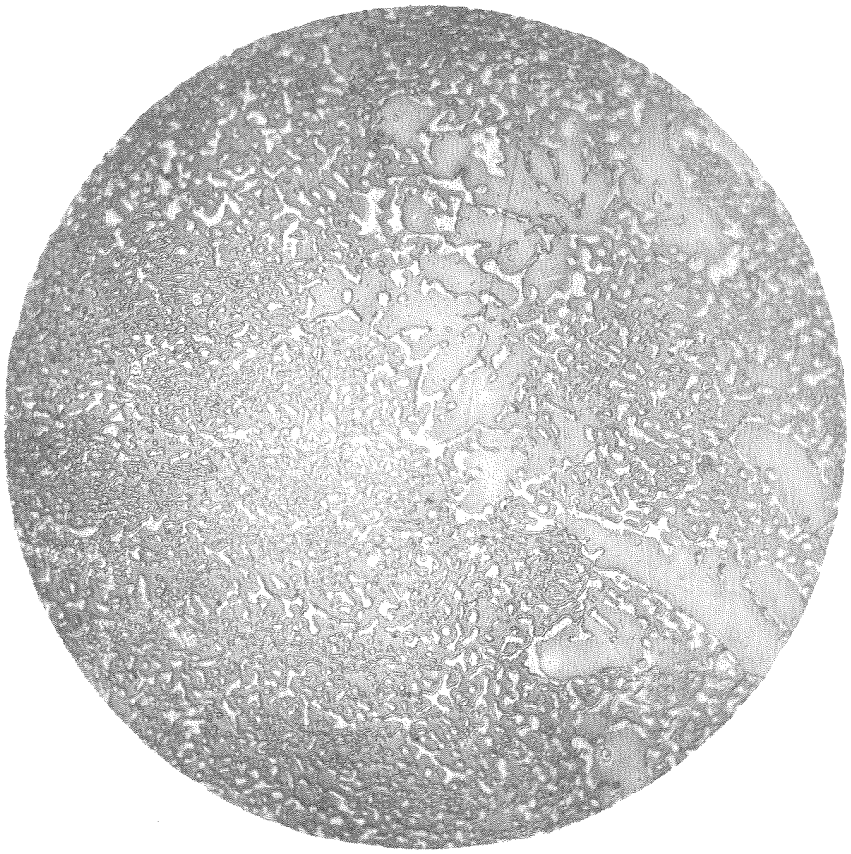

Fig. 72

(13A-2)
Annealed 1800° F.
Magnification 500X
Etch Murakami

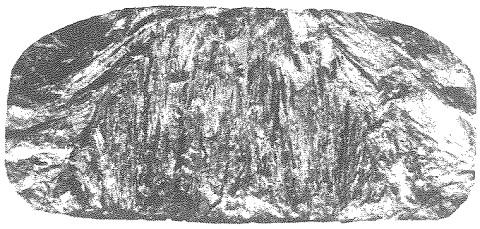

Fig. 73

(10)
As cast
Magnification 2.5X

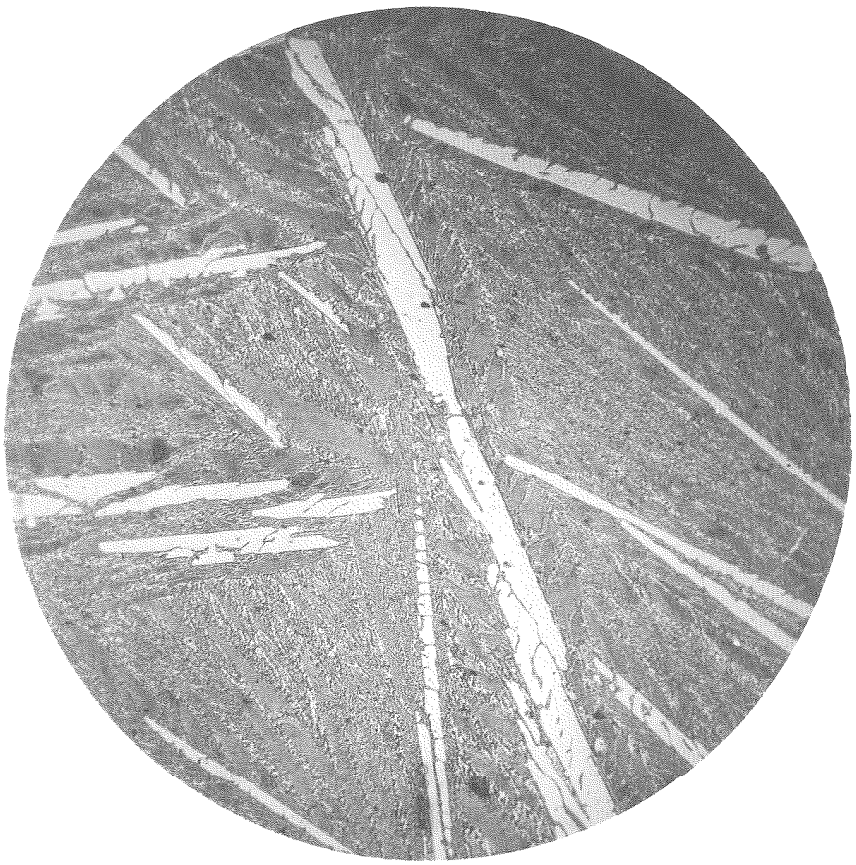

Fig. 74

(10-1)
As cast
Magnification 100X
Etch Murakami

Fig. 75

(1o-2)
As cast
Magnification 500X
Etch Murakami

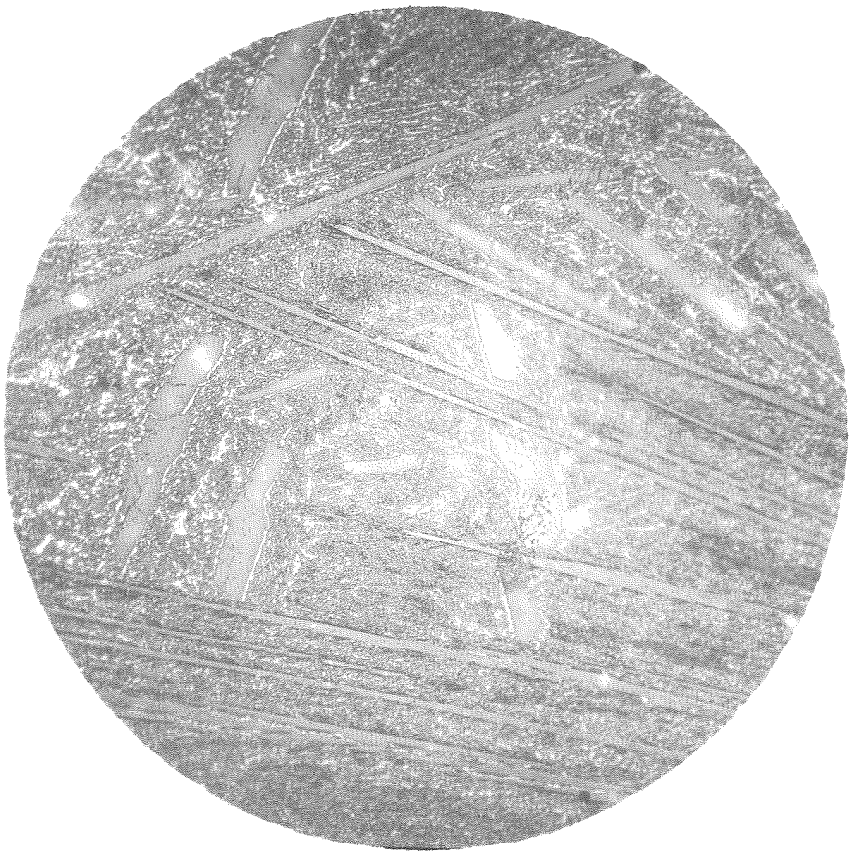

Fig. 76

(1OA-1)
Annealed 1800° F.
Magnification 1OOX
Etch Murakami

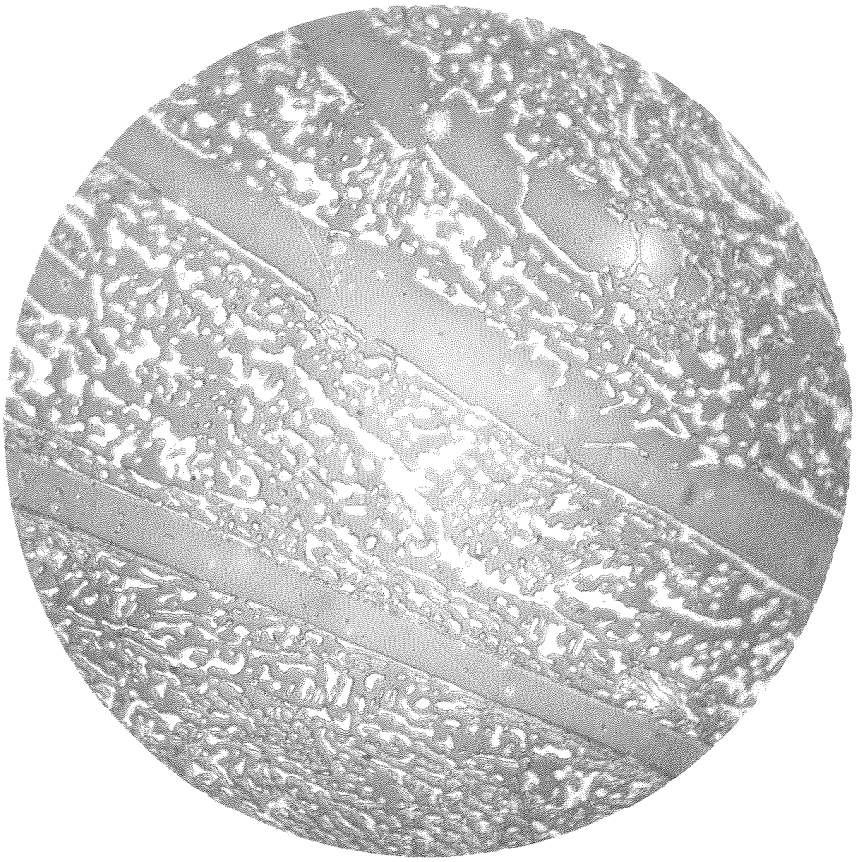

Fig. 77

(10A-2)
Annealed 1800° F.
Magnification 500X
Etch Murakami

alloy after annealing at 1800° F. Nothing unusual has occurred in this structure by annealing, except a coarsening of the fine eutectic structure by more thorough separation of the solid solution constituent.

Figure 78 shows the fracture of specimen number 15 containing 1.28% boron and 1.22% carbon. The fracture shows an extremely dense structure with very fine grain.

The photomicrographs show a structure which is far from what would be expected; viz., a large amount of ternary pearlite with some excess of iron carbide solid solution and iron boride. These are not apparent from Figures 79 and 80 in the cast condition and from Figures 81 and 82 which have been annealed at 1800° F. One explanation which might be offered for this structure, is that the iron carbide solid solution has been thoroughly divorced from the ternary pearlite producing the typical large rounded white structure which is surrounded by a binary-appearing pearlite. Such a condition is quite reasonable in view of the fact that equilibrium conditions undoubtedly did not exist and are hard to attain in this alloy.

Figure 83 shows the fracture of specimen number 12 containing 2.6% boron and 1.21% carbon. The fracture shows a very dense granular structure with considerable porosity in the casting.

In this case, we should expect considerable ternary eutectic with some excess of the ternary solid solution which, upon slow

Fig. 78

(15)
As cast
Magnification 2.5X

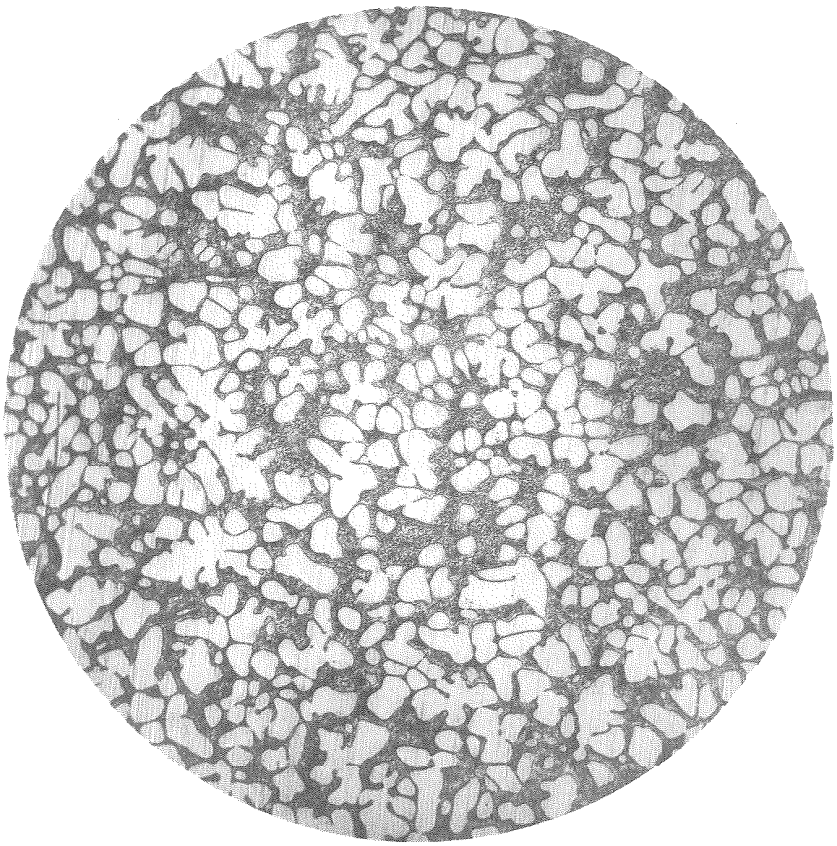

Fig. 79

(15-1)
As cast
Magnification 100X
Etch Murakami

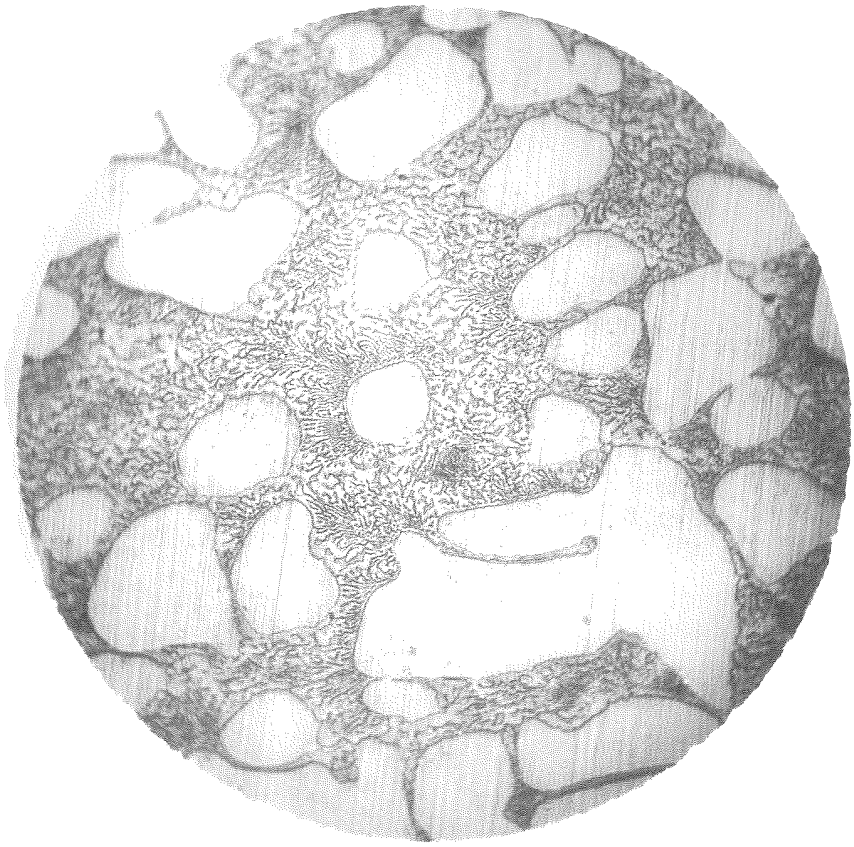

Fig. 80

(15-2)
As cast
Magnification 500X
Etch Murakami

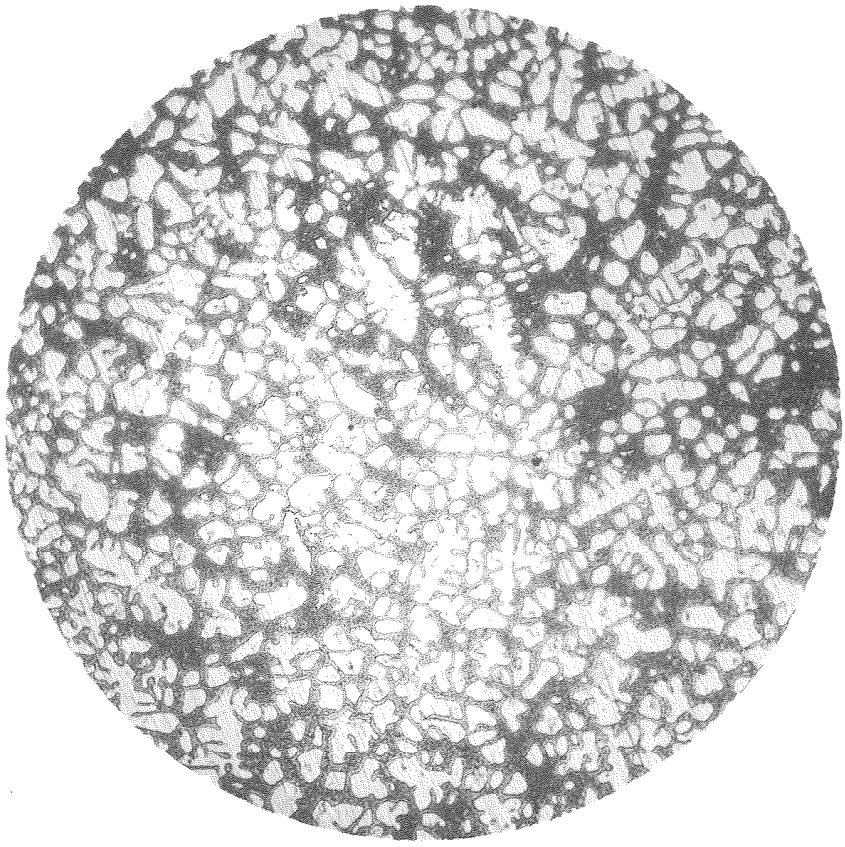

Fig. 81

(15A-1)
Annealed 1800° F.
Magnification 100X
Etch Murakami

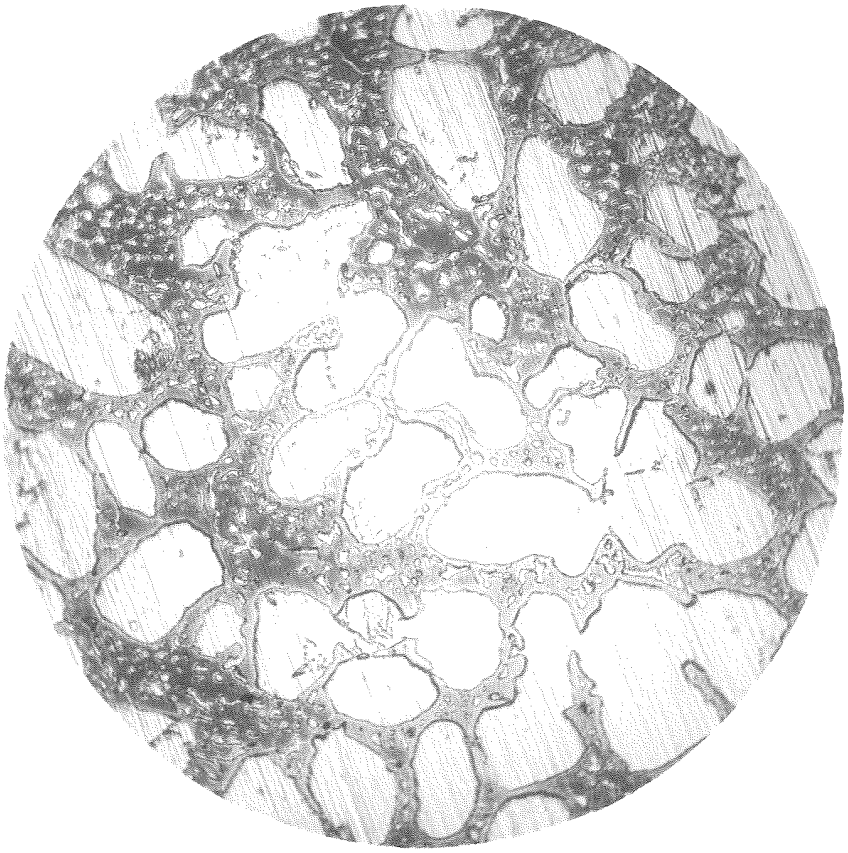

Fig. 82

(15A-2)
Annealed 1800° F.
Magnification 500X
Etch Murakami

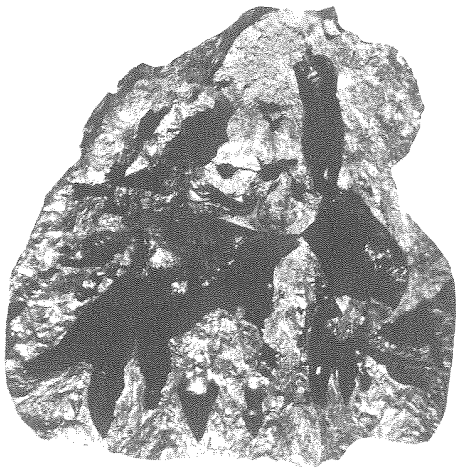

Fig. 83

(12)
As cast
Magnification 2.5X

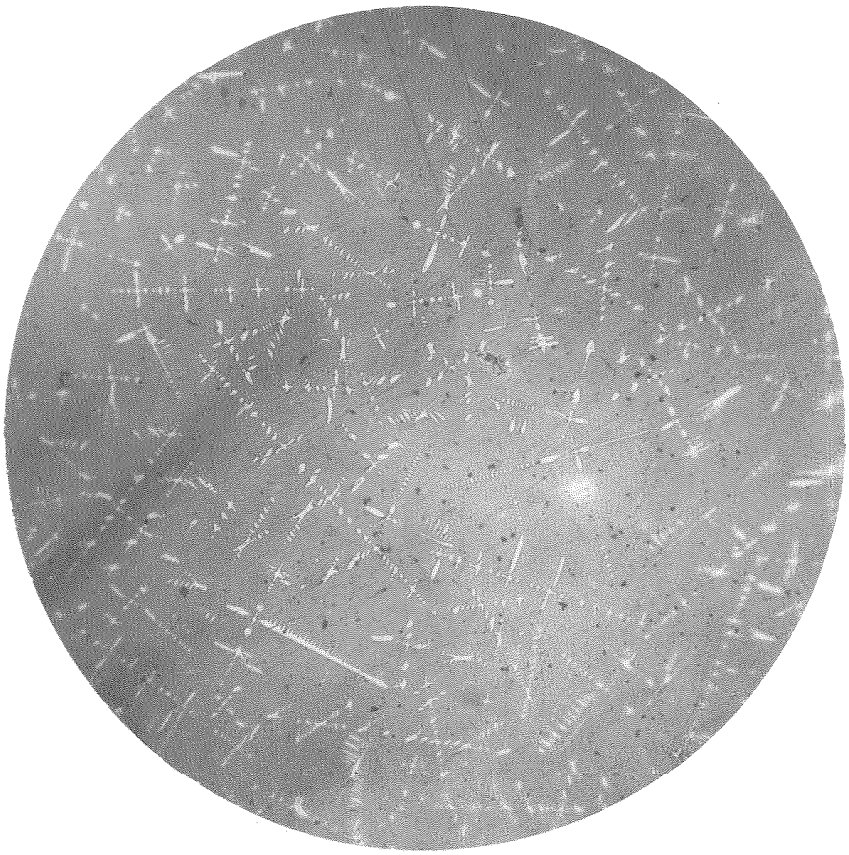

Fig. 84

(12-1)
As cast
Magnification 100X
Etch Murakami

cooling under equilibrium conditions would disintegrate to the ternary pearlite. This condition is actually shown in Figures 84 and 85. The white dendritic structure is the primary ternary solid solution while the ground mass is the ternary eutectic. This structure is almost completely removed by annealing at 1800° F., as shown by Figures 86 and 87, which should and does show this ternary eutectic as transformed to the ternary pearlite with some excess of iron carbide solid solution.

Figure 88 shows the fracture of the specimen number 16 containing 1.21% boron and 2.14% carbon. The fracture shows a very dense fine grain structure that has a tendency to cleave.

The structure in the case of this alloy should consist of an excess of ternary solid solution with ternary eutectic. This is shown in Figures 89 and 90, in which the white structure is the ternary solid solution and is surrounded by the ternary eutectic. Upon annealing this excess solid solution is not obliterated, but apparently does transform into the ternary pearlite, as indicated by Figures 91 and particularly 92. In Figure 92 some pearlite is distinguishable in the white structure. This ternary pearlite is very difficult to bring out with etching, and, hence, may in most cases be obscured. The ternary eutectic after annealing has been pretty well disintegrated into its constituents.

Figure 93 shows the fracture of specimen number 17 containing 1.18% boron and 2.41% carbon. The fracture shows a dense structure containing fine needles.

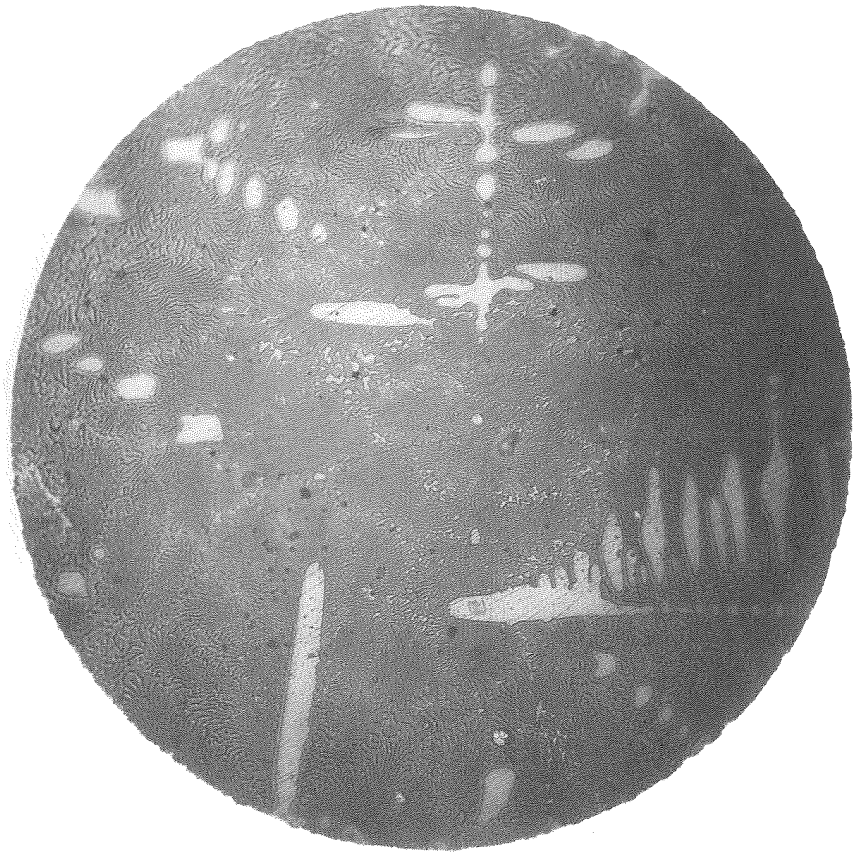

Fig. 85

(12-2)
As cast
Magnification 500X
Etch Murakami

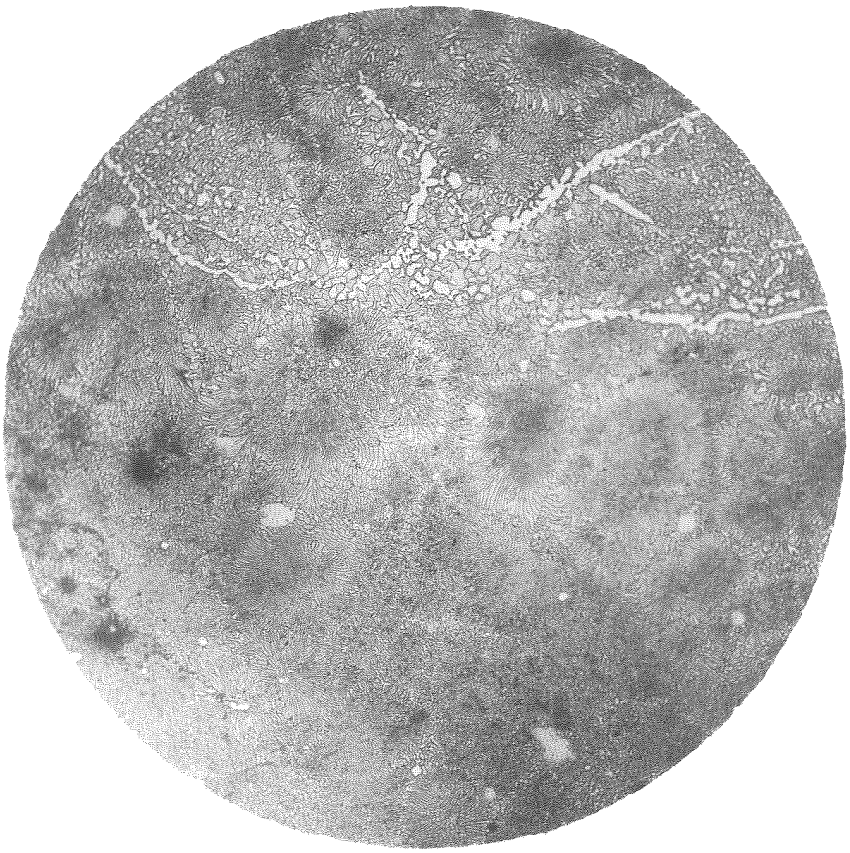

Fig. 86

(12A-1)
Annealed 1800° F.
Magnification 100X
Etch Murakami

Fig. 87

(12A-2)
Annealed 1800° F.
Magnification 500X
Etch Murakami

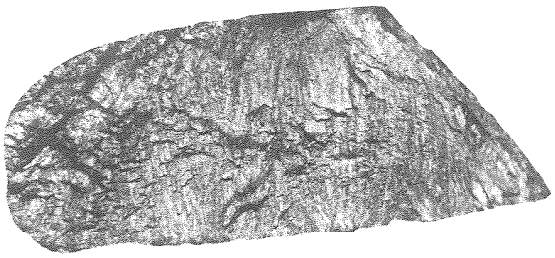

Fig. 88

(16)
As cast
Magnification 2.5X

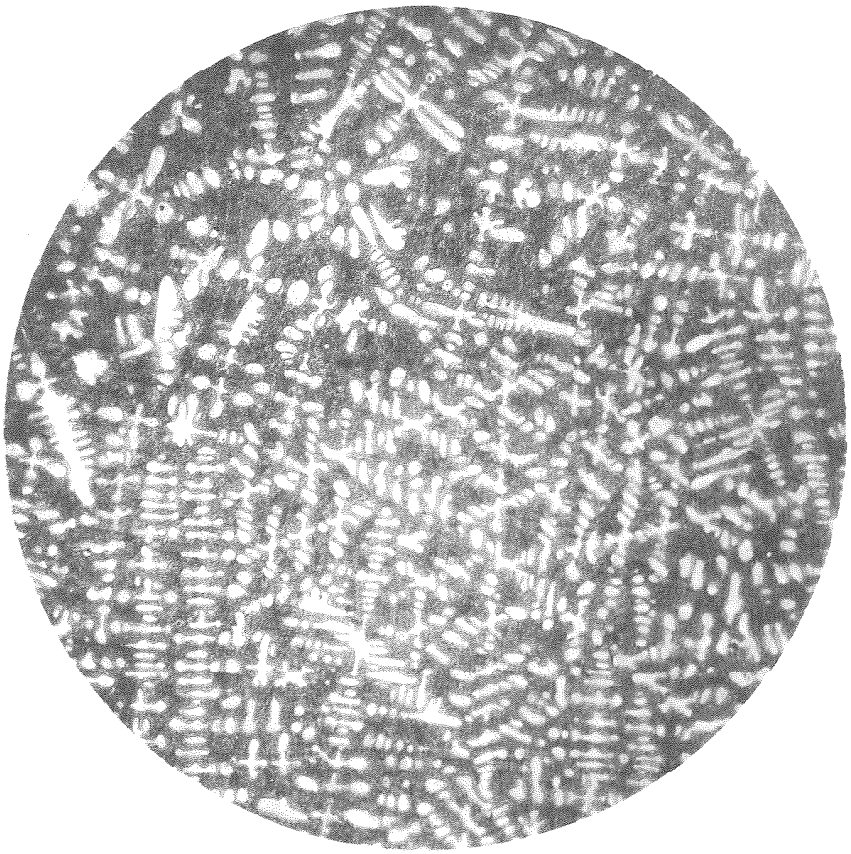

Fig. 89

(16-1)
As cast
Magnification 100X
Etch Murakami

Fig. 90

(16-2)
As cast
Magnification 500X
Etch Murakami

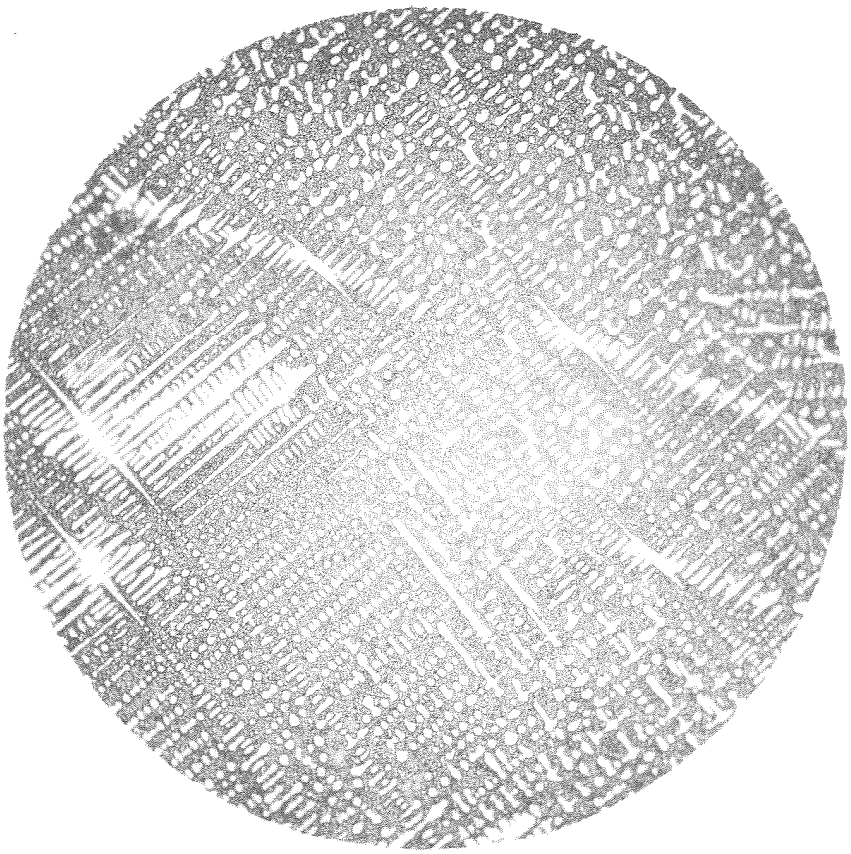

Fig. 91

(16A-1)
Annealed 1800° F.
Magnification 100X
Etch Murakami

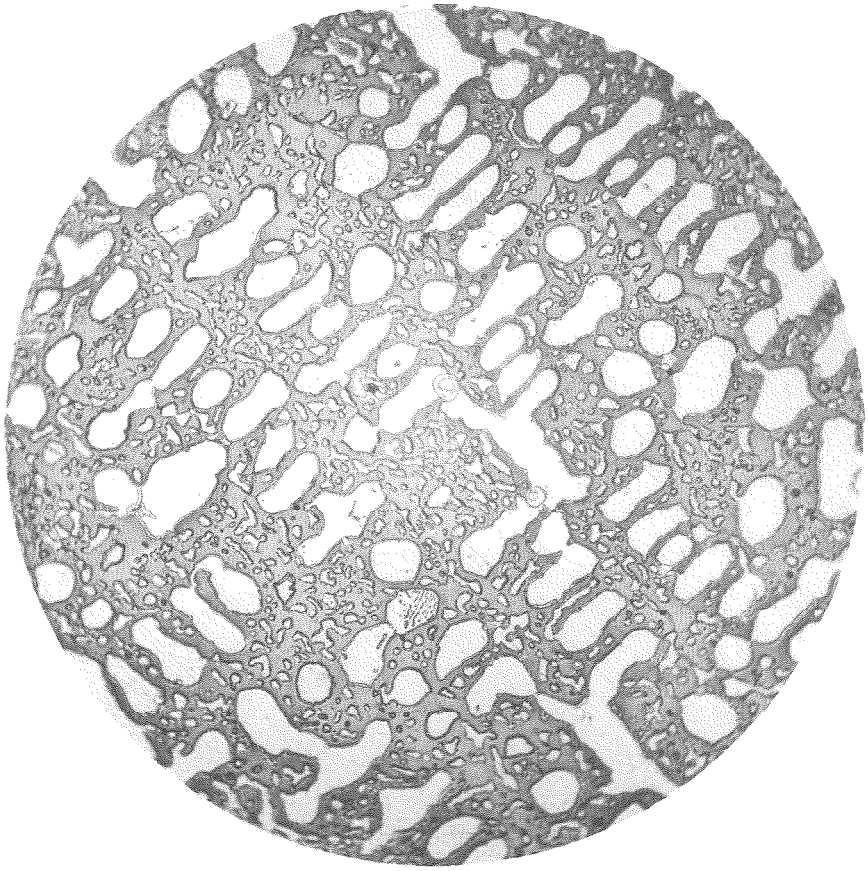

Fig. 92

(16A-2)
Annealed 1800° F.
Magnification 500X
Etch Murakami

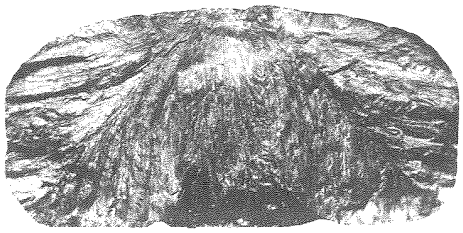

Fig. 93

(17)
As cast
Magnification 2.5X

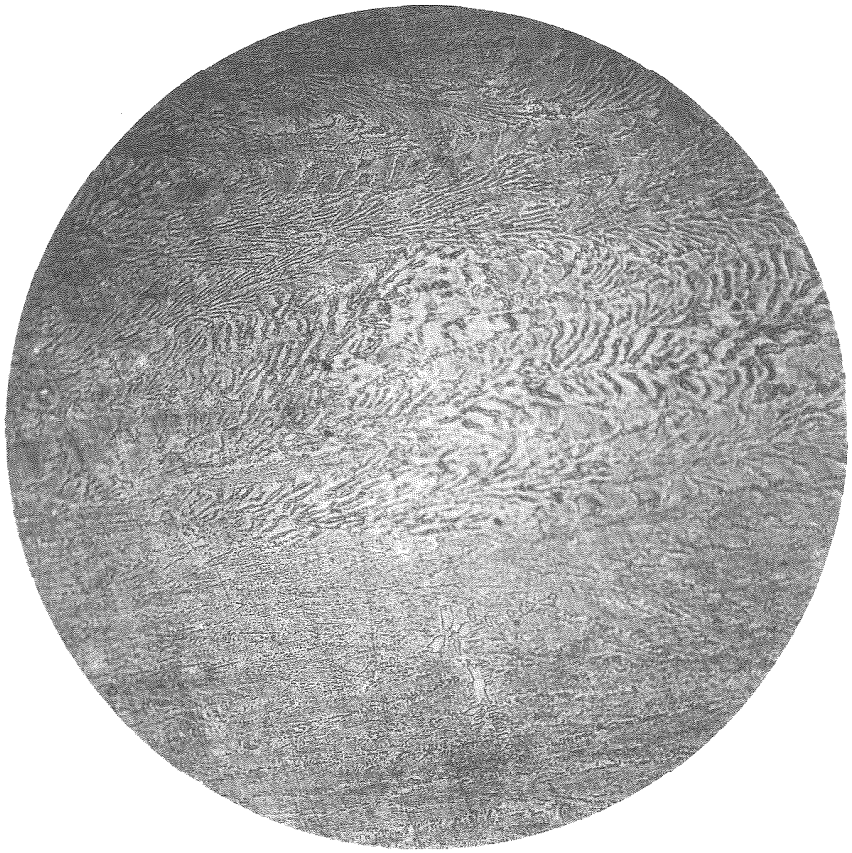

Fig. 94

(17-1)
As cast
Magnification 100X
Etch Murakami

According to the concentration triangle, this alloy should consist of ternary pearlite with some excess iron carbide solid solution. Figures 94 and 95 show this structure in which we have some iron carbide solid solution as the gray material surrounded by material probably formed from the eutectic, consisting initially of iron carbide solid solution and ternary solid solution. Figures 96 and 97 show the structure after annealing at 1800° F. The eutectic structure has been broken up completely, leaving the unresolved ternary pearlite (white) and the iron carbide solid solution.

Figure 98 shows the fracture of specimen number 18 containing 0.96% boron and 3.80% carbon. The fracture shows a dense material containing plates.

The microstructure of this alloy is shown in Figures 99 and 100 as cast showing primary separation of the iron carbide solid solution which has the form usually taken by pure iron carbide in a hyper-eutectic iron carbon alloy. This is surrounded by the eutectic which separated along the curve E_1R which presents more nearly the structure of a binary pearlite. Figures 101 and 102 show the structure after annealing at 1800° F. This shows that the eutectic structure has been very thoroughly disintegrated, leaving only the mixture of binary pearlite, consisting of iron, iron-boride solid solution (white) and iron carbide solid solution dark.

Fig. 95

(17-2)
As cast
Magnification 500X
Etch Murakami

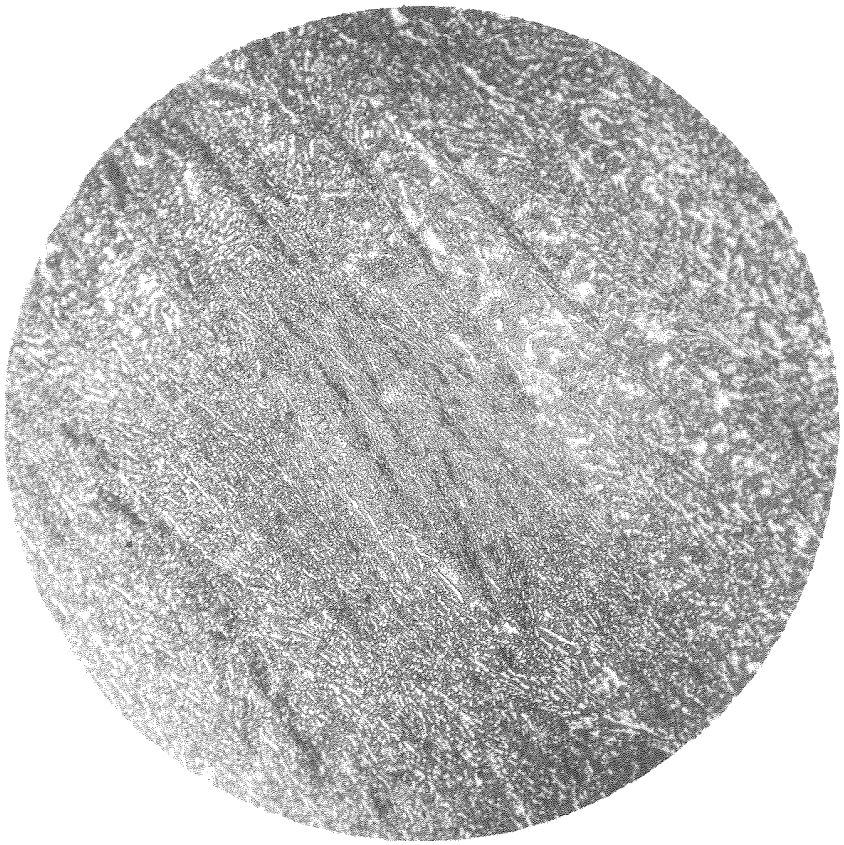

Fig. 96

(17A-1)
Annealed 1800° F.
Magnification 100X
Etch Murakami

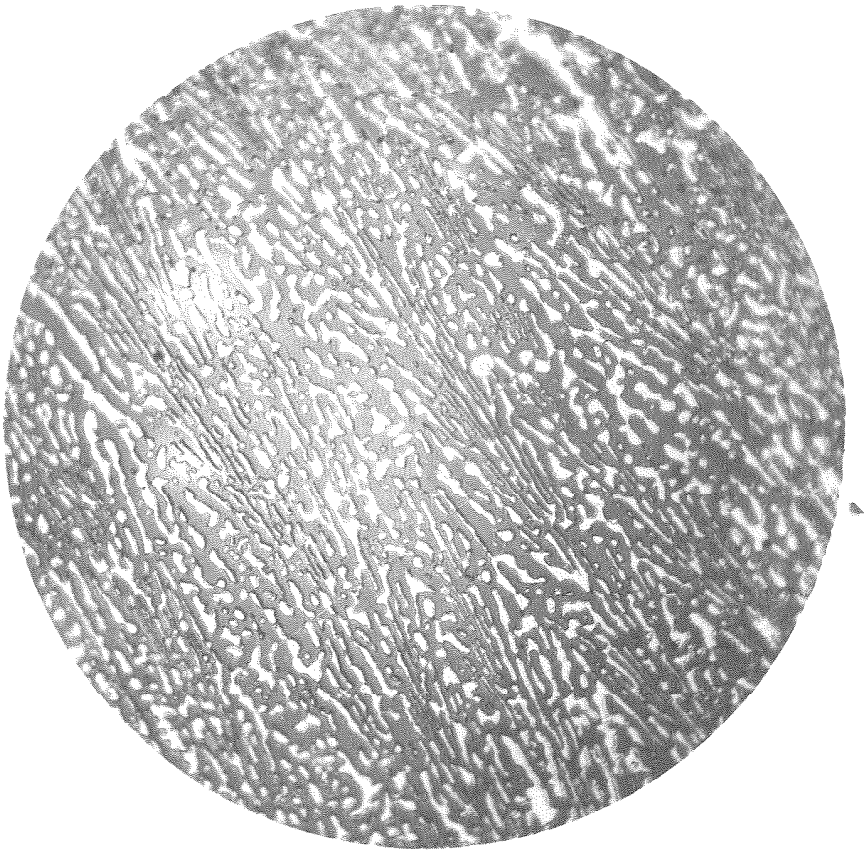

Fig. 97

(17A-2)
Annealed 1800° F.
Magnification 500X
Etch Murakami

Fig. 98

(18)
As cast
Magnification 2.5X

Fig. 99

(18-1)
As cast
Magnification 100X
Etch Murakami

Fig. 100

(18-2)
As cast
Magnification 500X
Etch Murakami

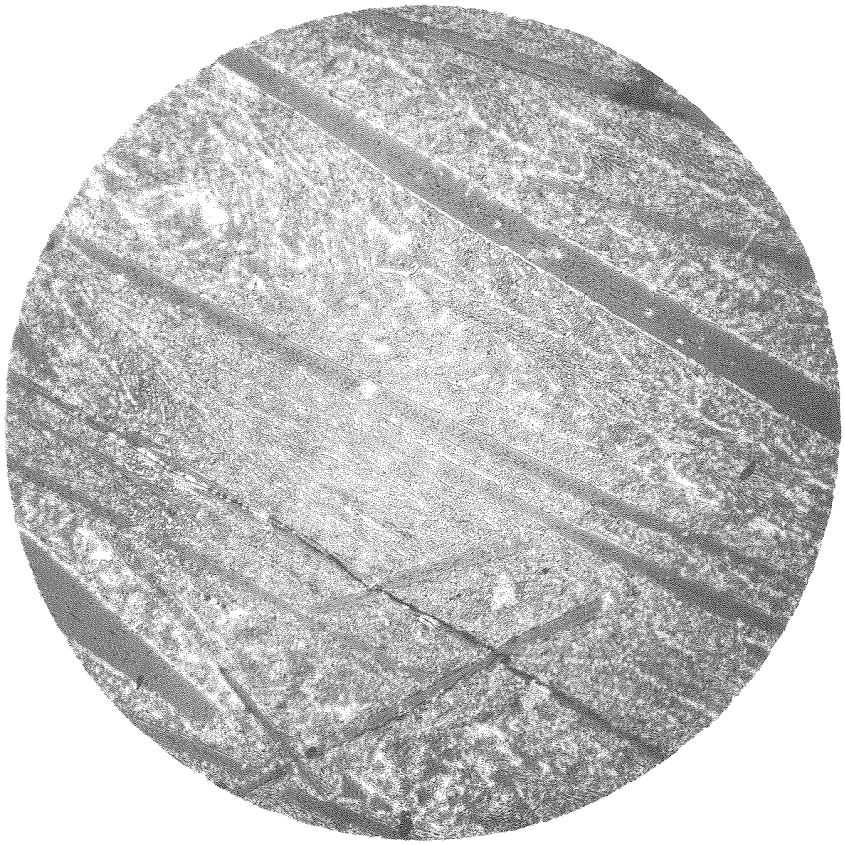

Fig. 101

(18A-1)
Annealed 1800° F.
Magnification 100X
Etch Murakami

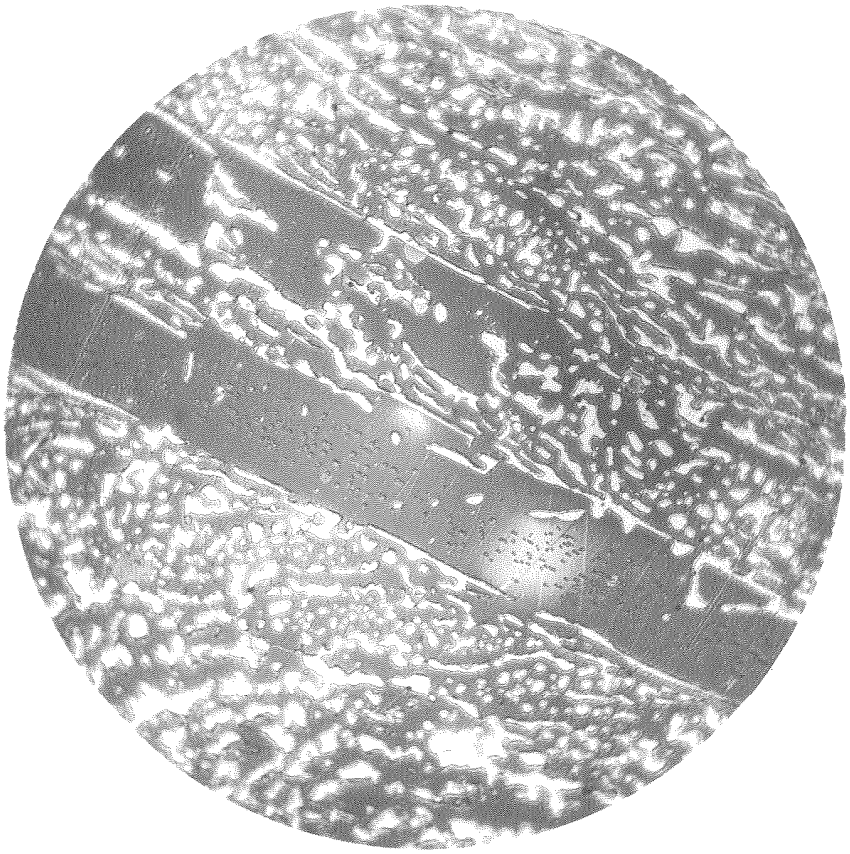

Fig. 102

(18A-2)
Annealed 1800° F.
Magnification 500X
Etch Murakami

The results of this part of the investigation check very well with the equilibrium diagram. The microscopic investigation of alloys for checking a complicated system, such as this, is very difficult, because absolute equilibrium or even conditions which approach equilibrium are very difficult to obtain. However, the results show, for all practical purposes, the structures obtained in this system follow the diagram proposed by Tammann and Vogel insofar as the liquid-solid transformations are concerned.

Structures of Commercial Alloys

As pointed out in the introduction, the most useful alloys have been found to lie in a relatively restricted composition range. For the remainder of this thesis, the structures and properties of alloys will be considered which, with a few exceptions, have proven to be of considerable value commercially in their resistance to wear. No attempt will be made here to discuss the relative merits of the various alloys from the standpoint of wear resistance since this thesis is concerned with the metallographic investigation. Hence, the remainder of the discussion of the experimental work will be devoted to the metallographic structure of the alloys in this region and their physical properties. The compositions of representative alloys used in this part of the research are listed in Table II. and plotted on the ternary concentration triangle shown in Figure 103. The specimen numbers underlined in this diagram refer to the alloys used in investigating the equilibrium diagram, as discussed in the previous section of the experimental work.

TABLE II. COMMERCIAL ALLOYS

Spec. No.	% Carbon Graphitic	% Carbon Total	% Boron	% Silicon	Figures As Cast	Figures Annealed
62-2	0.028	2.71	0.20	0.53	104,105,175	171,172,173,174
135		3.19	0.12	0.49	113,114,178,179	176,177
189		2.85	0.97	0.49	129,130	199,200
221		3.07	0.87		126	184,185
225		2.43	1.81	0.85	141,142	201,202
228		2.76	1.04			194,195,196,197
245		1.78	2.82	0.53	156,157,158,159	
246		2.53	2.94	0.51	160,161,162	
247		3.16	1.24	0.78	134,135	
248	0.83	3.84	2.88	0.30	152,153,154,155	212,213
249		0.12	5.00	0.49	167,168,169,170	214,215
255		3.05	1.40	1.61	136	
261		2.52	0.65	1.14	106,107	
262		3.73	1.20	1.21	127,128	
267		2.54	1.51	1.30	138,139	186,187,188,189, 190,191,192,193
268	2.30	3.42	0	1.44	116,117	
270	0.18	3.50	0.22	1.13	118,119	180,181
271	0.18	3.43	0.49	1.16	122,123	182,183
272	0.18	3.26	1.02	0.80	132,133	
276	0.22	3.03	1.70	1.36	143,144	203 to 211 incl.

TABLE II. COMMERCIAL ALLOYS, Continued

Spec. No.	% Carbon Graphitic	Total	% Boron	% Silicon	Figures As Cast	Annealed
277	0.53	3.05	2.57	1.10	150,151	
278	0.52	2.76	2.14	2.14	145,146	
279	0.80	2.34	2.57	4.25	147,148,149	
289	0	0	6.33		165,166	
291		0.41	6.33		163,164	
292		3.00	0		108,109	
293		3.00	0.10	1.50	110	
294		3.00	0.25	1.50	111	
295		3.00	0.50	1.50	112	
296		3.00	1.00	1.50	131	
297		2.50	0	1.50	115	
298		2.50	0.10	1.50	120	
299		2.50	0.25	1.50	121	
400		2.50	0.50	1.50	124	
401		2.50	1.00	1.50	125	
405		2.72	1.69	0.15	137	
406		2.29	1.63	0.91	140	

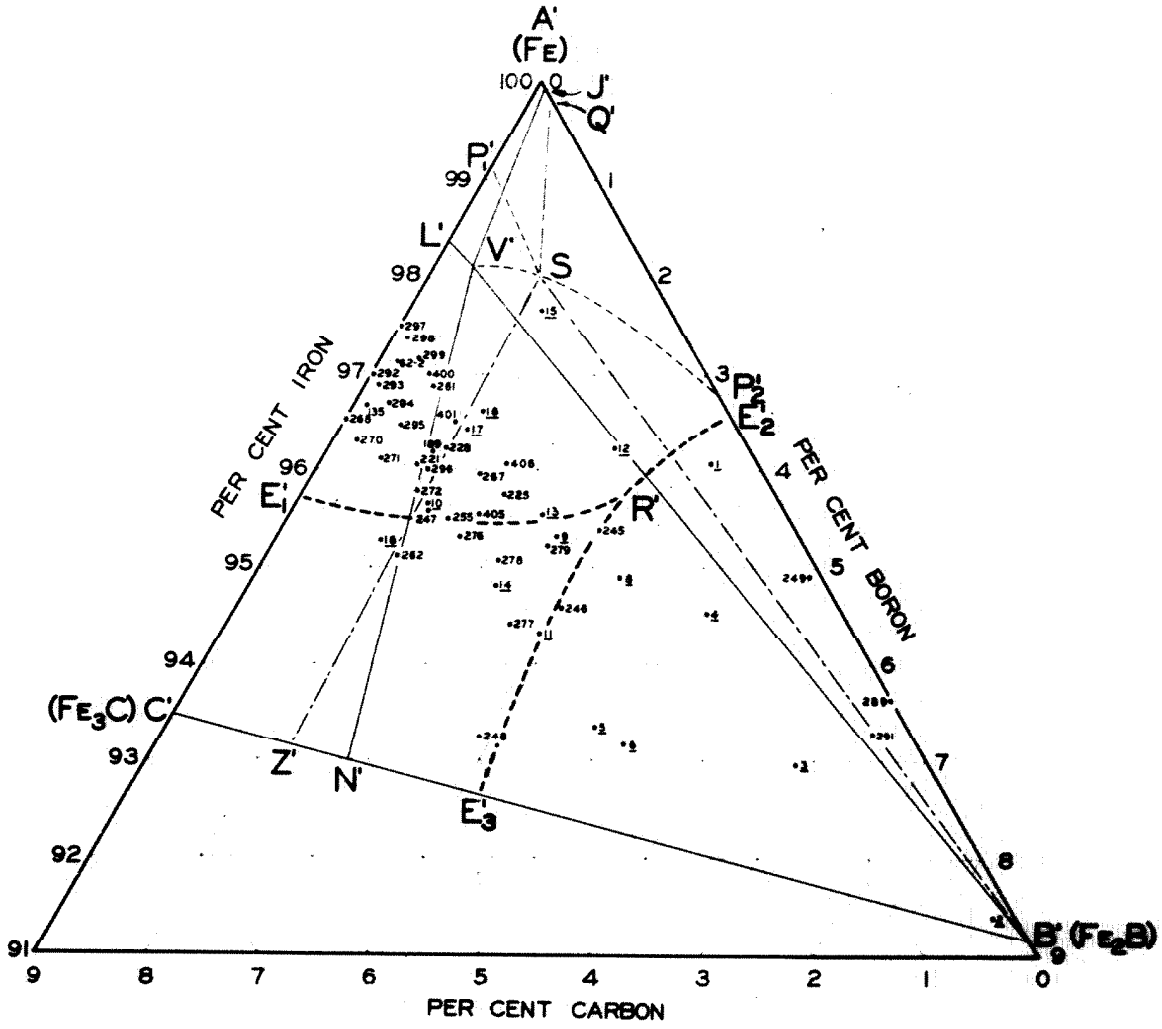

FIG. 103

CONCENTRATION TRIANGLE

The structures of these commercial melts will be investigated according to the different concentration fields. First consider specimen 62-2 having a structure consisting, first, of primary ternary solid solution, which breaks up into the ternary pearlite, and, second, a eutectic between the ternary solid solution and the iron carbide solid solution. In Figures 104 and 105 is shown this structure in which the white material is the iron carbide solid solution, the larger dark portions are pearlite, the very fine dark spotted groupings are from the eutectic between the ternary solid solution and the iron carbide solid solution.

Specimen 261, Figures 106 and 107, shows the same type of structure as the previous alloy. It is apparent that this alloy does lie within the region being considered, since this structure does persist and no excess of iron carbide solid solution is apparent.

Figures 108 and 109 show the structure of specimen 292 which is not justified according to the chemical analysis. The structure presented here would indicate that its composition should be of less carbon content, since a very definite pearlitic structure is observed for practically the entire area of the photomicrograph. This alloy contains about 1.5% silicon which might partially account for this effect, but certainly not completely.

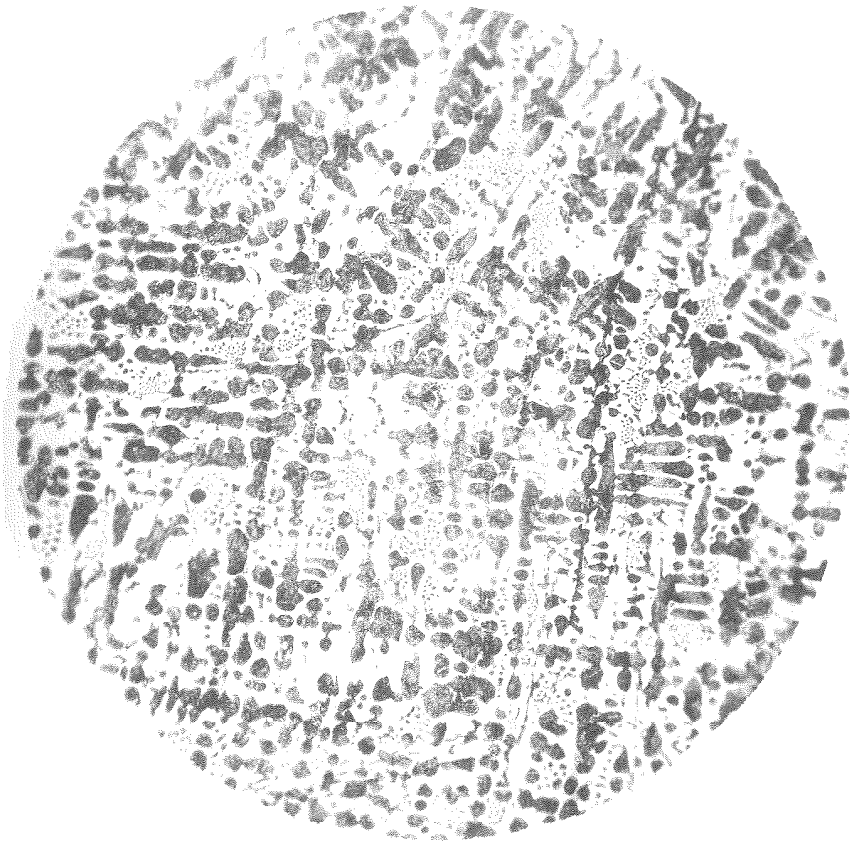

Fig. 104

(62-2A)
As cast
Magnification 100X
Etch 5% Picrol

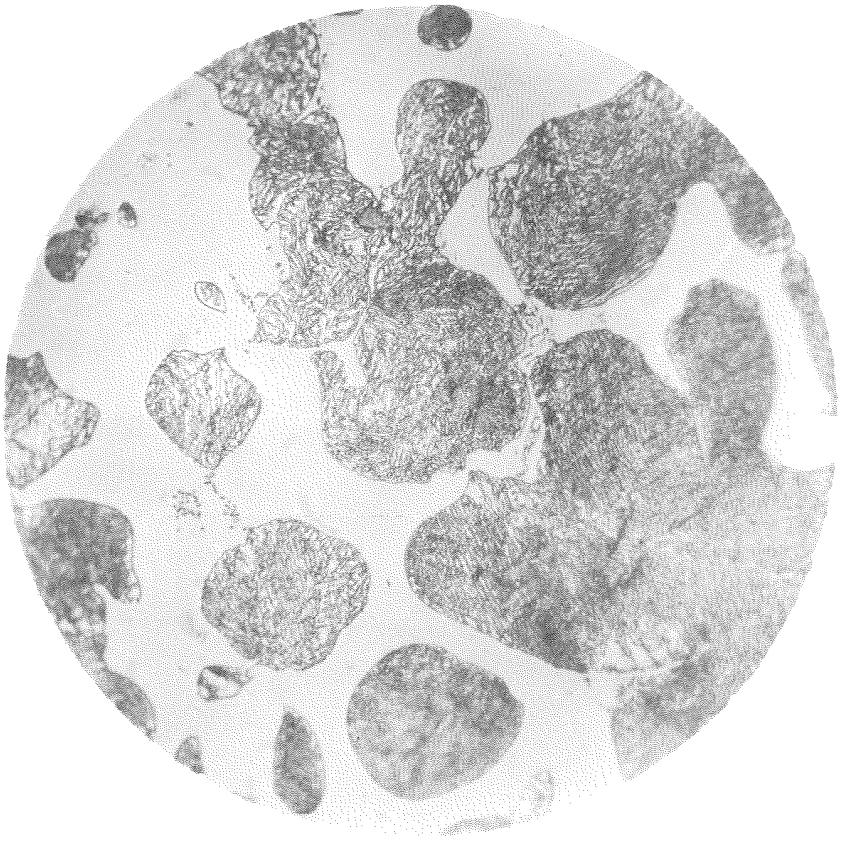

Fig. 105

(62-2B)
As cast
Magnification 1000X
Etch 5% Picrol

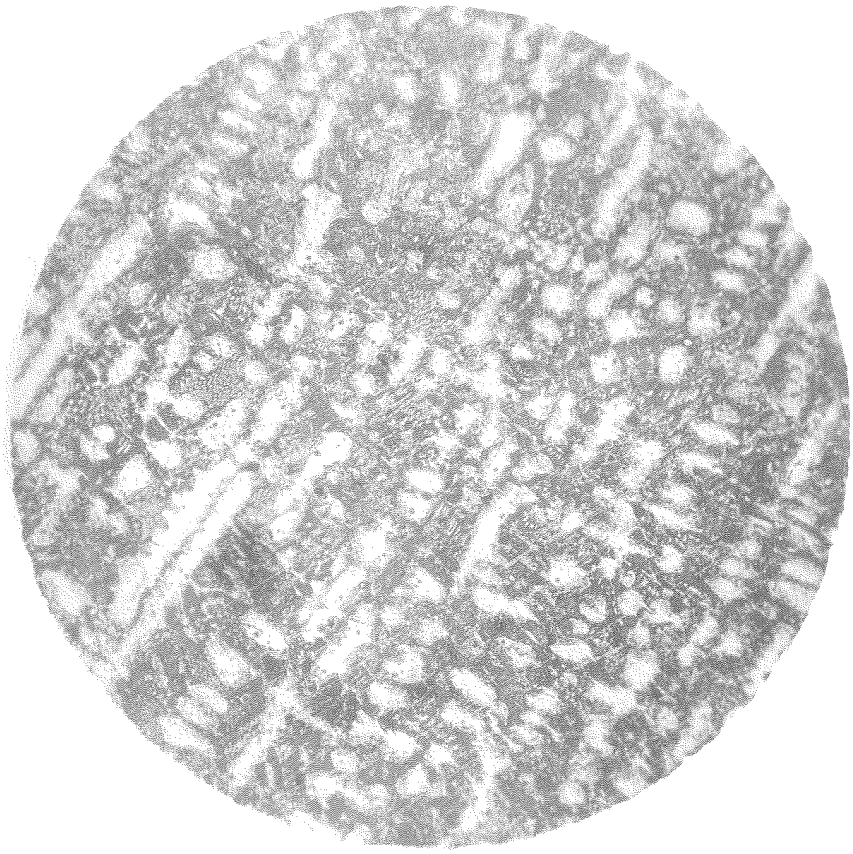

Fig. 106

(261AA)
As cast
Magnification 100X
Etch Murakami

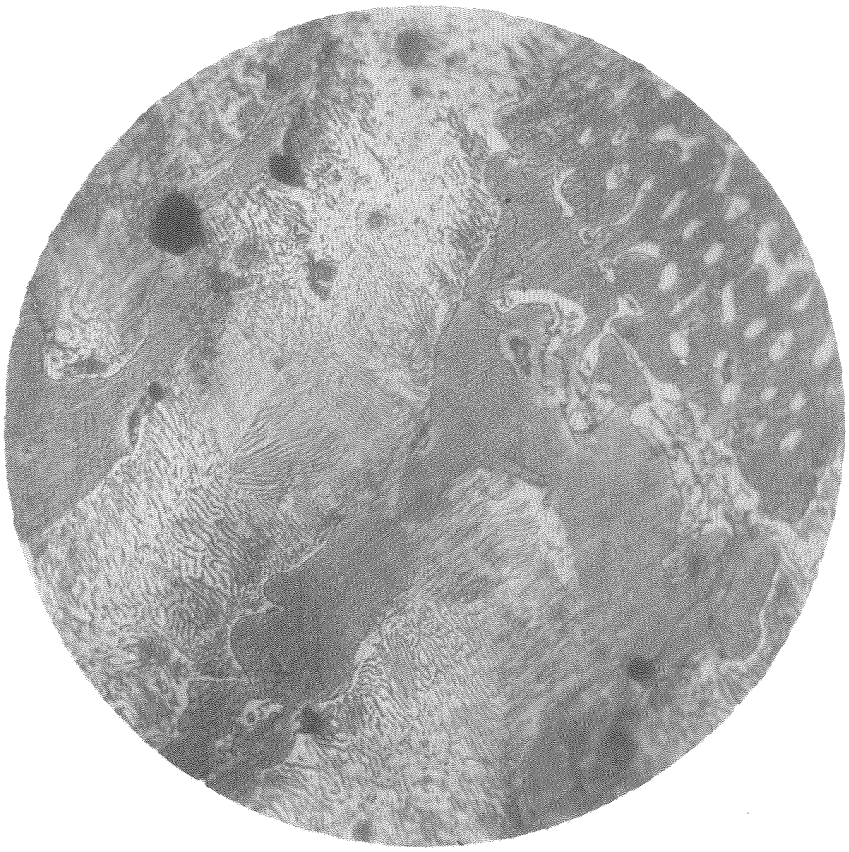

Fig. 107

(261AB)
As cast
Magnification 1000X
Etch Murakami

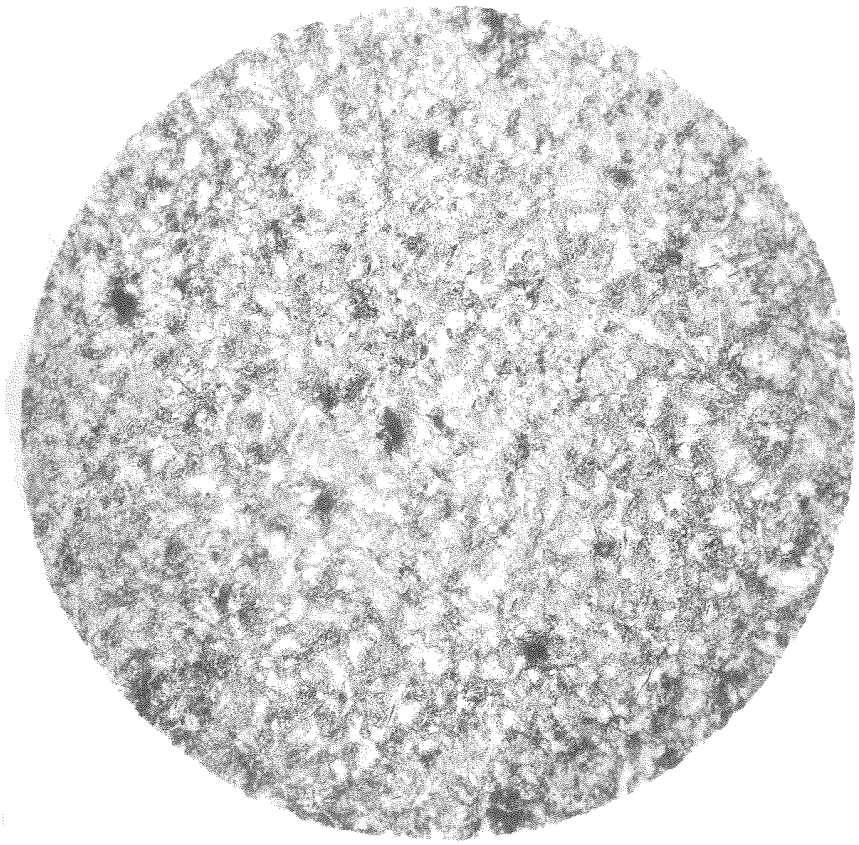

Fig. 108

(292B-2)
As cast
Magnification 100X
Etch 5% Picrol

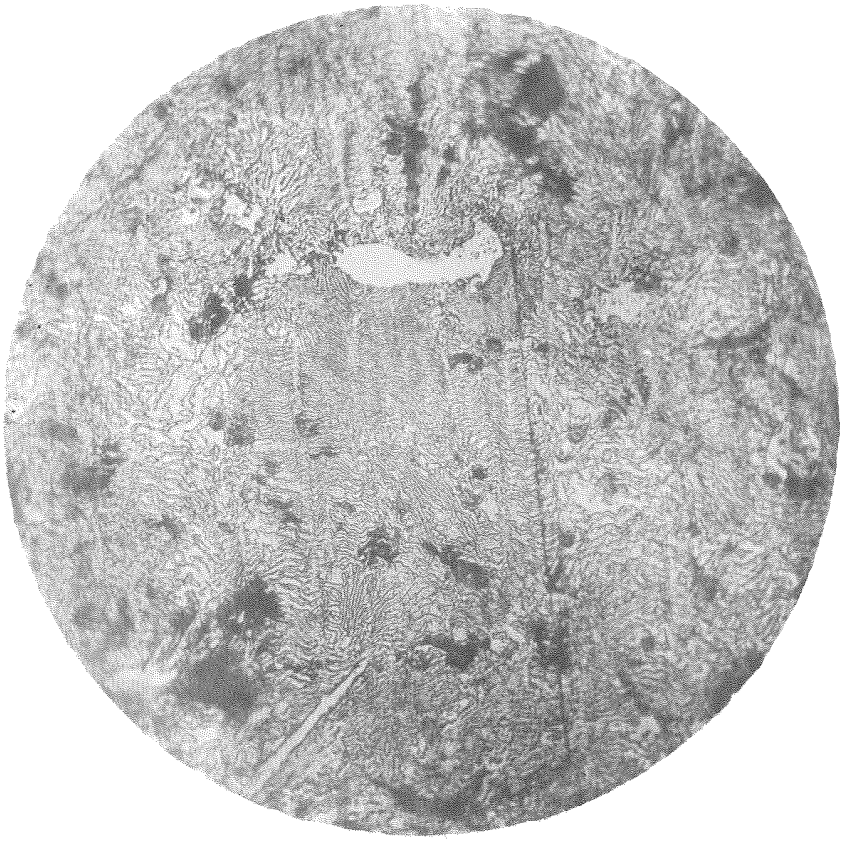

Fig. 109

(292B-3)
As cast
Magnification 1000X
Etch 5% Picrol

Figures 110, 111, and 112 show the structures obtained in specimens 293, 294, and 295, respectively. These specimens contain the same amounts of carbon with increasing amounts of boron, as indicated in the table. The structures are similar to those discussed above and are about as would be expected from a study of the equilibrium diagram.

Figures 113 and 114 show the structure of specimen 135, revealing a rather large amount of primary ternary solid solution which has disintegrated, as in the previous specimens, into pearlite. The surrounding white constituent is the iron carbide solid solution. The difference between the structure of this alloy containing only 0.49% silicon and the structure of specimen 293 (Figure 110) which contains 1.5% silicon should be particularly noted. This is very indicative of the influence of silicon on the structure of the alloys in this region. The effect seems to be to alter the transformation compositions so that a structure somewhat different from what would be expected is obtained.

Figure 115 shows the structure of specimen 297 which also has 1.5% silicon and compares favorably with the other structures in this region, in that it contains more material originating from the primary solid solution.

Figures 116 and 117 show the structure of specimen 268 in which there is no boron present. Due to the relatively high silicon

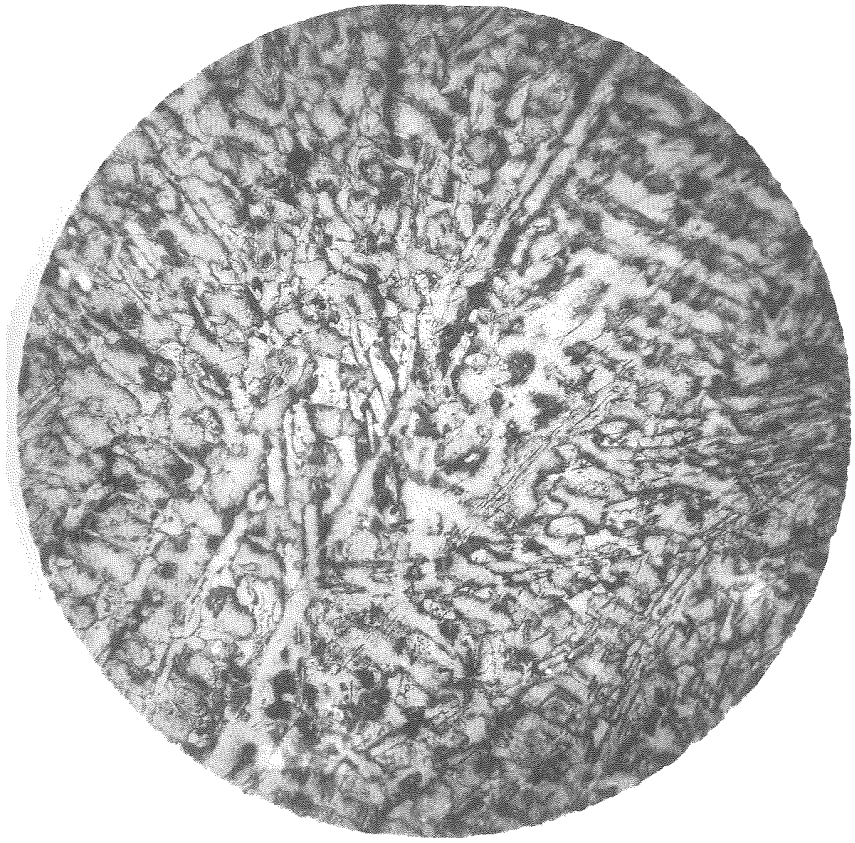

Fig. 110

(293B-1)
As cast
Magnification 100X
Etch Murakami

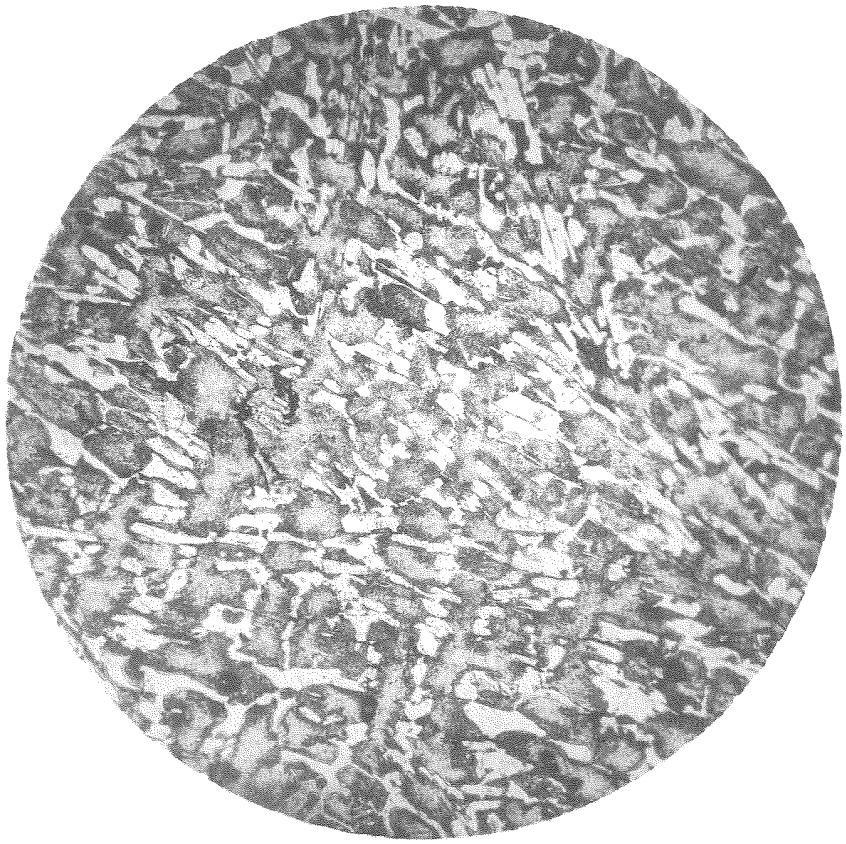

Fig. 111

(294A-1)
As cast
Magnification 100X
Etch Murakami

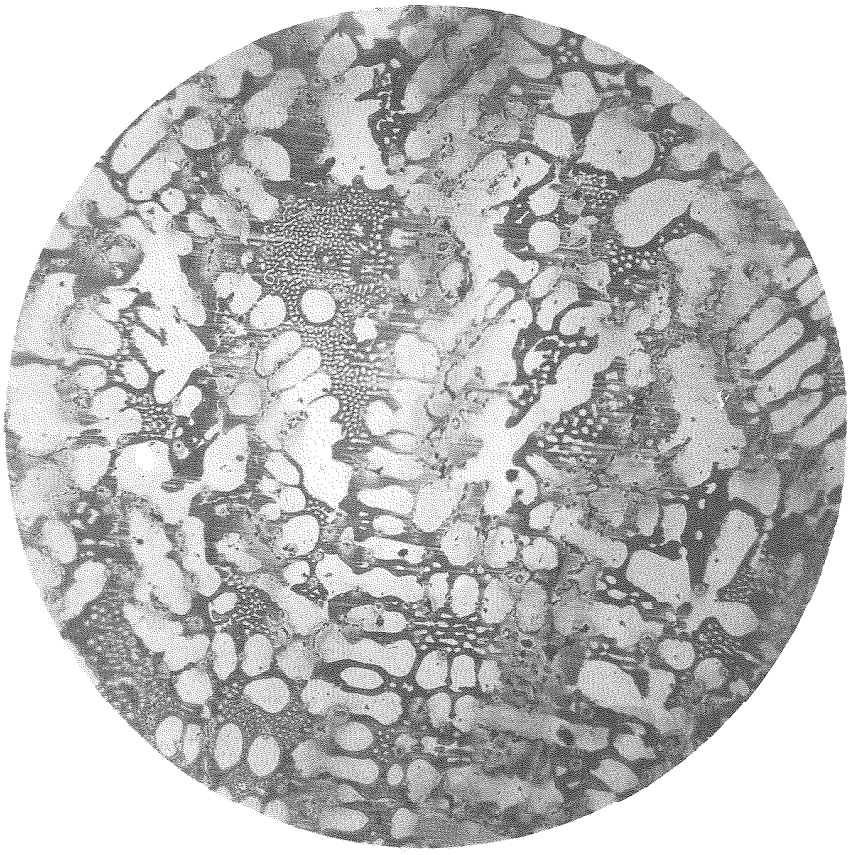

Fig. 112

(295B-1)
As cast
Magnification 100X
Etch Murakami

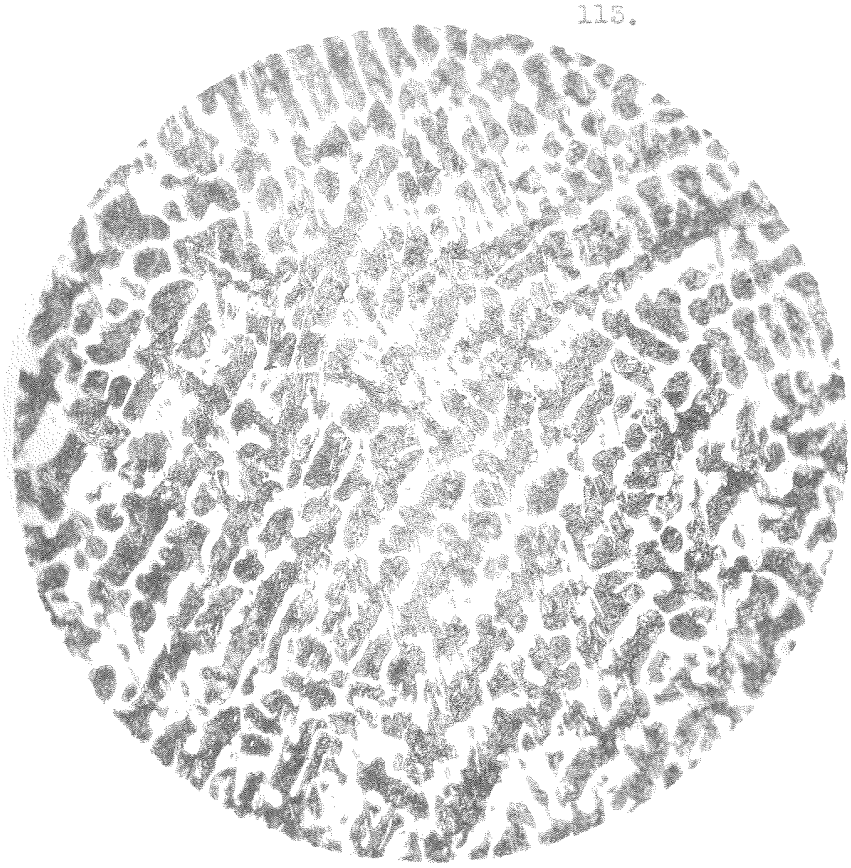

Fig. 113

(B135A)
As cast
Magnification 100X
Etch 5% Picrol

Fig. 114

(B135B)
As cast
Magnification 1000X
Etch .5% Picrol

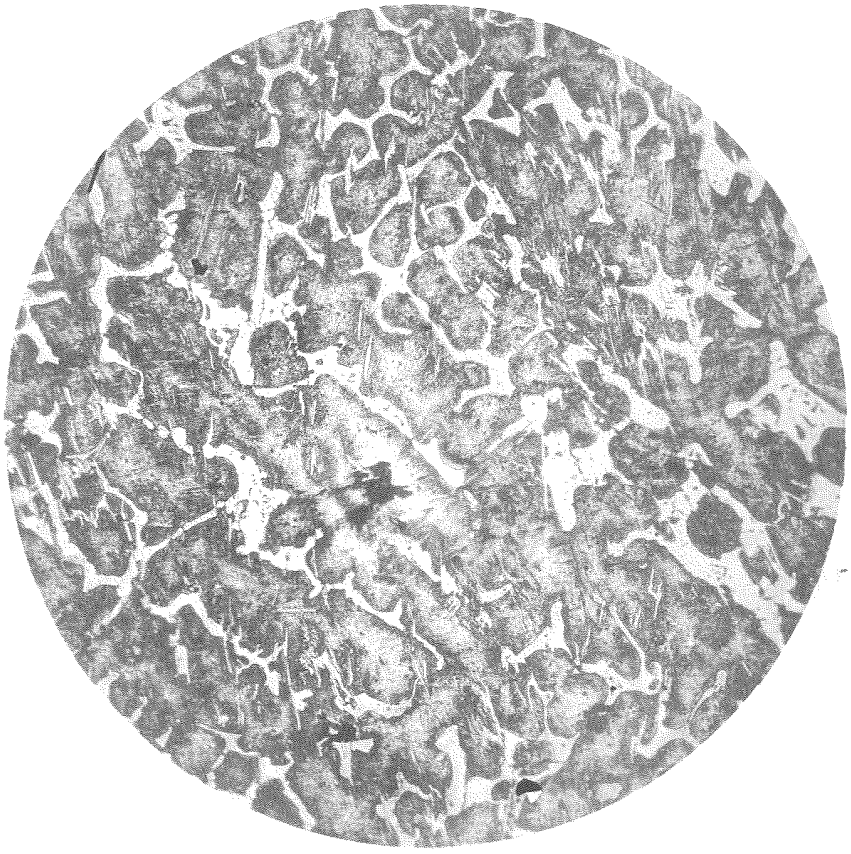

Fig. 115

(297B1)
As cast
Magnification 100X
Etch Murakami

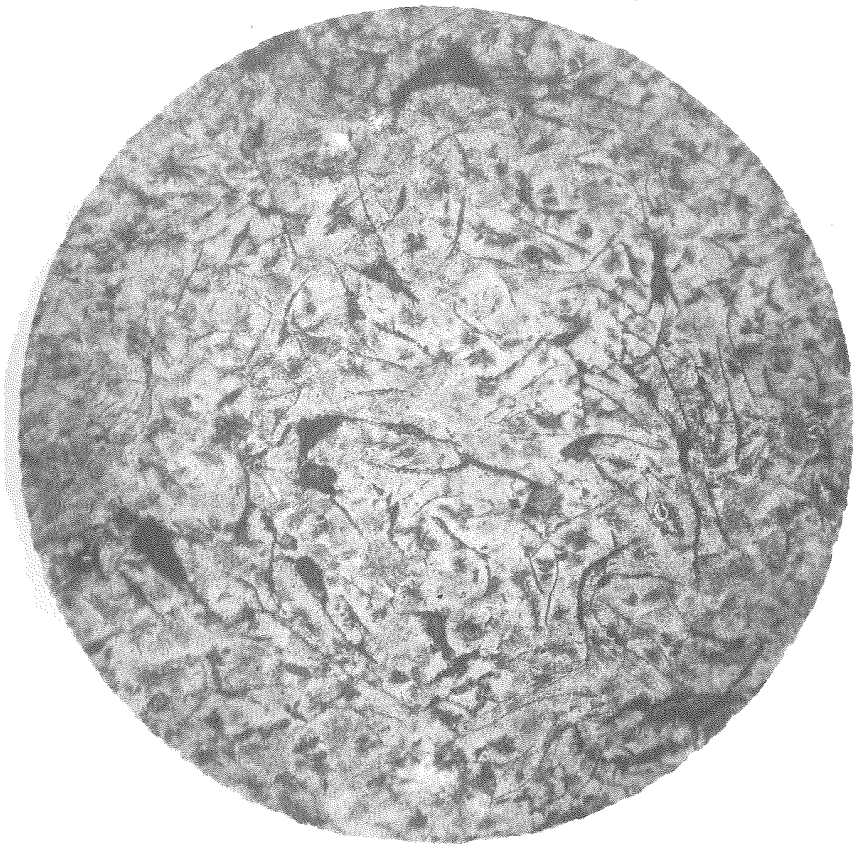

Fig. 116

(268BA)
As cast
Magnification 100X
Etch Murakami

Fig. 117

(268BB)
As cast
Magnification 1000X
Etch Murakami

content the iron carbide has been caused to dissociate to graphite and ferrite, as shown by the photomicrograph. The previous alloys seem to indicate that the iron carbide is rendered considerably more stable by the addition of boron in that some of the previously mentioned alloys contained almost as much silicon as did this particular alloy and no graphite separation was observed.

Figures 118 and 119 show the structure of specimen 270. In this case a small amount of disintegrated primary solid solution and a rather large proportion of eutectic are present. In Figure 118 the pearlitic material is the gray structure shown at higher magnification in Figure 119.

Figures 120 and 121 show the structures of two other alloys, 298 and 299, in this region which should show some eutectic. Figure 120 contains some eutectic, but only a very little, while Figure 121 shows none at all. These two specimens also contain 1.5% silicon which undoubtedly causes considerable alteration of the structure.

Figures 122 and 123 show the structure of specimen 271 in which the lightest constituent is the pearlite and the dark the iron carbide solid solution. Here we see considerable eutectic.

Figure 124 shows the structure of specimen 400 which contains 1.5% silicon and takes on the appearance, as discussed for some of the previous alloys. Some eutectic is apparent, though not as much

Fig. 118

(270BA)
As cast
Magnification 100X
Etch Murakami

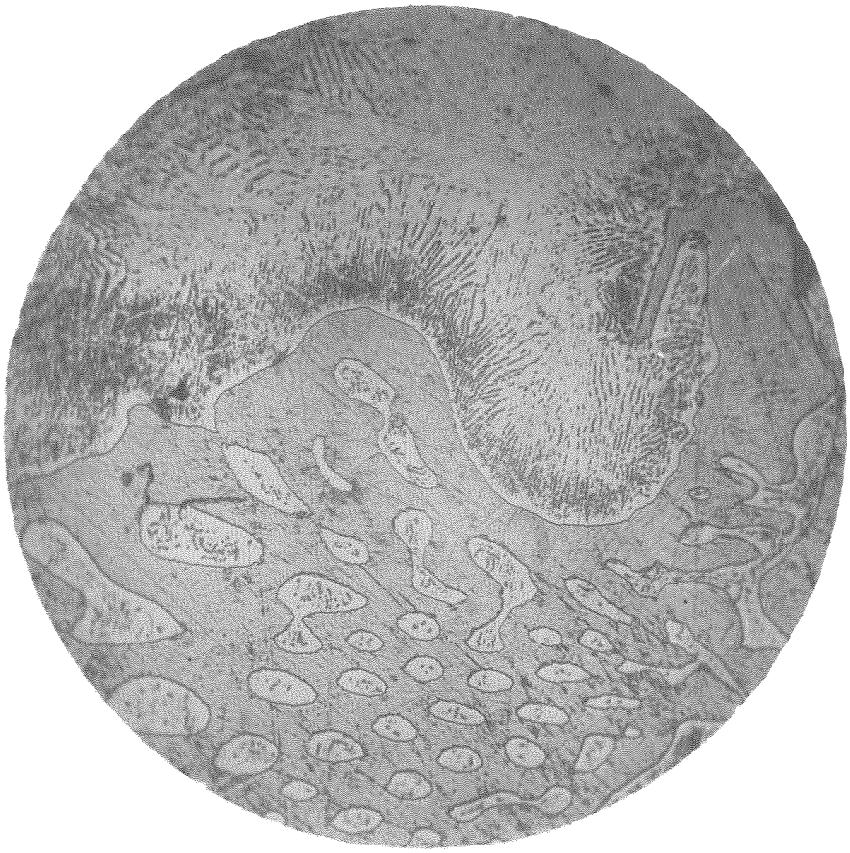

Fig. 119

(270BB)
As cast
Magnification 1000X
Etch Murakami

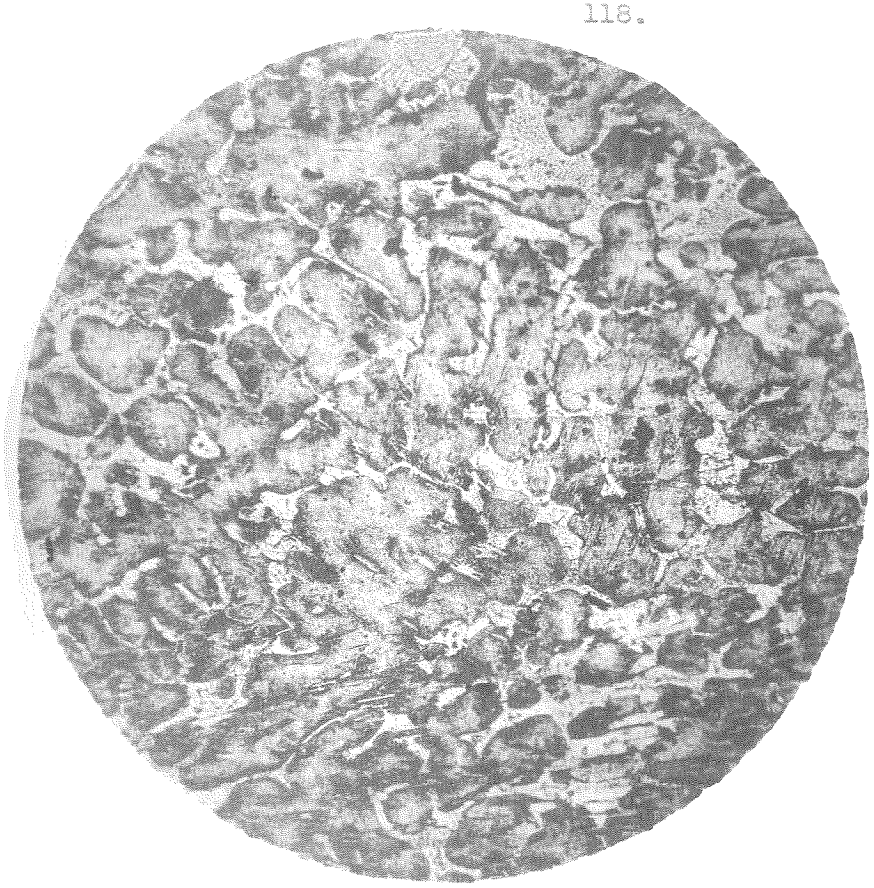

Fig. 120

(298B1)
As cast
Magnification 100X
Etch Murakami

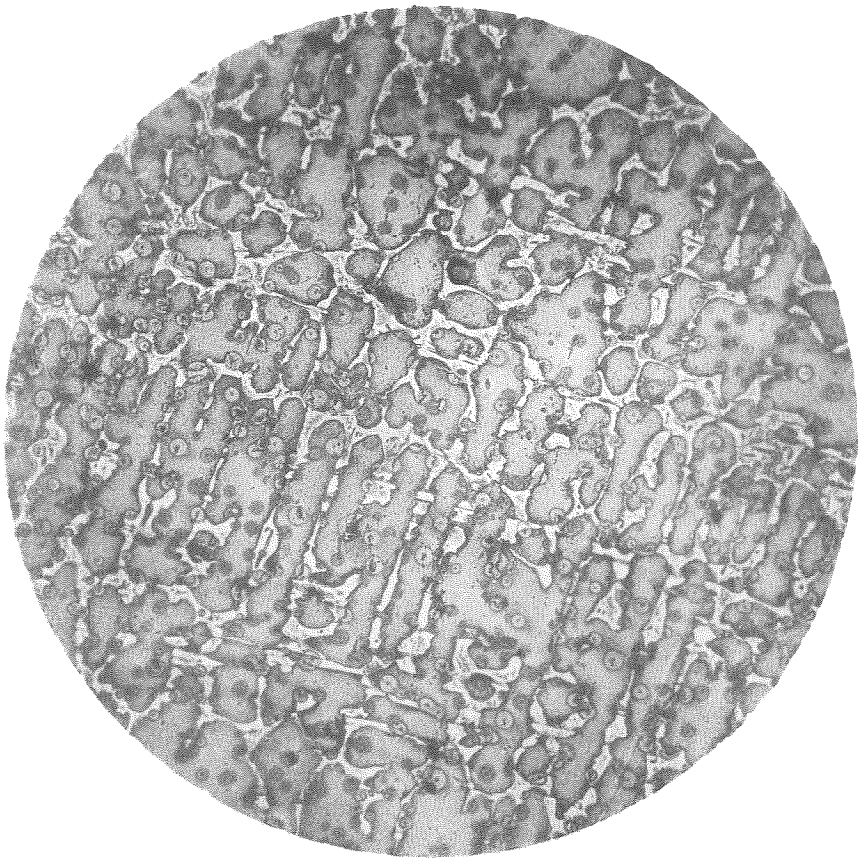

Fig. 121

(299B2)
As cast
Magnification 100X
Etch Murakami

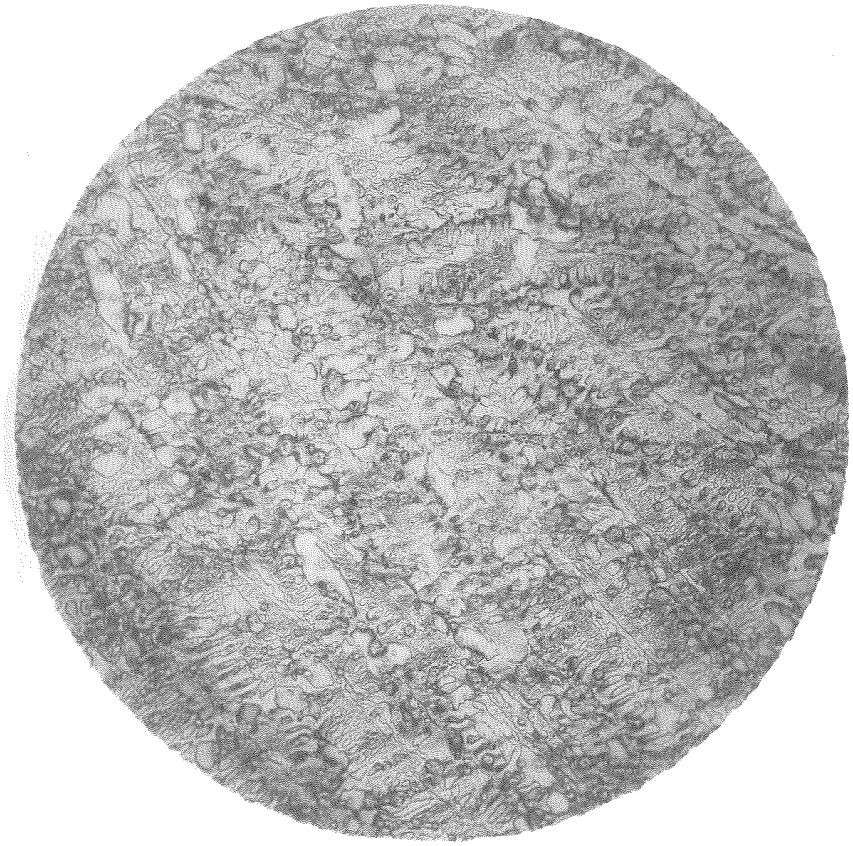

Fig. 122

(271BA)
As cast
Magnification 100X
Etch Murakami

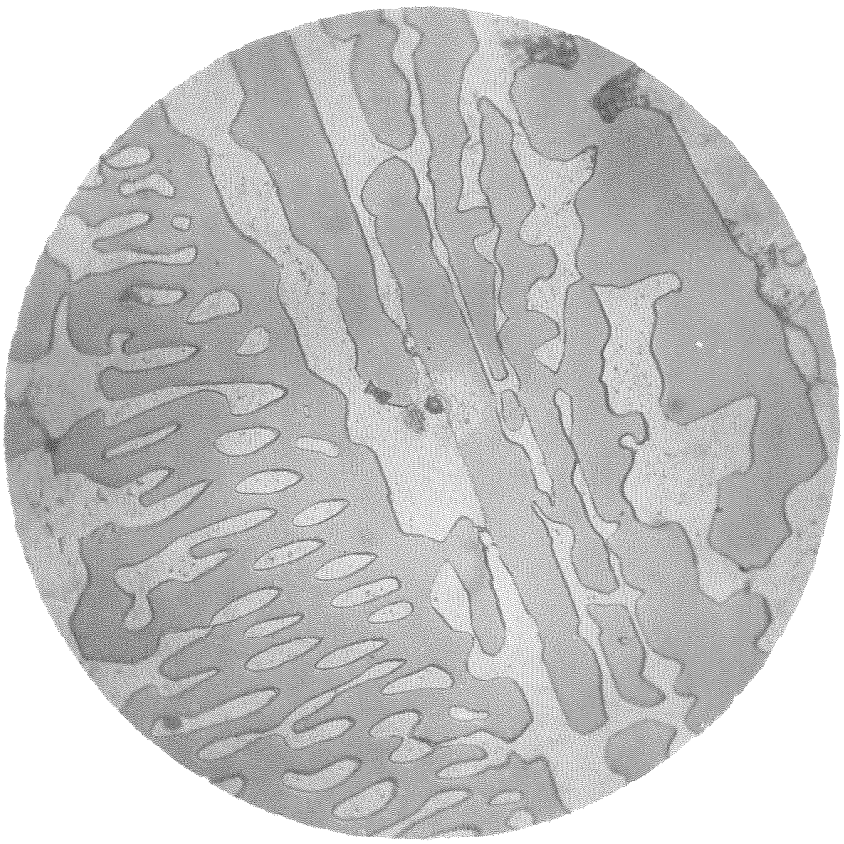

Fig. 123

(271BB)
As cast
Magnification 1000X
Etch Murakami

Fig. 124

(400B1)
As cast
Magnification 100X
Etch Murakami

Fig. 125

(221B)
As cast
Magnification 100X
Etch Murakami

as indicated by the diagram. This difference is undoubtedly due to the silicon present.

In Figure 125 is shown the structure of specimen 221 which, according to the chemical analysis, lies well below the eutectic curve and, hence, no primary iron carbide solid solution should be expected. However, the photomicrograph shows very definitely that primary iron carbide solid solution is present and is surrounded by eutectic. No reason for this discrepancy has been found other than that the chemical analysis is in error.

Figures 126 and 127 show the structure of specimen 262 which should show some primary iron carbide solid solution with the eutectic. The photomicrographs check this prediction very well. However, it is evident that no ternary pearlite of constant composition exists, which confirms the location of this field as shown on the composition triangle.

Now let us consider the alloys in the region NVB on the concentration triangle which have an excess of the ternary solid solution V.

Figure 128 shows the structure of specimen 401, which should contain some ternary eutectic, as indicated by the diagram.

Figures 129 and 130 show the structure of specimen 189 which should consist of some excess ternary solid solution, but actually

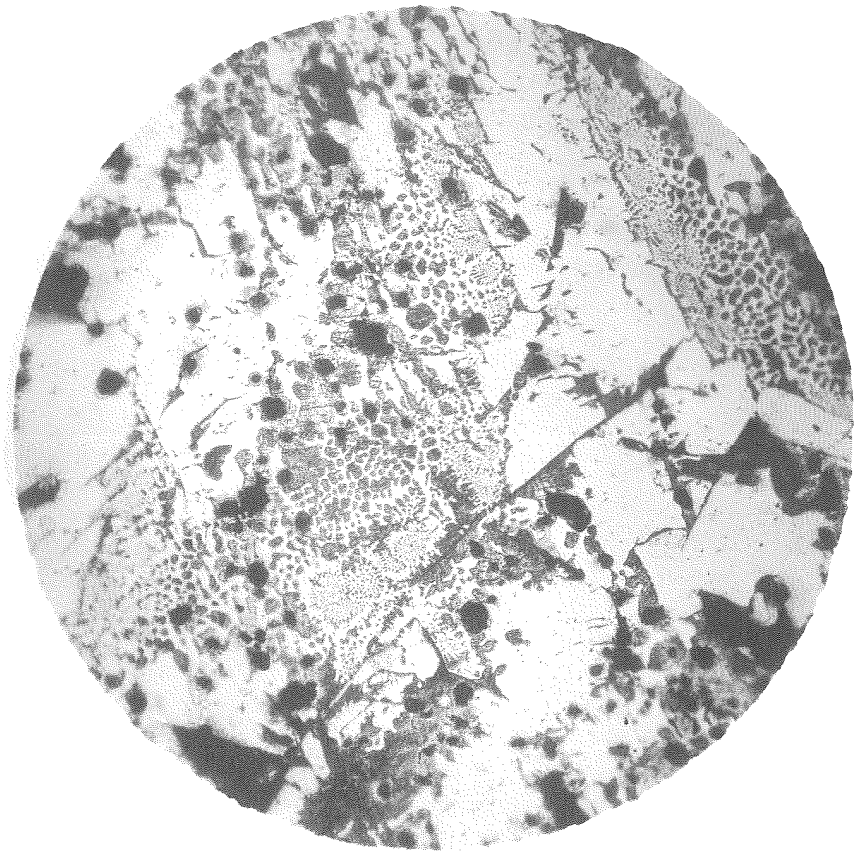

Fig. 126

(262AA)
As cast
Magnification 100X
Etch Murakami

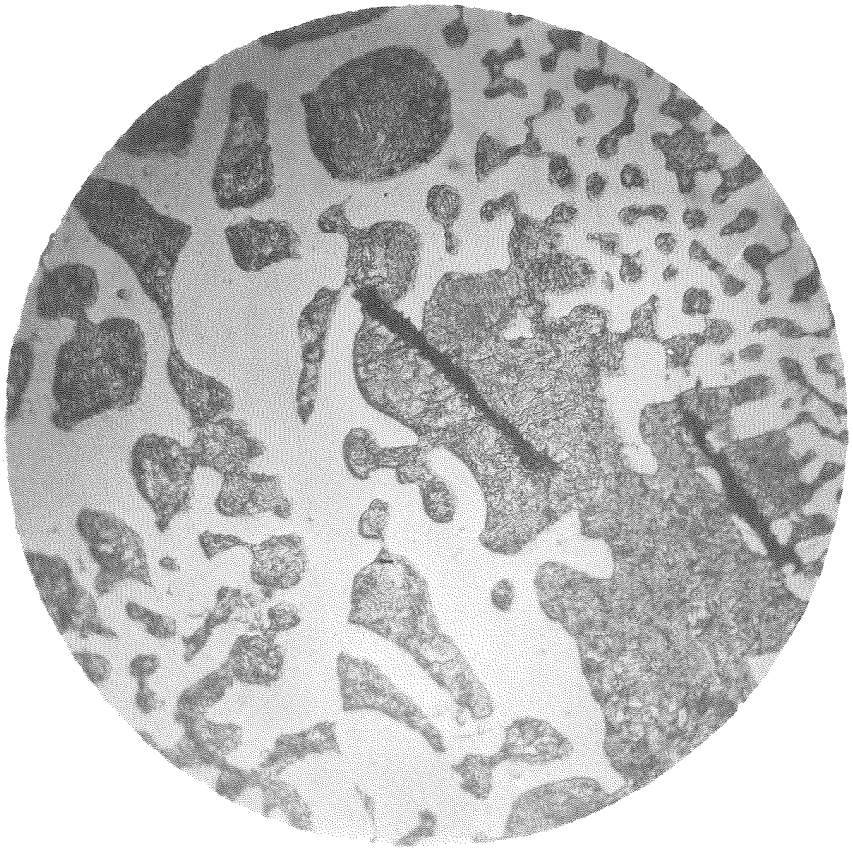

Fig. 127

(262AB)
As cast
Magnification 1000X
Etch Murakami

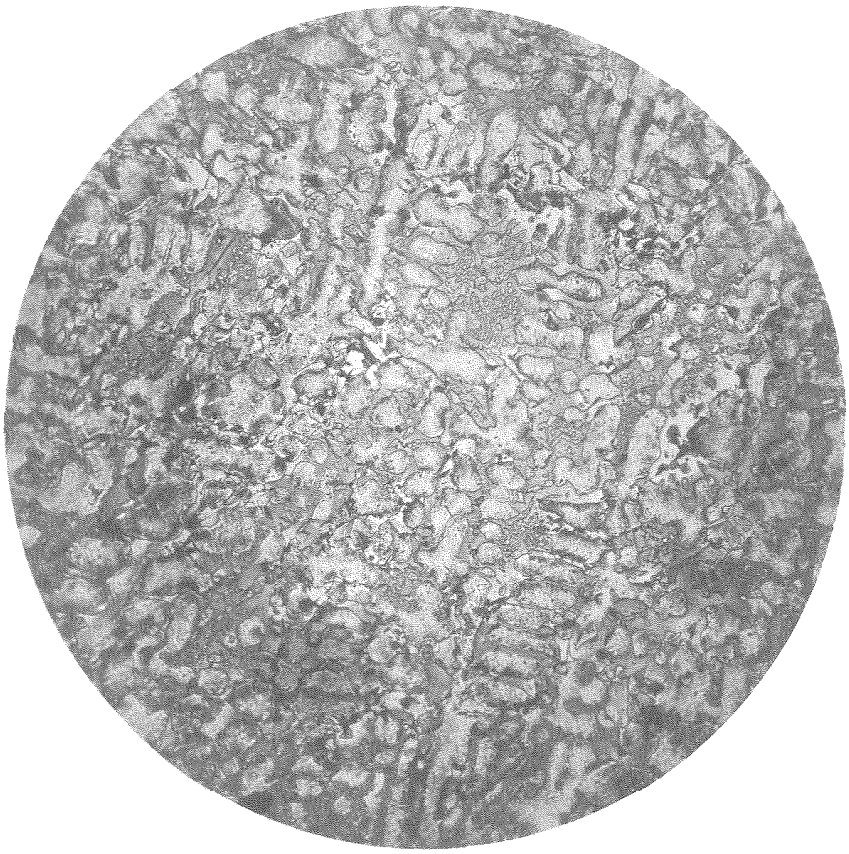

Fig. 128

(401B1)
As cast
Magnification 100X
Etch Murakami

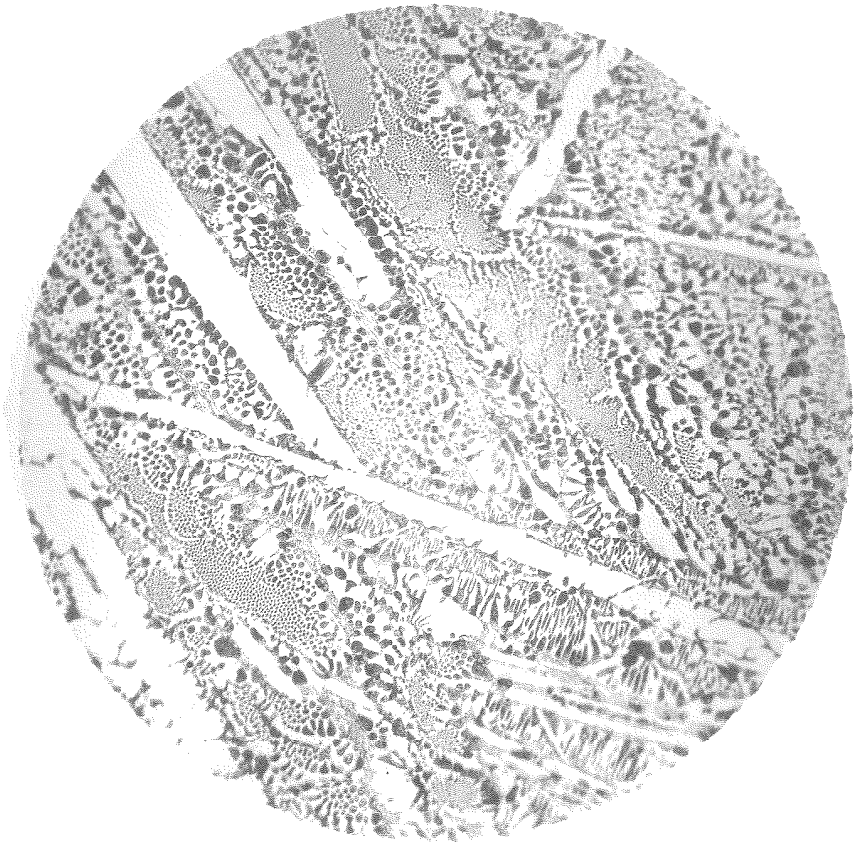

Fig. 129

(189A)
As cast
Magnification 100X
Etch 5% Picrol

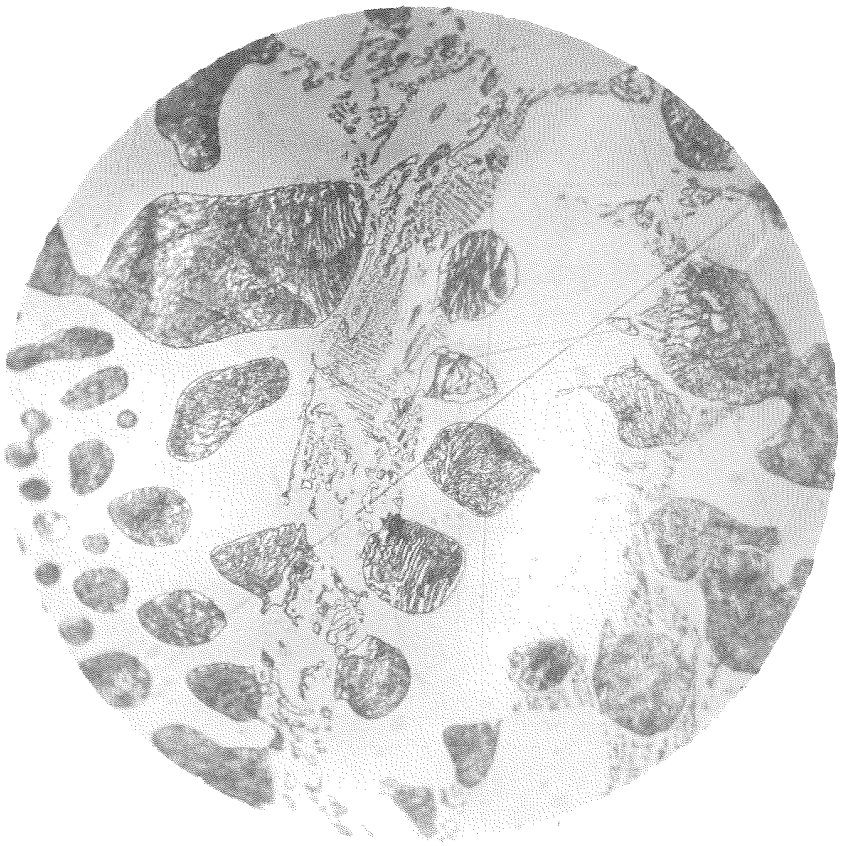

Fig. 130

(189B)
As cast
Magnification 1000X
Etch 5% Picrol

shows primary iron carbide solid solution. It is difficult to see how such a structure could be obtained with the analysis shown. It is conceivable that such a structure might be brought about by super-cooling, in which the composition of the remaining liquid would indicate a precipitation of primary iron carbide solid solution. This particular alloy is one which does not fit the equilibrium diagram.

Figure 131 shows the structure of specimen 296 in which we see primary separated pearlite drived from the ternary solid solution surrounded with a eutectic. From the structure of this alloy, it is certain that it lies very close, if not directly on the curve NV, since there is no indication of the formation of ternary eutectic which has a characteristic structure as will be seen in some of the photomicrographs later.

Figures 132 and 133 show the structure of specimen 272 in which we have nearly all eutectic, as is indicated there should be from the diagram. No ternary eutectic is visible in this structure and hence its composition lies either directly on or very close to the curve NV.

Figures 134 and 135 show the structure of specimen 247 in which there is some primary iron carbide solid solution present. This would indicate that the alloy actually lies on the other side of E1'R', that is on the side of higher iron carbide solid solution. Furthermore, no ternary eutectic is observed, only the binary

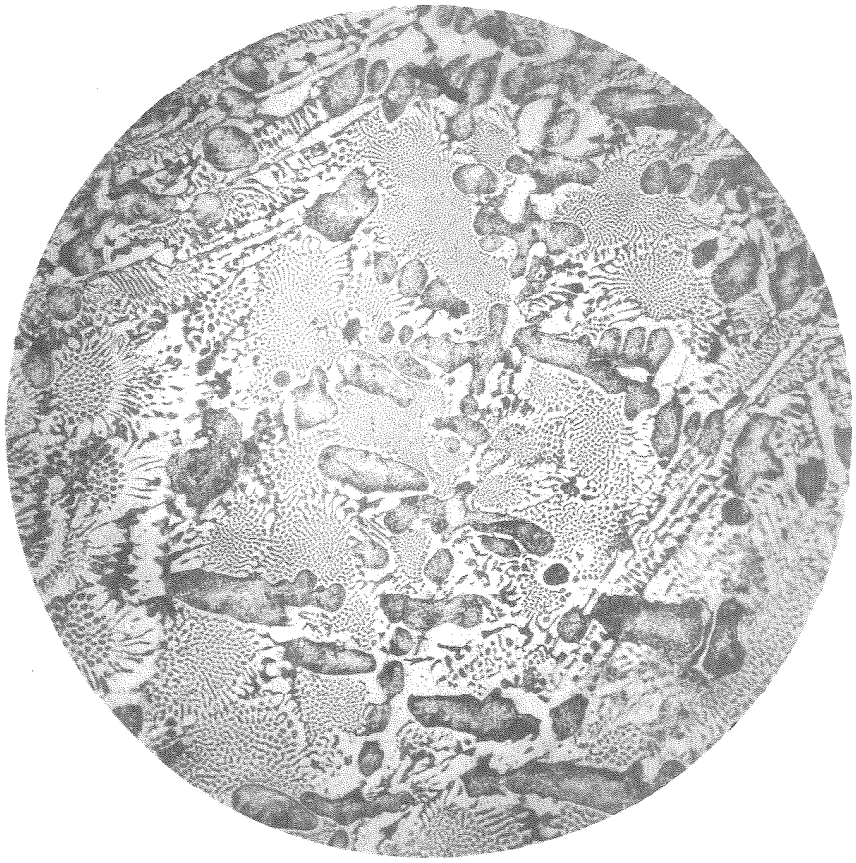

Fig. 131

(296B1)
As cast
Magnification 100X
Etch Murakami

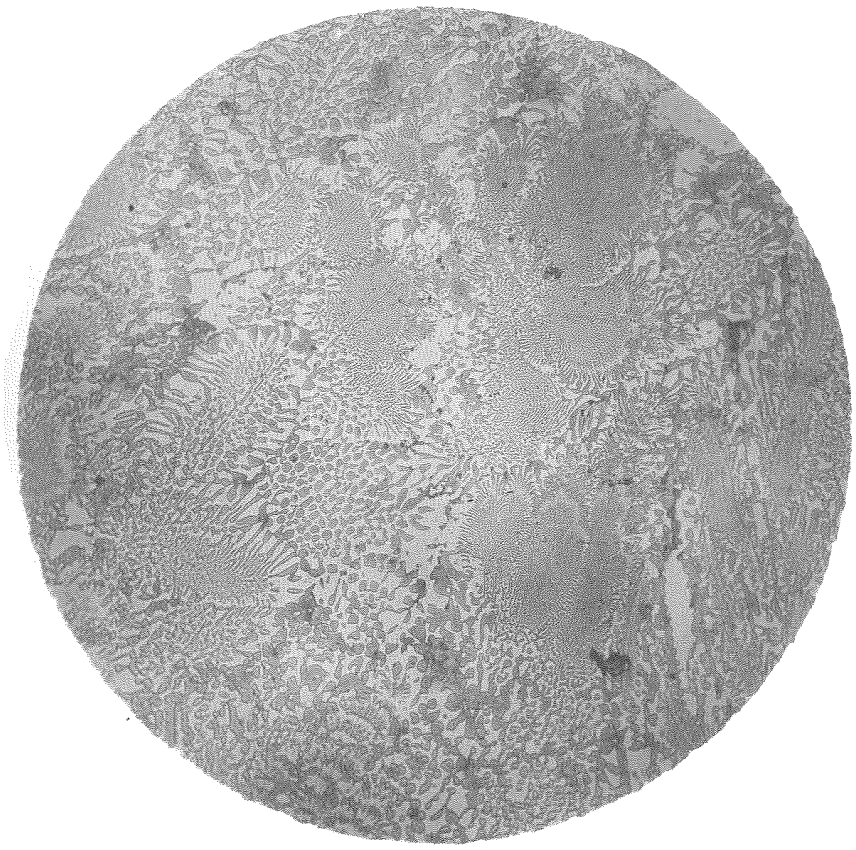

Fig. 132

(272AA)
As cast
Magnification 100X
Etch Murakami

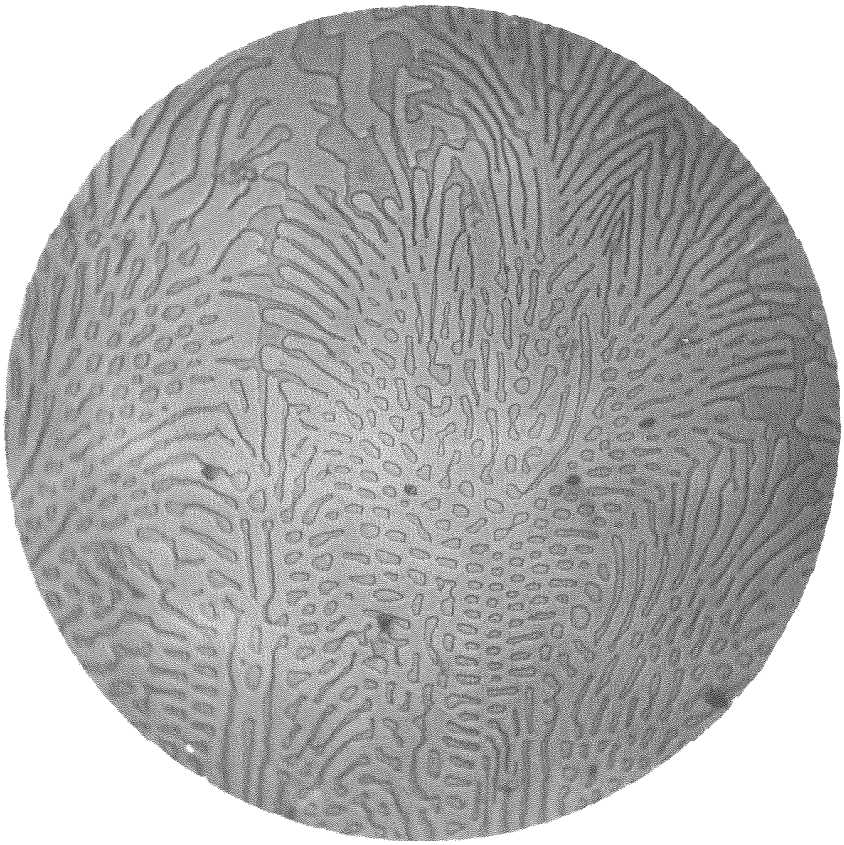

Fig. 133

(272AB)
As cast
Magnification 1000X
Etch Murakami

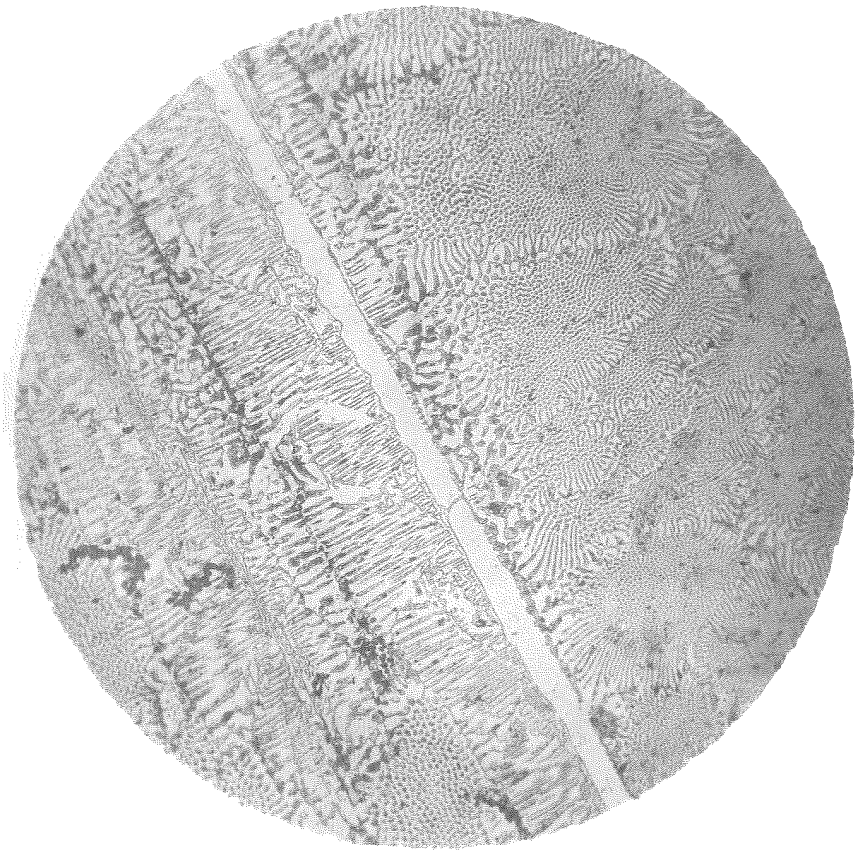

Fig. 134

(247BA)
As cast
Magnification 100X
Etch Murakami

Fig. 135

(247BB)
As cast
Magnification 1000X
Etch Murakami

eutectic of iron carbide solid solution and ternary solid solution. The structure of this alloy is further confirmed by that of specimen 10, shown in Figure 73, which is of approximately the same composition.

Figure 136 shows the structure of specimen 255, which still shows no ternary eutectic, but the structure of an alloy lying on the curve NV. No primary iron carbide solid solution is observed, indicating that it is very close to the eutectic curve.

Figure 137 shows the structure of specimen 405 in which there is a very slight indication of a ternary eutectic being formed in the interstices of the larger grains of transformed ternary solid solution.

Figures 138 and 139 show the structure of specimen 267, which shows an abundance of ternary eutectic with some excess of the ternary solid solution. This is the usual form of the ternary eutectic, as can be seen by comparison with Figures 68 and 69, which show the structure of specimen 13.

Figure 140 shows the structure of specimen 406 in which there is primary ternary solid solution disintegrated into pearlite with some very small amount of ternary eutectic. This does not fully agree with the structure of specimen 267, but this can be accounted for by the difference in silicon content. Specimen 267 contains

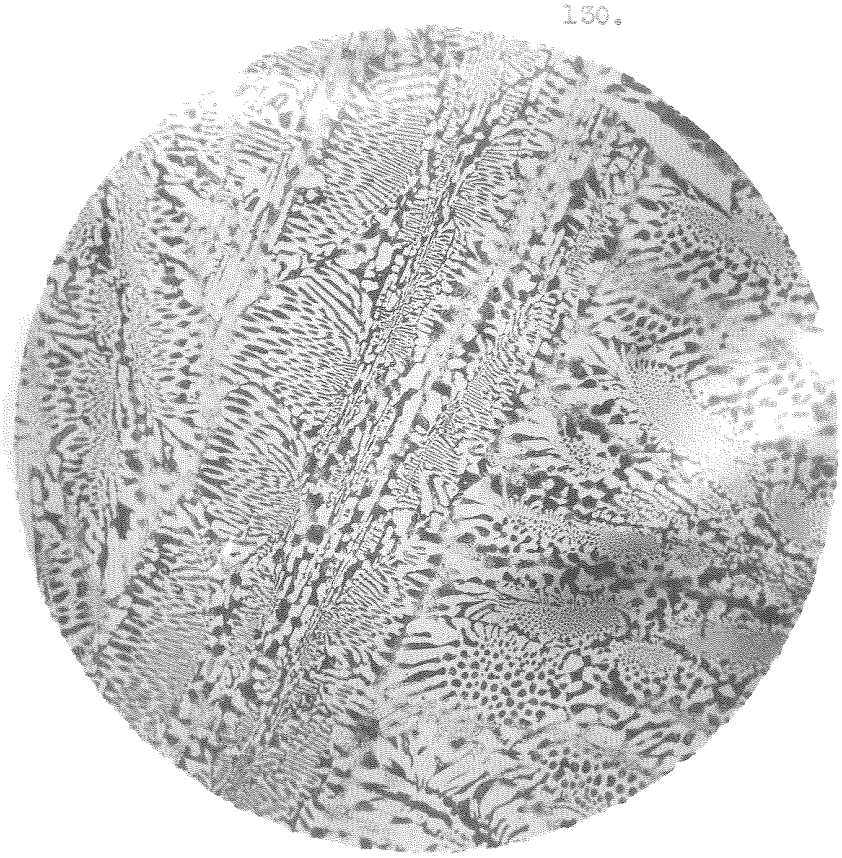

Fig. 136

(255AA)
As cast
Magnification 100X
Etch Murakami

Fig. 137

(405A1)
As cast
Magnification 100X
Etch Murakami

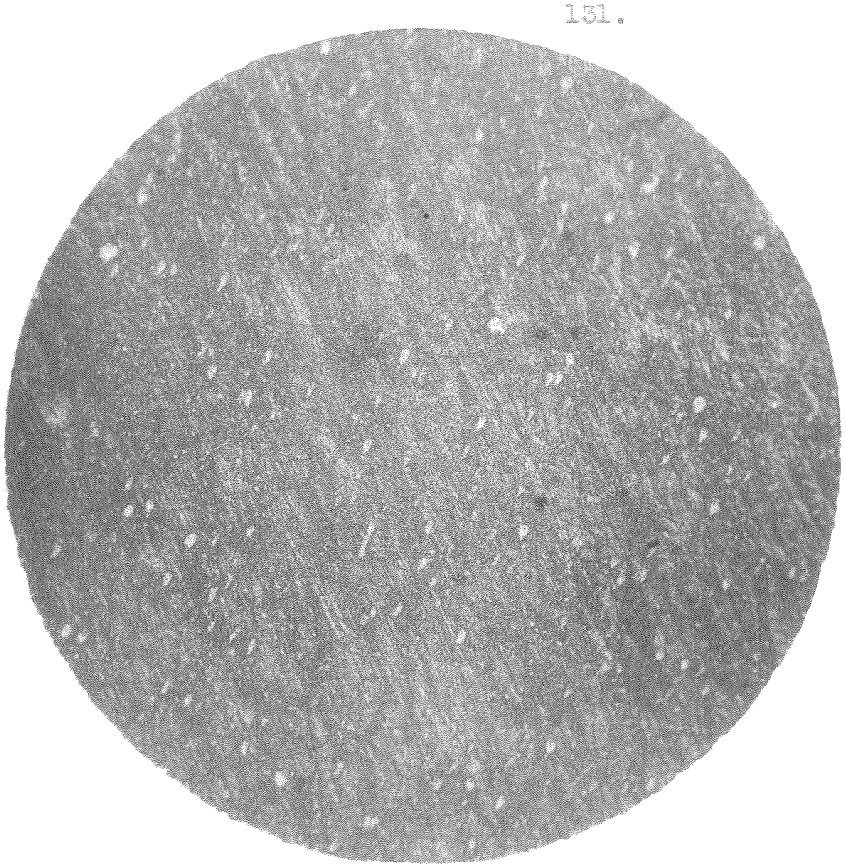

Fig. 138

(267-1A)
As cast
Magnification 100X
Etch Murakami

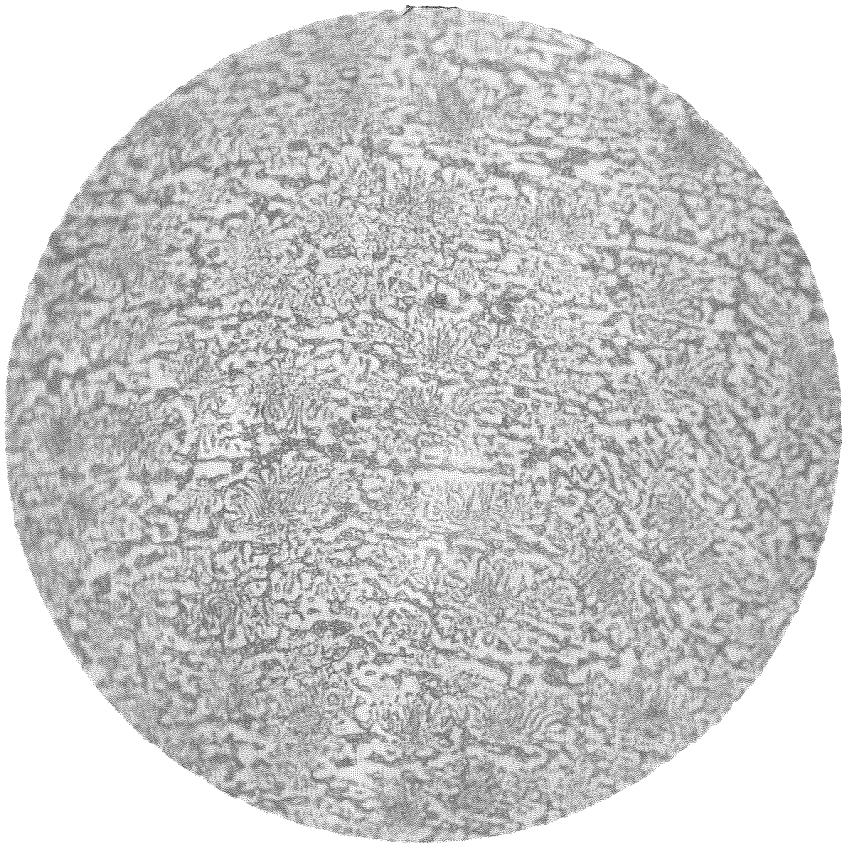

Fig. 139

(267-1B)
As cast
Magnification 1000X
Etch Murakami

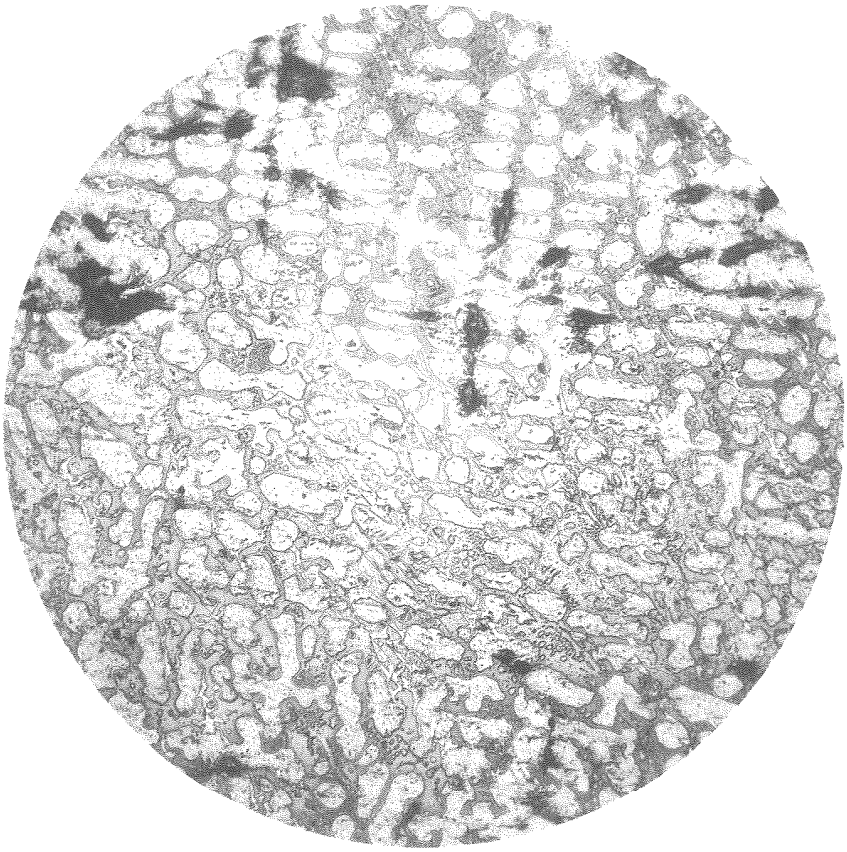

Fig. 140

(406B1)
As cast
Magnification 100X
Etch Murakami

more silicon than specimen 406 and, hence, as has been seen before, the structure is much finer and the transformation compositions are shifted considerably.

Figures 141 and 142 show the structure of specimen 225 in which we find the primary solid solution with considerable ternary eutectic. This structure agrees very well with the diagram.

Now consider the alloys in the region in which there is an excess of the iron carbide solid solution.

Figures 143 and 144 show the structure of specimen 276 in which is found an excess of the iron carbide solid solution surrounded by the ternary eutectic.

Figures 145 and 146 show the structure of specimen 278 in which there is an excess of the iron carbide solid solution surrounded by the ternary eutectic.

Figures 147, 148, and 149 show the structure of specimen 279 in which there is considerable primary iron boride surrounded by ternary eutectic. This structure does not check the equilibrium diagram and, in fact, should not since the alloy contains, according to chemical analysis, 4.25% silicon, which disturbs the conditions very markedly. Undoubtedly, the effect of silicon in this case is to shift the eutectic curve EgR to higher carbon contents and, hence, puts this alloy in position to precipitate primary iron boride.

Fig. 141

(225B)
As cast
Magnification 100X
Etch Murakami

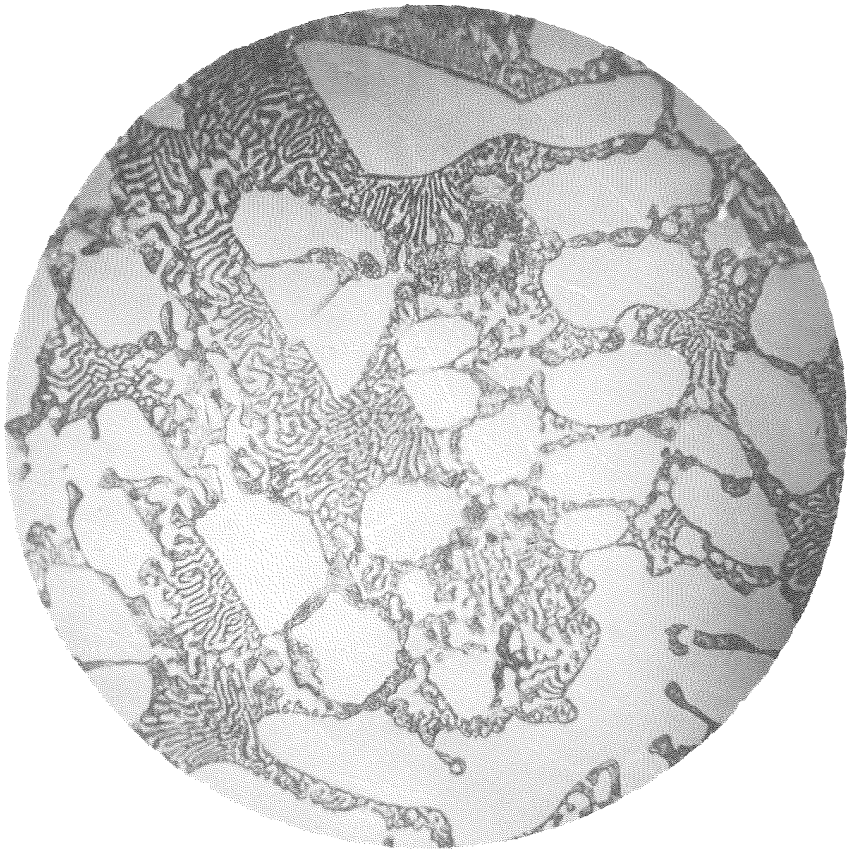

Fig. 142

(225A)
As cast
Magnification 1000X
Etch Murakami

Fig. 143

(276-1A)
As cast
Magnification 100X
Etch Murakami

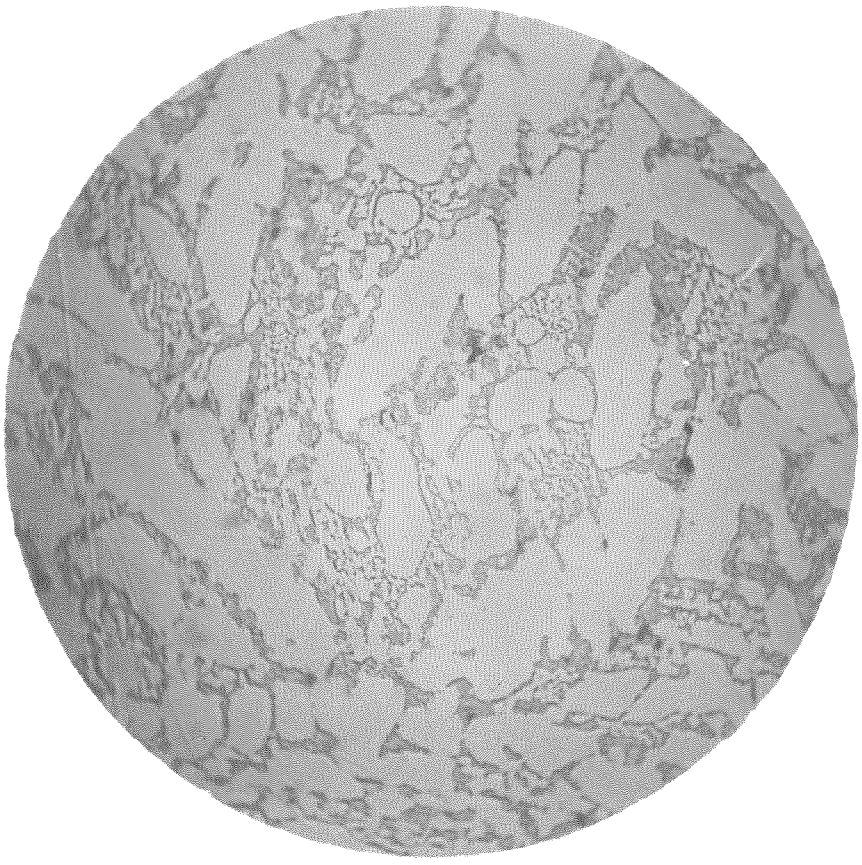

Fig. 144

(276-1B)
As cast
Magnification 1000X
Etch Murakami

Fig. 145

(278A)
As cast
Magnification 100X
Etch Murakami

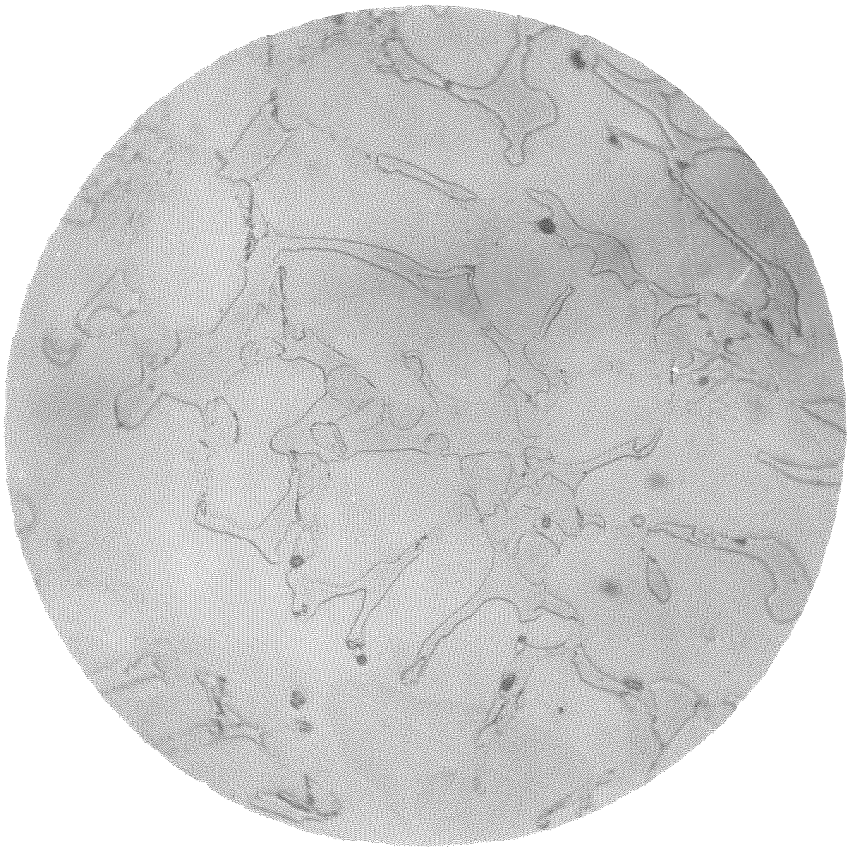

Fig. 146

(278B)
As cast
Magnification 1000X
Etch Murakami

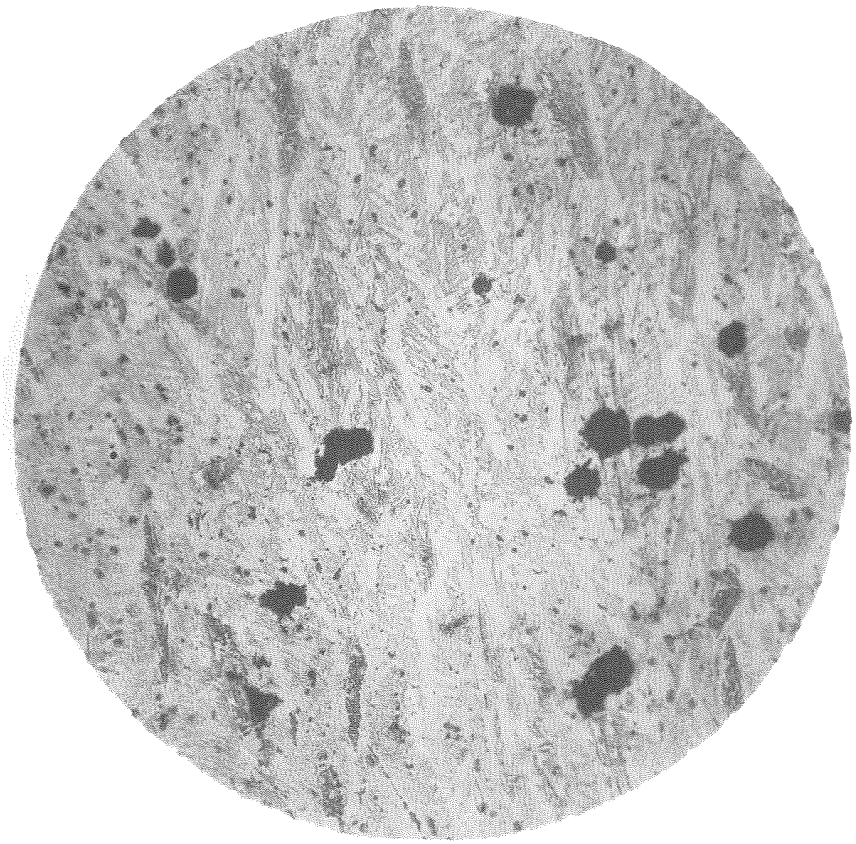

Fig. 147

(279A)
As cast
Magnification 100X
Etch Murakami

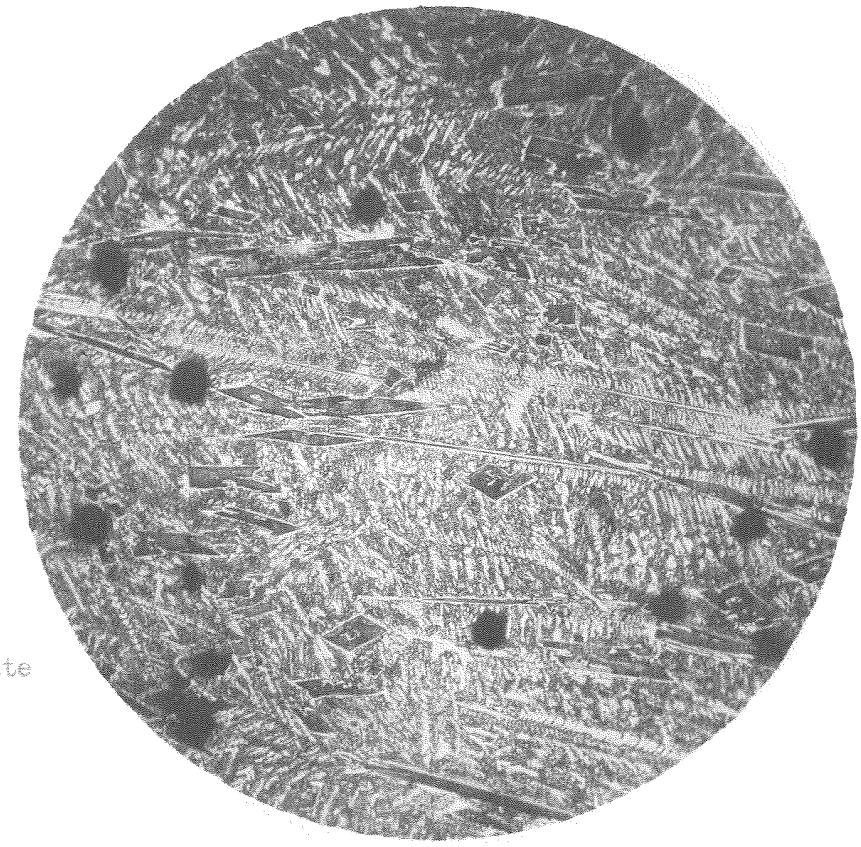

Fig. 148

(279E)
As cast
Magnification 100X
Etch
Neutral Sodium Picrate

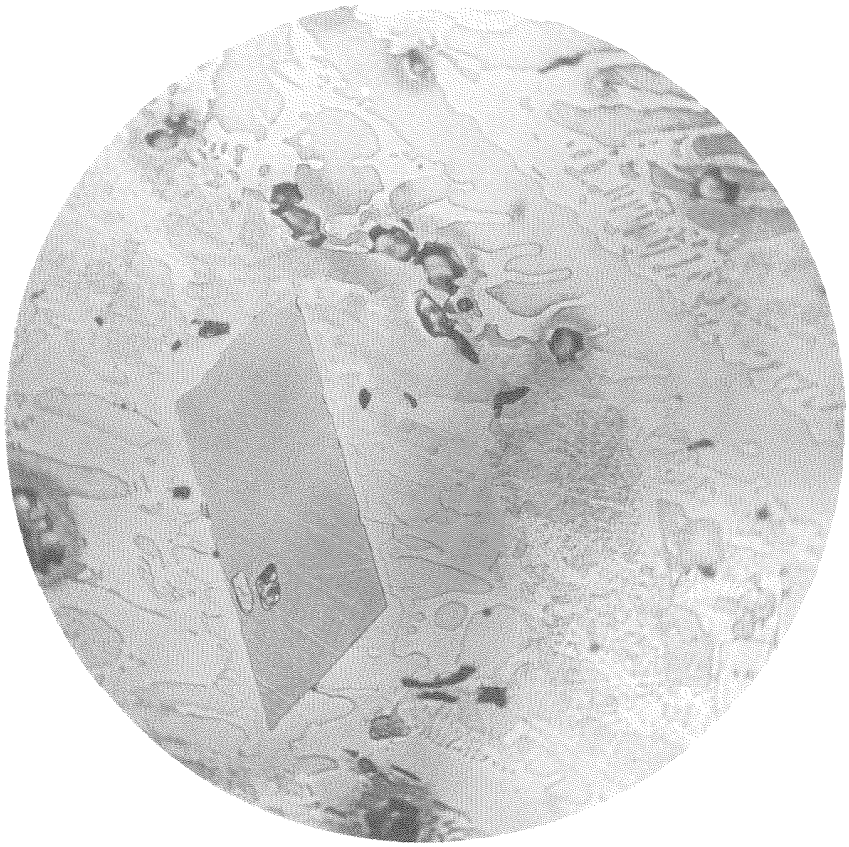

Fig. 149

(279C)
As cast
Magnification 1000X
Etch Murakami

Figures 150 and 151 show the structure of specimen 277 in which there is an abundance of iron carbide solid solution surrounded by a small amount of ternary eutectic. The black spots are shrinkage holes found in the castings.

Figures 152, 153, 154, and 155 show the structure of specimen 248 which is very close to the eutectic of iron carbide solid solution and iron boride and shows this in the photomicrographs. Figure 152 and 153 are at the same magnification, the difference being that 152 was taken with a Wratten B (Green) filter, while 153 was taken with a Wratten A filter (Red), hence, changing the contrast of the structure. This effect indicates the general outlines of the primary iron carbide solid solution that was formed and which later changed its composition during the transformation from the curve NV to ZS, the original position of disposition remains in the final structure. The ternary eutectic is also observed in this structure, as shown by Figure 154, and the pearlite structure is shown in Figure 155.

Figures 156, 157, 158, and 159 show the structure of specimen 245 which shows a very large amount of iron carbide solid solution which is derived from the eutectic and surrounded by some ternary eutectic. Also, there are some crystals of primary iron boride scattered through the structure, as shown in Figures 158 and 159. This alloy checks very closely the equilibrium diagram, except that a larger amount of iron carbide solid solution is present than would

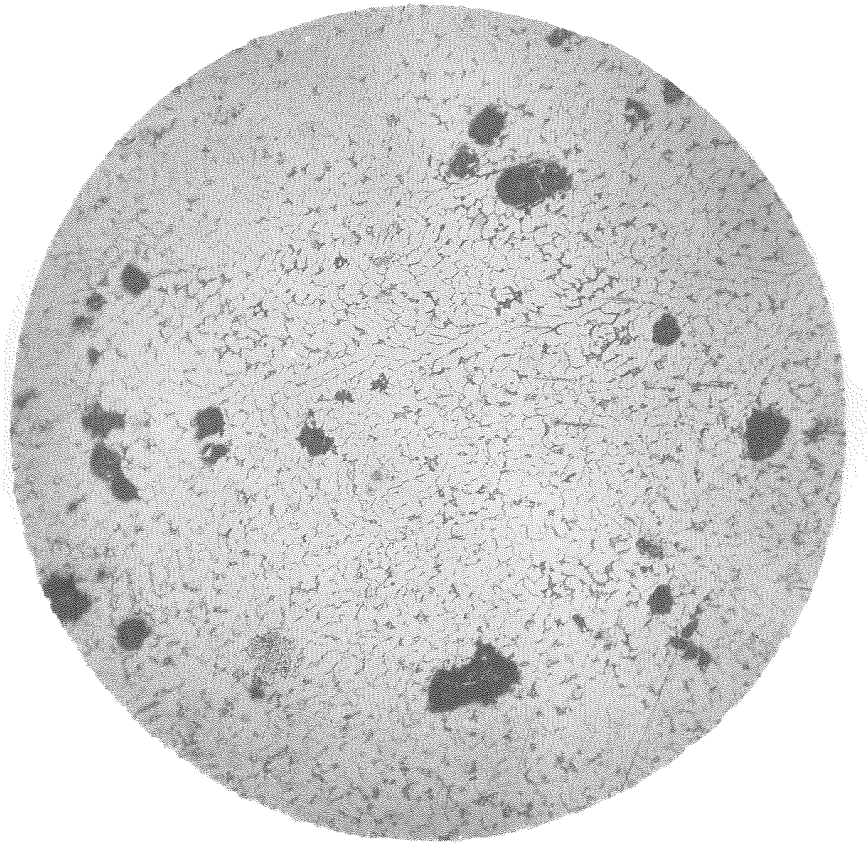

Fig. 150

(277A)
As cast
Magnification 100X
Etch Murakami

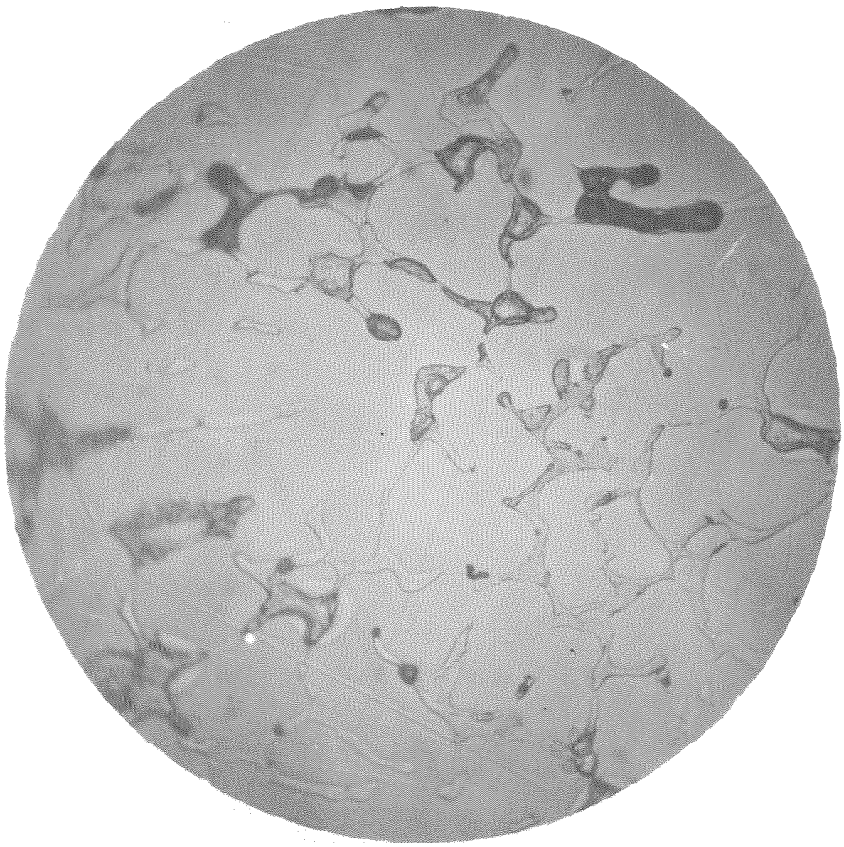

Fig. 151

(277B)
As cast
Magnification 1000X
Etch Murakami

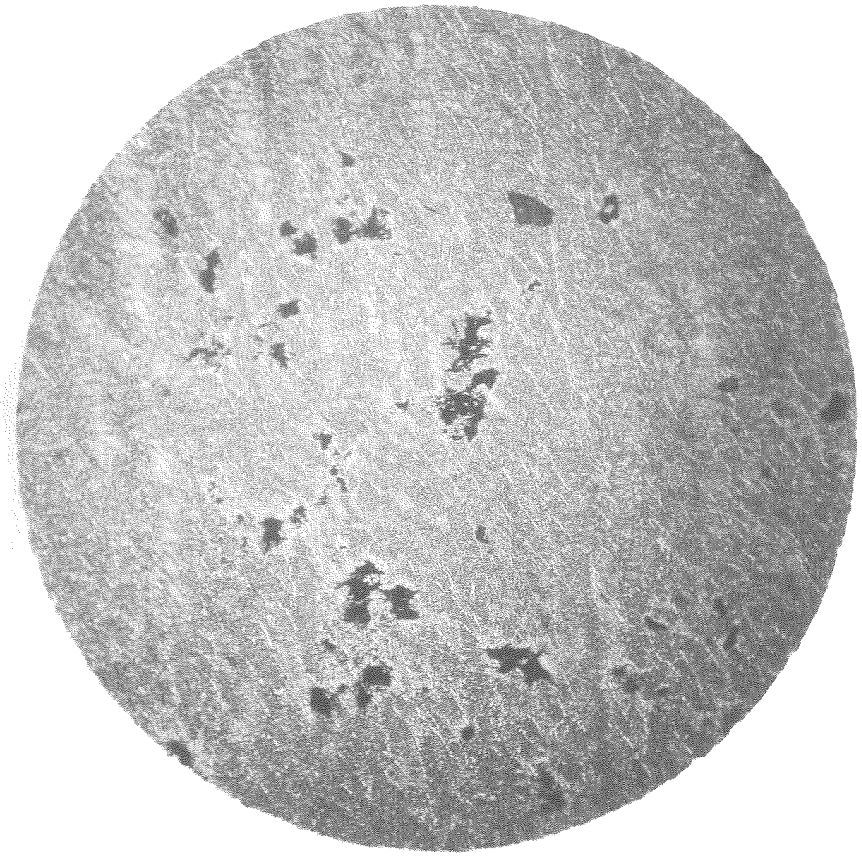

Fig. 152

(248A)
As cast
Magnification 100X
Etch Murakami
B Filter

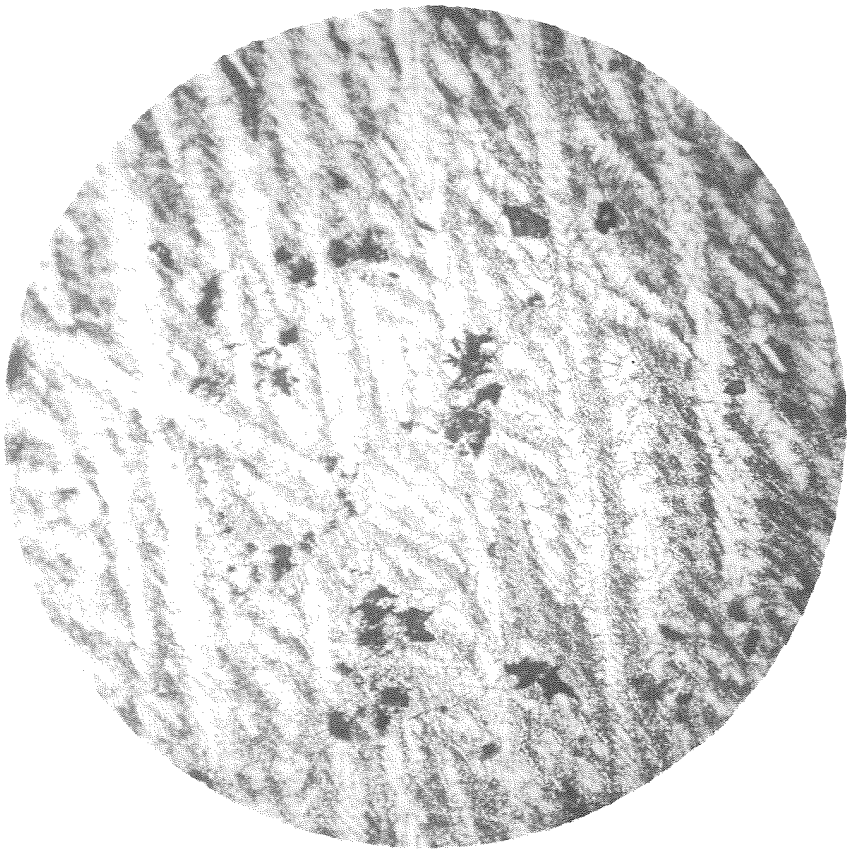

Fig. 153

(248B)
As cast
Magnification 100X
Etch Murakami
A Filter

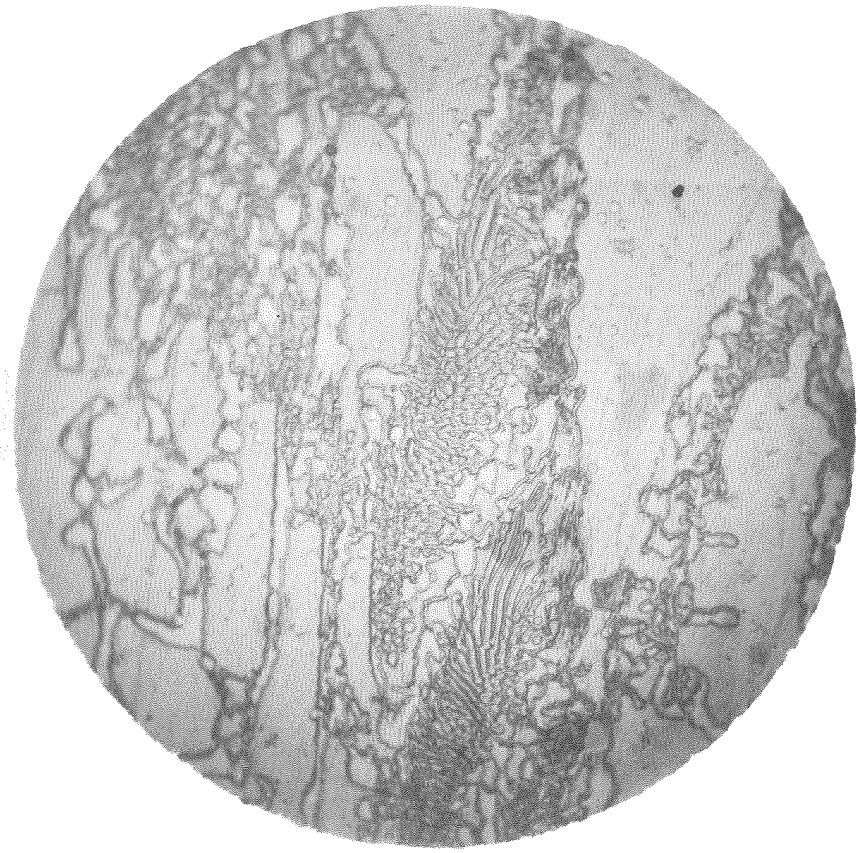

Fig. 154

(248D)
As cast
Magnification 1000X
Etch Murakami
B Filter

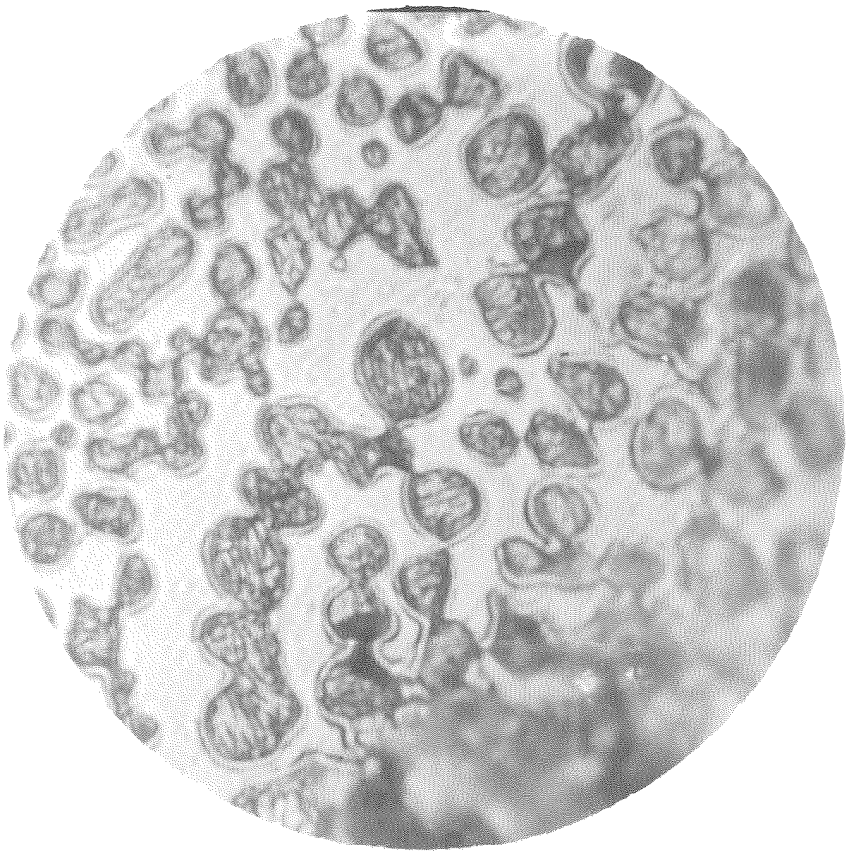

Fig. 155

(248E)
As cast
Magnification 3000X
Etch Murakami+
Nitol+Aqua Regia
C Filter

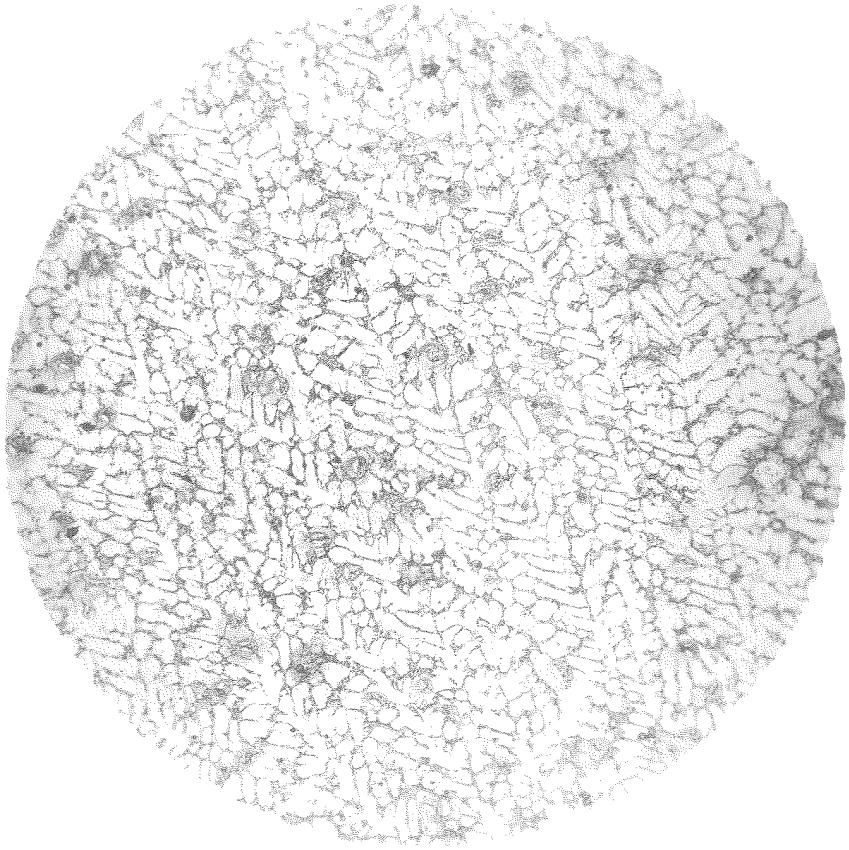

Fig. 156

(245A)
As cast
Magnification 100X
Etch Murakami

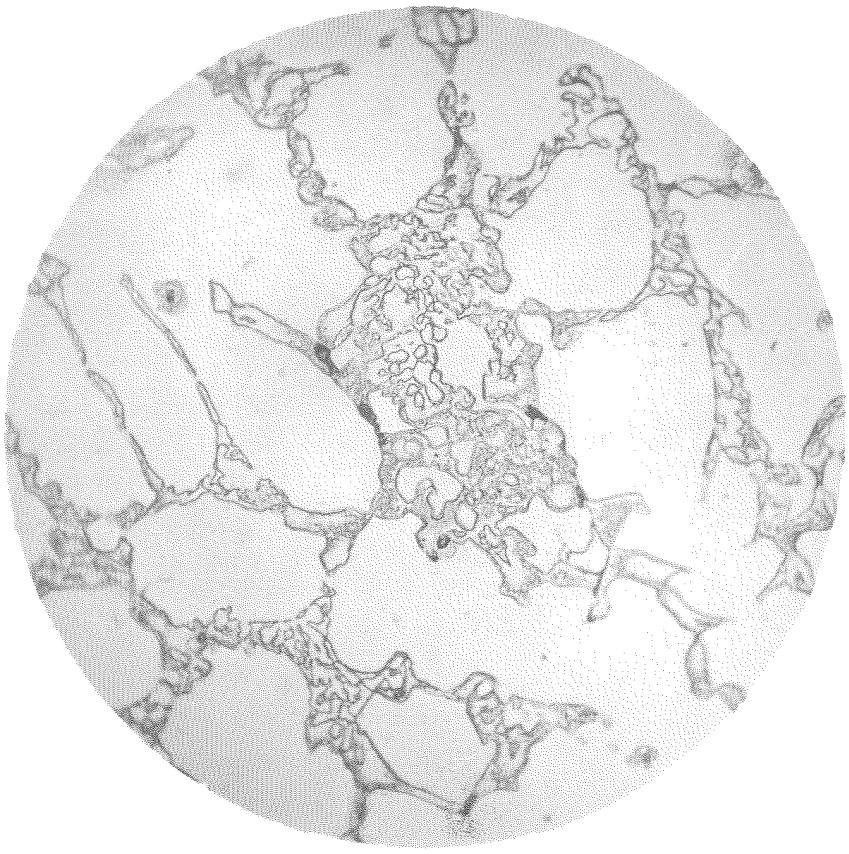

Fig. 157

(245B)
As cast
Magnification 1000X
Etch Murakami

Fig. 158

(245C)
As cast
Magnification 1000X
Etch
Neutral Sodium Picrate

Fig. 159

(245D)
As cast
Magnification 1000X
Etch
Neutral Sodium Picrate

be indicated from the diagram. This may be due to the effect of super-cooling.

Figures 160, 161, and 162 show the structure of specimen 246, which is very similar to that of the preceding alloy except that no primary crystals of iron boride were observed. This indicates that the composition is on the curve E_3R or else just to the left of it. The structure shows a large amount of iron carbide solid solution with some ternary eutectic. Figures 160 and 161 differ in that the first is taken with the Wratten B filter while the second is with the A (Red) filter showing a little better contrast and definition.

Figures 163 and 164 show the structure of specimen 291, which, from the chemical analysis, should be in the field BVJ. The photomicrographs indicate that a very fine structure, in which we have mostly a eutectic, has formed. Considering its position in the concentration triangle, we should expect some primary iron boride which does not appear in the photomicrographs. It is possible that, due to super-cooling, the eutectic between iron boride and a ternary solid solution is formed presenting the structure shown. This is about the only way the observed structure can be justified.

Figures 165 and 166 show the structure of specimen 289 which does not compare at all with the concentration diagram in that a

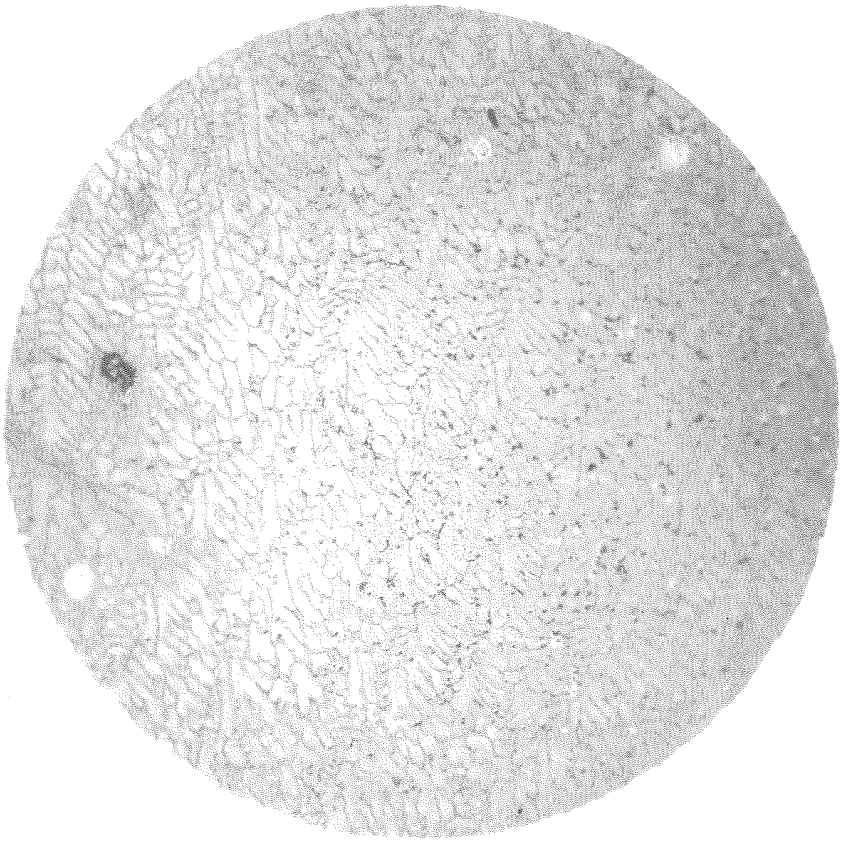

Fig. 160

(246A)
As cast
Magnification 100X
Etch Murakami
B Filter

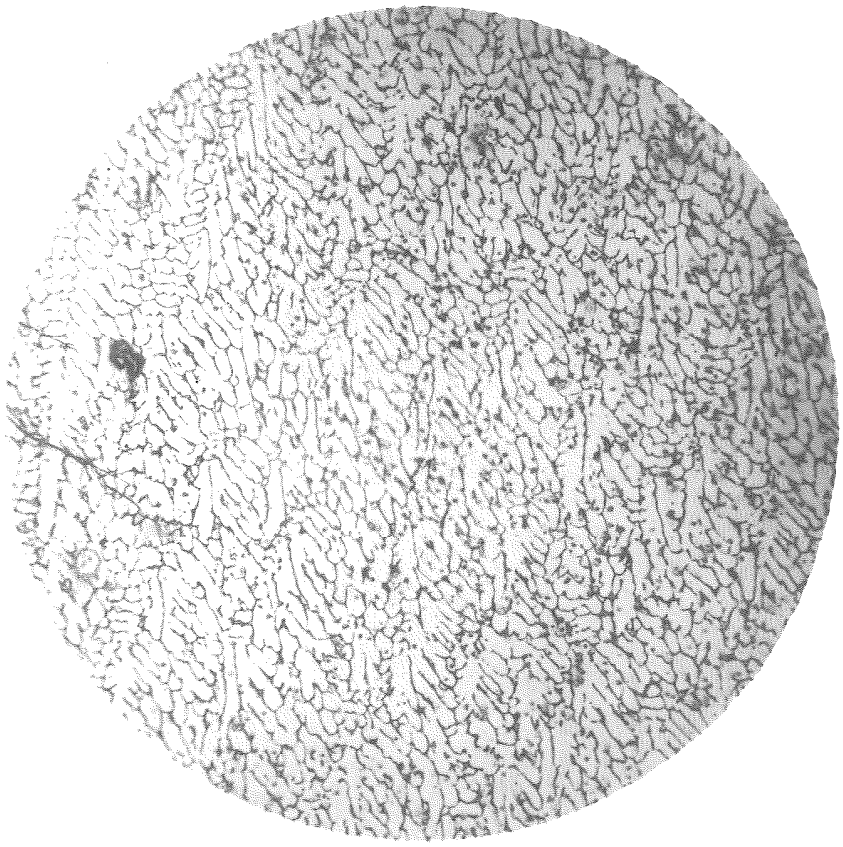

Fig. 161

(246C)
As cast
Magnification 100X
Etch Murakami
A Filter

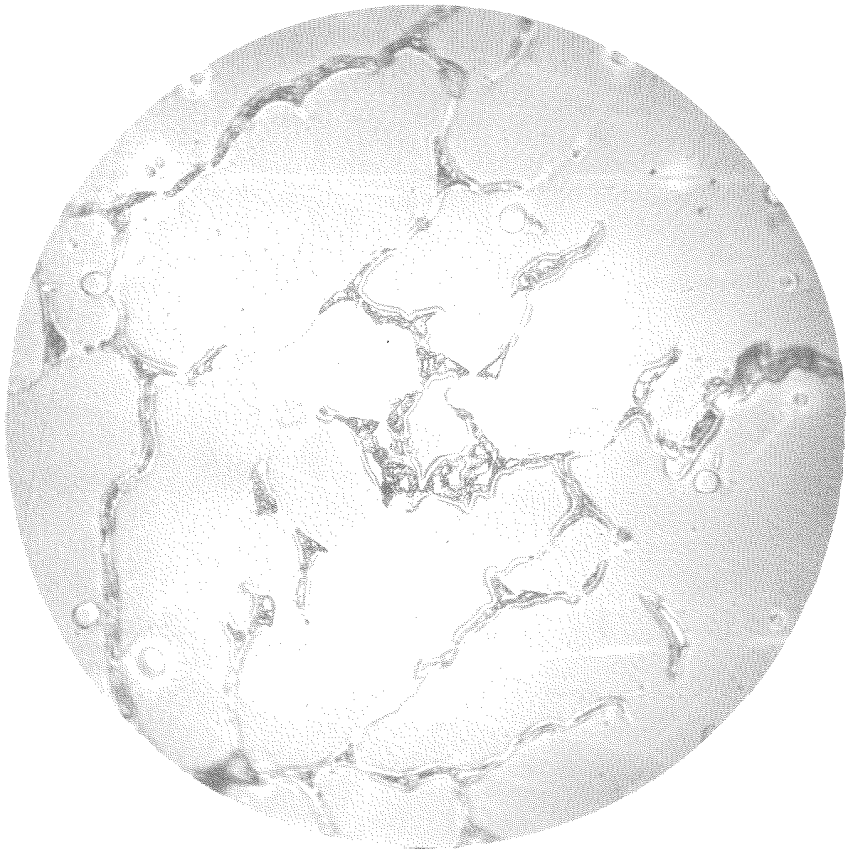

Fig. 162

(246B)
As cast
Magnification 1000X
Etch Murakami

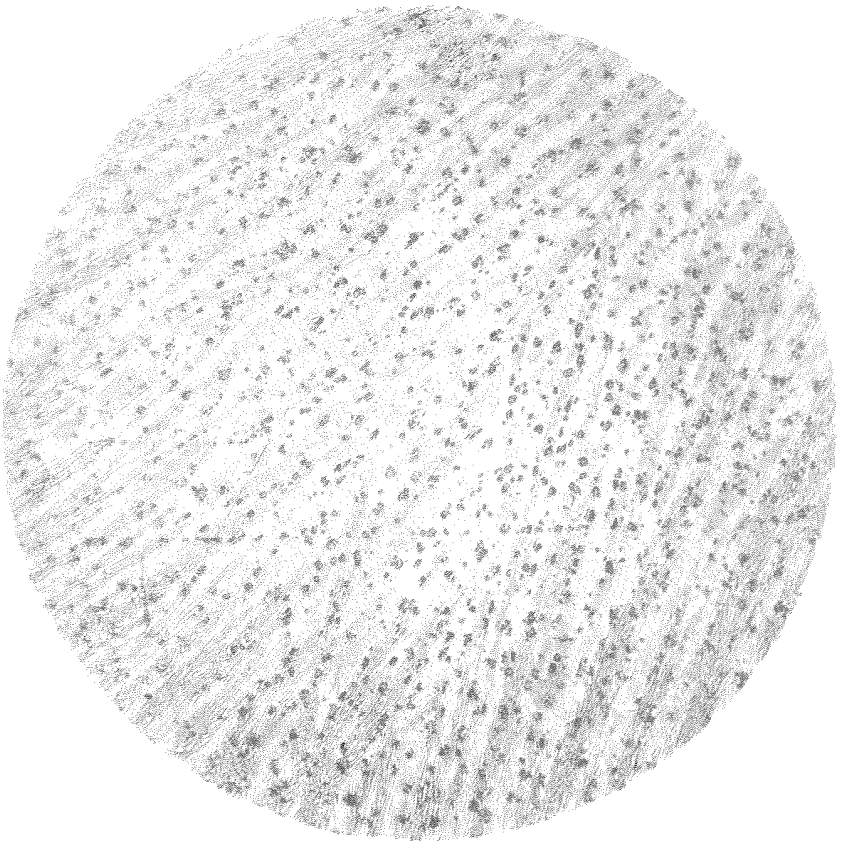

Fig. 163

(291A)
As cast
Magnification 100X
Etch Murakami

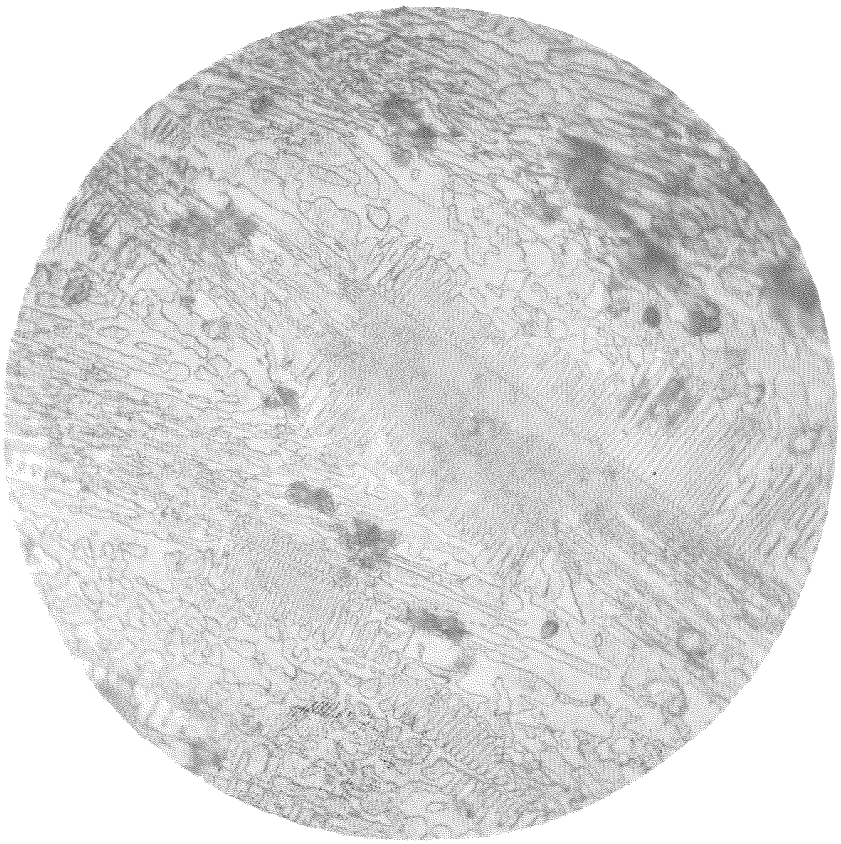

Fig. 164

(291B)
As cast
Magnification 1000X
Etch Murakami

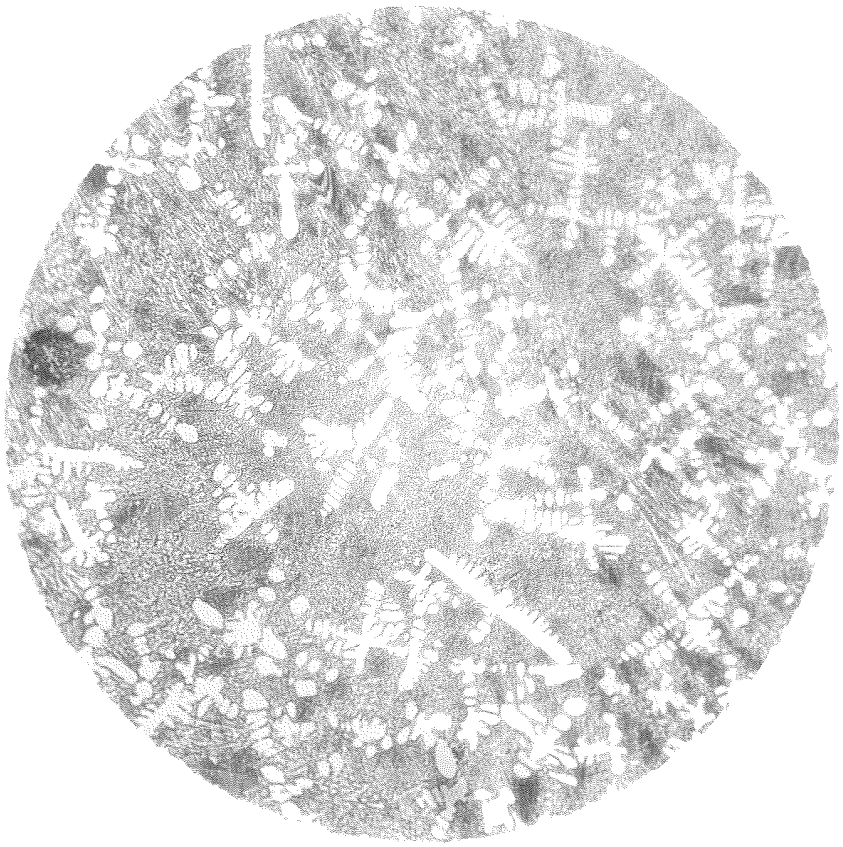

Fig. 165

(289A)
As cast
Magnification 100X
Etch Murakami

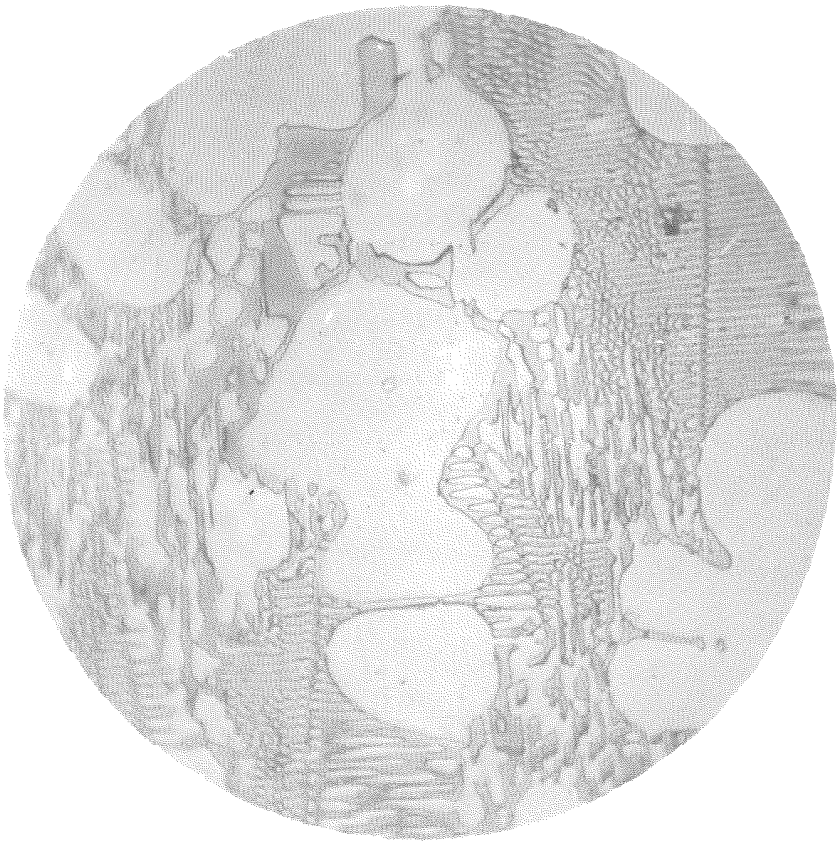

Fig. 166

(289B)
As cast
Magnification 1000X
Etch Murakami

primary constituent which takes on the appearance of the iron carbide solid solution is present. This primary constituent is surrounded by a eutectic material. In this research the primary iron boride has never been observed to precipitate in the form shown by this structure and hence impurities must be the source of trouble in this particular structure.

Figures 167, 168, 169, and 170 show the structure of specimen 249. The photomicrographs show the structure to consist of primary iron carbide crystals surrounded by a eutectic. This eutectic is between iron boride and the ternary solid solution. Figure 169 shows the structure of the primary iron boride surrounded by the eutectic and Figure 170 shows the structure of the eutectic.

In conclusion to this survey of the structures of the commercial alloys, we can say that the structures in general check very closely the equilibrium diagram. Discrepancies in the correlation are primarily due to non-equilibrium conditions or to the presence of impurities, particularly silicon. The effect of silicon has been pointed out in the description of the various structures. The principal effect seems to be to cause considerable refinement and a shifting of the transformation compositions toward the eutectic compositions.

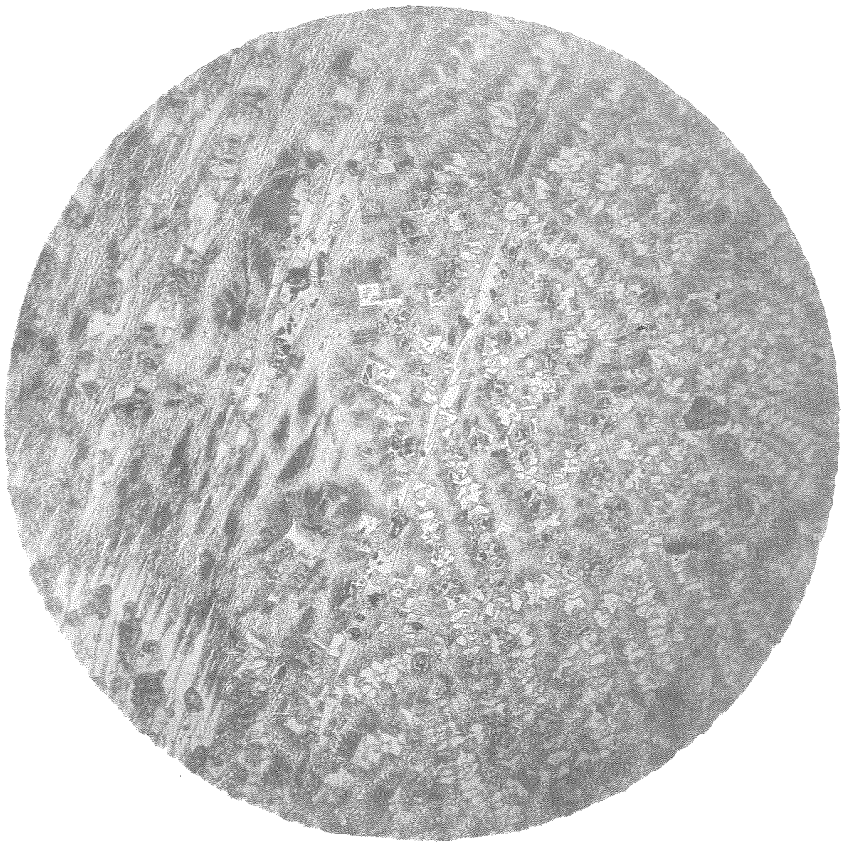

Fig. 167

(249B)
As cast
Magnification 100X
Etch Murakami

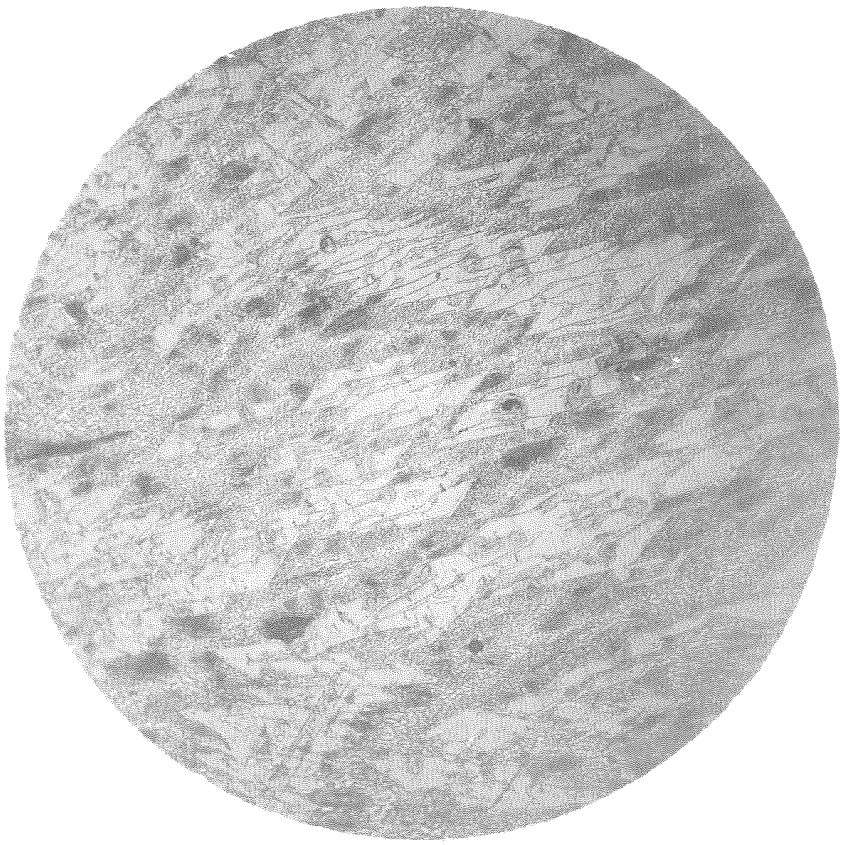

Fig. 168

(249C)
As cast
Magnification 1000X
Etch Murakami

Fig. 169

(249A)
As cast
Magnification 1000X
Etch Murakami

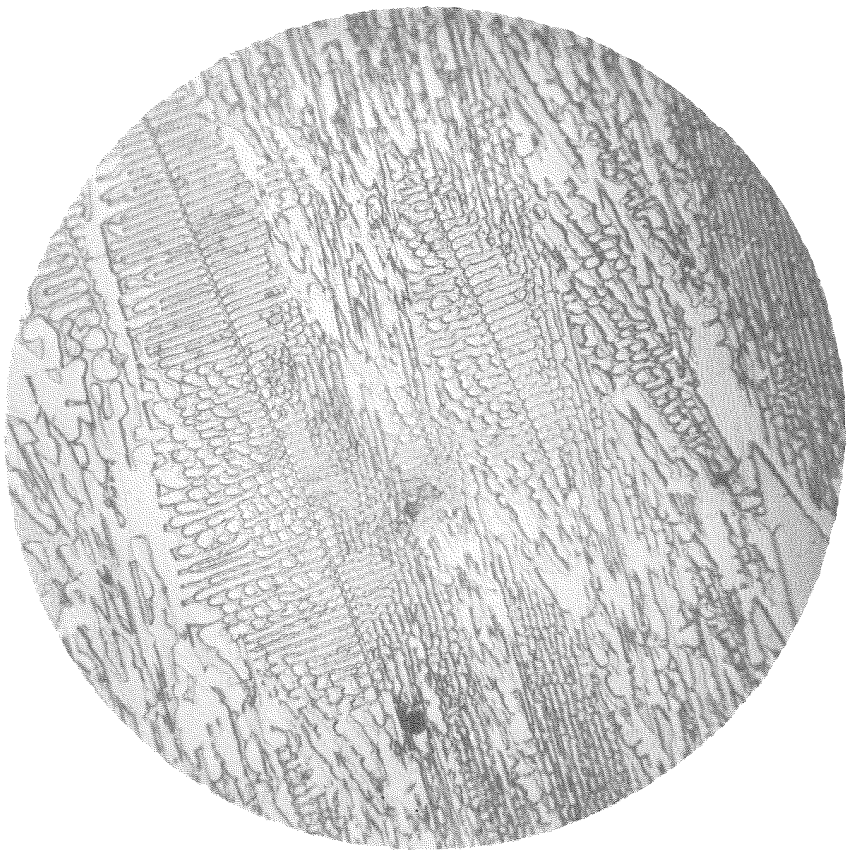

Fig. 170

(249D)
As cast
Magnification 1000X
Etch Murakami

Effect of Annealing on the Structures of Commerical Alloys

The previous section dealt altogether with melts that were cast in sand molds for commercial work. In cooling such as takes place in sand castings the transitions that take place may differ very greatly from transitions under equilibrium conditions or the alloy may be one in which diffusion takes place very readily and, hence, the relatively rapid cooling has little or no effect upon the structure. Therefore, it is desirable to determine the effect of annealing on the structures of these alloys. In the discussion to follow an attempt will be made to point out that annealing does change the structures of most of the alloys in that it allows conditions more nearly like those of equilibrium to exist, at least in the solid transformations. Most of the applications of these alloys are in the cast form and are not subjected to an annealing treatment, therefore, the only interest in the investigation of the effect of annealing is to determine the effect of such treatment on the structures in order to learn more of the equilibrium conditions.

First consider the alloys in the region CNVP1. Figures 171, 172, 173, and 174 show the structure of alloy 62-2 which has been annealed at 1800° F. for ten hours. This structure should be compared with Figures 104 and 105 which show the structure in the as

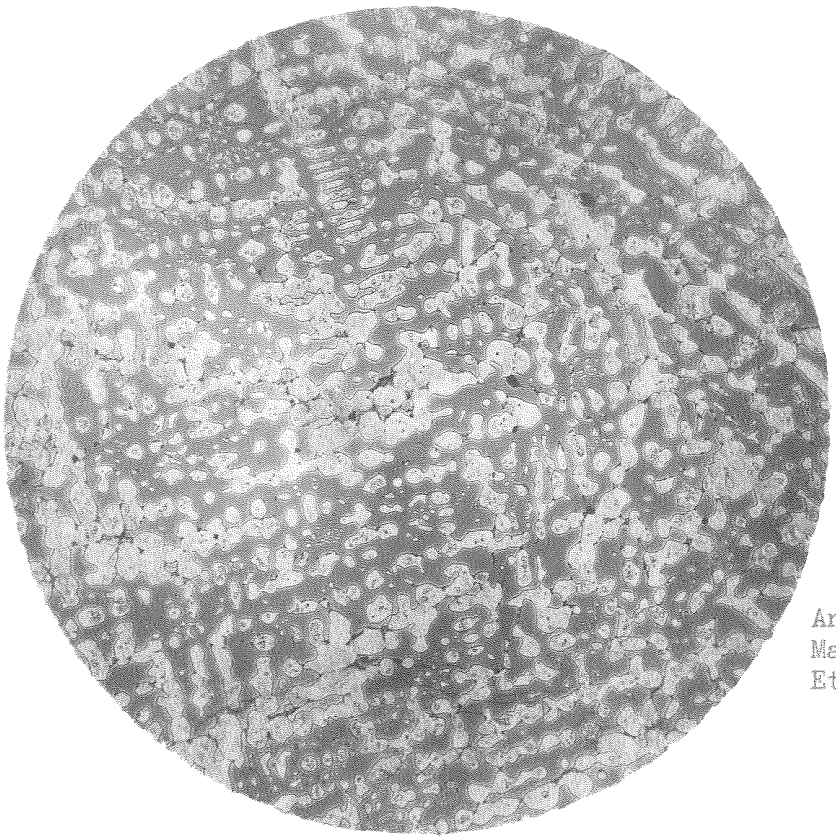

Fig. 171

(227A)
Annealed 10 hrs.1800°F.
Magnification 100X
Etch Murakami

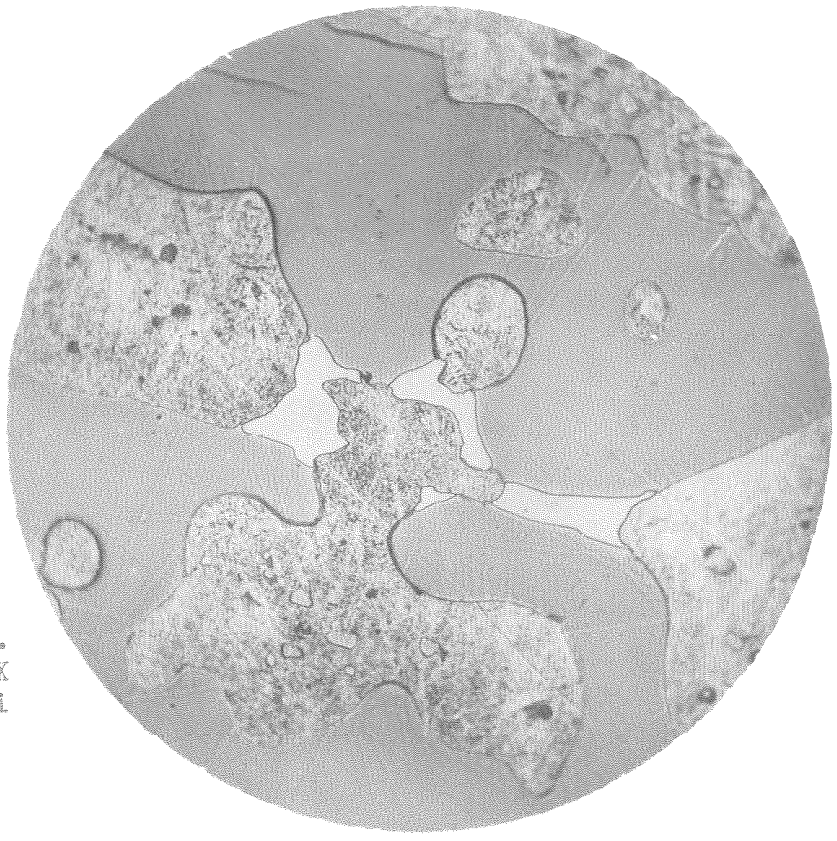

Fig. 172

(227B)
Annealed 10 hrs.1800°F.
Magnification 1000X
Etch Murakami

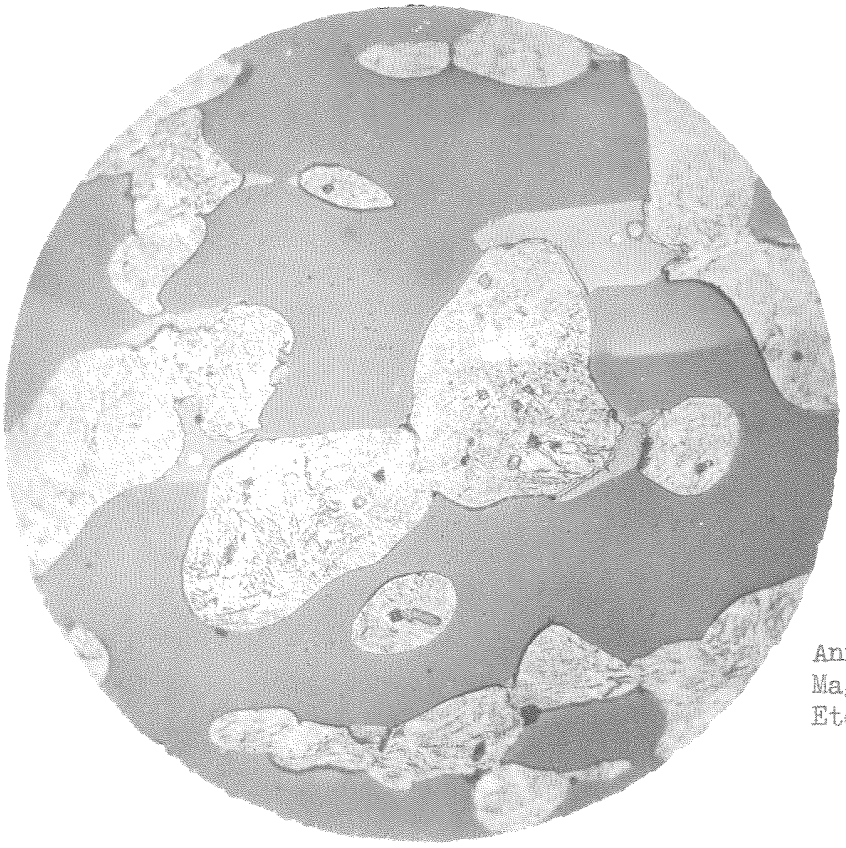

Fig. 173

(227C)
Annealed 10 hrs.1800°F.
Magnification 1000X
Etch Sodium Picrate

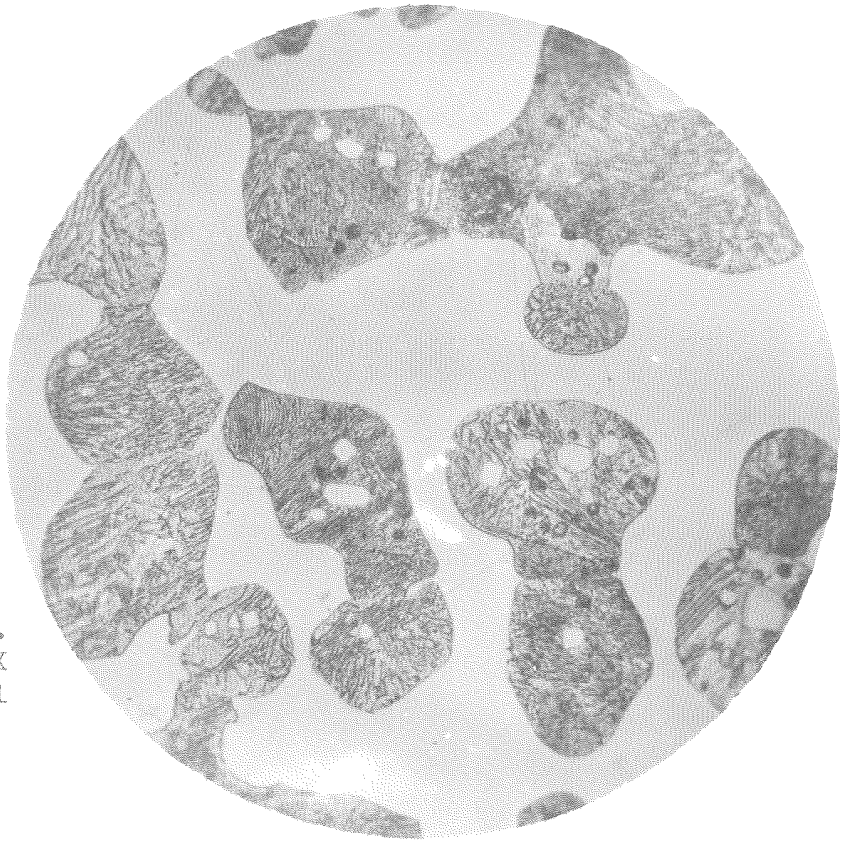

Fig. 174

(227D)
Annealed 10 hrs.1800°F.
Magnification 1000X
Etch 5% Picrol

cast condition. In comparing these figures one must bear in mind that Figures 104 and 105 were prepared by etching the specimen in 5% picrol while the photomicrographs of the annealed sample were prepared by etching in alkaline potasium ferricyanide. Figure 175 is inserted here to show the fine structure of the as cast alloy etched with the ferricyanide reagent. The larger grain such as that in the center is composed of the iron carbide solid solution and the surrounding material is the pearlite. Between two of these two solid solution crystals can be seen another constituent. In Figure 172 this matrix material is very definitely shown to be well coagulated. When the sample is etched with 5% picrol this matrix structure is not revealed, but some crystals, which have a tendency to be prismatic, are brought out in the pearlite grains. These figures seem to indicate that the iron boride has a tendency to coagulate in the pearlite, forming these crystals. The pearlite should consist of a fine mixture of iron boride in alpha iron and the iron carbide solid solution which contains iron boride in solution. It would appear that some iron boride has come out of solution in both cases, producing the structures observed.

Figures 176 and 177 show the structure of alloy 135 annealed at 1800° F. for ten hours. This structure should be compared with Figures 113 and 114. In addition to these last photomicrographs, Figures 178 and 179 show the structure of the as cast alloy etched

Fig. 175

(62-20)
As cast
Magnification 1000X
Etch Murakami

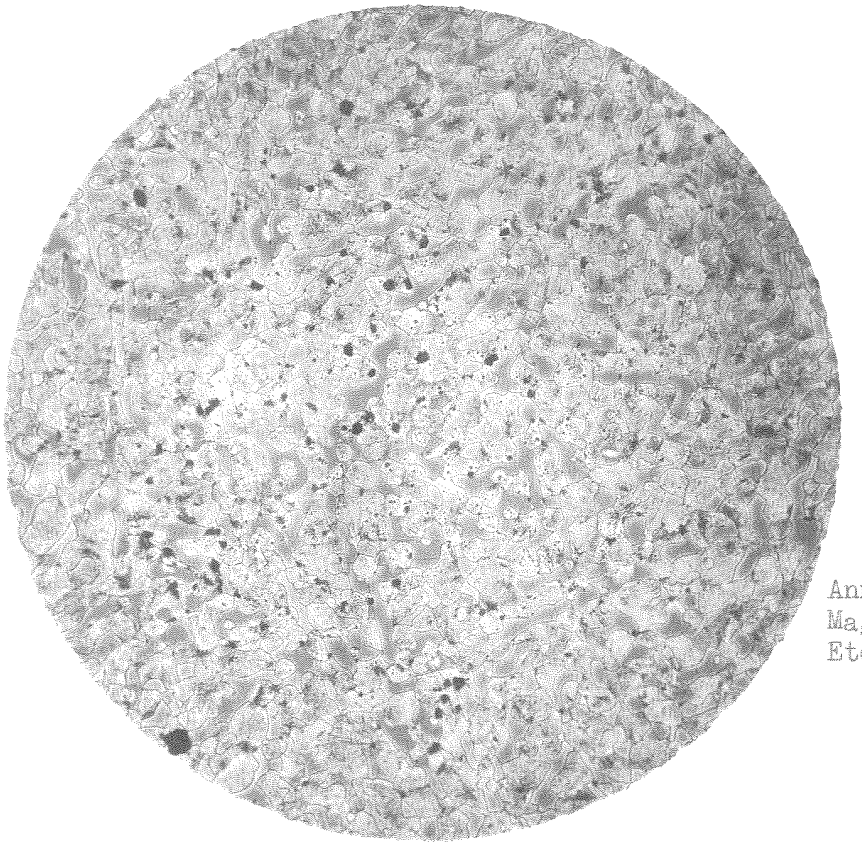

Fig. 176

(223B)
Annealed 10 hrs.1800°F.
Magnification 100X
Etch Murakami

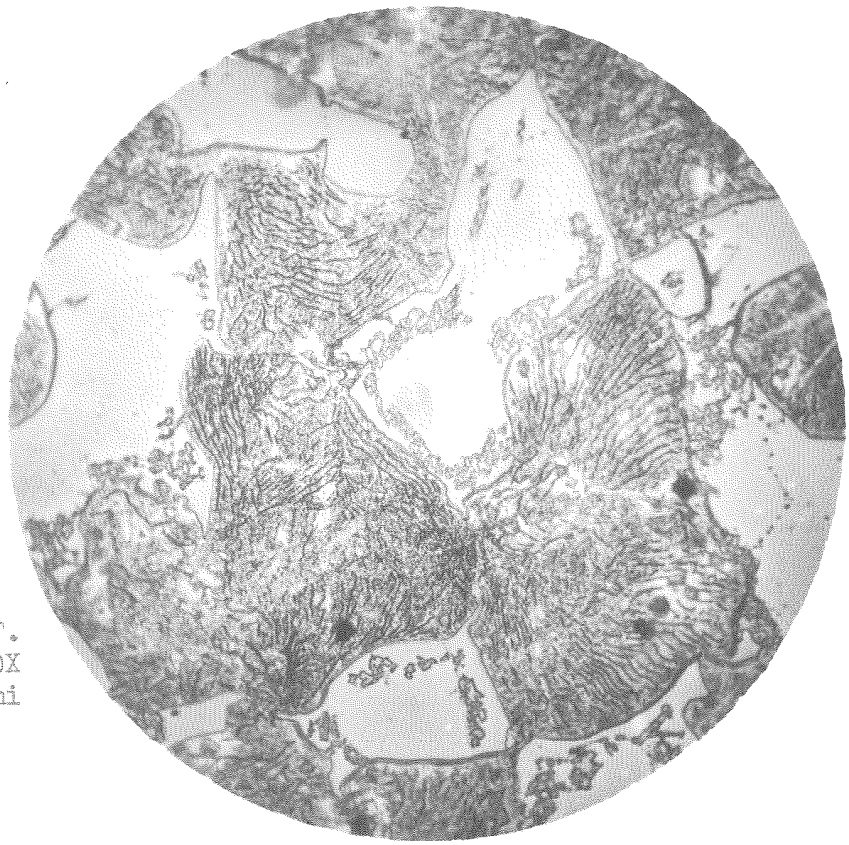

Fig. 177

(223A)
Annealed 10 hrs.1800°F.
Magnification 1000X
Etch Murakami

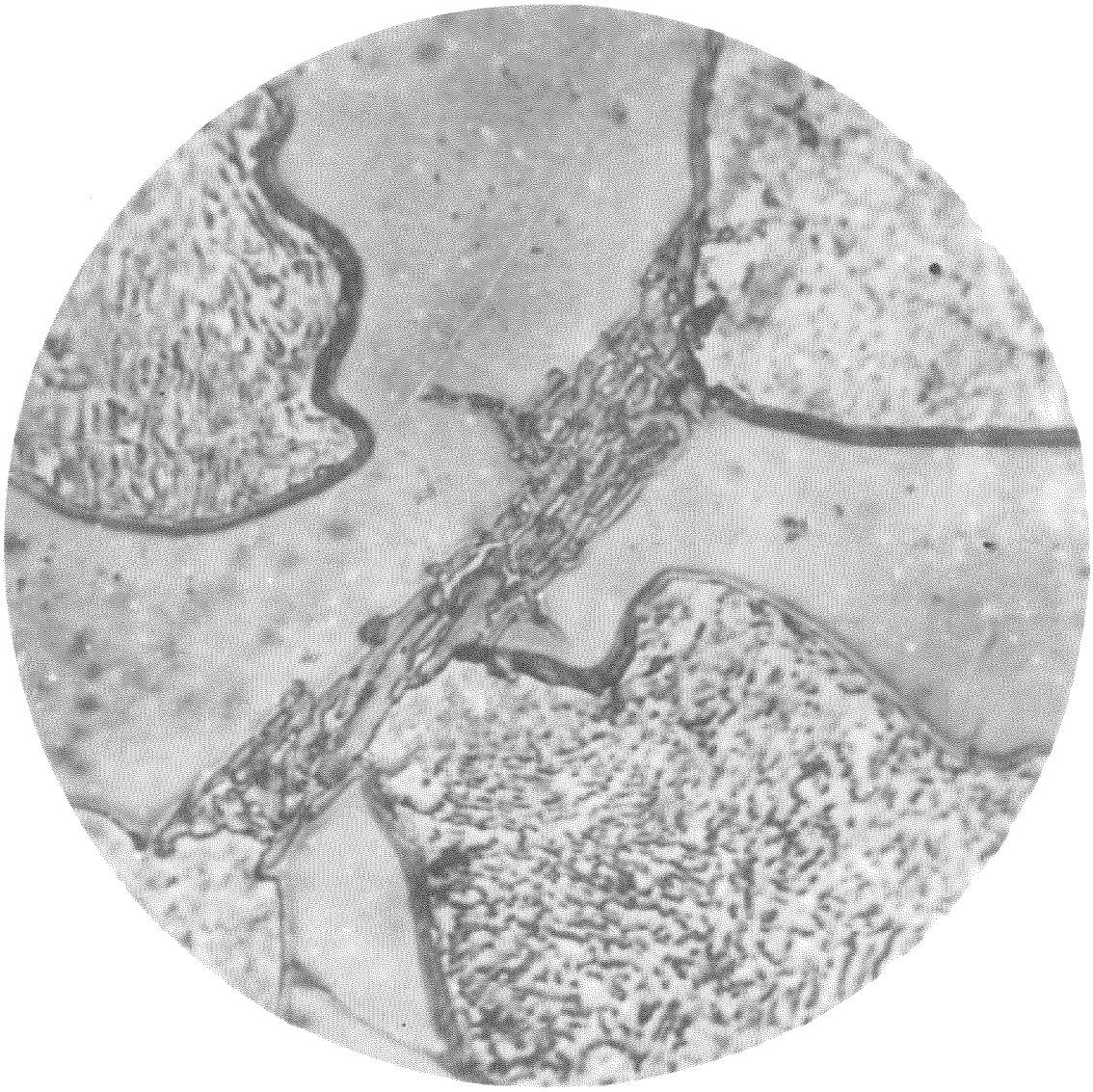

Fig. 178

(B135-D)
As cast
Magnification 3000X
Etch Murakami

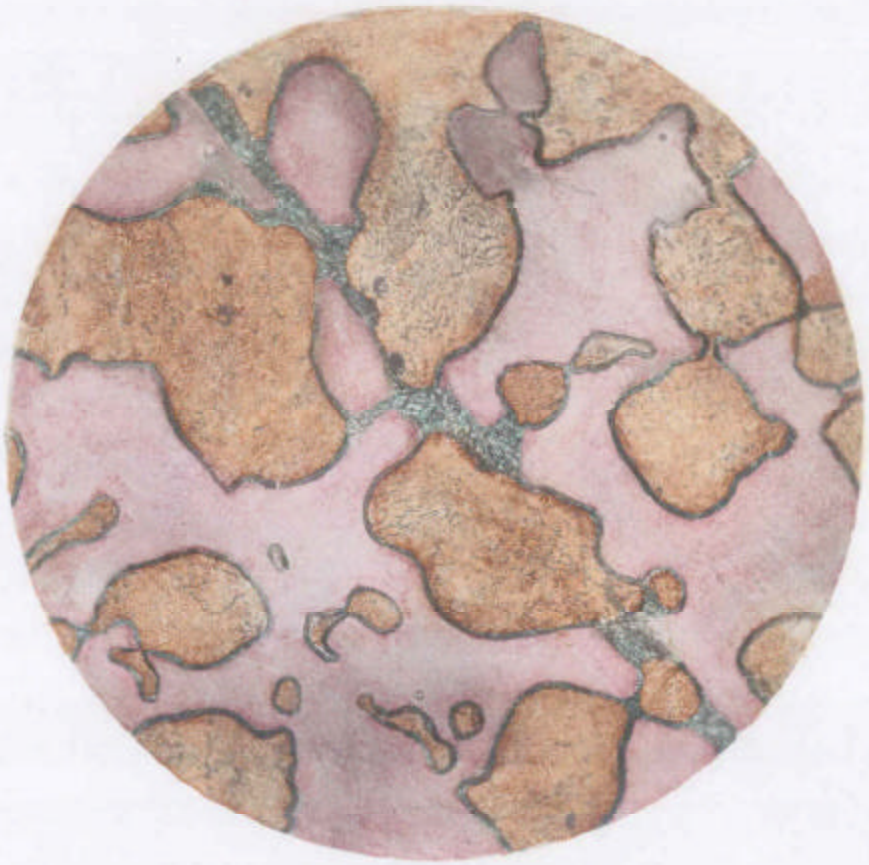

Fig. 179

(B135-C)
As cast
Magnification 1000X
Etch Murakami

with the ferricyanide reagent. These last two figures show definitely that a constituent is being thrown out of solution forming envelopes around the pearlite grains. In the annealed alloy these envelopes seem to have been broken up somewhat and coagulated. This series of photomicrographs also seems to substantiate the idea that iron boride is thrown out of solution. One distinguishing feature is the color of this constituent when etched with the ferricyanide reagent. When the specimen is etched for five minutes in a boiling solution, these precipitations are colored a blue green. It has been observed that in alloys containing primary iron boride, the boride crystals also take on this characteristic color when etched with this reagent. This is further proof that this constituent is iron boride which has been thrown out of solution. More cases will be cited to substantiate this statement.

Figures 180 and 181 show the structure of alloy 270 annealed at 1800° F. for eight hours. When these are compared with Figures 118 and 119 very little difference is observed except that somewhat more coagulation has occurred in the primary pearlite. However, at higher magnification none of the previously mentioned boride has come out of solution. This alloy contains about 1.13% silicon, whereas the others contained about 0.5%. This retention of the iron boride in solution may be attributed to the silicon content.

Figures 182 and 183 show the structure of alloy 271 annealed at 1800° F. for eight hours. Comparing these with Figures 122 and

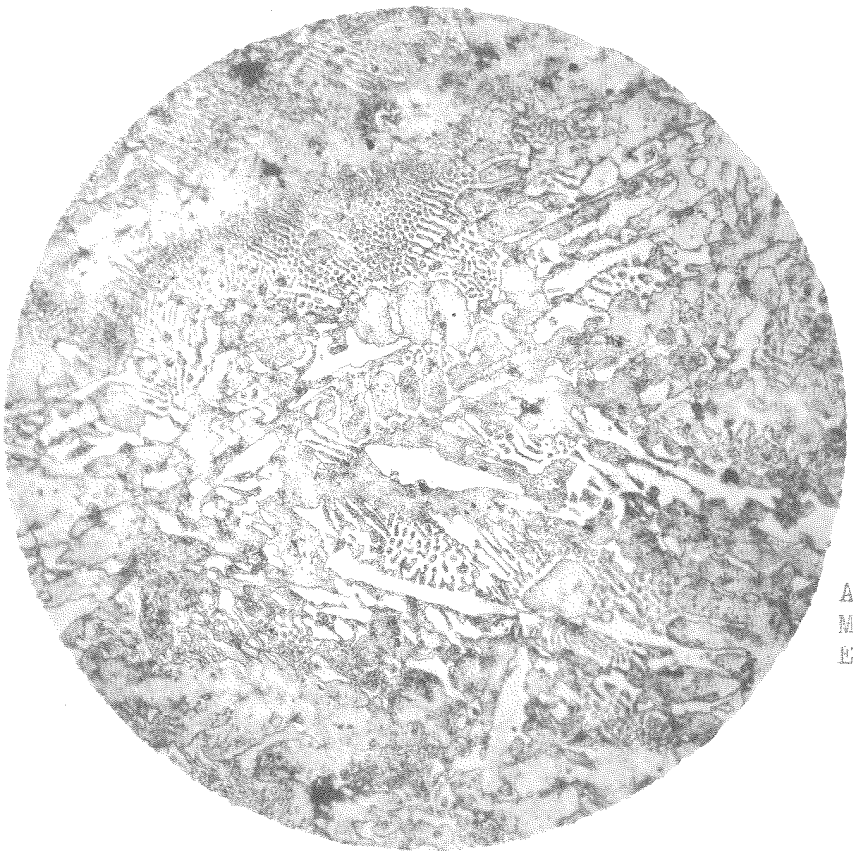

Fig. 180

(270-2BA)
Annealed 8 hrs.1800°F.
Magnification 100X
Etch Murakami

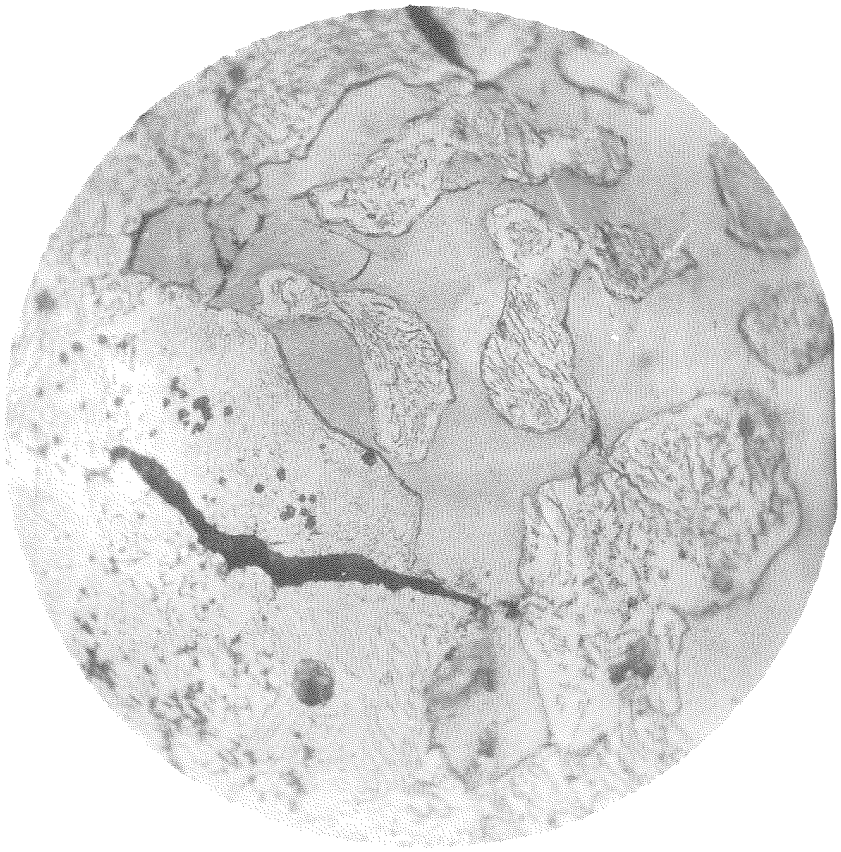

Fig. 181

(270-2BB)
Annealed 8 hrs.1800°F.
Magnification 1000X
Etch Murakami

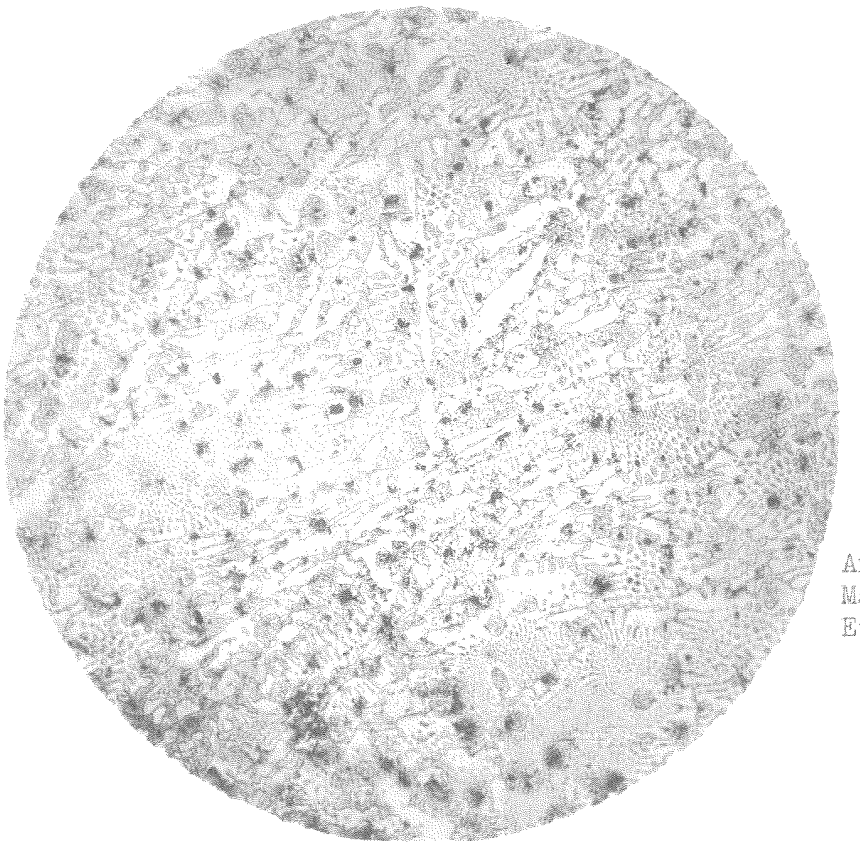

Fig. 182

(271-2BA)
Annealed 8 hrs.1800°F.
Magnification 100X
Etch Murakami

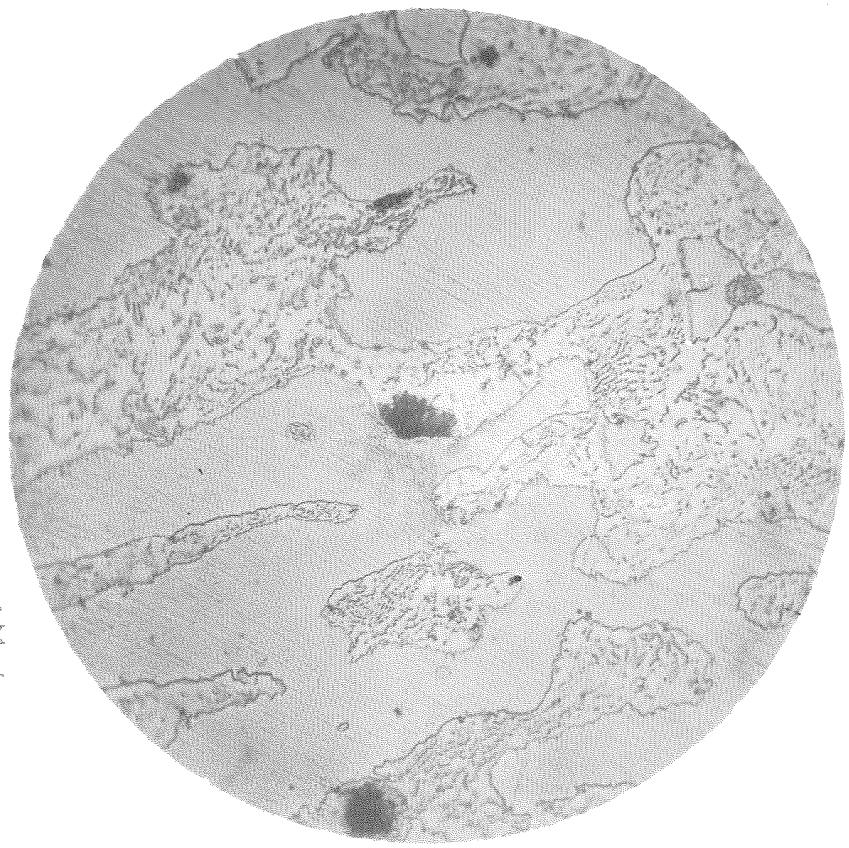

Fig. 183

(271-2BB)
Annealed 8 hrs.1800°F.
Magnification 1000X
Etch Murakami

123 we see very little difference, except possibly a little more uniform structure. Such a difference can be attributed to the heterogeneity found in such castings.

Figures 184 and 185 show the structure of alloy 221 annealed at 1800° F. for ten hours. In comparing these figures with Figure 125, it may be seen that the effect of annealing has been to remove some of the typical casting structure and to increase the grain size. Furthermore, as in some of the previous cases, a constituent which remains between the pearlite grains has been thrown out of solution. This interstitial material carries the characteristic blue green color, indicating the presence of iron boride.

This completes the study of the effect of annealing on alloys in this region. The principal point gained from this part of the research is that with long annealing iron boride is precipitated from solution, which may indicate that the solubility of iron boride is not as great as indicated by Tammann. Alloys in which the silicon was relatively high did not show this precipitation, which would indicate that Tammann's results were affected by the silicon, as indicated by Wever and Muller.

Now let us consider the region NVB for alloys containing the ternary solid solution V in excess of the ternary eutectic.

In order to determine the effect of the temperature at which alloys in this group are annealed, a group of specimens was cut

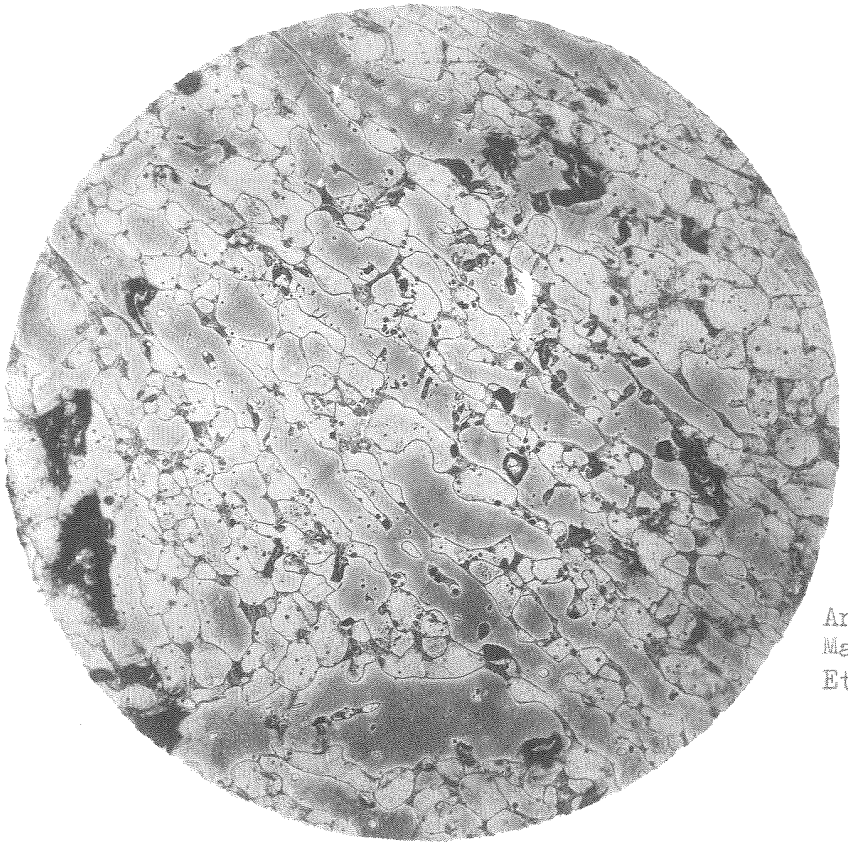

Fig. 184

(222B)
Annealed 10 hrs.1800°F.
Magnification 100X
Etch Murakami

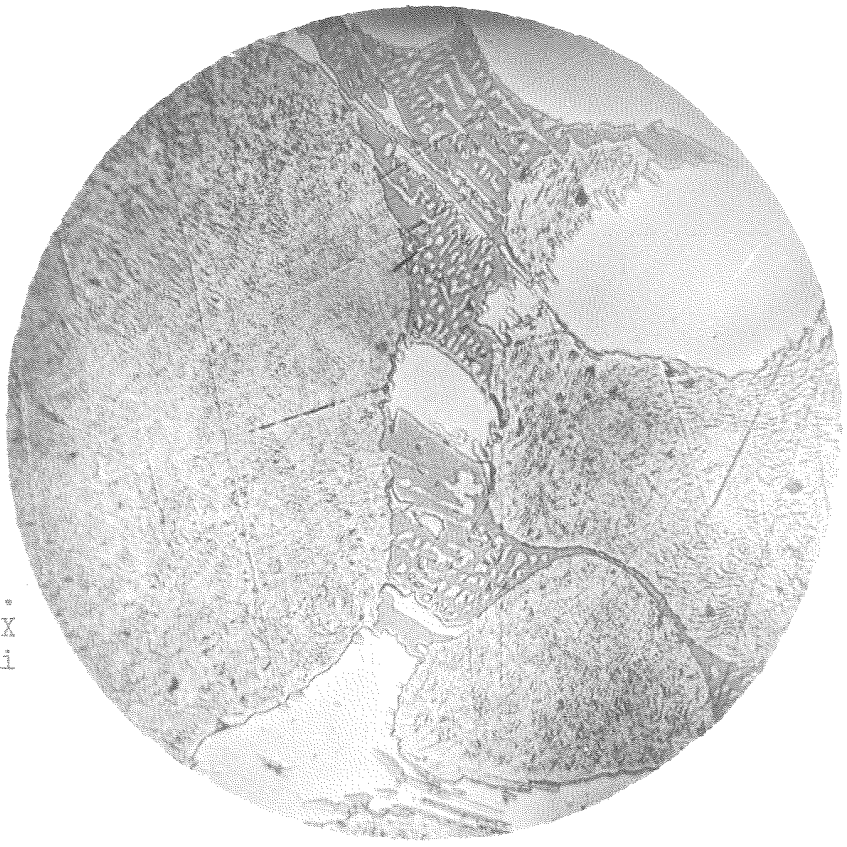

Fig. 185

(222A)
Annealed 10 hrs.1800°F.
Magnification 1000X
Etch Murakami

from alloy 267 and heated at different temperatures for a period of eight hours. One specimen was heated at 600° F., another at 800° F., another at 1000° F., another at 1200° F., another at 1400° F., another at 1600° F., and the last at 1800° F. No change in structure was observed until heating at 1400° F. Figures 138 and 139 show the structure in the as cast condition. Figures 186 and 187 show the structure after annealing at 1200° F. for eight hours. Comparing this structure with that in the as cast condition, no change can be observed. Figures 188, 189, 190, 191, 192, 193 show the structures obtained with higher annealing temperatures. The structure shown after casting consists of ternary eutectic and excess of the pearlitic constituent. However, at some temperature between 1200° F. and 1400° F. this ternary eutectic structure is nearly obliterated, probably due to complete diffusion at this temperature. The figures show a progressive coarsening, coagulation of the constituents, and finally the complete removal of the ternary eutectic structure. No noticeable precipitation of iron boride is observed, as in the previous discussion.

Alloy 228 containing 2.76% carbon and 1.04% boron, falling very close to the SZ curve, was given a special series of treatments. In this series, four specimens were used, of which one was heated for three hours, one for six hours, one for eight hours, and the last for ten hours at 1800° F. The structures obtained with such

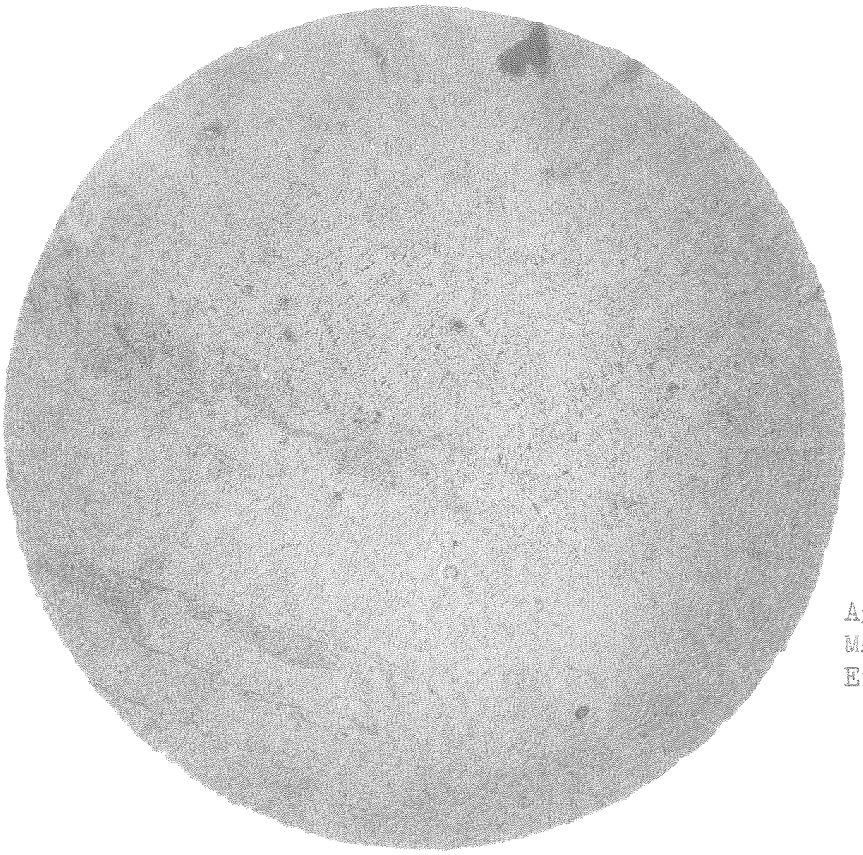

Fig. 186

(267-5A)
Annealed 8 hrs.1200°F.
Magnification 100X
Etch Murakami

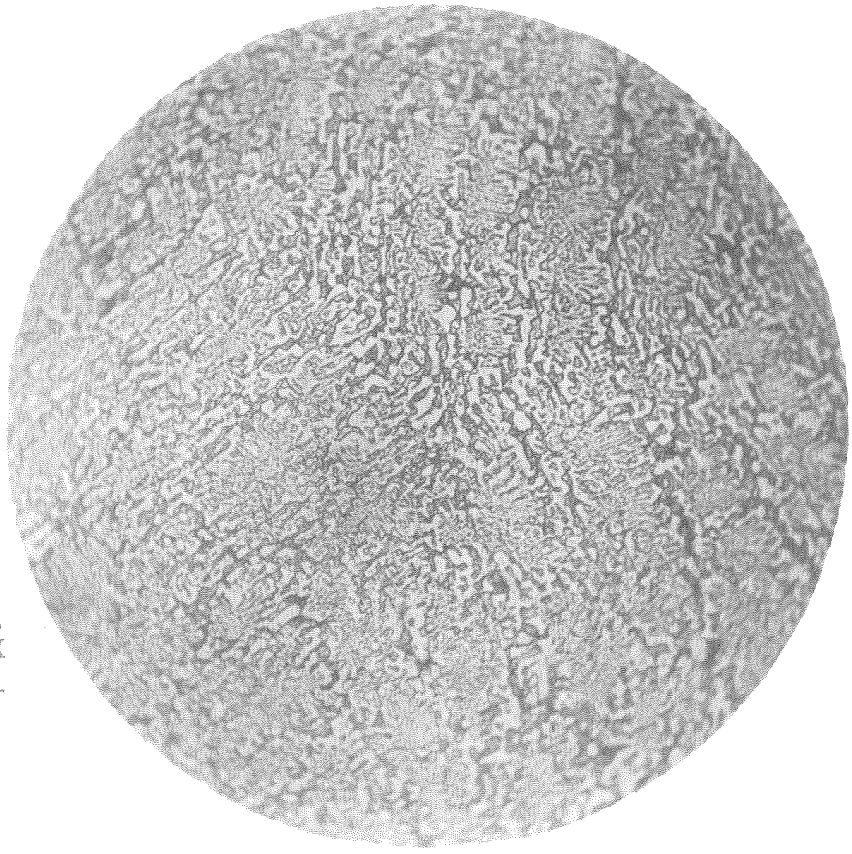

Fig. 187

(267-5B)
Annealed 8 hrs.1200°F.
Magnification 1000X
Etch Murakami

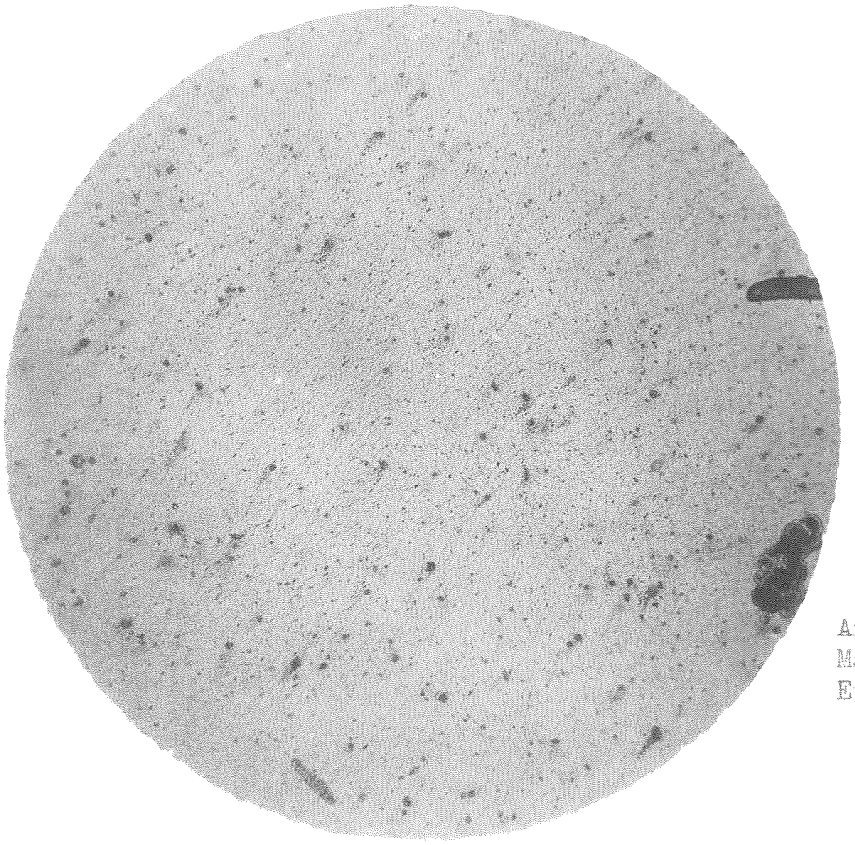

Fig. 188

(267-6D)
Annealed 8 hrs.1400°F.
Magnification 100X
Etch Murakami

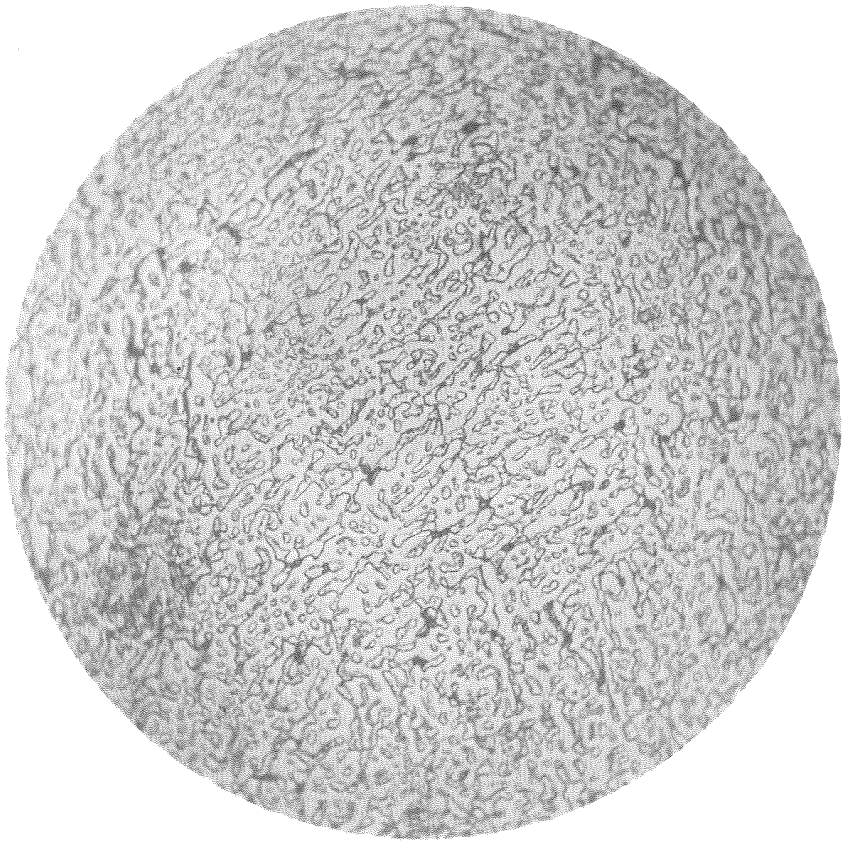

Fig. 189

(267-6E)
Annealed 8 hrs.1400°F.
Magnification 1000X
Etch Murakami

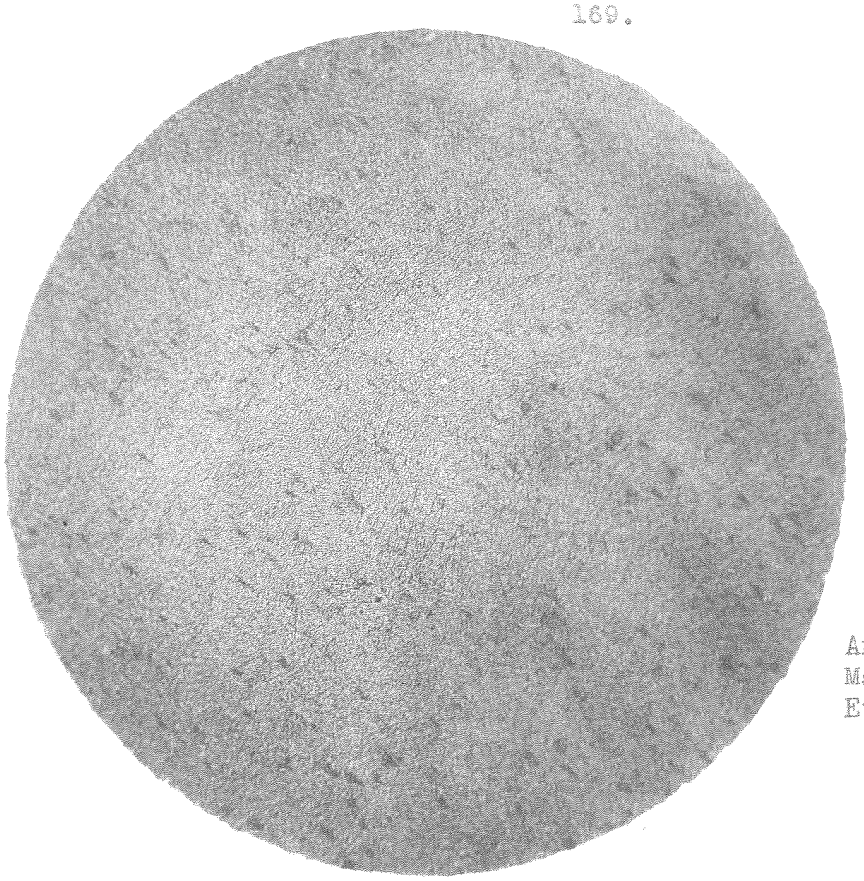

Fig. 190

(267-7A)
Annealed 8 hrs.1600°F.
Magnification 100X
Etch Murakami

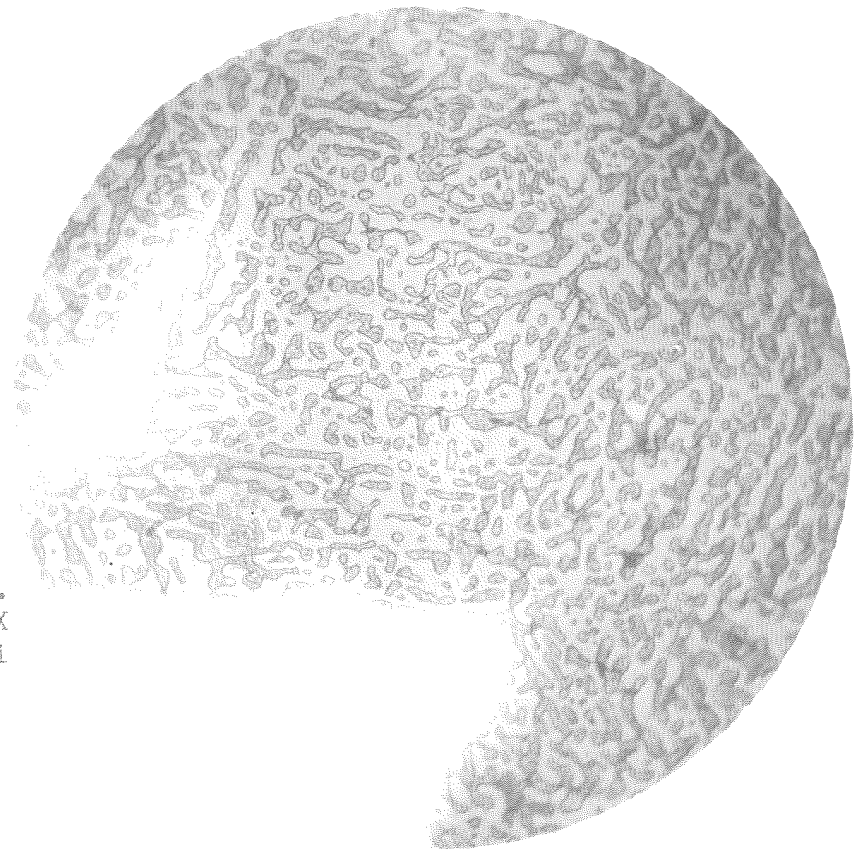

Fig. 191

(267-7B)
Annealed 8 hrs.1600°F.
Magnification 1000X
Etch Murakami

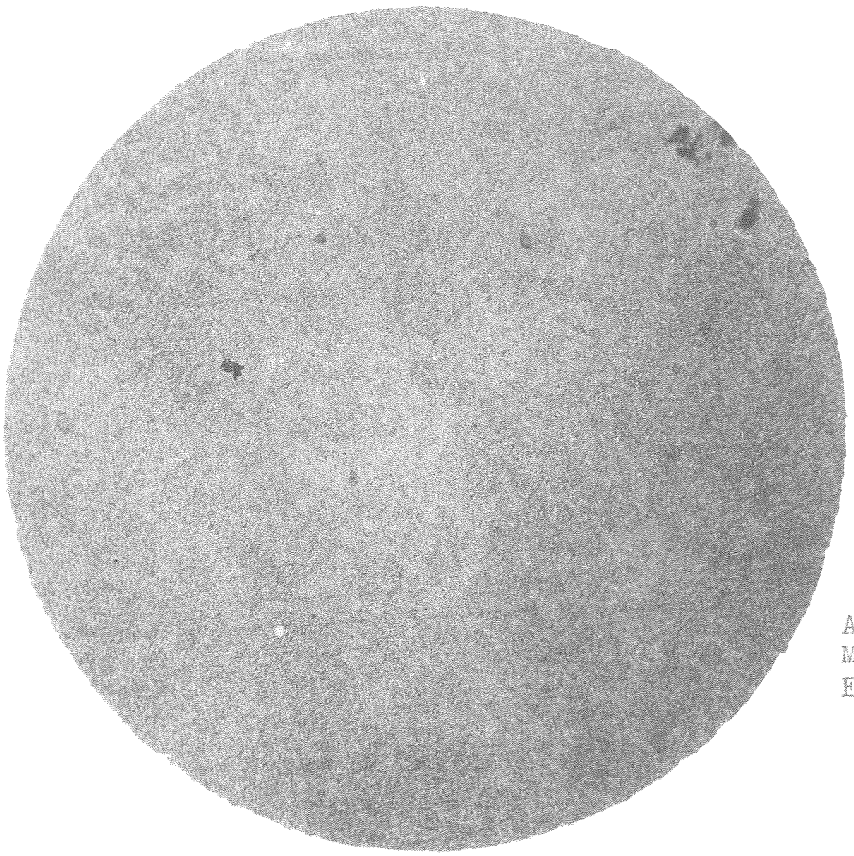

Fig. 192

(267-8A)
Annealed 8 hrs.1800°F.
Magnification 100X
Etch Murakami

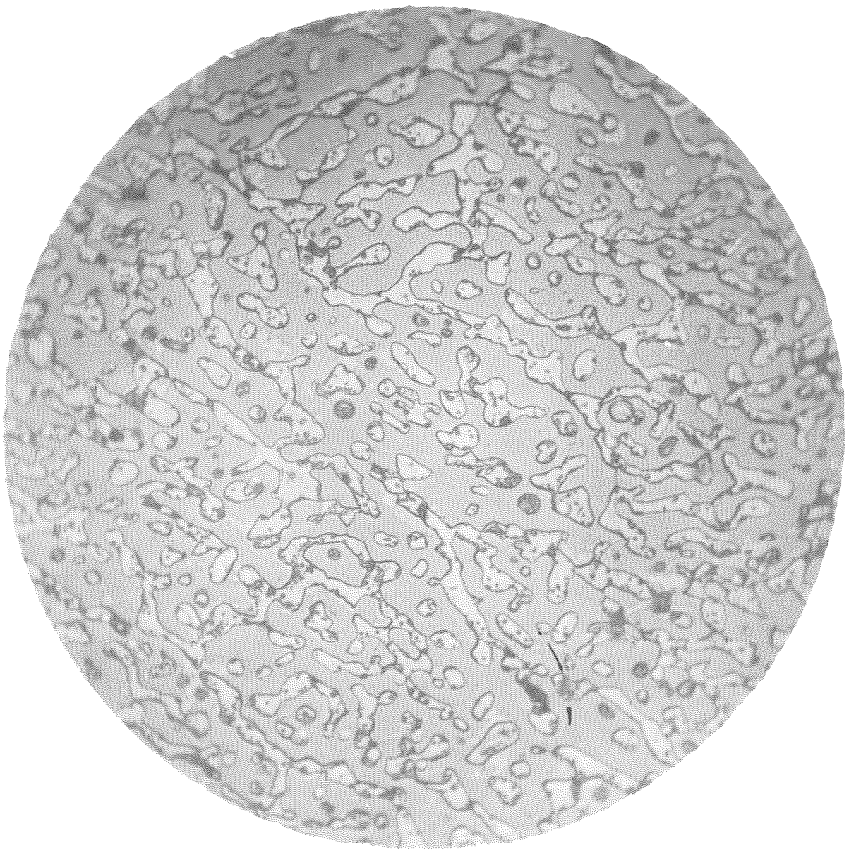

Fig. 193

(267-8B)
Annealed 8 hrs.1800°F.
Magnification 1000X
Etch Murakami

treatment are shown in Figures 194 to 197, inclusive, in order of increasing time. After annealing for three hours the structure is about as would be expected after casting. However, after six hours the blue green constituent, which we have previously observed, appears joined to a network surrounding the pearlite grains. With further annealing, this network structure disappears and the substance seems to coagulate considerably.

Another alloy which is very close to the one considered above is alloy 189, whose structure was shown in the as cast condition in Figures 129 and 130. These photomicrographs were prepared by etching the specimen in 5% picrol. Figure 198 shows the structure when the as cast specimen was etched with the ferricyanide reagent. This shows a segregation of material in the pearlite. Figures 199 and 200 show the structure of this alloy after annealing at 1800° F. for ten hours. Here we see a complete coagulation of this constituent which takes on the blue green appearance of the iron boride. This alloy contains a small amount of silicon, which further substantiates the statement of the solubility of iron boride.

Figures 201 and 202 show the structure of alloy 225 annealed at 1800° F. for ten hours. If this is compared with the structure of the alloy in the as cast condition, shown in Figures 141 and 142, it will be noted that the annealing has eliminated the eutectic structure, bringing about almost complete diffusion.

It should be noted that those alloys which lie approximately

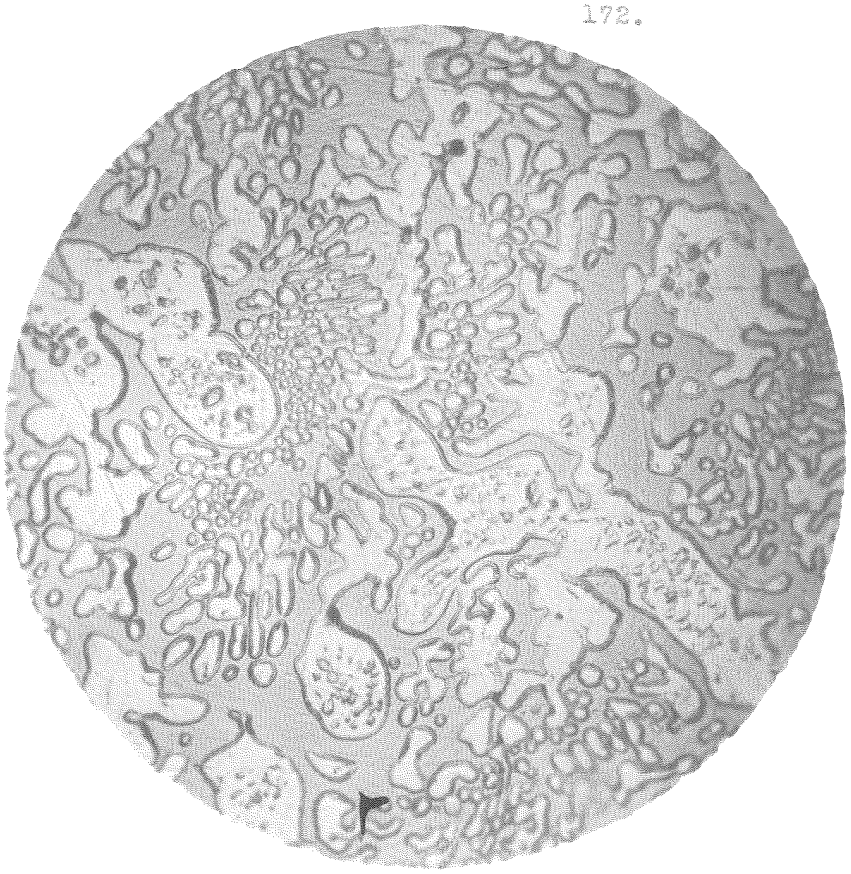

Fig. 194

(228-3A)
Annealed 3 hrs.1800°F.
Magnification 1000X
Etch Murakami

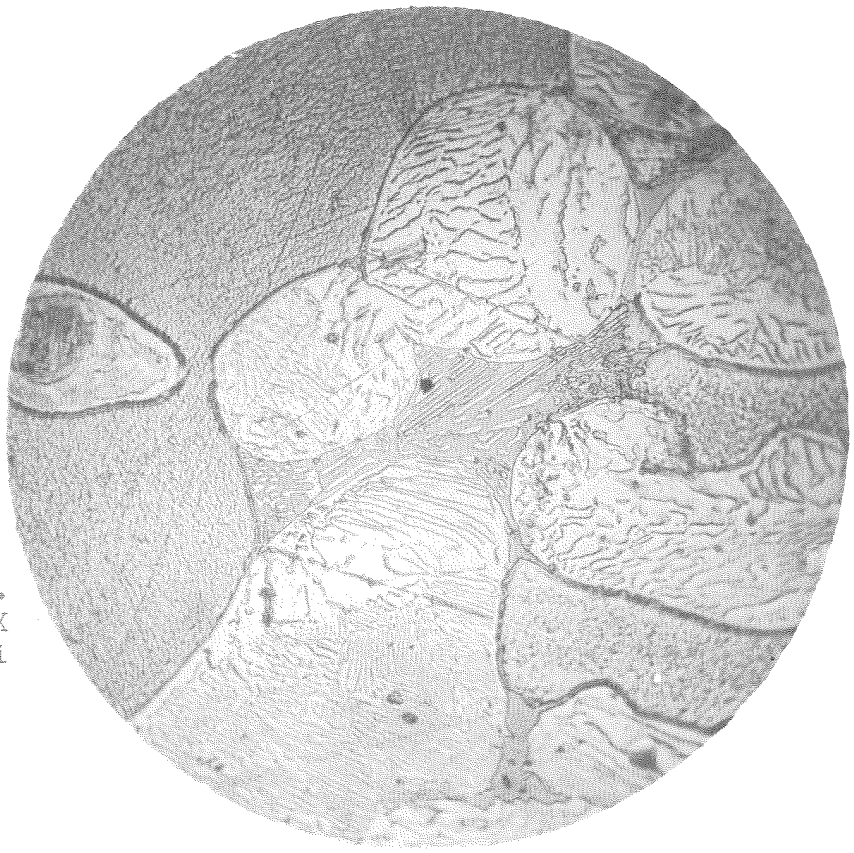

Fig. 195

(228-6B)
Annealed 6 hrs.1800°F.
Magnification 1000X
Etch Murakami

Fig. 196

(228-8A)
Annealed 8 hrs.1800°F.
Magnification 1000X
Etch Murakami

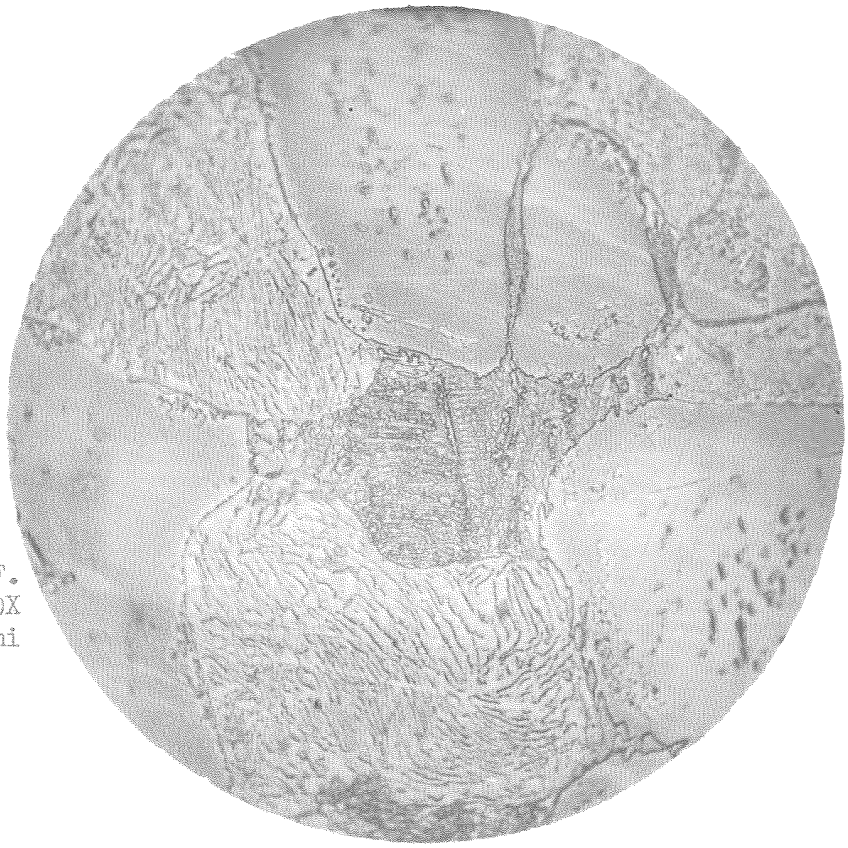

Fig. 197

(228-10A)
Annealed 10 hrs.1800°F.
Magnification 1000X
Etch Murakami

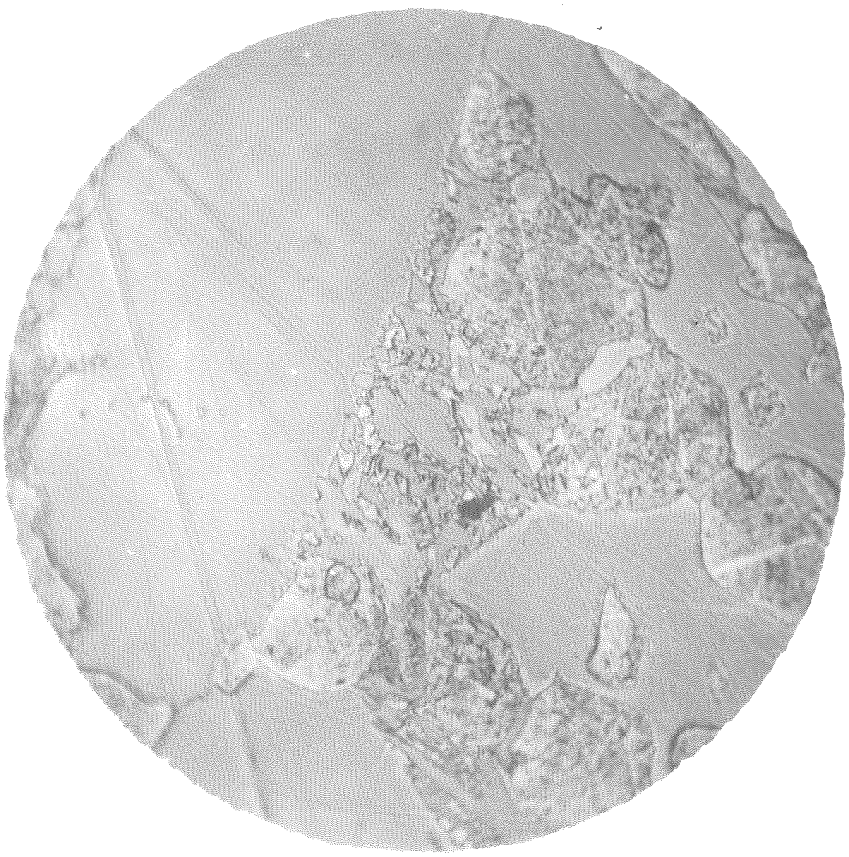

Fig. 198

(189C)
As cast
Magnification 1000X
Etch Murakami

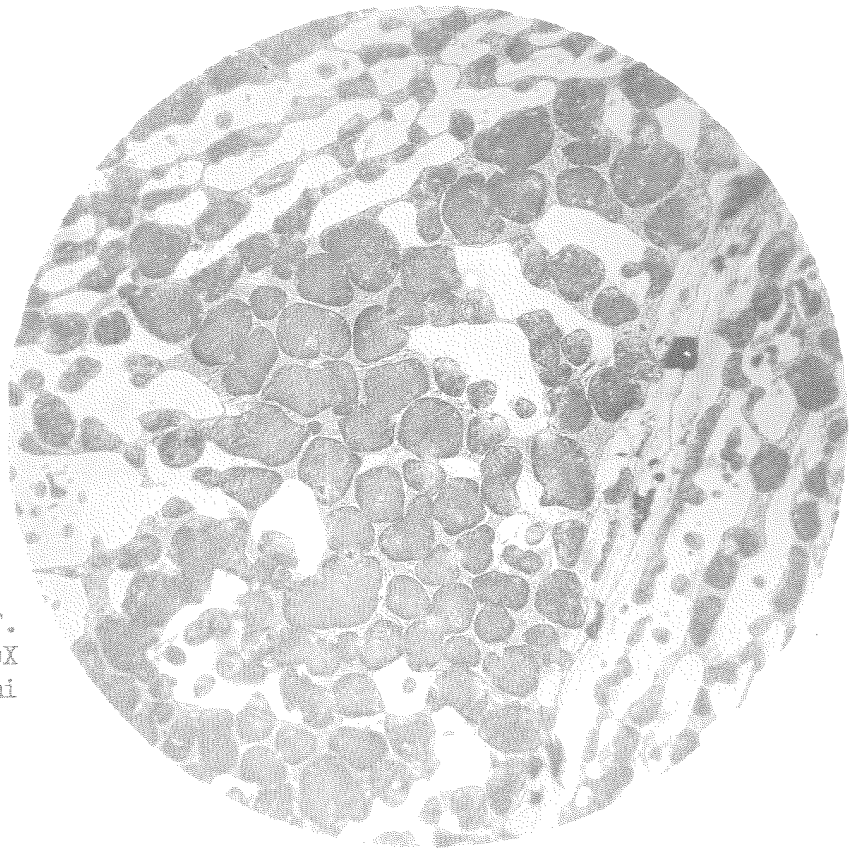

Fig. 199

(224G)
Annealed 10 hrs.1800°F.
Magnification 100X
Etch Murakami

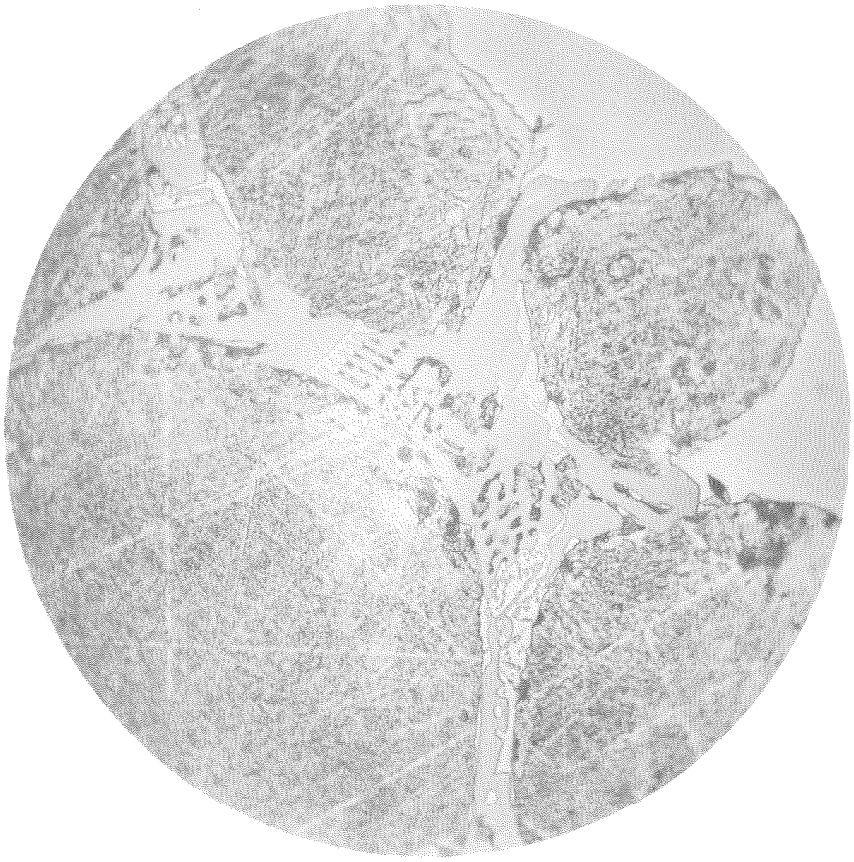

Fig. 200

(224H)
Annealed 10 hrs.1800°F.
Magnification 1000X
Etch Murakami

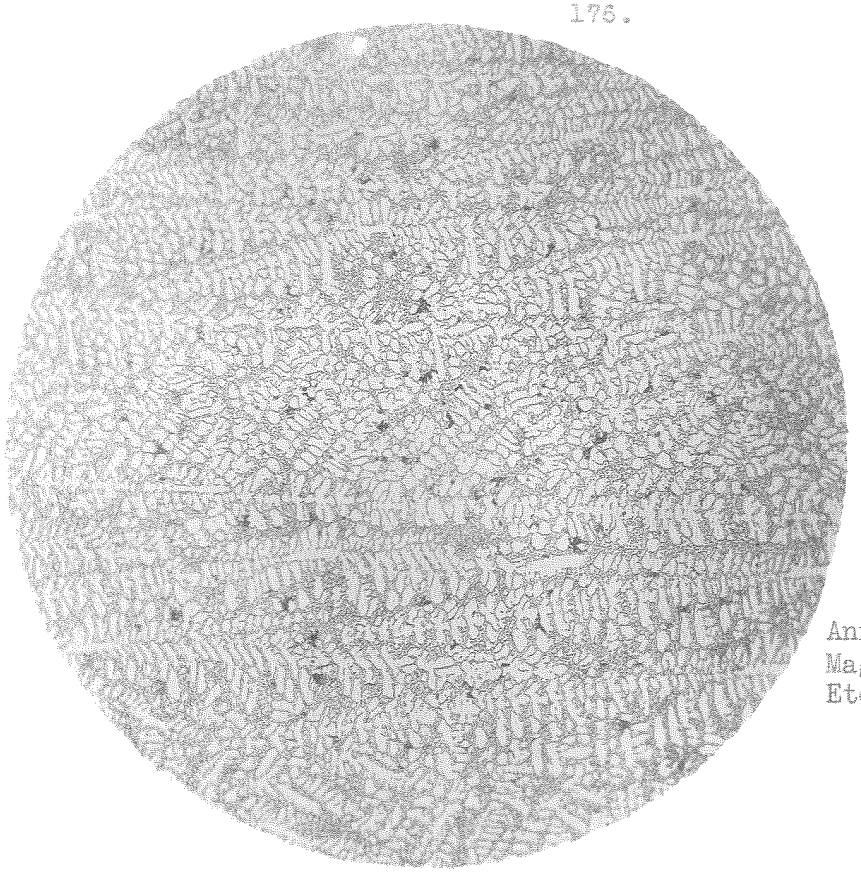

Fig. 201

(226A)
Annealed 10 hrs.1800°F.
Magnification 100X
Etch Murakami

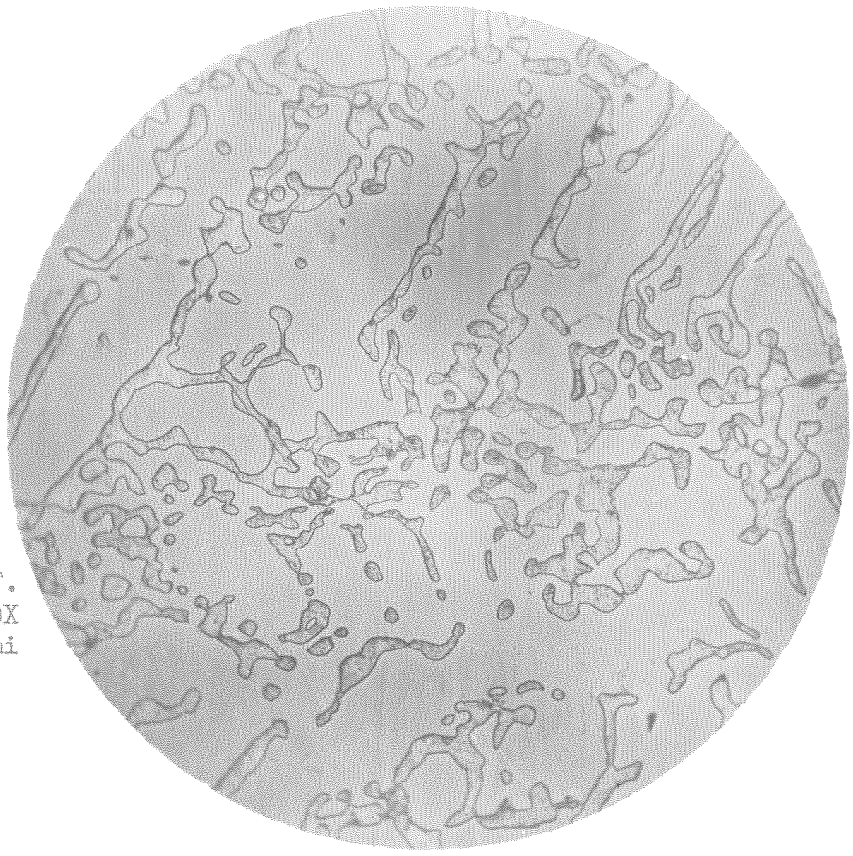

Fig. 202

(226B)
Annealed 10 hrs.1800°F.
Magnification 1000X
Etch Murakami

on the ZS curve have the property of displacing the boride constituent from solution, while those lying definitely in the triangle do not have this property, but merely an elimination of the eutectic structure occurs on annealing.

A few alloys within the triangle NVB in the region of primary iron carbide solid solution will now be considered. In Figures 203 to 211 is shown the effect of different annealing temperatures on alloy 276, Figures 143 and 144. The effect on this alloy is found between 1200° F. and 1400° F., as in the previous case, where the ternary eutectic is partially obliterated and, as the temperature is increased, the pearlitic structure agglomerates to the fullest extent and the ternary eutectic finally disappears.

Alloy 248, which has been annealed at 1800° F. for eight hours, also lies in this region and is shown in Figures 212 and 213. The as cast structure appears in Figures 152 and 153. The effect of the annealing is very noticeable in this case in that the ternary eutectic has entirely disappeared and all that remains is the ternary pearlite, which is readily brought out in Figure 213. It is very noticeable in all the alloys lying in this field that the distinction between the iron carbide solid solution and the iron boride is not resolved, due undoubtedly to the close similarity of their properties. In Figure 213 the structure enclosed by boundaries is not a homogeneous solution, as the photomicrograph would indicate, but is the ternary pearlite.

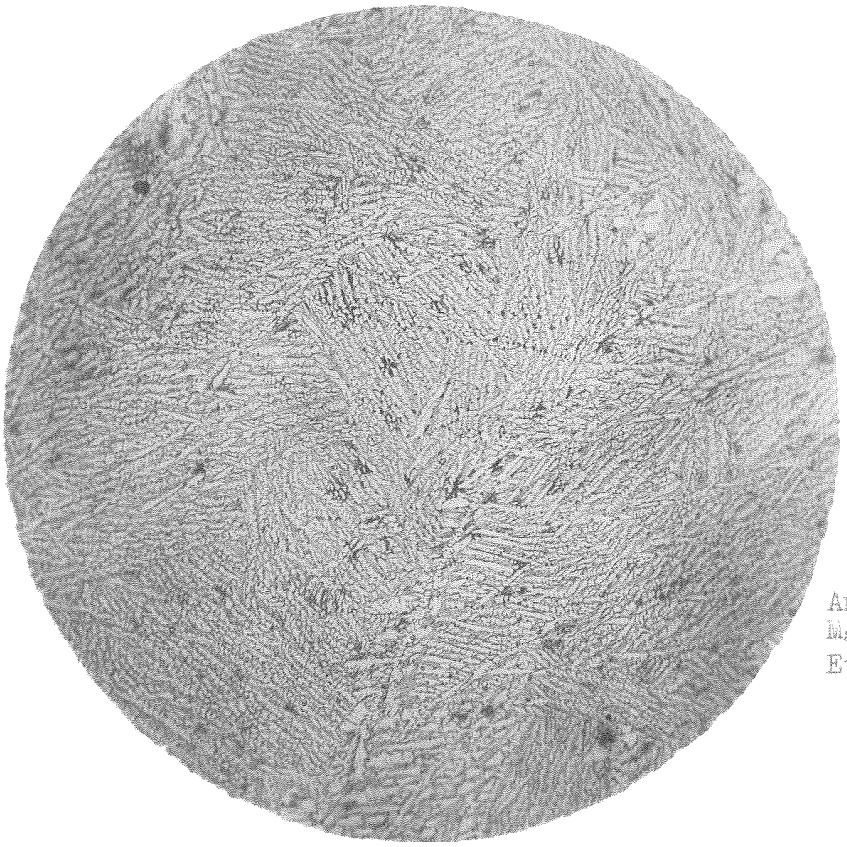

Fig. 203

(276-2A)
Annealed 8 hrs.1200°F.
Magnification 100X
Etch Murakami

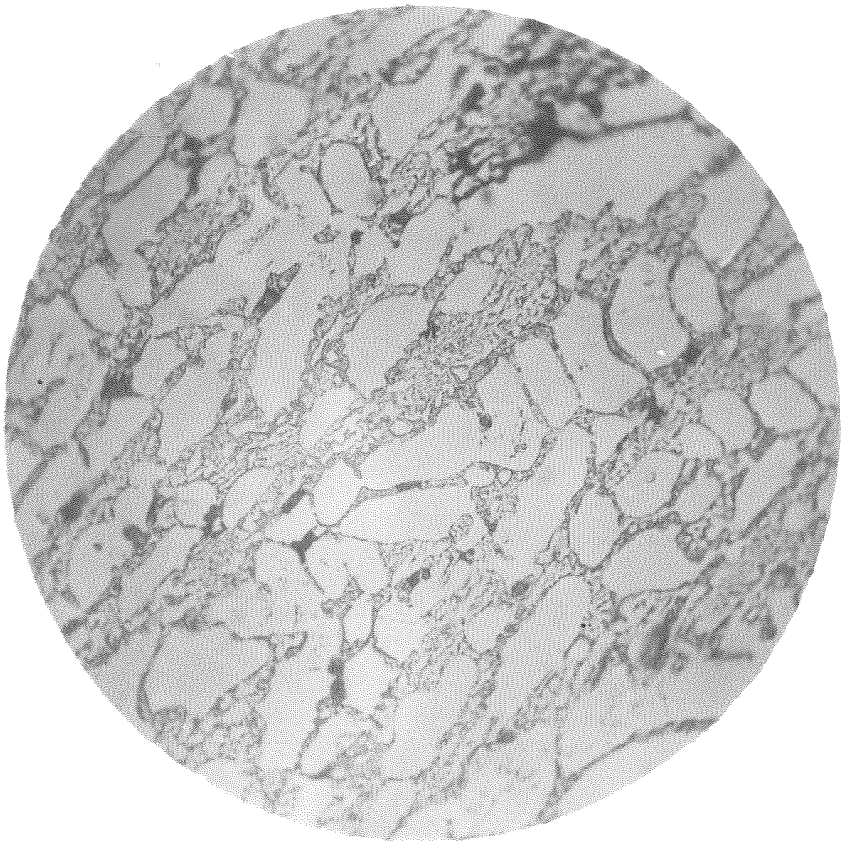

Fig. 204

(276-2B)
Annealed 8 hrs.1200°F.
Magnification 1000X
Etch Murakami

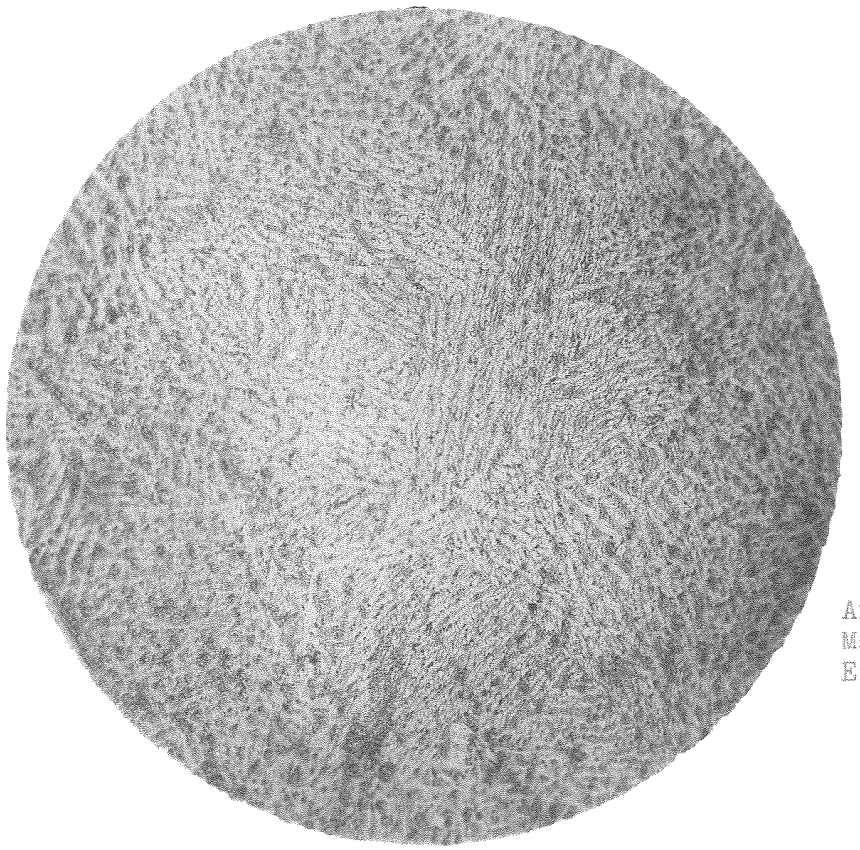

Fig. 205

(276-3A)
Annealed 8 hrs.1400°F.
Magnification 100X
Etch Murakami

Fig. 206

(276-3B)
Annealed 8 hrs.1400°F.
Magnification 1000X
Etch Murakami

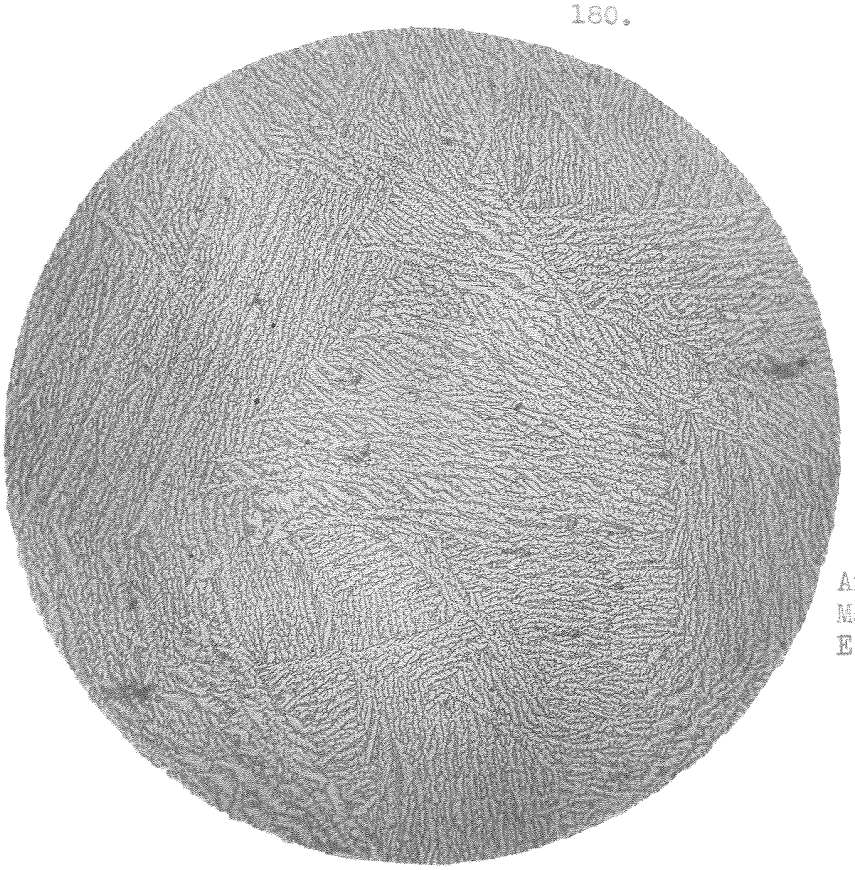

Fig. 207

(276-4A)
Annealed 8 hrs.1600°F.
Magnification 100X
Etch Murakami

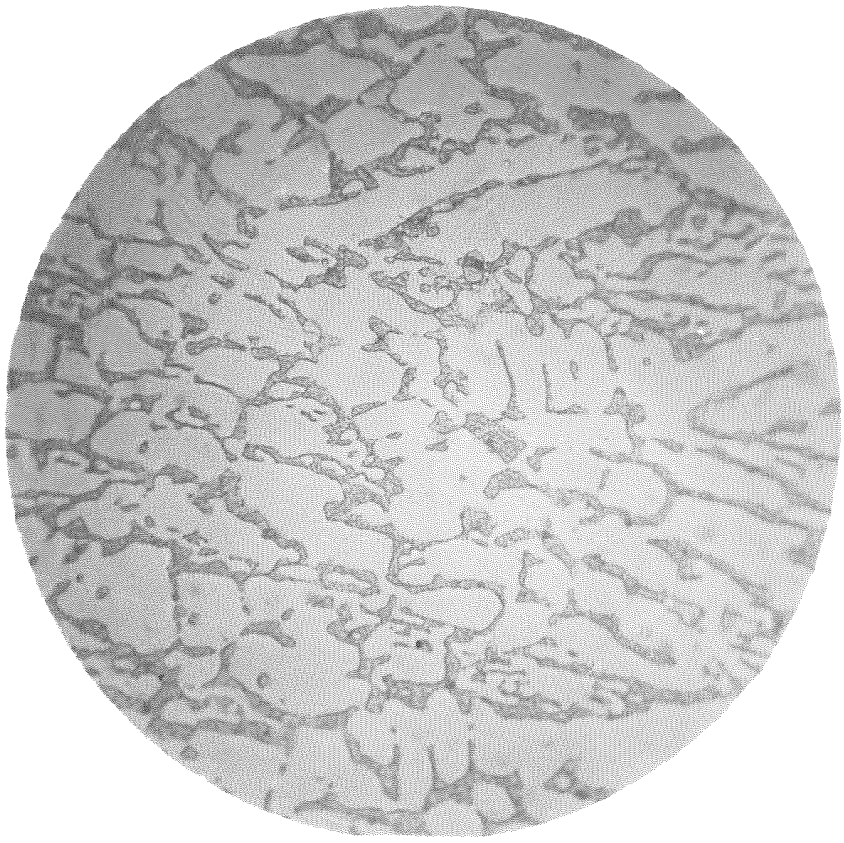

Fig. 209

(276-4B)
Annealed 8 hrs.1600°F.
Magnification 1000X
Etch Murakami

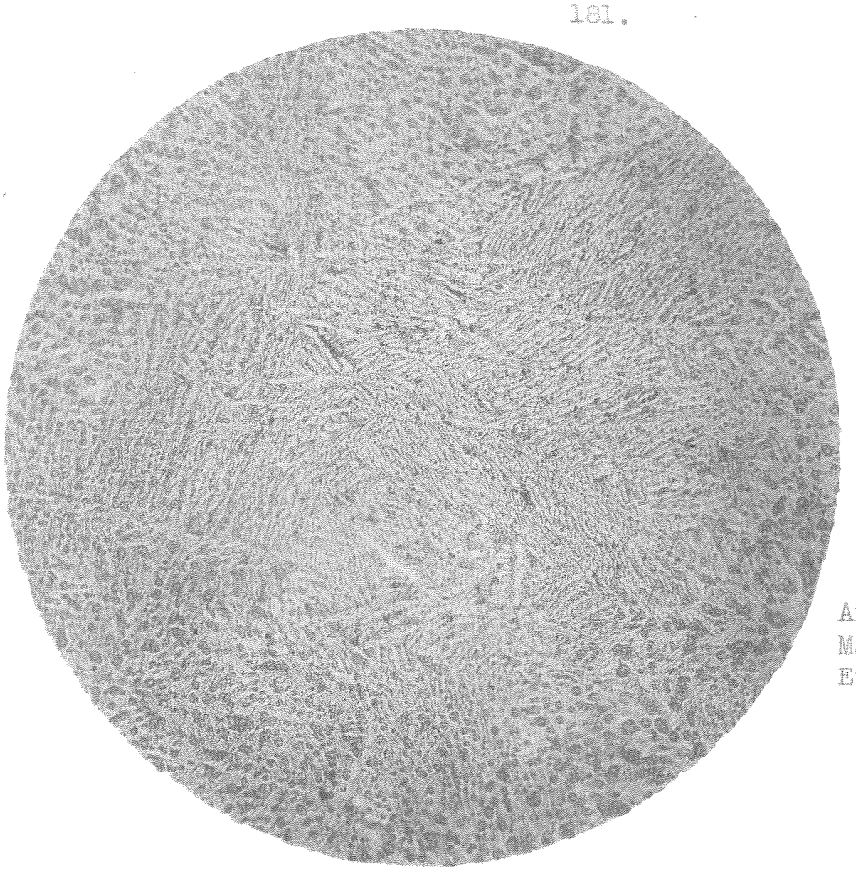

Fig. 210

(276-5A)
Annealed 8 hrs.1800°F.
Magnification 100X
Etch Murakami

Fig. 211

(276-5B)
Annealed 8 hrs.1800°F.
Magnification 1000X
Etch Murakami

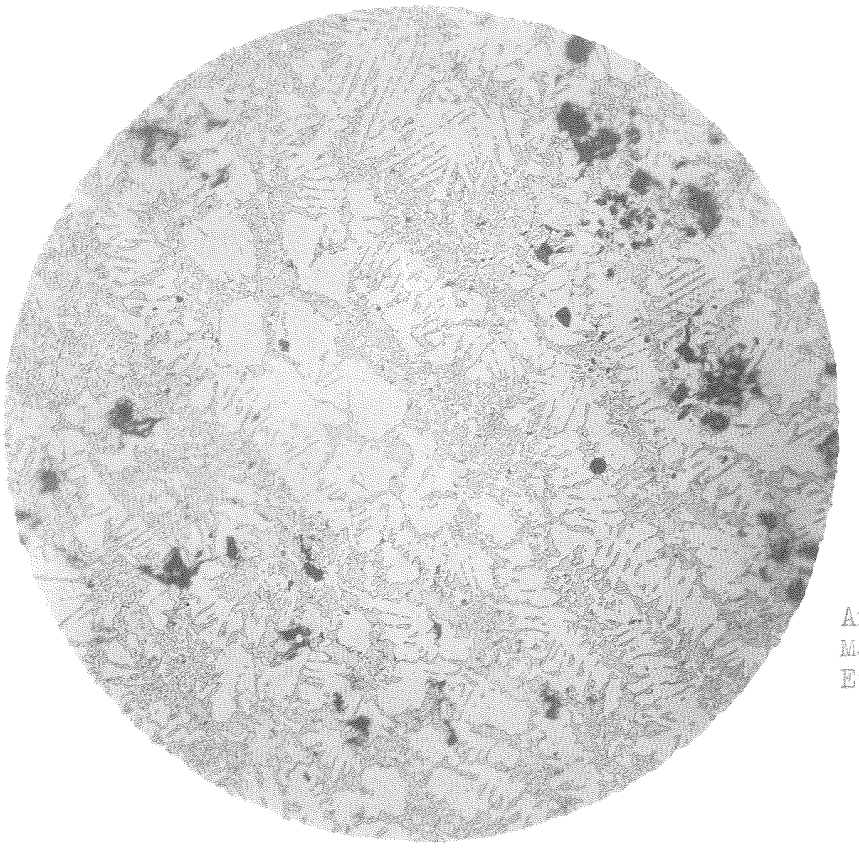

Fig. 212

(248-2A)
Annealed 8 hrs.1800°F.
Magnification 100X
Etch Murakami

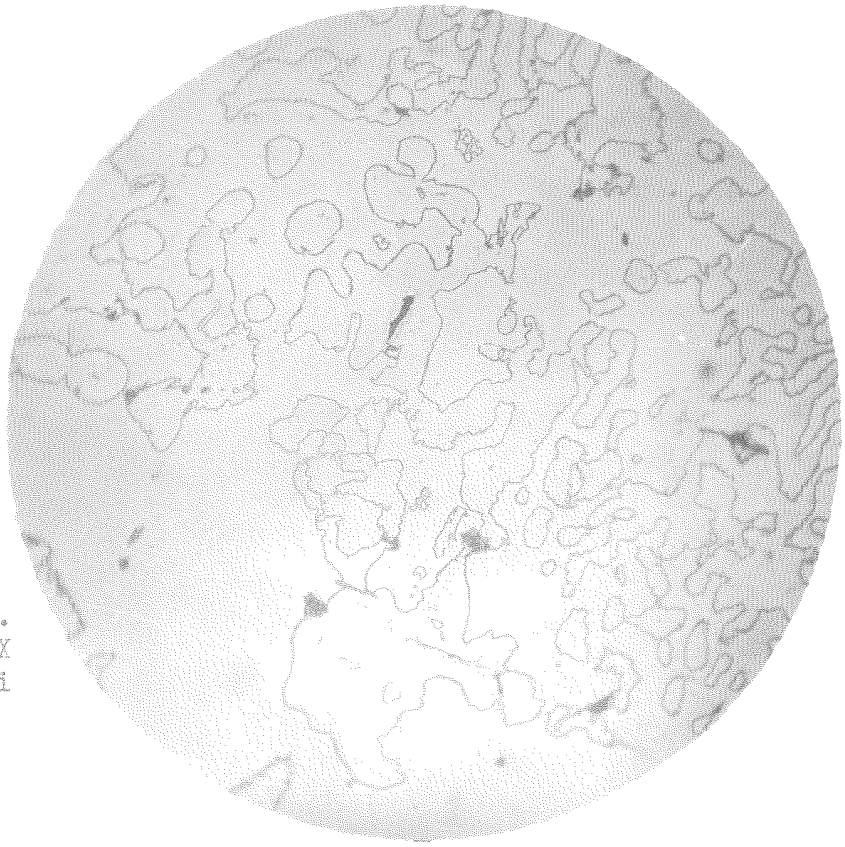

Fig. 213

(248-2B)
Annealed 8 hrs.1800°F.
Magnification 1000X
Etch Murakami

Figures 214 and 215 show the structure of alloy 249, which has been annealed at 1800° F. for eight hours. Comparing this structure with that of Figures 167 to 170, inclusive, about the only change that is noticeable is the loss in the eutectic structure which existed before annealing.

In conclusion to this part of the research, it can be said that upon annealing alloys in the range CNVL the pearlitic structure is broken up and that iron boride is precipitated from solution provided the silicon is low. In the triangular region NVB a loss of the ternary eutectic structure occurs, accompanied by an aggregation of the pearlite and a coarsening of the general structure. In the field BVJ between E_2 and B there occurs a loss of the eutectic structure and a general coagulation of the iron boride contained therein and a general coarsening.

Fig. 214

(249-2C)
Annealed 8 hrs.1800°F.
Magnification 100X
Etch Murakami

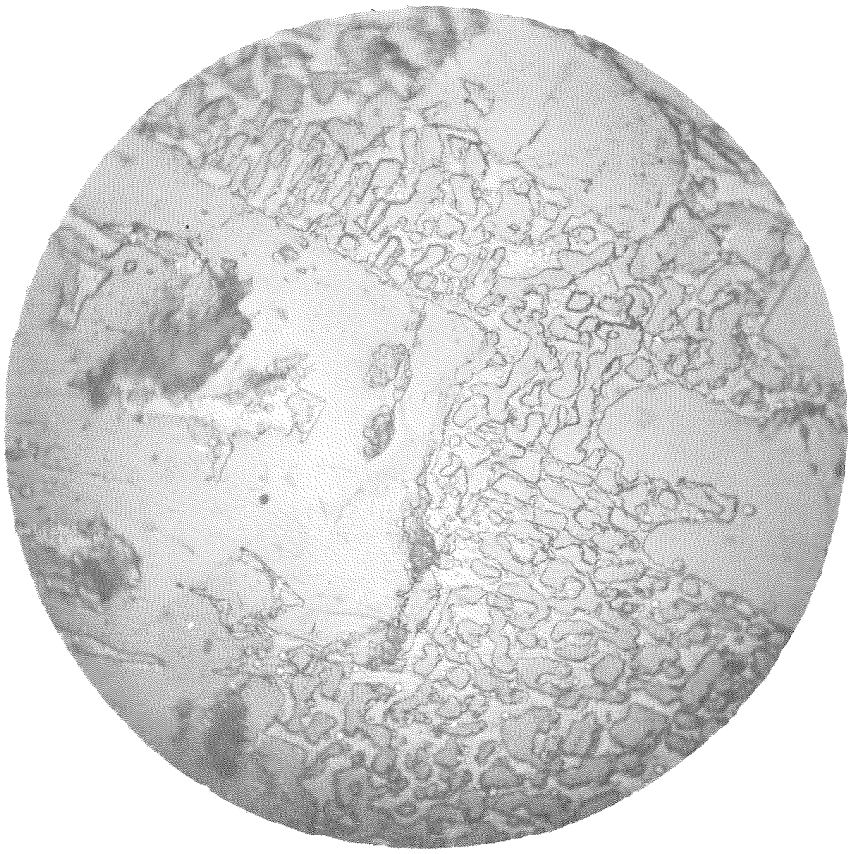

Fig. 215

(249-2D)
Annealed 8 hrs.1800°F.
Magnification 1000X
Etch Murakami

PART III.

PHYSICAL PROPERTIES

The most important considerations in the study of any metal or alloy are those concerning its physical properties. The metallographic structure is important chiefly because of the assistance it gives in explaining why certain properties exist. It is limited in its scope because of the fineness of the metal structure and the limitations of the optical method.

Alloys in this system, containing about three percent carbon and from one or two-tenths to two percent boron, have been found commercially valuable in their resistance to wear. Those alloys which exhibit the quality to resist wear have considerable hardness, of the order of 500 to 800 Brinell. Consequently, in this research some of the alloys in the useful range have been investigated for hardness and transverse strength, in order to have some basis for comparison with other materials. One series has been carried out to determine tensile and compressive strength and modulus of elasticity; another to determine the effect of boron on the thermal conductivity of these alloys.

The alloys used for determining the transverse and hardness properties were cast in sand molds in the form of the standard arbitration bar, thirteen inches long and one and one-quarter inches in diameter. The bars were allowed to cool in the mold. All

specimens were tested by placing them between fulcrums twelve inches apart and applying a load at the center of the bar in the 30,000 pound Universal testing machine. The modulus of rupture referred to as transverse strength was computed from the relation $S = MC/I$, where S is the modulus of rupture in pounds per square inch, M is the maximum moment at the center $(Pl/4)$ in inch pounds, C is the distance from the neutral axis to the extreme fiber in inches. Assuming the neutral axis at the center, C has been taken as equal to the radius. I is the moment of inertia of the section in $(\text{inches})^4$, P the load at the center, and l the length of the specimen in inches. Substitution of the specific values in the general expression gives the relation $S = 30.5\ P/d^3$.

Effect of Composition on Transverse Strength and Hardness

Table III. gives the composition and average results for the alloys used in this work. These results are plotted on a composition diagram shown in Figure 216, on which contours of transverse strength and hardness have been drawn. The values given are the averages of two tests made on each alloy. Table IV. gives the values for each of these tests. In reading this graph, it should be remembered that these alloys are commercial melts and, hence, there is some variation in silicon content which may cause some variation in the results.

TABLE III.

SUMMARY OF TESTS

Spec. No.	% C.	% B.	% Si.	Average Modulus of Rupture lbs/sq.in.	Deflection inches in 12 inches	Hardness Sclero-scope	Hardness Diamond Brinell
247	3.16	1.24	0.78	13,400	0.038	63	
255	3.05	1.40	1.61	21,010	0.020	62	
262	3.73	1.20	1.21	6,245	0.017	71	
268	3.42	0.00	1.44	52,300	0.109	32	235
269	3.67	0.09	1.42	47,500	0.080	43	315
270	3.50	0.22	1.13	52,600	0.041	57	523
271	3.43	0.49	1.16	30,525	0.024	68	649
272	3.28	1.02	0.80	25,100	0.019	66	705
276	3.03	1.70	1.36	32,675	0.025	75	800
292	3.00	0.00	1.50	75,400	0.117	38	286
293	3.00	0.10	-	75,450	0.057	49	496
294	3.00	0.25	-	69,800	0.056	51	479
295	3.00	0.50	-	62,850	0.047	53	556
296	3.00	1.00	-	45,600	0.034	57	567
297	2.5	0.00	-	82,300	0.082	32	356
298	2.5	0.10	-	95,750	0.074	46	425
299	2.5	0.25	-	80,600	0.066	48	462
400	2.5	0.50	-	70,100	0.051	47	506
401	2.5	1.00	-	55,300	0.046	51	522

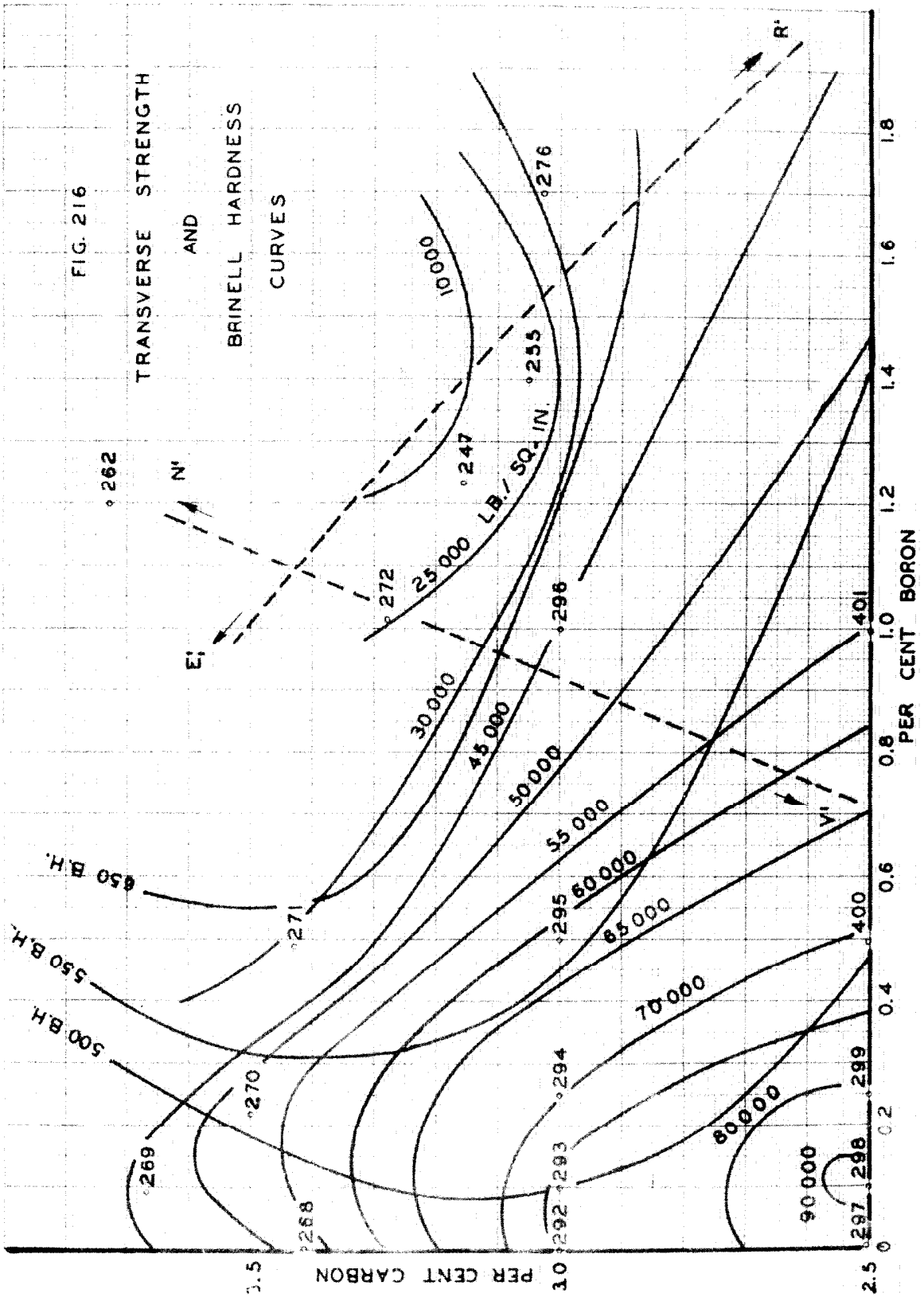
FIG. 216
TRANSVERSE STRENGTH
AND
BRINELL HARDNESS
CURVES
PER CENT CARBON
PER CENT BORON
LB./SQ. IN.
10000
25000
30000
45000
50000
55000
60000
65000
70000
80000
90000
650 B.H.
550 B.H.
500 B.H.
N'
E'
R'
V'
262
269
270
271
272
247
253
276
296
401
294
293
292
295
400
299
298
297

TABLE IV.

TEST DATA

Specimen Number	Diameter Inches	Load Pounds	Modulus of Rupture lbs/sq.in.	Deflection inches in 12 inches
247	1.231	820	13,400	0.038
255-1	1.281	1,450	21,020	0.018
255-2	1.305	1,530	21,000	0.023
262-1	1.275	410	6,030	0.012
262-2	1.278	450	6,560	0.021
268 A	1.274	3,510	51,800	0.107
268 B	1.233	3,240	52,800	0.111
269 A	1.259	3,120	47,800	0.078
269 B	1.231	2,880	47,200	0.083
270 A	1.257	3,060	47,100	0.037
270 B	1.232	3,340	58,100	0.046
271 A	1.261	1,870	28,400	0.025
271 B	1.230	1,860	32,650	0.023
272 A	1.256	1,440	25,100	0.019
272 B	1.23	1,190	19,540	0.016
276 A	1.271	2,190	32,650	0.025
276 B	1.234	2,010	32,700	0.026
292 A	1.26	4,000	61,000	0.090
292 B	1.25	4,860	76,000	0.115
292 C	1.25	4,790	74,800	0.120
293 A	1.24	4,970	79,600	0.059
293 B	1.24	4,460	71,300	0.055
294 A	1.23	4,720	77,300	0.063
294 B	1.24	3,900	62,400	0.050
295 A	1.24	3,890	62,200	0.051
295 B	1.22	3,780	63,500	0.044
296 A	1.24	2,780	44,400	0.032
296 B	1.24	2,930	46,800	0.036
297 A	1.22	4,540	76,300	0.086
297 B	1.24	5,520	88,300	0.074
298 A	1.24	5,820	93,300	0.075
298 B	1.24	6,140	98,200	0.073
299 A	1.22	4,440	74,600	0.054
299 B	1.22	5,150	86,600	0.070
400 A	1.23	4,130	67,700	0.049
400 B	1.23	4,420	72,500	0.054
401 A	1.26	3,380	51,600	0.041
401 B	1.24	3,690	59,000	0.052

From the trend of the transverse strength curves, it is indicated that the highest strength and lowest hardness will occur at about the point V, Figure 103, and also that the hardness increases as we go into the region of excess or primary iron carbide solid solution. This is in agreement with the equilibrium diagram, in that we know a material with larger amounts of iron carbide solid solution possesses inherent hardness. An example of this characteristic hardness is found in iron-carbon alloys containing excess iron carbide.

The hardness determinations were made with a Monotrone hardness testing machine with which several readings were taken and the average values entered in the table.

Heat Treatment

A series of tests was made to determine the general physical properties of the alloys in the region CNVL, Figure 103. For this test alloy 62 was used. More tests were not made because of the expense of grinding the specimens. It was felt that the tests made on this particular alloy would be indicative of the properties of alloys in this region. Another interesting result observed in these tests is the effect of silicon on the physical properties. This particular alloy (62) contains only 0.53% silicon, while the alloys used in the transverse and hardness tests previously mentioned, contained about 1% or more of silicon.

Tests were made of this material in the as cast, annealed, and normalized conditions. Some specimens were quenched in various media, but the data is not included here, since unsatisfactory results were obtained. The specimens to be heat treated were placed in the furnace at 1650° F. for one hour and then cooled, as indicated in Table VI. The summary of average results of these tests are listed in Table V.

Specimens for the tension tests were cast in black-washed sand molds and were allowed to cool to room temperature. The test specimens were ground to a uniform diameter in the working section and given large fillets at the ends to accommodate their support in special grips. The supporting grips were suspended from spherical seats, insuring against eccentric loading. The results of these tests are shown in Table VI.

Specimens for the compression tests were ground to a one inch diameter and a height of one and one-eighth inch. The specimens were placed on spherical heads in the testing machine. The results are given in Table VII.

The specimens for the transverse tests were rough castings of the same dimensions as those previously described. Results are given in Table VIII.

The averages of several Scleroscope hardness determinations on these specimens are reported in the Tables mentioned above.

TABLE V.

Specimen Number	Condition of Material	Tensile Strength #/sq.in.	Compressive Strength #/sq.in.	Modulus of Rupture #/sq.in.	Hardness Scleroscope
D-12	As Cast	19,635	227,000	26,100	64 - 80
D-13	Cooled in Furnace from 1650° F.	24,530	224,000	31,000	57 -61
D-14	Cooled in Air from 1650° F.	22,450	247,500	27,180	69 -76

The Modulus of Elasticity = 34,000,000 lbs. per sq. in.

TABLE VI.

TENSILE TESTS

Spec. No.	Diameter Inches	Area sq. in.	Total Load at Break lbs.	Ultimate Strength lbs./in.^{2}	Sclero-scope Hardness	Condition
1	0.579	0.263	4,830	18,350	65	As Cast
2	0.574	0.259	5,110	19,770	64	As Cast
3	0.568	0.253	4,790	18,920	61	As Cast
4	0.573	0.260	5,600	21,500	66	As Cast
9	0.560	0.246	6,490	26,400	59	Cooled in Furnace from 1650° F.
10	0.565	0.251	5,680	22,650	59	Cooled in Furnace from 1650° F.
7	0.568	0.253	5,890	23,300	69	Cooled in Air from 1650° F.
8	0.581	0.265	5,720	21,600	69	Cooled in Air from 1650° F.

TABLE VII.

COMPRESSION TESTS

Spec. No.	Diam. in.	Area sq. in.	Load at Break lbs.	Ultimate Strength #/sq.in.	Length (L) inches	L/D	Sclero-scope Hardness	Condition
1	0.970	0.739	177,440	240,000	1.094	1.13	75.4	As Cast
2	0.974	0.745	159,460	214,000	1.101	1.13	77.5	As Cast
3	0.970	0.739	164,620	222,000	0.959	0.99	56.9	Cooled in Furnace from 1650° F.
4	0.970	0.739	167,808	226,000	1.110	1.14	61.2	Cooled in Furnace from 1650° F.
5	0.974	0.745	179,790	241,000	1.109	1.14	75.2	Cooled in Air from 1650° F.
6	0.970	0.739	187,720	254,000	1.119	1.15	76.3	Cooled in Air from 1650° F.

TABLE VIII.

TRANSVERSE TEST

Spec. No.	Diameter inches	Area sq.in.	Load at Center lbs.	Deflec. in 12 inches	Modulus of Rupture lb./sq.in.	Condition
1	1.224	1.179	1695	0.02	28,200	As Cast
2	1.223	1.178	1440	0.021	24,000	As Cast
3	1.217	1.161	1600	0.021	27,100	Cooled in Furnace from 1650° F.
4	1.205	1.141	2000	0.030	34,900	Cooled in Furnace from 1650° F.
5	1.225	1.180	1940	0.028	32,250	Cooled in Air from 1650° F.
6	1.215	1.160	1300	0.020	22,100	Cooled in Air from 1650° F.

One of the tension specimens in the as cast condition was used for the determination of modulus of elasticity. The method was to determine deflections for equal increments of applied load over a two inch gauge length. The deflections were determined with a Huggenberger Tensometer which allowed the determination of deflections to 0.0000299 inches in the gauge length. The results of this test will be found in Table IX. The value was found to be thirty-four million pounds per square inch. This is somewhat higher than is found for white cast iron with a value of about thirty-two million pounds per square inch as a maximum.

From this set of tests, it can be concluded that annealing increases the tensile strength and modulus of rupture and decreases the hardness of these alloys. Cooling in air decreases the tensile and transverse strengths over the annealed material, but increases over the as cast condition. The effect of annealing and air cooling is primarily due to the reheating of the cast material thereby obtaining a more uniform structure.

Other specimens were used to determine the effect of quenching on the alloy. Quenching in any media is very detrimental to these alloys, in that large cracks are developed rendering them worthless. The hardness is increased to some extent by quenching, due to the existence of partially decomposed ternary solid solution. The data obtained on these quenching tests is omitted here.

TABLE IX.

STRESS STRAIN DETERMINATION FOR COMPUTATION

OF MODULUS OF ELASTICITY

Total Load lbs.	Unit Load lbs.sq.in.	Total Deflection Reading	Total Deflection Difference	True Deformation in./in.
000		0.62	0	0
500	1900	0.64	0.02	0.0000300
1000	3800	0.68	0.06	0.0000900
1500	5200	0.72	0.10	0.0001500
2000	7600	0.75	0.13	0.0001950
2500	9500	0.79	0.17	0.0002545
3000	11400	0.83	0.21	0.0003145
3500	13300	0.86	0.24	0.0003590
4000	15200	0.90	0.28	0.0004190

D = 0.579 inches

A = 0.263 sq. in.

Thermal Conductivity

The thermal conductivity of alloys in the iron, iron-carbide, iron-boride system has proven to be of considerable interest, because of the particularly low value obtained. A series of alloys, listed in Table X., was used for determinations of thermal conductivity. The coefficients of thermal conductivity were determined by B. H. Sage and Earl S. Hill of the California Institute of Technology by measuring the flow of heat through bars similar in dimension to those used for the transverse tests. In this case all test bars were finished ground. Heat was supplied by an electrically heated brass block soldered to one end of the bar. The quantity of heat flowing through the bar was determined by the rise in temperature of a known stream of water flowing through a similar brass block soldered to the other end of the bar. The rise in temperature of the water was determined by two short range thermometers placed in insulated wells. The rate of flow of water was determined by weighing. The temperature gradient was measured by thermometers inserted at the ends of the bar. Water temperatures were read to 0.02° F. The entire apparatus was heavily lagged and was calibrated by means of a bar of low carbon steel, from which it was found that no correction for heat loss was necessary. The results of these tests are tabulated in Table X. and the values plotted against boron content in Figure 217.

TABLE X.

Spec. No.	Total Carbon %	Graphitic Carbon %	Silicon %	Boron %	Thermal Conductivity B.t.u./hr./sq./ft./ °F./ft.
268	3.42	2.30	1.44	0.00	27.5
269	3.67	2.08	1.42	0.09	20.2
270	3.50	0.18	1.13	0.22	7.5
271	3.43	0.18	1.16	0.49	6.0
272	3.28	0.18	0.08	1.02	5.2
276	3.03	0.22	1.36	1.70	4.6

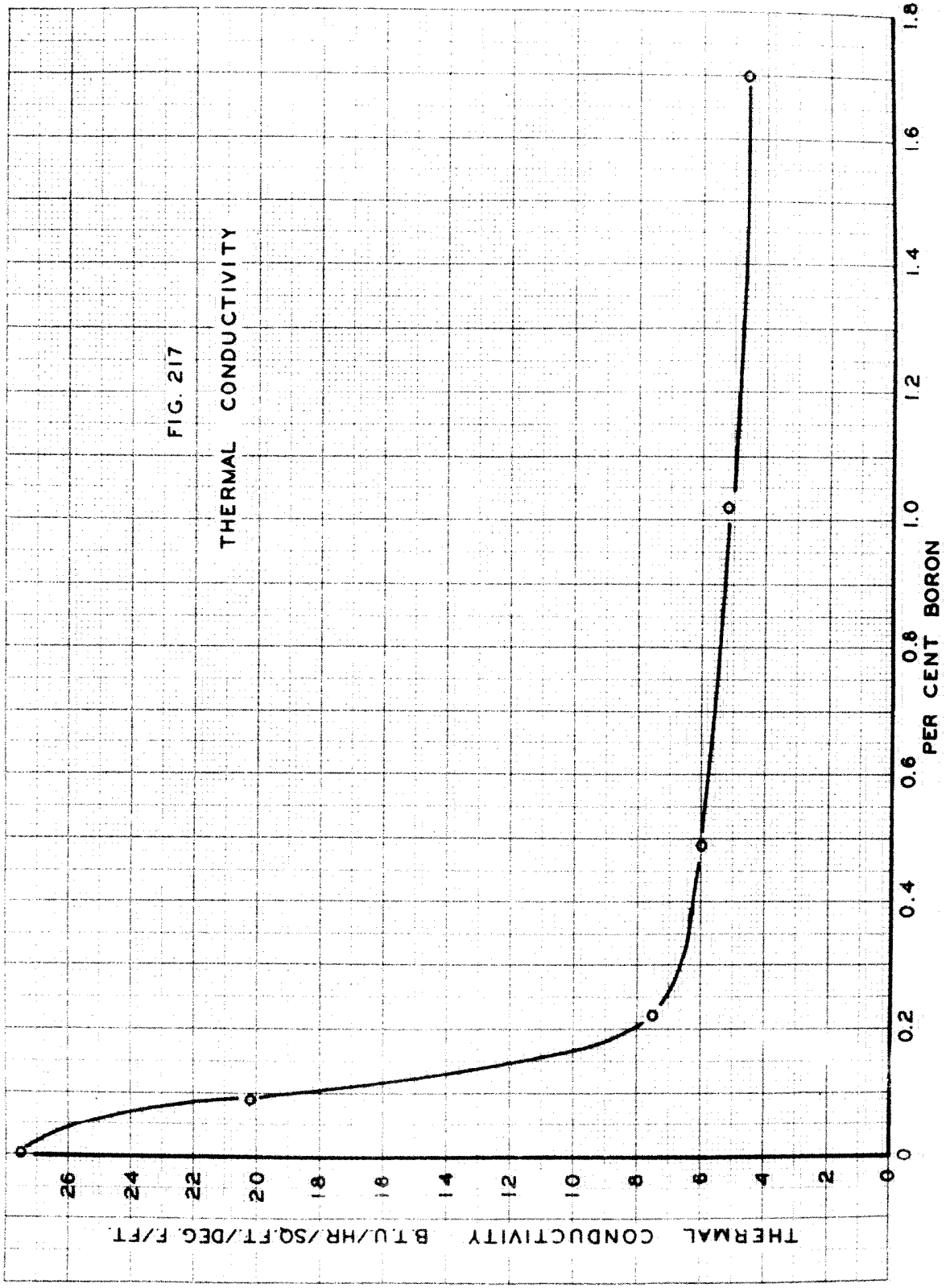
FIG. 217
THERMAL CONDUCTIVITY
THERMAL CONDUCTIVITY B.T.U./HR./SQ.FT./DEG. F/FT.
0
2
4
6
8
10
12
14
16
18
20
22
24
26
0
0.2
0.4
0.6
0.8
1.0
1.2
1.4
1.6
1.8
PER CENT BORON

The effect of boron is very noticeable on the thermal conductivity. It may be noticed that the thermal conductivity decreases very sharply and that the amount of graphitic carbon decreases in about the same way. This fact may account in some way for the drop in thermal conductivity, but the drop in graphitic carbon content can be attributed to the presence of boron.

SUMMARY

(1) As a result of this research the equilibrium relations of the iron, iron-carbide, iron-boride system, as proposed by Vogel and Tammann, have been checked metallographically for the liquid solid transformations throughout the composition range.

(2) The equilibrium relations of the iron, iron-carbide, iron-boride system, as proposed by Vogel and Tammann for the transformations in the solid state, have been checked metallographically in all regions of the system with the exception of that region containing less than about one percent boron. In this case discrepancies were found in the commercial alloys in that the solubility of iron boride in alpha iron was not as great as suggested by Vogel and Tammann. Such solubility was found in alloys containing silicon in excess of one percent.

(3) The solubility of iron boride in alpha iron has been found to be increased by the presence of silicon.

(4) The hardness of alloys in this system has been found to increase with increase of carbon and boron content.

(5) The transverse strength of alloys in this system has been found to decrease with increase in carbon and boron content to a very low value.

(6) Annealing of the alloys in the iron, iron-carbide, iron-boride system has been found to cause coagulation of iron

boride in the metallographic structure.

(7) Annealing of alloys in this system has been found to increase slightly the transverse strength and tensile strength without great loss in hardness.

(8) The thermal conductivity of iron, iron-carbide, iron-boride alloys containing about 3.5% carbon has been found to be decreased from 27.5 to 4.6 B.t.u./hr./sq.ft./° F./ft. with increasing boron content of from zero percent to 1.7%.

BIBLIOGRAPHY

Ternary System Fe-B-C, - Vogel & Tammann
Z. anorg. allgem. Chem. 123, 225-275.

Fe-B Alloys, - Richards
J. Ind. Eng. Chem. 10, 851-854.
Chem. Met. Eng. 19, 501-504 (1918).

Fe-B, Lievenie,
L'age de fer 36, 733-735 (1920).

Preparation of Ferro-Boron, - Parravano & Mazzetti
Atti. cong. noz. chim. appl. 1923, 258-259.

Reduction of Boron, -
Patent British 160, 427 March 18, 1921.

Reactions of Boron and Iron, - Tammann & Schaarwachter
Z. anorg. allgem. Chem. 167, 401-410 (1927).

X-Ray Analysis of Fe-B System, - Bjurstrom & Arnfelt
Z. physik Chem. Abt. B, 4, 469-474, (1929).

System Fe-B, - Wever & Müller
Mitt. K. W. Inst. Eisen f. Dusseldorf, 11, 193-223 (1929).

Fe-B Alloys, - F. Wever
Z. tech. Physik 10, 137-138 (1929).

Binary Systems with Boron, - Hägg
Z. physik Chem. Abt. B, 6, 221-232 (1930).

Binary System Fe-B, - Wever & Müller
Z. anorg. allgem. Chem. 192, 317-336 (1930).

Effect of Boron on Grey Iron, - Smith & Aufderhaar
Iron Age 126, 1583-1587, 1688-1693, (1930).

Alloyed Castings, - Kothny-Giesserei
Ztg. 27, 291-300, 323-327, (1930).

Hardening Phenomenon of Fe & B. Alloys, - Wasmuht
Arch. Eisenhutten. 5, 261-266 (1931-32).

Iron Boron Alloys & 18-8 Steels, - Wasmuht
Metals & Alloys 3, 105-110 (1932).

Hardness of Iron-Boron Alloys, - Wasmuht
Krupp Monatsch 12, 273 (1931).

Boron Alloys, -
Patent British, 20, 377 Sept. 1907.

Effect of Boron on Magnetic and Other Properties of Electrolytic Iron Melted in Vaccua, - Yensen
Univ. Ill. Exp. Sta. Bul. 77 (1915).

Behavior of Boron Towards Nickel, - Giebelhausen
Zeit. anorg. Chem. 91, 251-262 (1915).

Iron-Boron & Iron-Carbon Alloys, - Cheywskii & Herdt
Iron Age 98, 396-397 (1916).

Solid Solution of Manganoboron & Ferroboron, - Hoffmann
Chem. Ztg., 34, 1349-1350

Making Ferroboron, - Hansen
Patent U.S., 982,135 Jan. 17

Goldschmidt's Ferrous & Manganous Borides & Ignition Residue, -
Chem. Ztg. 34, 1045-1046

Making Ferroboron in Electric Furnace, - Tone
Patent U.S. 1,035,919 Aug. 20

Production of Boron Alloys, - Halvorsen
Patent Norw. 20844 Oct. 19, 1909.

Study of Magnetic Properties of Alloys of Fe, Co., Ni, Mn, with B, - Jassoneix
Orig. Com. 8th, Intern. Congr. Appl. Chem. 2, 165-174.

Boron Iron or Steel, -
Patent Japan 42,203 April 4, 1922.

Cementation of Iron or Steel with Boron, - T. Miyaguchi
Patent U.S. 1472850 Nov. 6; U.S. 1472851
Patent British 193,917; British 193,918.

Manufacture of Ferroboron or Boron Steel, - Miyaguchi
Patent British 195,678 Nov. 3, 1921.

Case Hardening Iron with Boron, - Chiyevski
J. Iron & Steel Inst. (Advanced Copy) 1917, 3 pages.

Case Hardening of Steel by Boron and Nitrogen, - Campbell & Fay
Ind. Eng. Chem. 14, 719-723 (1923).

Alloys Containing B, Cr., & Fe., - A. G. de Golyer
Patent U.S. 1,493,191 May 6.

Cementation of Fe., Ni., & Co., by Means of Boron, - Fesczczenko-Czopowsk
Trav. ac. miens. Cravovie 1925 No. 5.
Rev. metal 23 (Extraits) 267-268 (1926).

Cementation by Means of Boron, - Parrovano & Mozzetti
Atti. accad. Lincei (V) 31, ii, 424-425 (1922).

Experiments with Rare Metals in Steels, - Gillett & Mach.
Trans. Am. Electrochem. Soc. 43, preprint (1923).

Cementation of Boron into Iron, - T. Miyaguchi
Patent British 193,918 Nov. 3, 1921.

Boron Steels, - Freytag & Jenge
Mitt. Vers.-Anst. Dortmunder, Union 1922, 9-21.

Boron in Iron Alloys, - Walter
Patent U.S. 1,519,388 Dec. 16.

Ternary System Fe.-Ni., - Chiyevskii & Mekhailovskii
Rev. soc. russe metal I, 547-559, (1915).
Rev. metal (Extracts) 14, 16-21 (1917).

Alloys for Tools, Etc., - Lohmann
Metall. Ges.
Patent British 157,774 Jan 10, 1921.

Fe Alloy Containing 0.75-4% Boron, - Pacz
Patent Canada 294,853 May 19, 1925.

Alloy for Cutting Tool, - Wessler
Patent Canada 273,209 August 16, 1927.

Wear Resisting Alloy, - Field & Franks
Patent U.S. 1,626,726 May 3.

Cementation of Fe., Steel, Ni., & Co. with B. & Be, - Fetchenko & Tchopeivski
Collected Papers from Przegladu Techniczego 1926, 525-530, 545-547, 657-660, 692-694, 705-707; 1927, 73-78, 787-792, 832-836.
J. Inst. Metals 38, 460.

Alloy for Welding Rods, - Franks (to Oxweld Acet. Co.)
Patent U.S. 1,671,417 May 29.

Ferroboron & Boron Steel, - Miyaguchi
Patent U.S. 1,674,119 June 19.

Hard Metallic Alloys, - Lohmann
Patent U.S. 1,652,027 Dec. 6.

Manufacture of Sheets Containing Si. or B. (Core Sheets), - Siemens & Halske A. G.
Patent German 469,368 Jan. 10, 1925.

Action of Addition Elements in Steel, - Persoz
Aciers. spec. 3, 249-255 (1928)
Foundry Trade Journal 40, 181-182 (1929).

Binary System Fe.-B, Fe.-Be., Fe.-Al., - Wever & Müller
Mitt. K. W. Inst. Eisenforsch, Düsseldorf 11, 193-223 (1929).

Hard Compound for Making Tool, - Deiner
Patent German 504,484 Feb. 13, 1926.